COMPUSOFT

ENGINEERING

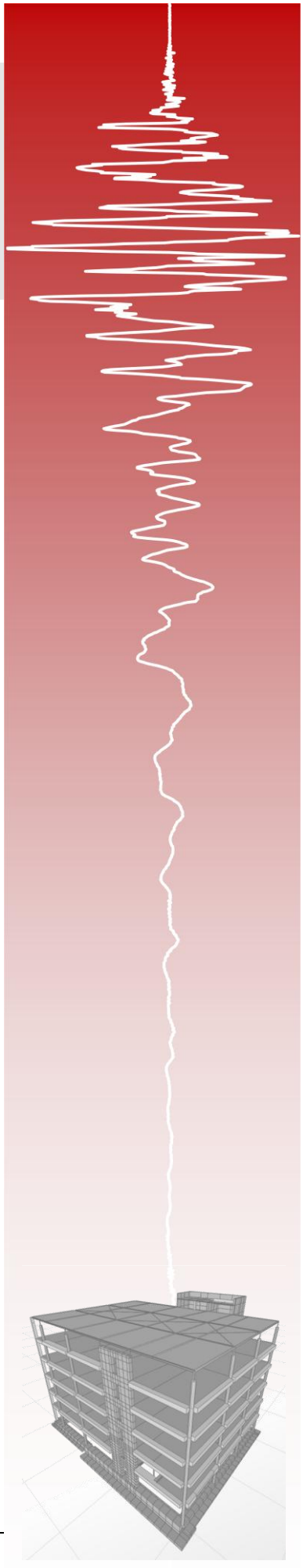

CTV Building

Non-Linear Seismic Analysis Report

Ref: 11033-00

Revision 0

February 2012

Prepared by: Derek Bradley

Tony Stuart

Reviewed by: Dr. Barry Davidson

For: StructureSmith Ltd and

The Department of Building & Housing

Compusoft Engineering Limited, PO Box 9493, Newmarket, Auckland, New Zealand.
Telephone: +64 9 522 1456 www.compusoftengineering.com

Revision History

Revision number	Date of Issue	Report status
0	9 February 2011	Formal Issue

Limitations

This report has been prepared for StructureSmith Ltd and the Department of Building & Housing, and the findings presented within the report are for their sole use. The findings are not intended for use by other parties, and may not contain sufficient information for the purposes of other parties or other uses. The client will place no reliance on any draft reports, incomplete documents, and/or verbal advice.

Compusoft Engineering Limited undertakes professional services using a degree of care and skill normally exercised, under similar circumstances, by reputable consultants practicing in this field at the current time. No other warranty, expressed or implied, is made as to the professional advice presented in this report.

Contents

List of figures

List of Tables

1. Introduction

Compusoft Engineering Limited was engaged by StructureSmith Ltd to undertake a non-linear seismic analysis of the CTV building which collapsed as a consequence of the 22nd February 2011 Lyttelton aftershock. It is the intent that the analyses outlined within this report further enhance the understanding of the CTV performance during the 4th September 2010 Darfield earthquake, and the February 2011 Lyttelton aftershock.

The non-linear analyses outlined in this report are intended to;

- Assist with the identification of the probable sequence of failure.
- Report displacement and storey drift demands, identifying the onset and progression of damage throughout the structure.
- Monitor seismic demands on critical structural elements.
- Determine whether column hinging is expected, and if so, to what extent.
- Investigate the significance and effect of vertical accelerations on the performance of the structure.
- Investigate the variances in structural form i.e. the contribution of the masonry infill panels, and precast spandrel panels to the seismic response and performance of the structure.

The models used for all analyses have been based on building geometry, record structural drawings [1], material tests [2], along with published guidance on the hysteretic behaviour of detailing present within the CTV building.

2. Building description

The CTV building was a 6 storey structure of reinforced concrete construction with plan dimensions of approximately 31 m by 23 m. An overall impression of the complete structure is shown in Figure 1. Construction consisted of 200 mm thick in situ composite concrete Hi-Bond floors supported by precast concrete half-beams, shell beams and in situ concrete columns. A lightweight roof was supported from concrete columns that cantilever off the level 6 floor plate. At the north of the building a series of 300 mm thick reinforced concrete walls were used to support a stair and lift core that projects two storeys above the upper floor plate. A 400 mm thick reinforced concrete coupled shear wall system was situated on the south face of the building. These walls were considered to form the primary seismic resisting system. Frame action was engaged through stiffness compatibility with the walls and contributed to the overall lateral resistance of the structure, particularly the torsional resistance. Figure 2 below indicates the reinforced concrete framing and wall elements that were present (note that the model is presented with north oriented to the right). Foundations were comprised of pads supporting the internal columns, with a series of in situ concrete inverted 'tee' beams supporting the perimeter columns and walls as shown in Figure 3. Inter-storey height was typically 3.24 m with 3.70 m for the bottom storey (3.825 m to top of foundations).

The lower 3 levels of the western perimeter frame were in-filled with reinforced concrete masonry panels. An additional feature was a series of precast concrete spandrel panels that were present on the north, east, and south perimeter frames.

Terminology used to describe floor levels within this report has been selected to match that used in the record structural drawings and ongoing investigation reports, with ground floor referred to as level 1, and the level 1 columns spanning between levels 1 and 2.

Figure 4 presents the building grid system used in both the original design and the analysis model.

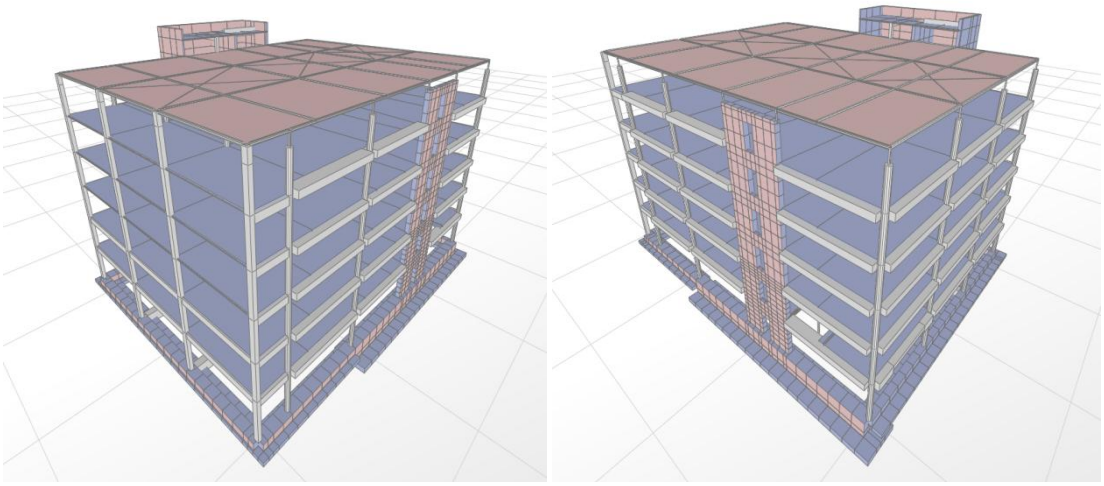

Figure 1: Overall view of the CTV structural model (viewed from SW & SE respectively)

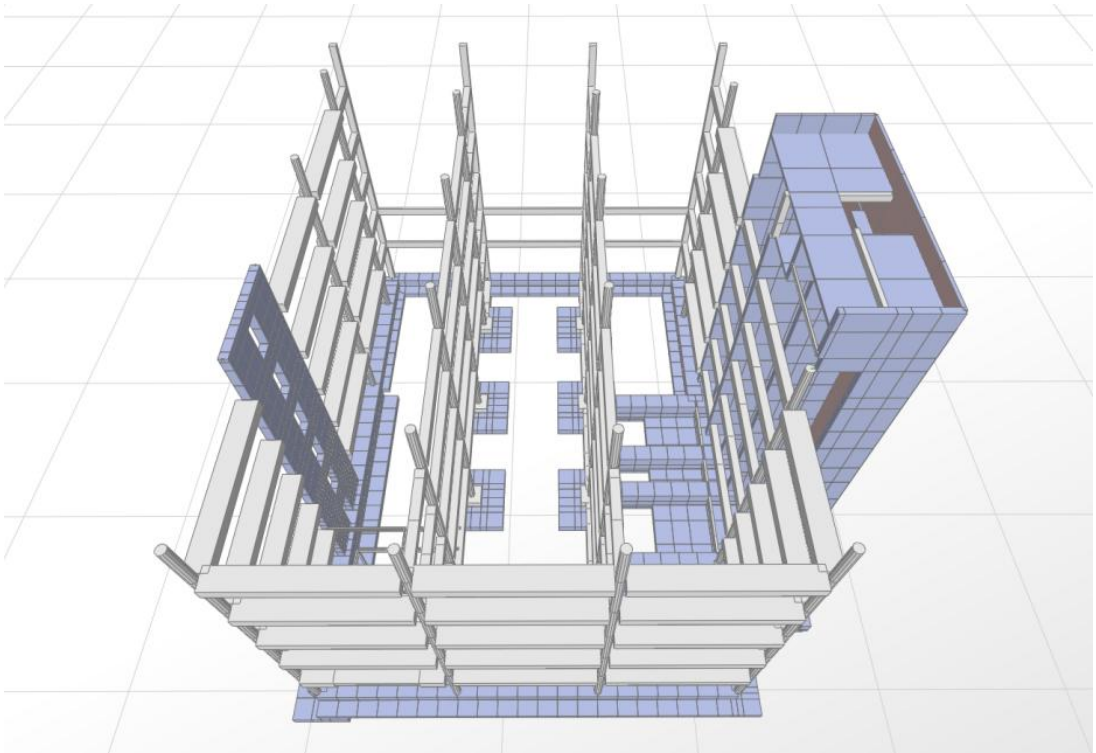

Figure 2: CTV structural model viewed from the east (slabs omitted for clarity)

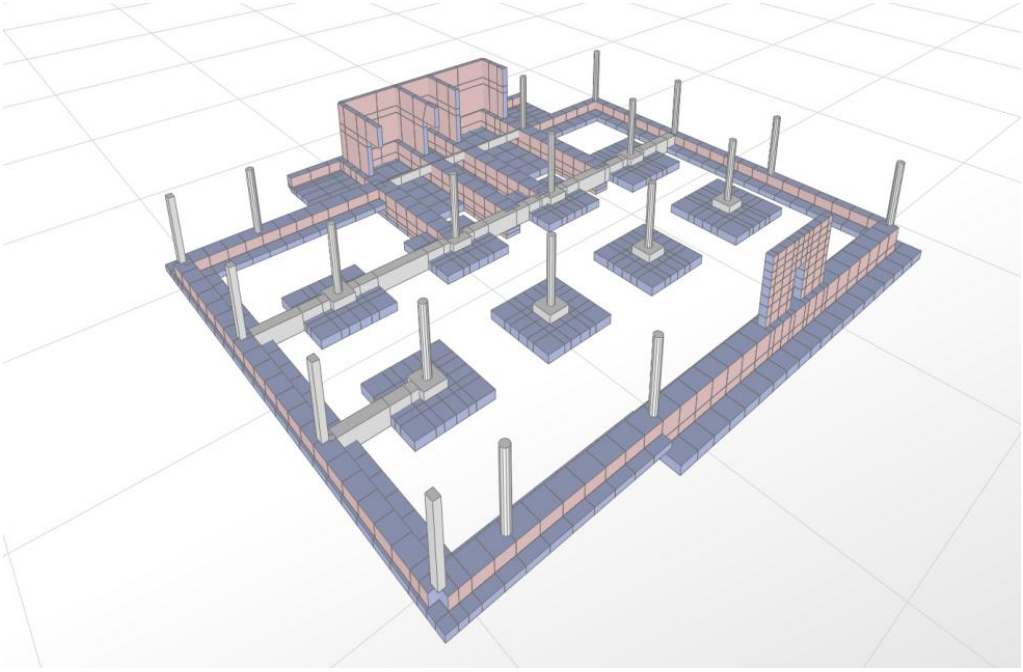

Figure 3: CTV foundation arrangement viewed from the south-west.

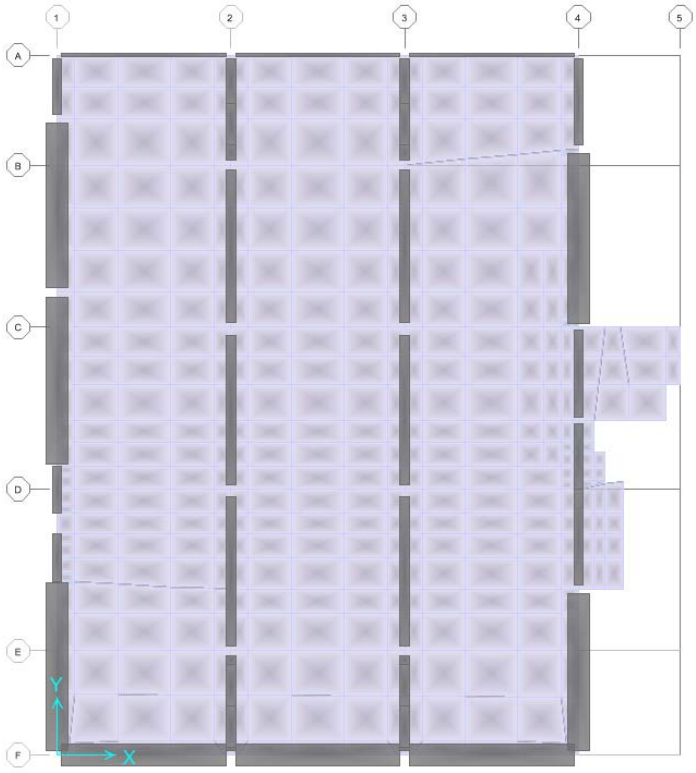

Figure 4: Building Grid System.

3. Analysis Procedure Overview

Three dimensional models of the building were formed using the SAP2000 Advanced (v14.2.4) [3] finite element program. These models were used to evaluate the seismic actions using non-linear pushover, and non-linear time history methods in accordance with accepted good practice, and recent advances in the understanding of the seismic performance of structures.

As requested by StructureSmith the analysis of the CTV building has investigated/considered three different structural configurations denoted „*MODEL A*", „*MODEL B*", and „*MODEL C*" as outlined below;

- MODEL A - *Concrete walls and frames only*
  Reinforced concrete frames and shear walls are considered to be the only structural elements that resist seismic actions. Masonry infill panels and precast concrete spandrel elements are assumed to be effectively isolated such that that they cannot influence the seismic response and performance of the building.
- MODEL B - *Model A with masonry infill*
  The structural form described in MODEL A above except the masonry infill panels are not effectively isolated from the frame elements and will contribute to the seismic response.
- MODEL C - *Model A with precast spandrel panels*
  The structural form described in MODEL A above except the precast spandrel panels are assumed to interact with the frame elements and will contribute to the seismic response.

The overall seismic analysis procedure for the CTV building consisted of the following stages:

1. Undertake a non-linear gravity analysis on the structure using suitable imposed loadings and allowing for deformations of the foundation system.

2. Undertake a nonlinear static pushover analysis of the structure for the two primary directions starting from the end state of the gravity analysis. This

enables a better understanding of the non-linear performance of the structure to be developed, and helps to partially verify assumptions of the adopted analysis parameters. Pushover analyses results to be reviewed and the model adjusted as necessary.

3. Align the axes of the ground acceleration records from the September 2010 and February 2011 events to the principle axes of the CTV Building. Note that the three ground acceleration records used have been assessed by Tonkin & Taylor [4] as the most appropriate for the CTV site from the nearby records that are available.

4. Undertake non-linear time history analyses using a selected time history record for the September 2010 event. Initially undertake analyses for each of the primary directions separately and then perform an analysis that incorporates all directions of the acceleration time history record including the vertical component. Analyses to assume that there is no pre-existing structural damage.

5. Post-process results, and check results for the selected earthquake record versus observed performance and damage level following the September 2010 earthquake.

6. Review appropriateness of the record with regard to matching reported damage to that observed and re-assess assumptions on non-linear input data as necessary.

7. Undertake a non-linear time history analysis using the three adopted time history records for the February 2011 event. Analyses to assume no pre-existing structural damage.

8. Process results and review performance.

Note that this process was performed for *MODEL A* and *MODEL B* as identified above, although *MODEL B* was subject to fewer earthquake records. Only steps 1 and 2 were undertaken for *MODEL C*.

4. Material Properties

4.1. Concrete

The mean in situ unconfined compressive strengths of the concrete elements have been evaluated via two methods as below:

1. Testing of core samples taken from structural components of the structure [2].
2. NZSEE guidelines [5] which recommend that the mean strength of in situ concrete can be taken as 1.5 times the specified lower characteristic design strength. Ground beams properties have been assessed using this method.

Where not demonstrated through testing, the elastic stiffness of the concrete has been derived following the provisions of NZS3101:2006, Cl5.2.3 [6] as below:

$$E_C = 3320\sqrt{f_c'} + 6900\ (MPa)$$

Where f_c' is taken as the mean in situ unconfined strength of concrete (in MPa).

Where the nonlinear behaviour of concrete material is included in the analyses the stress-strain properties as presented in Figure 5 and Table 1 below have been adopted. These relationships have been used in the determination of capacities and element stiffness throughout.

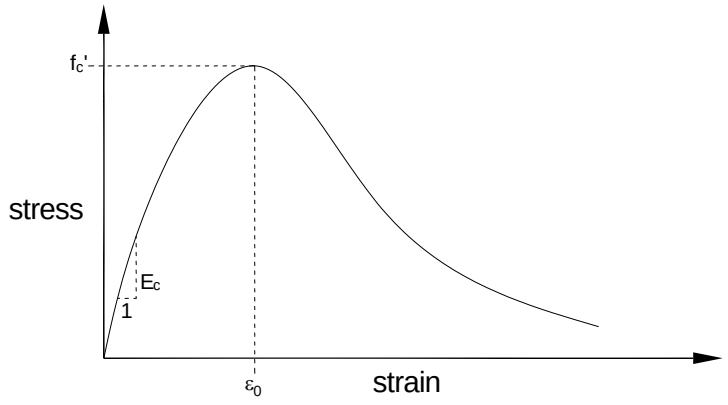

Figure 5: Concrete stress-strain curve

Table 1: Concrete stress-stain parameters

Material	f_c' (MPa) Specified	f_c' (MPa) Expected (NZSEE)	$f_{c\ mean}'$ (MPa) Tested	f_c' (MPa) Adopted	E_c (GPa)
PC Beams	25	37.5	25	25	23.5
Ground beams	20	30	Not Tested	30	25.1
Columns L1 - L2	35	52.5	- (16)[4]	37.5 (16)[4]	27.2 (20.2)[4]
Columns L2- L3	30	45	25.3	32.5	25.8
Columns L3- Roof	25	37.5	27.6	27.6	24.3
Floor Slabs	25	37.5	24.7	24.7	23.4
Shear Walls	25	37.5	33.5	33.5	27.6[3]

Notes:

1. ε_0 to be taken as 0.002 throughout.
2. ε_{cu} to be taken as 0.004 [7].
3. Average value determined via testing [2].
4. Value in parentheses are for column C18 (GL D/E 4) at Level 1.

4.2. Reinforcement

Reinforcing steel stress-strain properties have been determined from testing of materials extracted from the as-built structure. Where no test data is available, material properties have been adopted which are consistent with the period in which the structure was constructed [8]. Nonlinear behaviour of reinforcement material has been included in the analysis using the stress-strain properties presented in Figure 6 and Table 2.

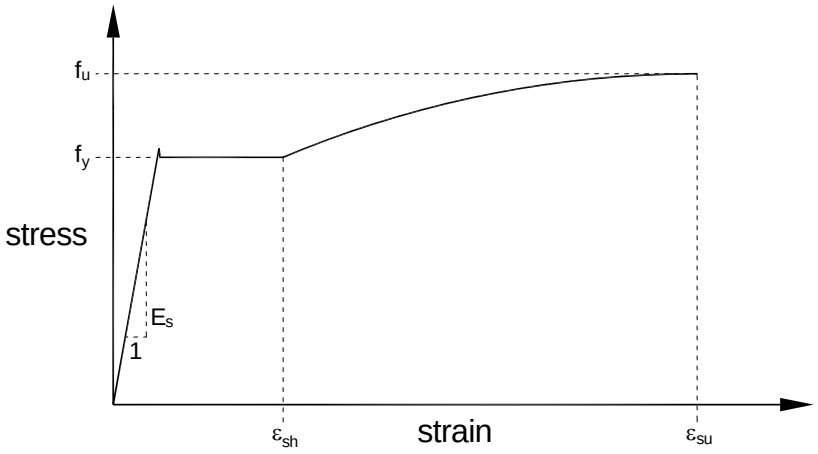

Figure 6: Reinforcing steel stress-strain curve

Table 2: Reinforcing steel stress-strain parameters.

Grade	Es (GPa)	fy (MPa)	ε_{sh}	ε_{su}	fu (MPa)
G275	205	321.3	0.0220	0.202	451.0
G380	205	448[1]	0.0097	0.168[1]	603[1]
664 Mesh	205	615[1]	0.01	0.042[1]	665[1]

Notes:

1. Mean values obtained via testing [2]

5. Structural Elements

5.1. Soil Structure Interaction

In order to incorporate the potential lift-off of foundation elements in the model, non-linear link elements have been incorporated that represent the gapping behaviour of the foundations. Soil stiffness was considered to behave in a linear manner for compressive strains, with applied soil stiffness as determined by Tonkin and Taylor as being most likely for the soil conditions at the site [4].

It is expected that modelling the effects of any period shift due to foundation flexibility through gapping would outweigh the potential benefits of modelling the plastic behaviour of the soil [9]. No allowance was made for any suction that may be present between the soil and underside of the foundation beams. Table 3 and Figure 7 present the soil stiffness and foundation designation used in the analysis, with additional information presented in Appendix C. Based upon post earthquake inspections of the site it has been considered that the level of liquefaction observed would not have had a significantly adverse affect on the performance of the building and as such the effects of liquefaction have not been considered [4].

5.2. Foundation Elements

The foundation system consists of a series of large reinforced concrete pads and flanged ground beams. The pads are modelled using shell objects with suitable thickness. The ground beams are typically modelled as an assemblage of shell objects to form the overall section and provide the necessary bearing area. Effects of backfill present on top of the foundations has been considered assuming that only the soil contained within vertical planes bounding the foundation width is able to be mobilised, and has a soil density of 18 kN/m^3.

Table 3: Expected soil stiffness

Foundation Element	Compressive Stiffness (MN/m^3)
1	122.7
1a	130.89
1b	65.98
2	85.4
2a	53.14
3	117.22
3a	78.59
4	159.69
4a	73.94
5	104.35
6	185.42

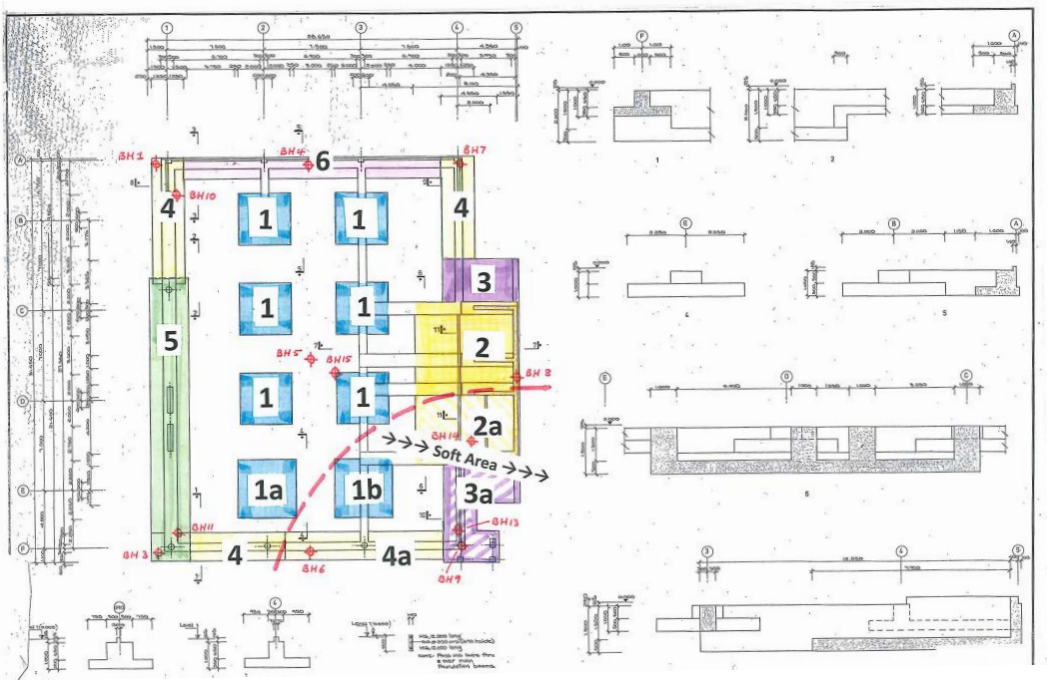

Figure 7: CTV foundation element location plan [1]

5.3. Reinforced Concrete Frames

Reinforced concrete frames consisting of beam and column elements are incorporated in the analysis model as elastically responding frame elements. To account for the effects of concrete cracking, the effective elastic stiffness of the reinforced concrete frame sections has been determined based upon the moment-curvature relationship [7] as below:

$$EI_{eff} = \frac{M_Y}{\phi'_Y}$$

where „M_y" is the first yield bending moment, and „ϕ_y" is the curvature at first yield using material strengths as per Section 4, member geometry and reinforcement as specified in the record drawings. Figure 8 below presents the effective stiffness relationships used for the columns in the analysis model, with the effective stiffness properties from NZS 3101:2006 [6] shown for comparison. Table 4 presents the stiffness modifiers used for a selection of beams.

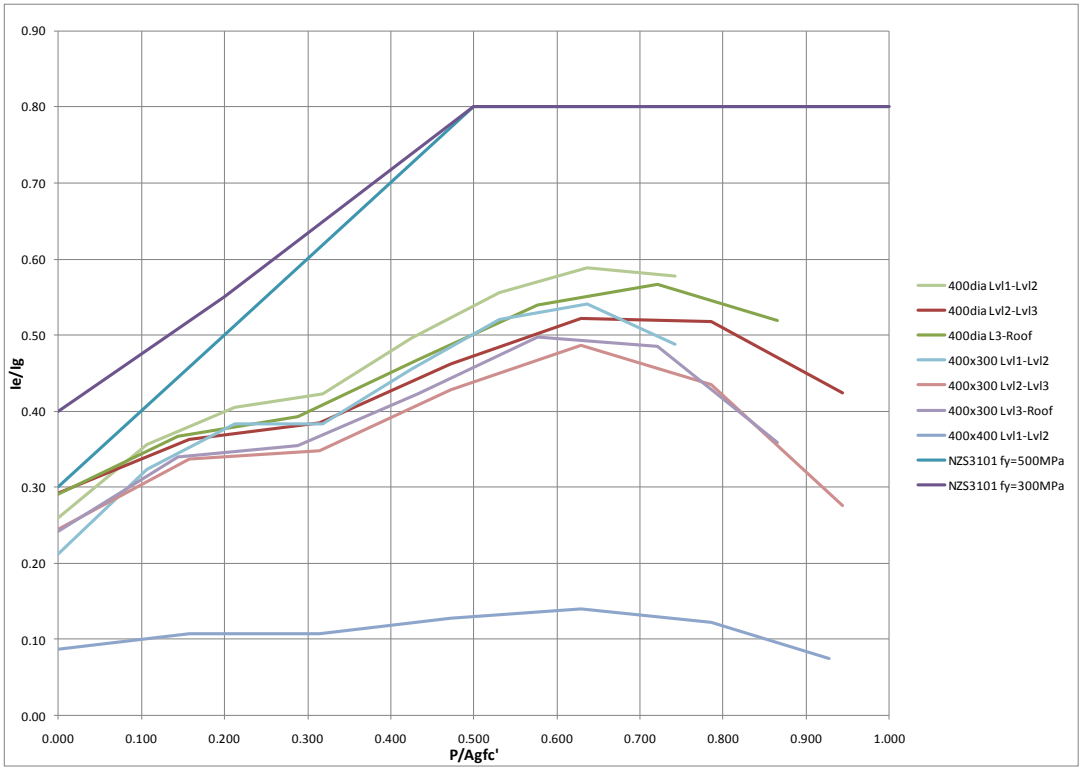

Figure 8: Effective column stiffness relationship.

Table 4: Stiffness modifiers for elastically responding beam elements.

Structural Component	Effective Section Property, I_e
GL C Core Ground Beam (rect)	0.64 I_g
GL C/D Core Ground Beam (rect)	0.25 I_g
GL D/E Core Ground Beam (rect)	0.39 I_g
GL 1 2m Ground Beam (tee)	0.31-0.39 I_g
GL 3 Ground Beam (rect)	0.22-0.49 I_g
Typical 550x400 Beam (tee)	0.43 I_g
Typical 550x960 Beam (L)	0.20 I_g

Inelastic material behaviour for the beams and columns is incorporated by way of discrete hinges that are defined as appropriate for the section properties and expected hysteretic behaviour. This is discussed in the following sections.

5.3.1. Column Hinges

Column hinges are incorporated to represent the non-linear flexural behaviour of the columns. These hinges have been defined as rigid plastic, isotropic interacting M-M hinges i.e. hinges that yield based upon the interaction of biaxial bending moments at the hinge location. This approach has been undertaken in order to improve speed of solution, efficiency, and analysis stability. It should be noted that these hinges do not incorporate strength degradation during hysteretic cycling, and have no plastic rotation limitations applied. As a consequence of this the analysis will progress past the point at which theoretical column failure would occur. The benefit of this approach is that trends in the building performance can be better examined, as the analysis will not be terminated upon reaching the first instability. Column hinge performance will therefore be required to be assessed post-analysis.

Hinge capacity has been determined using the interaction surface for each column section using material properties outlined in Section 4 and the gravity axial action present at the time of the earthquake as detailed in Section 6. Moment-curvature analyses incorporating the identified gravity load has been used to determine hinge moment rotation behaviour.

The adopted column plastic hinge length (L_p) considers strain penetration (L_{sp}) into the beam-column joint zone and has been determined using the following relationship [7]:

$$L_p = kL_c + L_{sp} > 2L_{sp}$$

where,

$$k = 0.2\left(\frac{f_u}{f_y} - 1\right) \leq 0.08$$

$$L_{sp} = 0.022 f_{ye} d_b$$

and L_c is the length between the critical section and the point of contra-flexure in the member under consideration.

Hinges are located at the top and bottom of the column section adjacent to the beam face. Figure 9 below indicates the typical reinforcement arrangement for a 400 mm diameter and a 400 mm x 300 mm column.

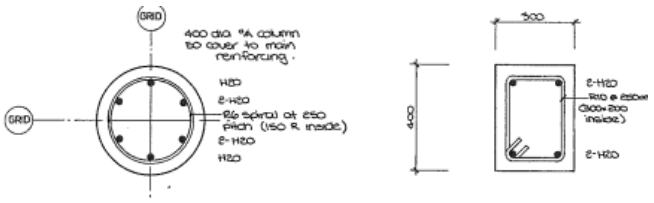

Figure 9: Typical column reinforcement. [1]

Examination of the eccentric column connection between the top of the column located at grid 4 D/E (referenced as C18 on the structural drawings) and the north core wall as seen in Figure 10, has indicated that the detailing present is not capable of transferring the significant axial forces that would result from moderate seismic demands. As such, this connection has not been included in the analysis model, with column C18 assumed to behave as a cantilever above Level 6.

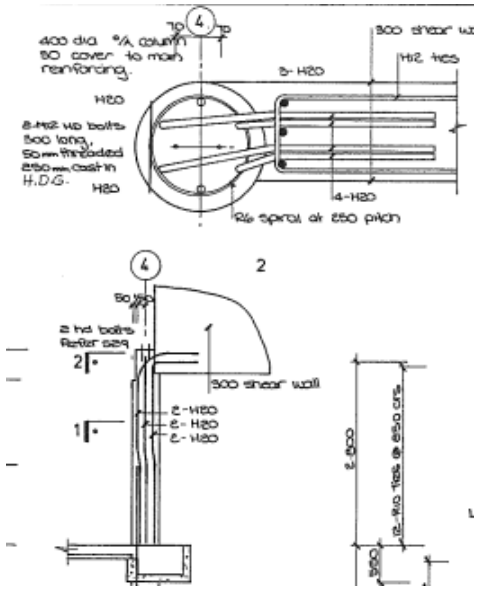

Figure 10: Column at GL 4 D/E (C18) to wall connection detailing at roof level. [1]

5.3.2. Beam Hinges

Beam hinges are incorporated in the analysis model as discrete non linear link elements located where inelastic demand is shown to occur. Hinges have been positioned at the location of the highest flexural demand which typically occurs at the column face for each beam. Plastic hinge lengths have been determined in a similar manner to that used for the columns (refer Section 5.3.1).

Beam flexural strength and rotational capacity was determined via moment-curvature analysis of the section including the contribution of the slab acting in flexure. It has been assumed for analysis purposes that beam hinge formation is not limited by the capacity of bar anchorages. A Takeda hysteresis model [10] was used to consider the degradation of hinge stiffness under cyclic loading.

For all precast beams, anchorage of positive (bottom) reinforcement occurs via hooks into the beam-column joint zone which can be seen in Figure 11 and Figure 12 below. Top steel anchorage in exterior beam column joints is via hooked bars similar to the typical bottom steel anchorage (as seen in Figure 11).

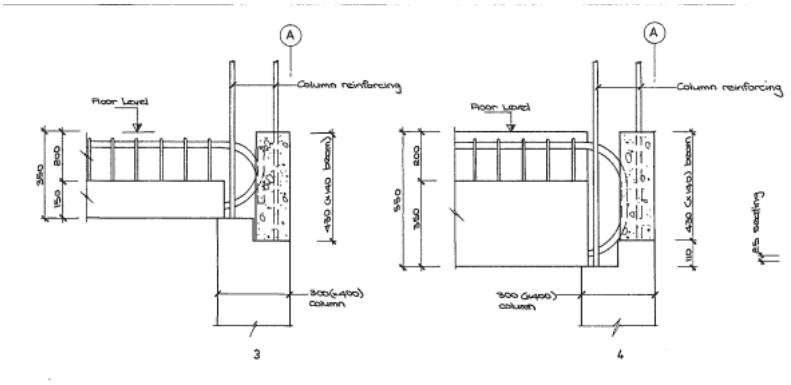

Figure 11: Reinforcement anchorage in Grid A beam column joint zone [1]

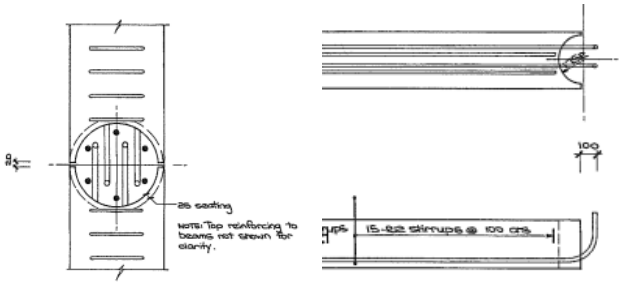

Figure 12: Typical bottom reinforcement anchorage in interior beam column joint zone [1]

Physical evidence has indicated that the positive reinforcement of the beam along gridline 4 between grids B and C was not effectively anchored into the wall on grid C at levels 3 and 4 [2]. To reflect this finding no positive moment capacity has been provided in the model at these locations [1].

5.3.3. Beam-Column Joints

Beam-column joint performance and capacity may have been influenced by the detailing of reinforcement used in the construction. Potential non-linearity in the beam column joints has not been explicitly modelled. Appendix B contains a discussion on the expected performance of the detailing present and the assessment approach undertaken. Joint demand/capacity ratios were assessed post analysis.

[1] Note that post analyses it has been confirmed that in addition to levels 3 and 4, beam bottom steel (between grids B and C) was not effectively anchored at levels 1, 5, and 6 into the wall at grid C

5.4. Reinforced Concrete Shear Walls

The building contains two reinforced concrete shear wall systems. Each of these systems was modelled using nonlinear layered shell elements which incorporate inelastic material effects at a fibre level. Where significant inelastic demands were not expected, the wall was modelled using linear elastic shell elements with stiffness modifiers determined from moment curvature analyses similar to those undertaken in Section 5.3. The stiffness modifiers determined via these analyses along with those determined following the provisions of NZS3101:2006 [6] are presented in Figure 13 below based on the gravity axial load.

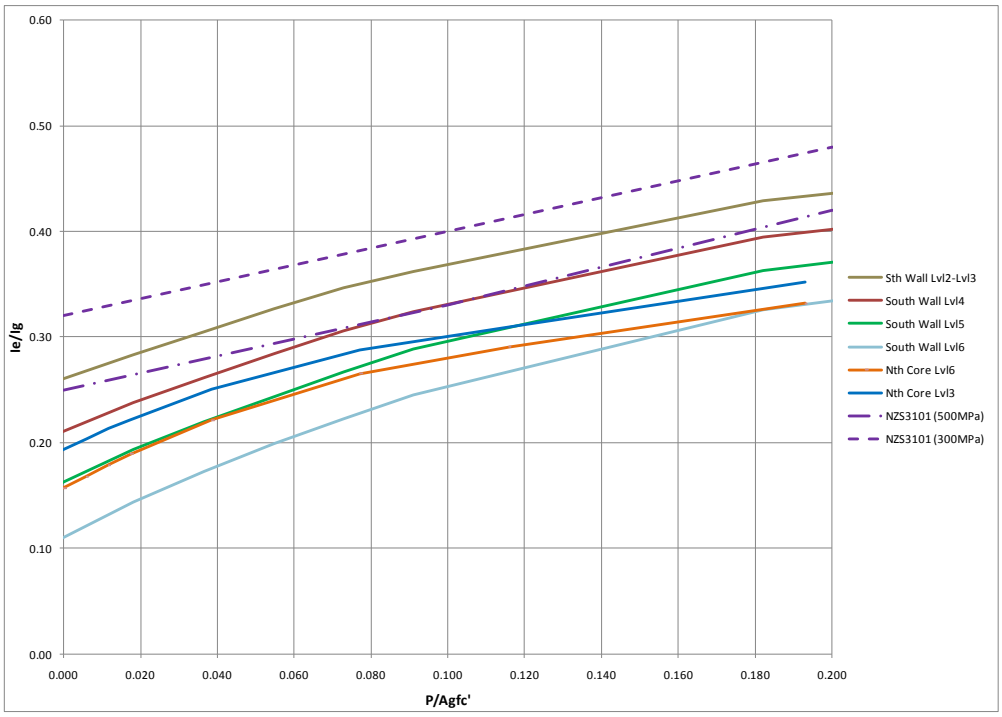

Figure 13: Effective wall stiffness relationship

Confining reinforcement was detailed for the boundary regions of all reinforced concrete shear walls in the lower two storeys. It was considered appropriate to model the nonlinear stress strain behaviour of the concrete fibres in these regions based on the Mander [11] confined concrete model. Between boundary regions, and for wall elements above the level 3 floor plate, concrete material in the layered shell element was assumed to be unconfined.

On the south shear wall diagonally reinforced coupling beams connected the two portions of wall (as seen in Figure 14 below). Typical span to depth aspect ratio of the coupling beams was 0.76 but varied from 0.55 at the bottom to 1.2 at the top of the wall. Modelling of the diagonally reinforced coupling beams has been based upon the approach documented in

Appendix A, with non linear links substituted for the fibre elements to reduce computation time.

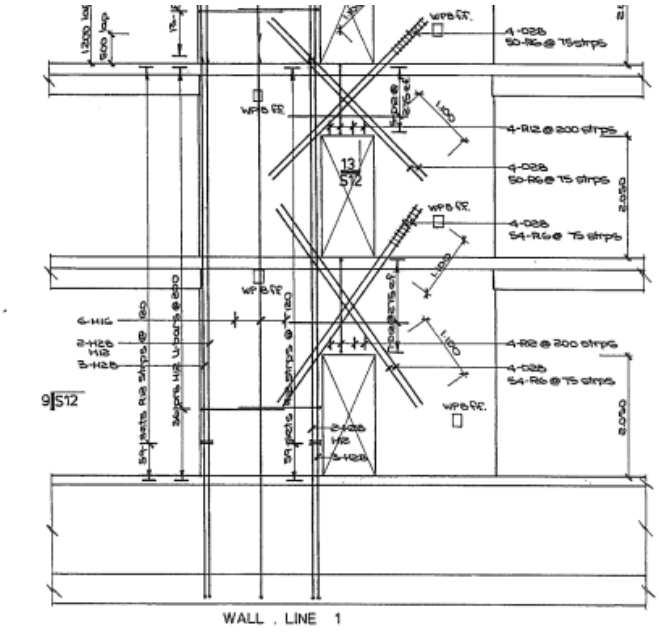

Figure 14: Southern shear wall typical coupling beam reinforcement arrangement [1]

5.5. Masonry Infill Panels.

Masonry infill panels were constructed on the western side of the CTV building between ground and level 4. Although detailed as having 25mm separation joints to columns (refer Figure 15 below) there is some uncertainty about the effectiveness of the separation. It has therefore been deemed appropriate to model the potential effect of the masonry on the building response in Model B. As such masonry has been assumed to be integral with the primary structure and is therefore 'active' in resisting seismic shears from the commencement of the earthquake.

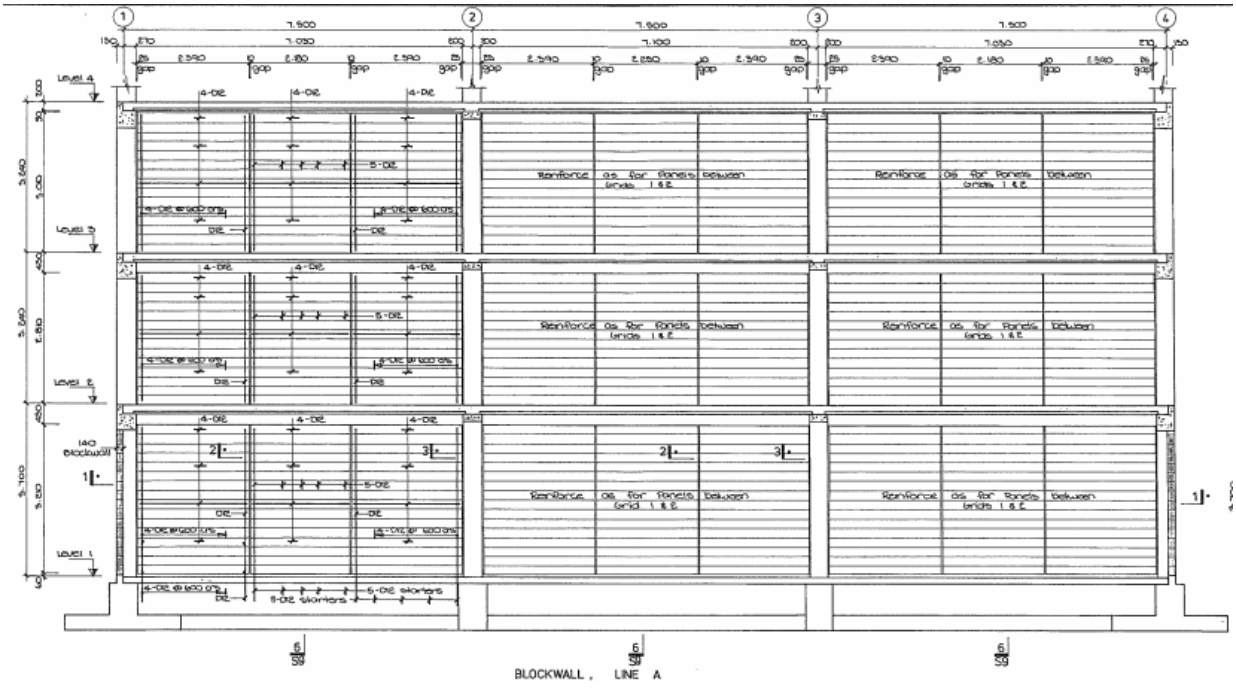

Figure 15: Record structural elevation of masonry infill panels [1]

Calculations by the DBH Technical Review Committee based on cantilever flexural capacity of the 2.3 m wide masonry panels indicated that the maximum shear contribution of each 7.5 m masonry bay is between 210 kN and 300 kN at yield, with strength degradation likely to commence at approximately 20 mm displacement. As such, masonry behaviour has been modelled using stiff elastic shell elements to mimic the stiffness contribution the walls provide to the supporting beams, with a tri-linear link connecting the masonry to the underside of the floor/beam above to replicate the inelastic behaviour. Hysterestic behaviour of the masonry link has been based upon the Takeda model. Figure 16 below shows the inelastic force displacement 'backbone' relationship that has been adopted for masonry.

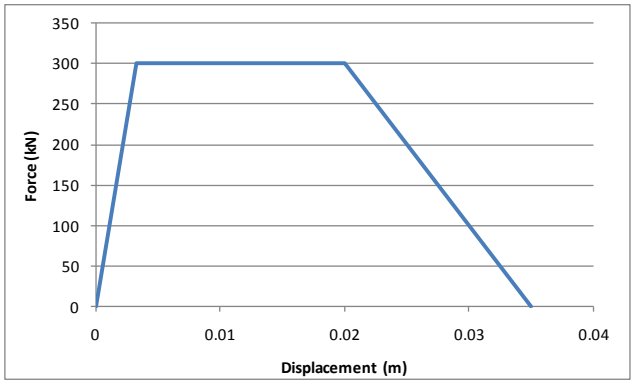

Figure 16: Masonry panel force displacement relationship.

5.6. Precast Concrete Cladding Spandrels

Precast concrete cladding spandrel units were located on the perimeter of the building. Figure 17 shows a cross section of a typical panel taken from the record structural drawings.

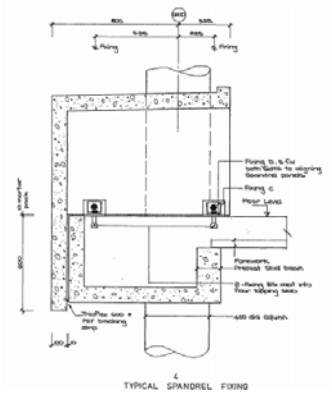

Figure 17: Typical spandrel panel section

A potential mechanism in this system is the column interaction with the precast spandrel elements. Should seismic drifts exceed the separation gap provided between the two elements, there is potential for the column to bear directly against the top edge of the spandrel.

In Model C, spandrels have been modelled as planar linear elastic shell elements located along the column centre lines as shown in Figure 18. Spandrel-column interaction was achieved through the use of a gapping link element situated between the column element and the spandrel panel. Links were located at the top level of the spandrel and are shown in green in Figure 18. In order to obtain an upper bound on the influence of the spandrels, it was assumed that there is no gap present between the column and spandrel elements i.e. the spandrel bears against the column. An additional flexural hinge has been included in the

column above the gapping link element to accommodate any potential hinging caused through spandrel interaction.

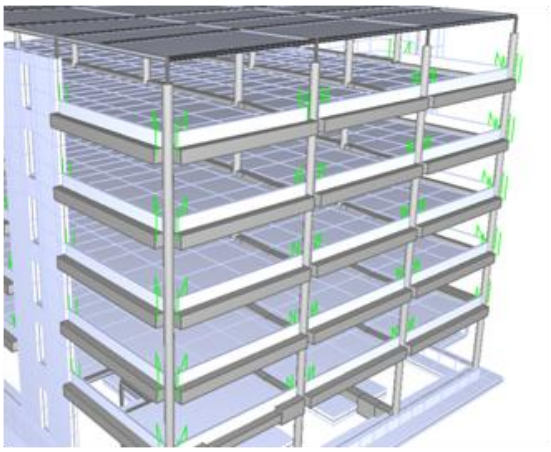

Figure 18: Model C screenshot showing spandrel panels.

The potential effects of the spandrels have only been considered for non-linear pushover analyses to provide a sensitivity analysis on results. As spandrels were not included in the time history analyses, consideration of this should be made during the assessment of the columns.

5.7. Floors

Review of the lateral load paths has indicated that diaphragm integrity at the interface with shear walls may have been an important consideration in the determination of the seismic performance of the structure. As such, the flexibility of each floor level has been modelled with in-plane stiffness based on the average thickness of the concrete slab (173 mm). For the purposes of the analysis the stiffness of the slab elements have been considered to have $0.5A_{gross}$ for in-plane actions. Diaphragms were assumed to behave in a linear-elastic manner, with diaphragm actions monitored at interfaces with shear walls.

The floor diaphragm connections to the north core lift shaft walls on grids D and D/E have been identified as an area of potential connection failure. As a consequence of a lack of specific tie reinforcement it was assumed that there is no tensile or gravity connection between the slab and these walls at levels 2 and 3. At levels 4 to 6 a retrofitted steel angle tie (or 'drag bar') provided limited tensile and gravity connection to the slab at the tips of walls D and D/E. Multi-linear links have been used to provide a 'fuse' that will transfer the expected upper bound tensile capacity of the retrofitted connection only with no limitation on the

compressive load transfer capability. Nominal tensile connection capacities for the drag bar and it's connections, and the corresponding ultimate displacements have been provided by Hyland Fatigue & Earthquake Engineering and StructureSmith, and are listed in Table 5 below. Gravity transfer at this interface is expected to be limited by slab reinforcement yielding so has been taken as zero for the purposes of seismic analysis.

Table 5: Modelled diaphragm (drag bar) connection capacities

Wall	Level	Tensile Capacity (kN)	Displacement at Disconnection (mm)	Compressive Capacity (kN)
D	2	0	0	Not limited
	3	0	0	Not limited
	4	320	2.3	Not limited
	5	420	2.4	Not limited
	6	603	2.6	Not limited
D/E	2	0	0	Not limited
	3	0	0	Not limited
	4	403	2.8	Not limited
	5	503	3.0	Not limited
	6	540	3.0	Not limited

Floor diaphragm connections to the other north core walls on grids 5, C and C/D, and to the south wall on grid 1 were assumed to remain connected for the purposes of the seismic analysis. Maximum diaphragm actions at these locations are reported (in Sections 9 and 10) at these locations for assessment by others.

For out-of-plane demands (i.e. plate action) the floors have been considered to have stiffness corresponding to $0.5I_{gross}$ at mid-span, with the effective stiffness adjacent to beam lines and columns taken as the average positive and negative bending stiffness determined by moment-curvature analysis considering the reinforcement present. In the determination of the slab flexural stiffness the contribution of the metal decking has been ignored as the decking would not have been effectively anchored at the beam support where the positive (sagging) flexural demands are greatest.

6. Loadings

6.1. Gravity Loadings

For combination with seismic loads a gravity load combination has been developed following the requirements of NZS1170.0:2002 Section 4 [12]. This gravity load combination also formed the basis for consideration of P-delta effects in the seismic analyses. In this combination live load allowances have been combined with the initial staged dead load analysis as a separate loading step as follows,

$$E_d = G + \sum \Psi_{C,i} \Psi_{A,i} Q_i$$

Taking „G" as the sum of all dead type loadings incorporating element self weights, plus any superimposed dead load (SDL) allowances that are required to be considered, and „$\sum \Psi_{C,i} \Psi_{A,i} Q_i$" given as sum product of all individual components of imposed loading as presented in Table 6 below.

Table 6: Basic load pattern definitions

Gravity load component	Load allowance (kPa)	Ψ_C	Ψ_A
DL	Self weight	1.0	1.0
SDL	0.55	1.0	1.0
Plant LL	5.0	0.6	1.0
Toilet LL	2.0	0.4	1.0
Office LL	3.0	0.4	1.0
Roof LL	0.25	0	1.0

Note that the use of ψ_A equal to 1.0 for office live load could slightly over-estimate column compression demand in lower levels of the structure by between 2 and 7 percent. For the purpose of determining gravity actions in the upper levels of the structure it is believed that a ψ_A equal to 1.0 suitably represents the gravity actions.

It should be noted that level 3 and the east side of level 6 of the CTV structure are understood to have been untenanted at the time of the earthquake. No live load allowance has been included at these locations.

Table 7 below presents the global base reaction reported at the model origin (i.e. {x,y,z}={0,0,0}= Level 1 at grid reference F/1) for each load type arising from a linear analysis.

Table 7: Global base reactions for basic load patterns (linear)

Gravity load case	FZ (kN)	MX (kNm)	MY (kNm)
DL	35458	492755	482464
SDL	4647	65608	59200
Plant LL	364	5014	8951
Toilet LL	135	2220	3307
Office LL	7437	119468	87223
Roof LL	0	0	0

6.2. Dynamic Mass

The dynamic mass used in the seismic analyses was determined following the provisions of NZS1170.5:2004, Cl 4.2 [13] where,

$$W_t = G + \sum \Psi_{E,i} \Psi_{A,i} Q_i$$

taking „G" based on all dead loads (plus superimposed dead loads), „$\sum \Psi_{c,i} \Psi_{A,i} Q_i$ " as the sum product of the individual imposed loadings as per Table 8 below.

Table 8: Imposed loading allowances (for derivation of dynamic mass)

Gravity load component	Load allowance (kPa)	ψ_E	ψ_A
DL	Self weight	NA	NA
SDL	0.55	NA	NA
Plant LL	5.0	0.6	0.74
Toilet LL	2.0	0.3	0.5
Office LL	3.0	0.3	0.5
Roof LL	0.25	0.0	0.0

Seismic mass associated with the load component „*DL*" has been obtained through explicit modelling of the structural elements. All other tributary masses outlined in Table 8 have been incorporated via distributed loads applied to the floor/roof elements in order to accurately proportion mass for slabs and beams etc. Note that as for Section 6.1 no live load has been included in the development of the dynamic mass for the untenanted levels. The distribution of seismic mass in the analysis model is as presented in Figure 19 below.

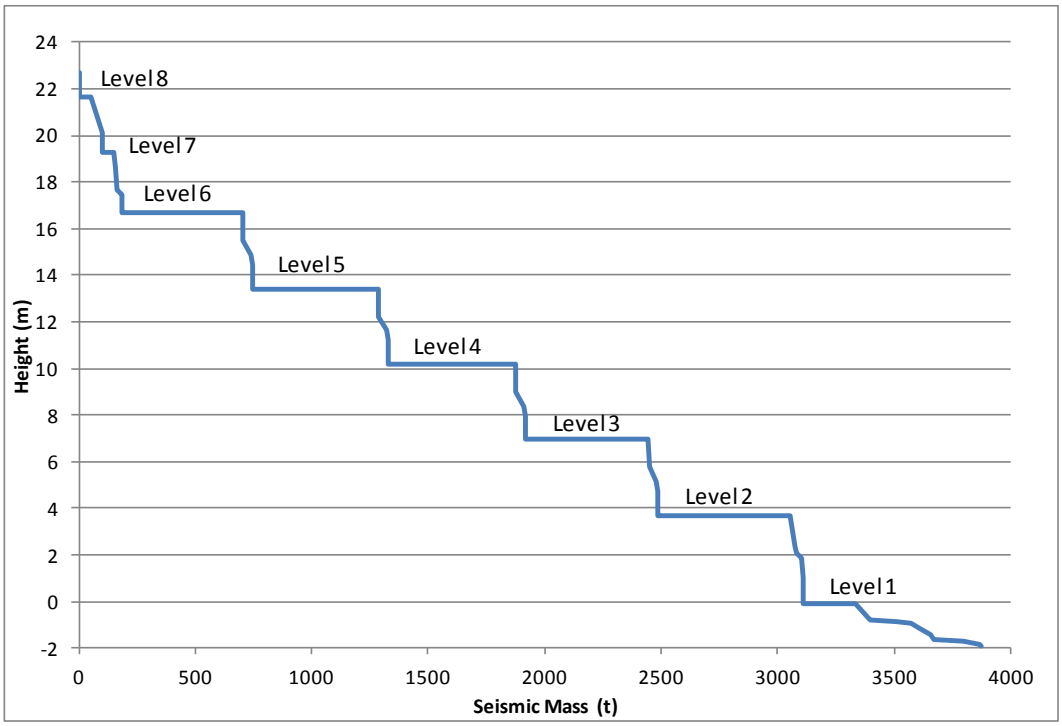

Figure 19: Seismic mass distribution

7. Seismic Analyses

7.1. Modal Analysis

Modal analysis has been carried out for Model A and Model B considering dynamic mass as outlined in Section 6.2. The results of this analysis are presented in Table 9 and Table 10 below (showing modes with more than 5% mass participating only), with X, Y, and Z representing the north, west, and vertical axes respectively.

Table 9: Modal participating mass ratios : '*MODEL A*'

Mode	Period (sec)	UX	UY	UZ	∑UX	∑UY	∑UZ	RZ	∑RZ
1	1.29	0.61	0.01	0.00	0.61	0.00	0.00	0.19	0.19
2	1.02	0.00	0.37	0.00	0.61	0.38	0.00	0.01	0.20
3	0.43	0.00	0.25	0.00	0.61	0.63	0.00	0.40	0.60
21	0.25	0.00	0.00	0.07	0.64	0.69	0.14	0.00	0.63
45	0.21	0.00	0.00	0.11	0.76	0.72	0.34	0.00	0.66
78	0.09	0.00	0.01	0.07	0.78	0.81	0.71	0.01	0.78
92	0.04	0.06	0.02	0.00	0.94	0.91	0.86	0.06	0.90
95	0.02	0.00	0.00	0.05	0.95	0.94	0.96	0.00	0.91

Table 10: Modal participating mass ratios : '*MODEL B*'

Mode	Period (sec)	UX	UY	UZ	∑UX	∑UY	∑UZ	RZ	∑RZ
1	1.15	0.43	0.09	0.00	0.43	0.09	0.00	0.16	0.16
2	0.83	0.16	0.33	0.00	0.59	0.42	0.00	0.01	0.17
3	0.41	0.01	0.21	0.00	0.59	0.63	0.00	0.40	0.57
21	0.25	0.00	0.00	0.06	0.63	0.68	0.14	0.00	0.62
42	0.21	0.06	0.01	0.01	0.75	0.72	0.22	0.01	0.65
45	0.21	0.00	0.00	0.09	0.75	0.72	0.34	0.00	0.65
78	0.09	0.00	0.01	0.08	0.78	0.81	0.70	0.01	0.76
100	0.01	0.02	0.01	0.00	0.98	0.99	1.00	0.02	0.93

7.2. Non-Linear Static (Pushover) Analysis

In order to gain an initial view of the anticipated seismic performance of the building a nonlinear static analysis (often referred to as a "Pushover") was undertaken for each of the analysis models described in Section 3. This pushover was used to verify that the finite elements employed for each of the structural mechanisms outlined in Section 5 were performing as expected.

Pushover analyses were undertaken in each of the two orthogonal directions i.e. north/south (N/S) & east/west (E/W) independently. The pushover cases consist of a displacement controlled, force based analysis with the load vector based upon a triangular load distribution, and inertia force applied to each mass degree of freedom in the model. Based upon the fundamental periods of vibration obtained from section 7.1 a building centre of mass target displacement of 200 mm has been taken for the N/S direction and 150 mm has been taken as the target displacement for the E/W direction. These values are approximately equivalent to the current Building Code [14] elastic displacement demand considering, subsoil type D, Z=0.30, and Sp=1 as can be seen in Figure 20 below. It has been assumed that the level 6 displacement demand is approximately 1.5 times greater than the building centre of mass demand.

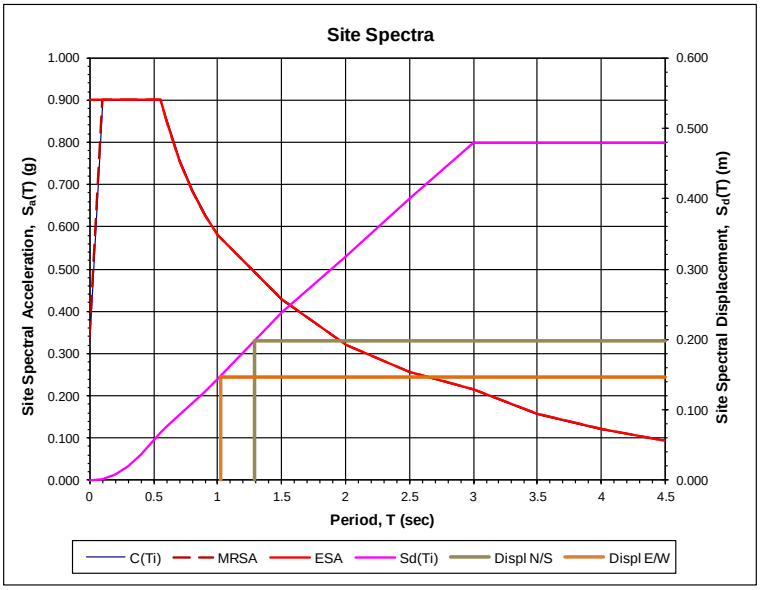

Figure 20: Site spectral displacements.

7.3. Nonlinear Dynamic (Time History) Analysis

Non-linear time history analyses have been undertaken incorporating inelastic behaviour for the two analysis models as outlined in Section 3. Two seismic event scenarios are considered in these analyses which are denoted as the „*Darfield*" event, and the „*Lyttelton*" event in this report. The details of these events as obtained from GNS Science [15, 16] are presented in Table 11 below.

Table 11: Seismic event information

Event Name	Reference Number	Local Date & Time	Epicenter Location	Magnitude	Focal Depth
Darfield	3366146	04Sept2010, 0435hrs	43.55°S, 172.17°E	M_L 7.1	11 km
Lyttelton	3468575	22Feb2011, 1251hrs	43.60°S, 172.71°E	M_L 6.3	5 km

7.3.1. Analysis Ground Motions

In an attempt to approximate the ground shaking that was experienced at the CTV site for each of the two events, a suite of three acceleration time history records were adopted following the recommendations of Tonkin and Taylor [4]. These were records recorded at other locations in the Christchurch CBD, with (according to Tonkin & Taylor) similar geologic profiles to that present at the CTV site. The adopted records are presented in Table 12 below.

Table 12: Adopted earthquake record information

Station Name	Station ID	Station Location
Christchurch Cathedral College	CCCC	43.53°S, 172.65°E
Christchurch Hospital	CHHC	43.53°S, 172.63°E
Christchurch Botanic Gardens	CBGS	43.53°S, 172.62°E

The acceleration time histories were obtained from GNS Science [17, 18] and have been processed in order to align the axes of the recorded motions to purely north/south (denoted as component N00E) and east/west (denoted as component N90E) components to coincide with the principle axis of the CTV building. No processing has been undertaken on the vertical components of the records.

Figure 21 through Figure 26 below present the site 5% damped response spectra for the three (processed) components of the Darfield and Lyttelton events respectively. Also presented for reference is the mean of the recorded components and the elastic spectra used for design purposes at the site derived in accordance with NZS1170.5:2004 [13] considering site subsoil class D, Z=0.22 (i.e. that applicable for a new building design in Christchurch during February 2011), and Sp=1.0.

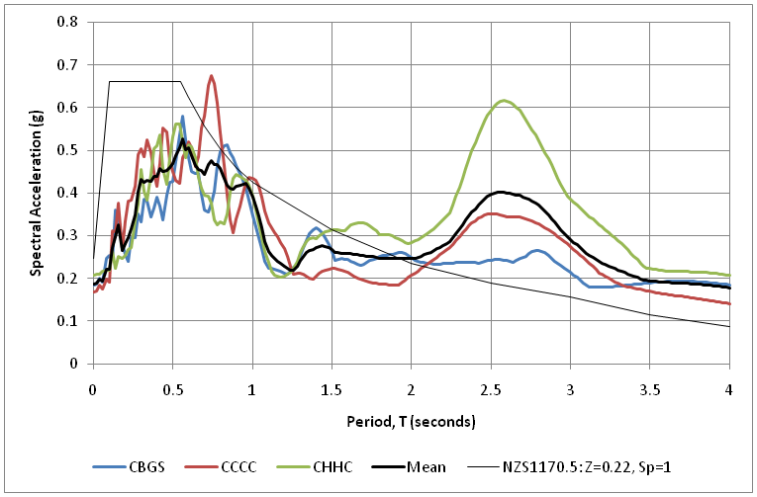

Figure 21: Darfield N00E 5% damped response spectra (north/south)

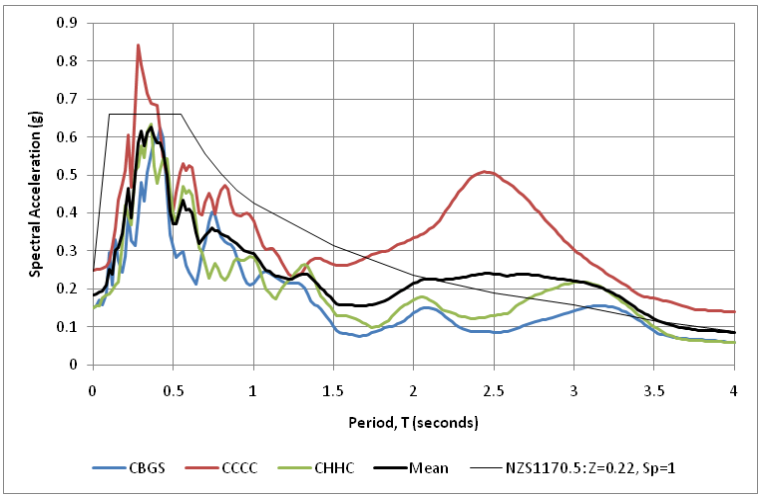

Figure 22: Darfield N90E 5% damped response spectra (east/west)

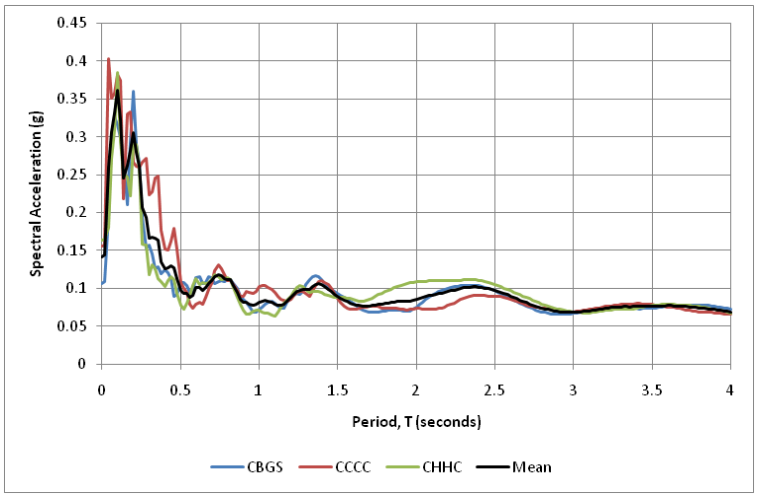

Figure 23: Darfield Vertical 5% damped response spectra

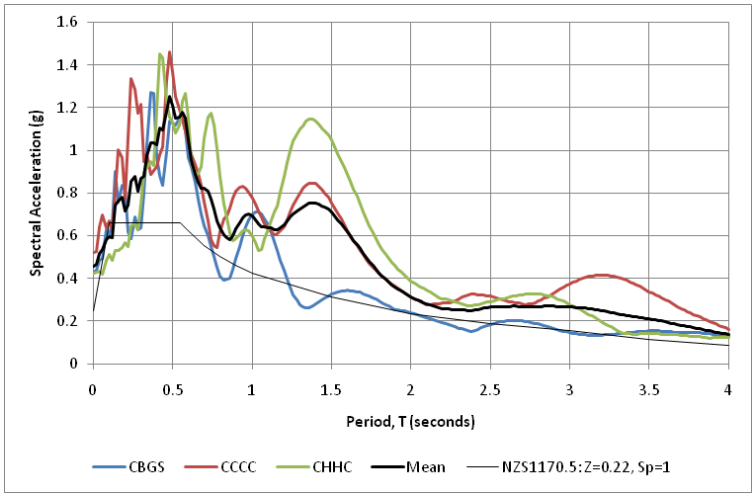

Figure 24: Lyttelton N00E 5% damped response spectra (north/south)

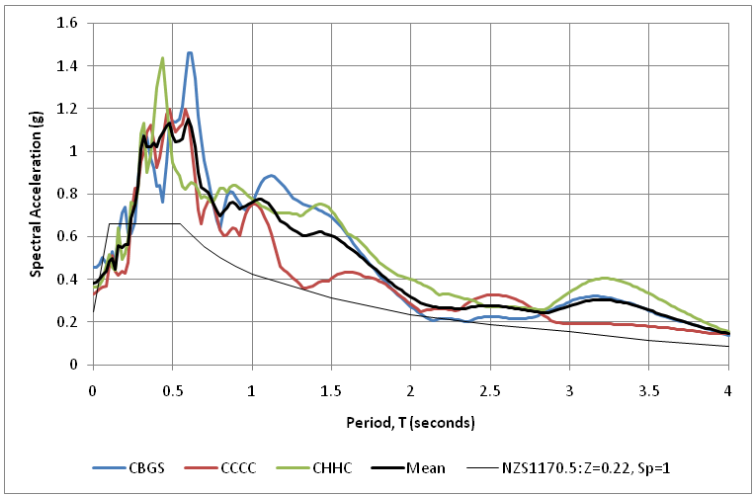

Figure 25: Lyttelton N90E 5% damped response spectra (east/west)

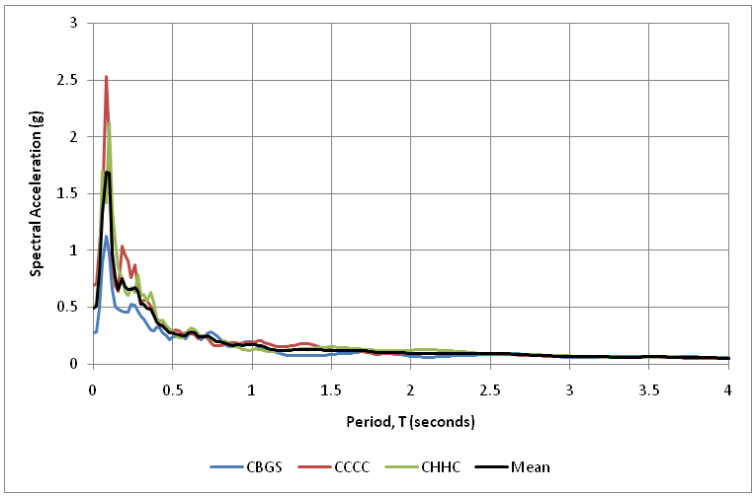

Figure 26: Lyttelton Vertical 5% damped response spectra

The records as supplied by GNS have arbitrary stop and start times that encompass many seconds of very small ground vibration. Incorporation of the entire record into the analysis would add no benefit to the understanding of the structural response or performance, and would only add considerable analysis time. For the purposes of the non linear time history analysis runs, reduced length records have been used to reduce computation times. Record start and finish times have been selected to ensure that all significant shaking is captured by the analysis and are presented in Table 13. All results contained with this document have been presented relative to the adopted start time of each acceleration time history record. Appendix D contains the acceleration time history records used for these analyses.

Acceleration time history records for the Darfield event were much longer in duration than for the Lyttelton event. To reduce analysis time only the CBGS record was analysed for Darfield. The CBGS record was chosen as the spectral accelerations were the closest to the mean of the three time history records for the period ranges of interest i.e. 0.8 to 1.5 seconds, and as such was likely to provide a reasonable understanding of the building demands.

Table 13: Adopted record start and finish times

Station Name	Event	Start Time (sec)	Finish Time (sec)
Christchurch Botanic Gardens (CBGS)	Darfield	28.90	40.90
Christchurch Cathedral College (CCCC)	Lyttelton	15.04	23.90
Christchurch Hospital (CHHC)	Lyttelton	16.00	27.20
Christchurch Botanic Gardens (CBGS)	Lyttelton	16.50	25.50

7.3.2. Damping

Elastic Structural Damping

Elastic damping for the structure has been incorporated in the time history analyses by way of mass (α) and stiffness (β) proportional damping coefficients, commonly referred to as Rayleigh damping. A common criticism of the Rayleigh damping method is that it considers only the initial stiffness in its determination of level of damping. In order to consider the

reduced level of damping appropriate during inelastic cycling of structural elements a tangent stiffness damping model is often considered as being preferable [7]. To address this issue a reduced damping coefficient, „ξ*„ for the fundamental period has been specified for use in determining the damping coefficients. This adopted method more closely approximates the tangent stiffness approach.

Observed damage of the CTV building after the Darfield event indicated that the ductility demand of the structure was nominal. On this basis, unmodified Rayleigh damping was adopted for Darfield analysis runs. Table 14 below presents the input parameters adopted in determining the Rayleigh damping coefficients for analyses of the Darfield event.

Table 14: Rayleigh damping parameters - Darfield

	Period, T (sec)	Damping, ξ*(%)
First	1.29	5
Second	0.05	5

Using the parameters presented in Table 14 the mass and stiffness proportional damping coefficients are determined as follows:

- Mass Proportional Coefficient, α 0.4689
- Stiffness Proportional Coefficient, β 7.661×10^{-4}

For the Lyttelton event it was necessary to estimate the building displacement ductility capacity in order to select an appropriate level of damping. From the bi-linearised pushover plot in Figure 37 of Section 8 the approximate ductility capacity of the structure is between 1.5 and 2.4 depending on the direction of demand. For the purpose of the non linear time history analyses a ductility of 2.5 was assumed for the structure. Table 15 below presents the input parameters adopted in determining the Rayleigh damping coefficients for analyses of the Lyttelton event.

Table 15: Rayleigh damping parameters - Lyttelton

	Period, T (sec)	Damping, ξ*(%)
First	1.29	2.8
Second	0.05	2.8

Using the parameters presented in Table 15 the mass and stiffness proportional damping coefficients are determined as follows:

- Mass Proportional Coefficient, α 0.2606
- Stiffness Proportional Coefficient, β 4.291×10^{-4}

Figure 27 below presents a plot of equivalent viscous damping vs structure period obtained using the above coefficients.

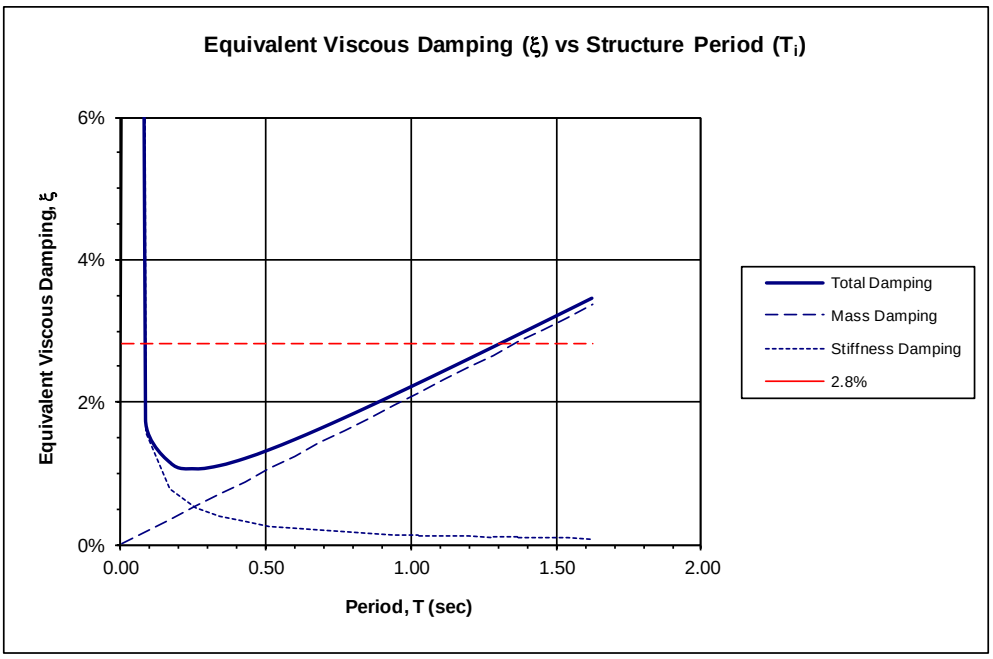

Figure 27: Equivalent viscous damping vs structure period - Lyttelton

Radiation Damping

It has been considered that the adopted acceleration time histories inherently contain a component of radiation damping and given the uncertainties over the actual site accelerations, and material properties, the incorporation of additional radiation damping is expected to be insignificant and as such has not been incorporated.

8. Non-Linear Pushover Results

8.1. Model A

Force displacement plots for the push-over analyses are presented in Figure 28 for Model A. Displacements have been recorded at a node located at approximately the centre of mass of level 6. Figure 29 and Figure 30 present the base shear components recorded at the top of the foundation beams for each of the primary structural elements.

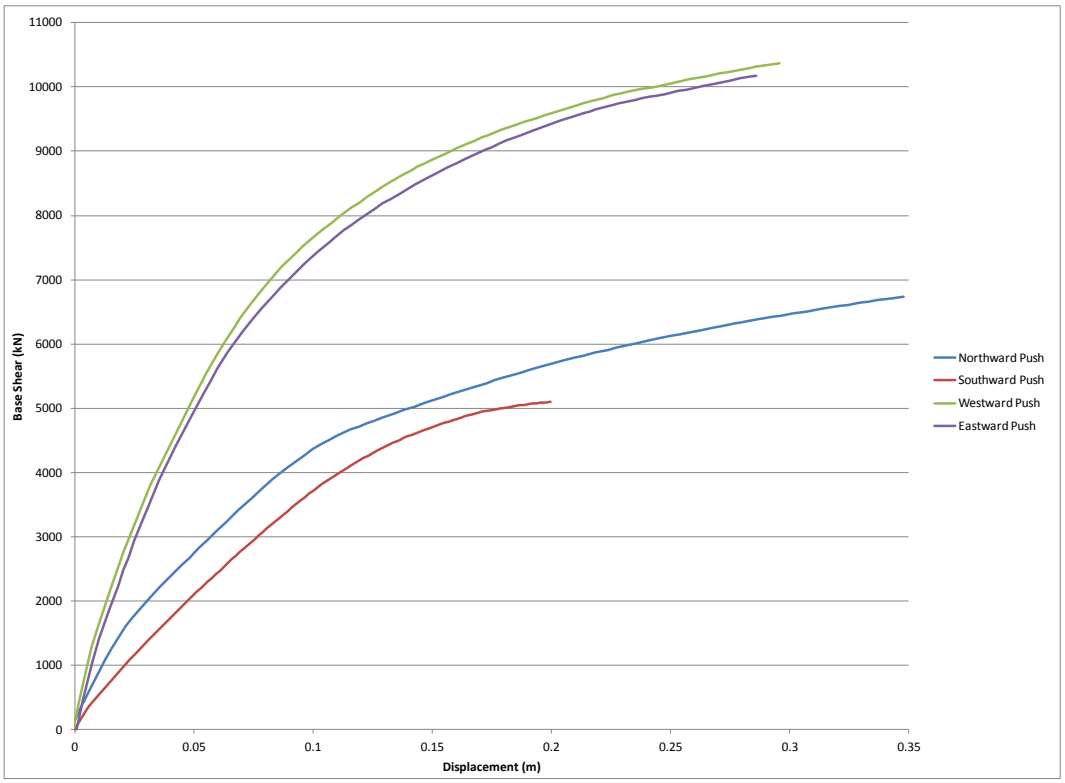

Figure 28: Model A force-displacement relationship.

It can be seen from the pushover plots that the building responds to the imposed lateral loading in a highly non-linear manner.

The east/west base shear displacement plots are curved in shape. Plot profiles for both the east and west directions are almost identical indicating a similar building response in each of these directions.

North/south response appears to have more localised sections of non-linearity and can be characterised by a tri-linear and bi-linear plots respectively. Initial response of the building in

the northward direction is stiffer than in the southward direction, which can be attributed to the differences in the foundation behaviour under the north core for these directions.

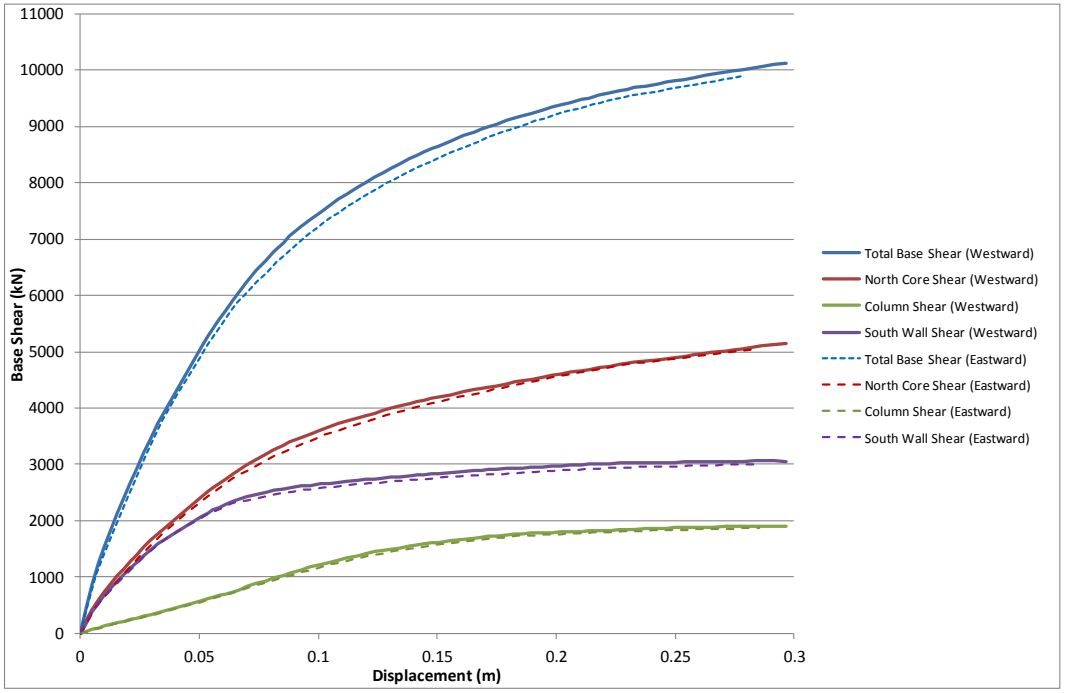

Figure 29: Model A base shear components - east/west direction.

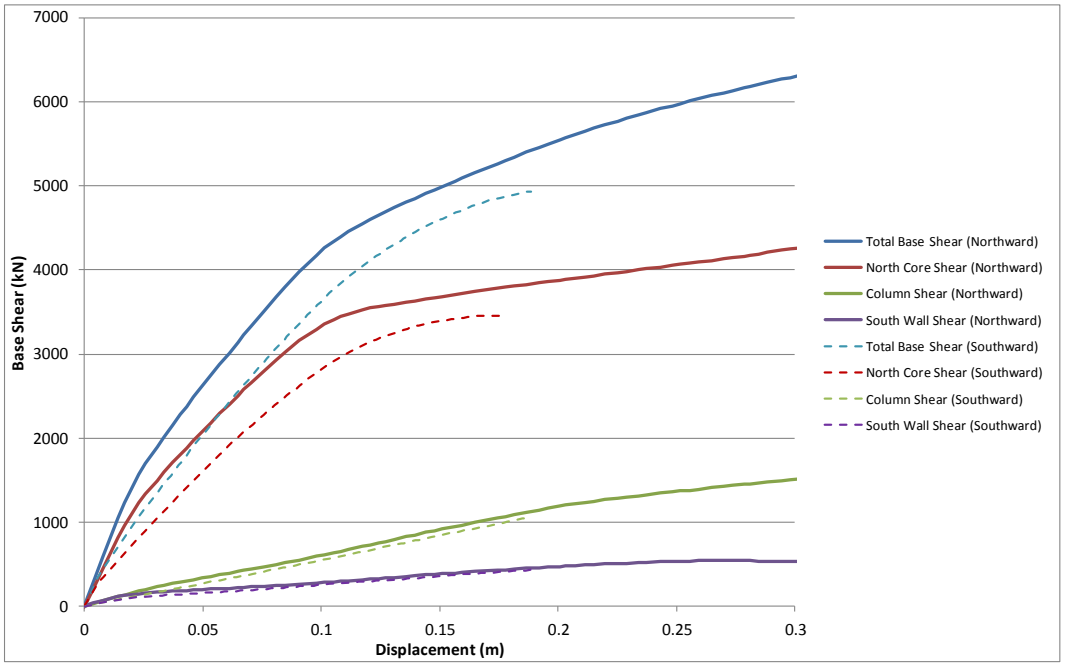

Figure 30: Model A base shear components - north/south direction.

Components of base shear are similar in each of the directions of loading with the exception of the north core in the north/south direction. As can be seen in Figure 30, more base shear is

carried by the core for an applied northward load than for a loading direction toward the south. This is due to the mobilisation of additional gravity from the beams and slab along gridline 4 as the southern edge of the core wall webs move upwards with core rotation to the north. These shears provide a restoring force that restrains the wall rotation, requiring higher shears to generate the same centre of mass displacement at level 6.

Pushover analyses have indicated that the response of the building in the east/west direction to be significantly torsional. Figure 31 to Figure 34 present the variation in displacement profile between the approximate centre of mass (at Level 6) and the building perimeter gridlines for each direction under consideration. East/west displacement on gridline 1 is approximately three times greater than that on grid 4, and can be seen in Figure 31 and Figure 32. This is a consequence of the difference in relative stiffness between the north core and the coupled shear wall on grid 1. As the coupled shear wall on gridline 1 yields the torsional response of the building is further exacerbated.

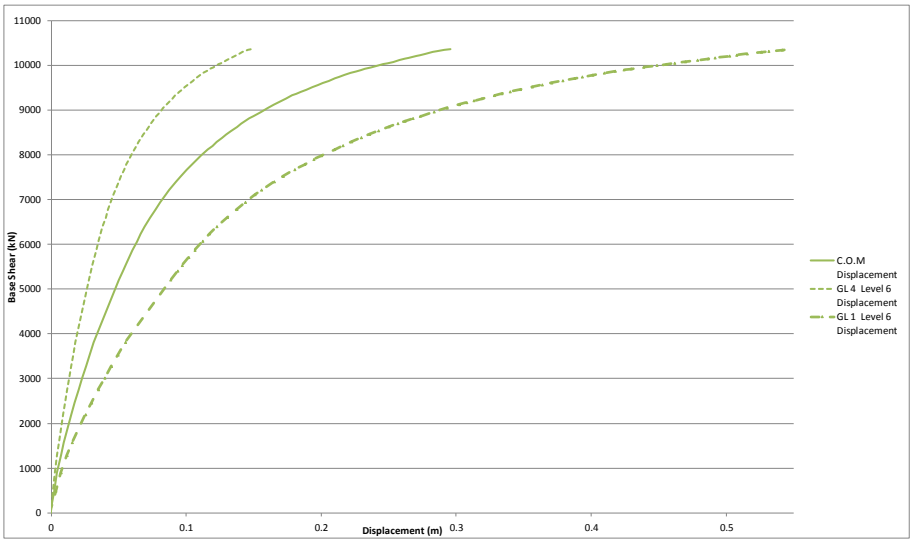

Figure 31: Model A Level 6 western pushover displacement profile.

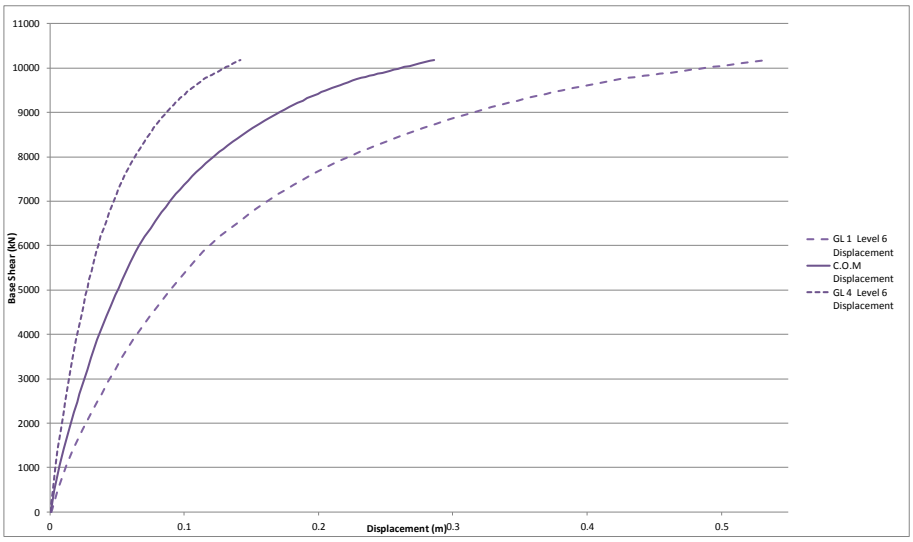

Figure 32: Model A Level 6 eastern pushover displacement profile.

Little torsional behaviour is exhibited through loading in the north/south direction. As can be seen in Figure 33 and Figure 34 there is almost no difference in displacement between grid A and grid F under north/south loading.

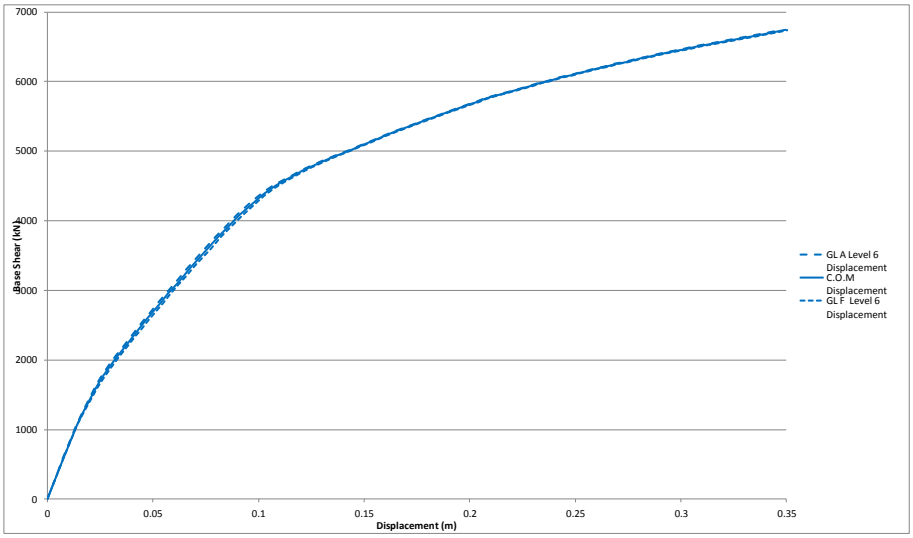

Figure 33: Model A Level 6 northern pushover displacement profile.

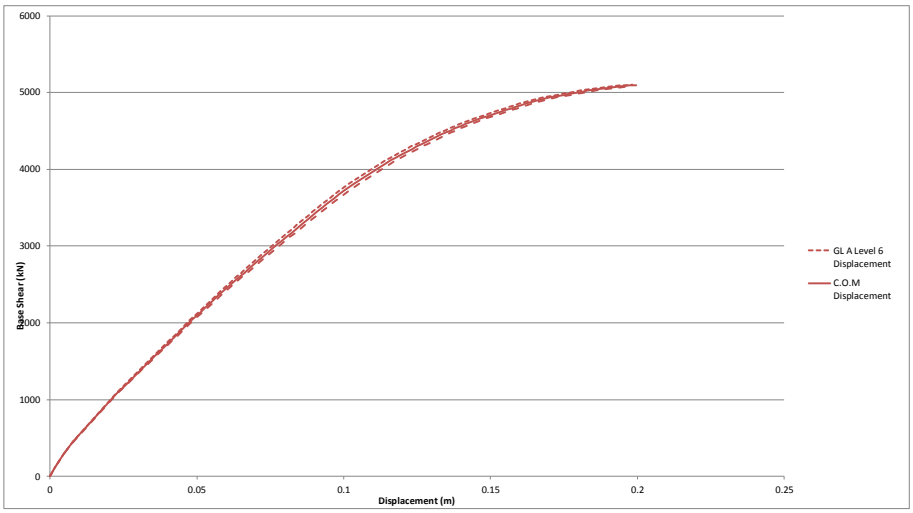

Figure 34: Model A Level 6 southern pushover displacement profile.

8.2. Model B

Figure 35 presents the force versus displacement pushover plots for Models A and B for the centre of mass displacement range expected for the Darfield earthquake. From this it is apparent that the addition of masonry stiffens the initial response of the structure. As the masonry degrades in strength and stiffness the pushover plots converge to that of Model A, with building response expected to match that of Model A once the masonry has fully degraded

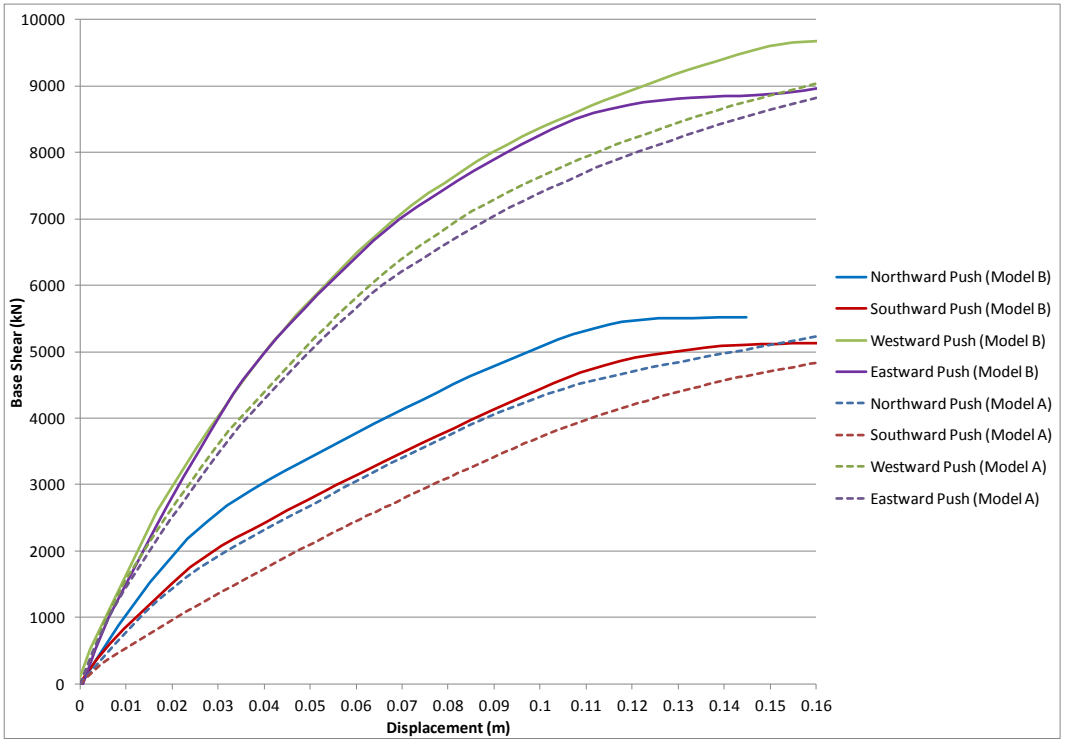

Figure 35: Model A & Model B pushover force displacement comparison.

8.3. Model C.

Figure 36 presents the effect spandrel interaction has on the pushover plots for indicative northward and eastward directions of loading. For the purpose of comparison the pushover plots for Model A and Model B have also been included.

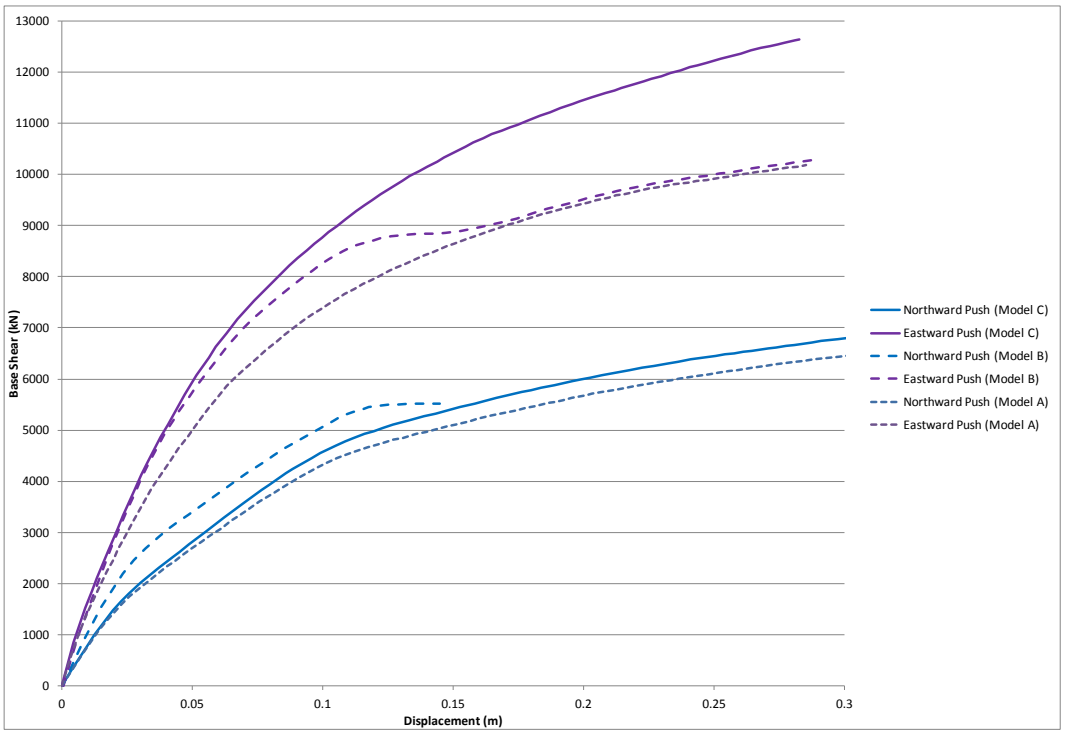

Figure 36: Pushover force displacement variations for north and east directions.

As can be seen in Figure 36, the addition of spandrels increases the building stiffness in each of the directions under consideration. Spandrel interaction has a more significant effect on building response in the east/west direction than for the north/south direction. Note that column shear and spandrel connection strength limitations have not been incorporated so the effect of the spandrels is likely to have been overestimated at moderate to high displacements in the pushover analysis.

8.4. Building Displacement Ductility Capacity.

Figure 37 presents the Model A pushover plots that have been bi-linearised in order to obtain an estimate on the building displacement ductility capacity. The building displacement capacity being defined as the point at which at least three column hinges have exceeded their ultimate plastic rotation limit i.e. the rotation at which a concrete strain of 0.004 would have been reached. Included in the plots are the level 6 c.o.m displacements at which the pushover predicts that three column plastic hinges have rotated past their plastic limit. Three hinges have been selected to account for variability in material strengths, and demands. From the bi-linearised plots the ductility displacement capacity can be estimated for the building.

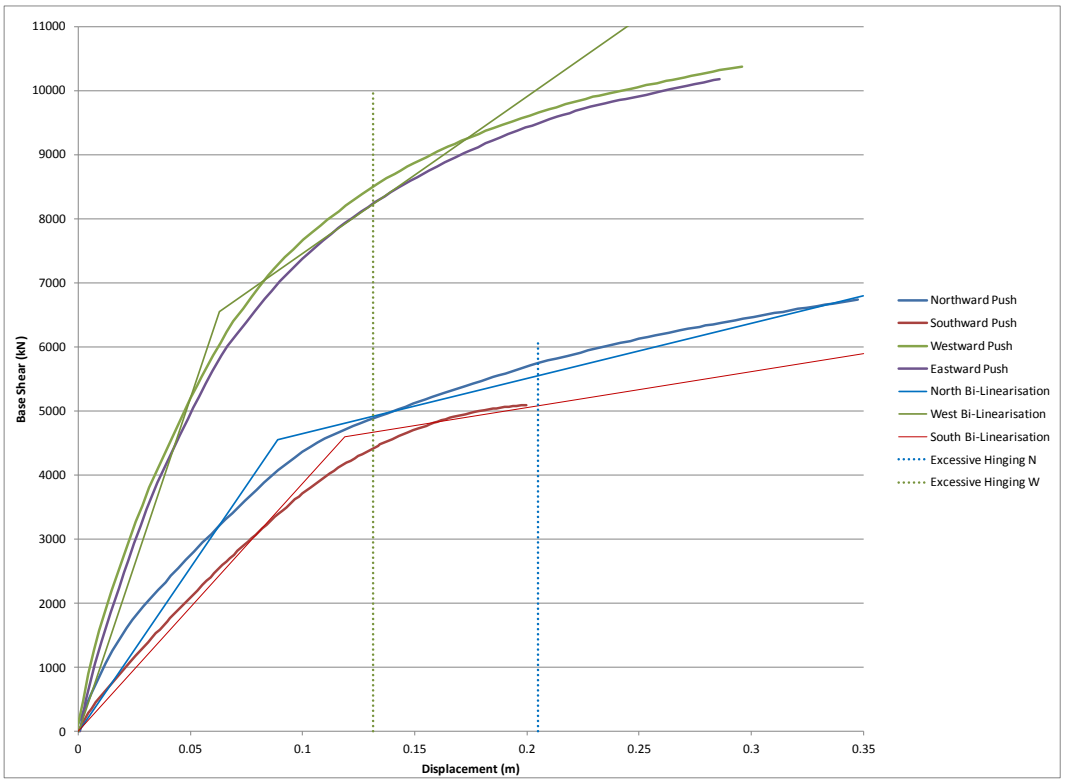

Figure 37: Bi-linear pushover plots

From Figure 37 the ductility capacity can be estimated as being 1.9 to 2.1 in the east/west direction, and between 2.2 and 2.4 for the north/south direction. It should be noted that given the shape of the pushover plots it is difficult to approximate the building performance as a bi-linear plot for the purpose of determining the ductility capacity for the building as a whole. A likely range of ductility capacity for the structure at the point where column hinge rotations become excessive is 1.5 to 2.5.

Table 16 below contains a summary of the storey drifts required to initiate hinging i.e. the drift at which the nominal section capacity has been reached, using the Model A pushover results. Drifts have been calculated using interstorey displacement in the direction of loading at the onset of hinging in the columns i.e. Frame 1 and 2 drifts have been calculated using the interstorey displacements from a westward loading and, Frame F drifts have been determined using displacements from a northward loading. For the purposes of this report the drift that initiates column hinging has been defined as the average of the storey drifts that cause the first and second hinges to form on a given frame line. Also included is a comparison of the Frame 1 and Frame F drifts that initiate hinging assuming spandrels were installed against the columns with no gap present i.e. for Model C.

Table 16: Pushover drifts initiating column hinging (% of storey height).

Level	Frame				
	1	**2**	**F**	**1 spandrels**	**F spandrels**
5	0.75	0.85	0.88	0.53	0.73
4	0.82	0.91	0.97	0.58	0.77
3	0.90	0.94	1.01	0.64	0.81
2	0.94	0.94	1.04	0.66	0.88
1	0.99	0.93	-	0.85	0.94

9. Non Linear Time History Darfield Results

9.1. Model A

Results presented are a summary of the analyses only. Additional results can be found in Appendix E. All results are presented for the earthquake acceleration time history recorded at the Christchurch Botanical Gardens (CBGS) using all three components of the record.

9.1.1. Drifts and Displacements

Figure 38 and Figure 39 indicates the north/south storey drifts for the perimeter frames located on grid A, and grid F for Model A and Model B. Note that the drift at the onset of column hinging predicted by the pushover analyses has been presented for Frame F in Figure 39.

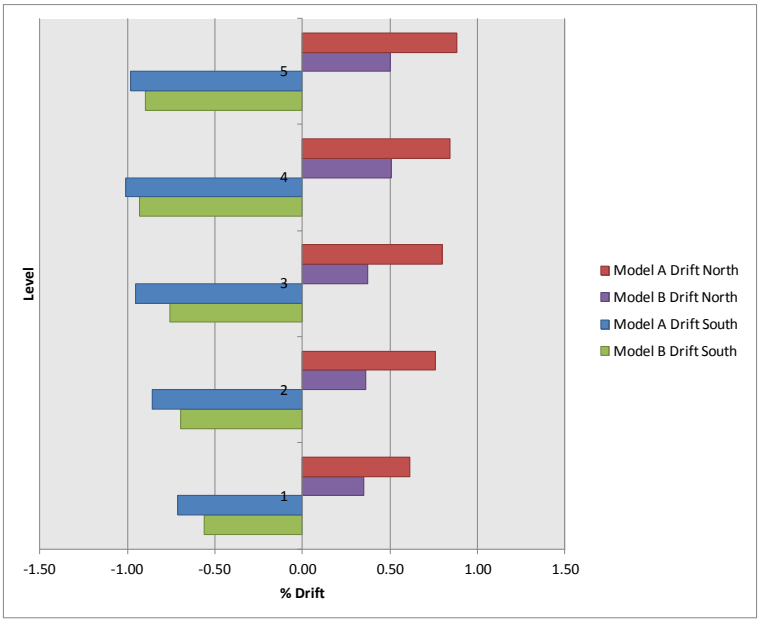

Figure 38: Frame A north/south storey drifts - Darfield.

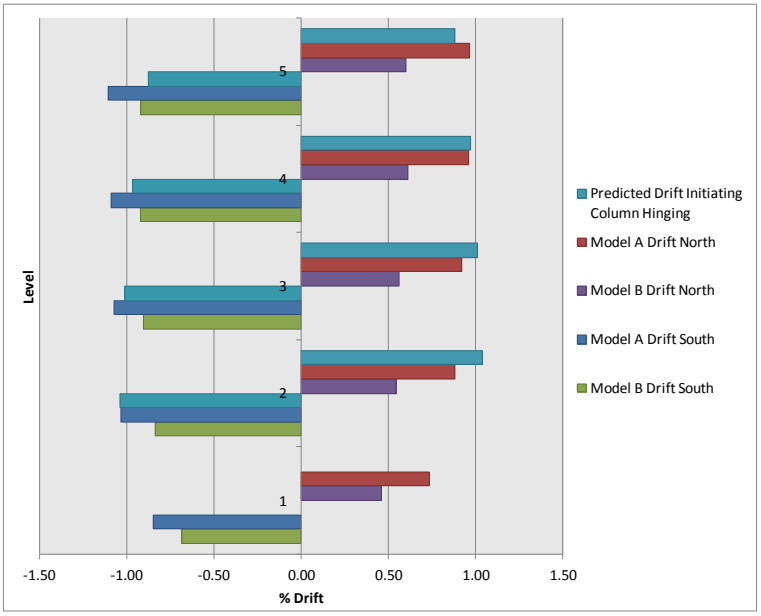

Figure 39: Frame F north/south storey drifts - Darfield.

Figure 40 and Figure 41 indicates the east/west storey drifts for the perimeter frames located on grid 1, and grid 4 for Model A and Model B. Note that the drift at the onset of hinging predicted by the pushover analyses has been presented for Frame 1 in Figure 40.

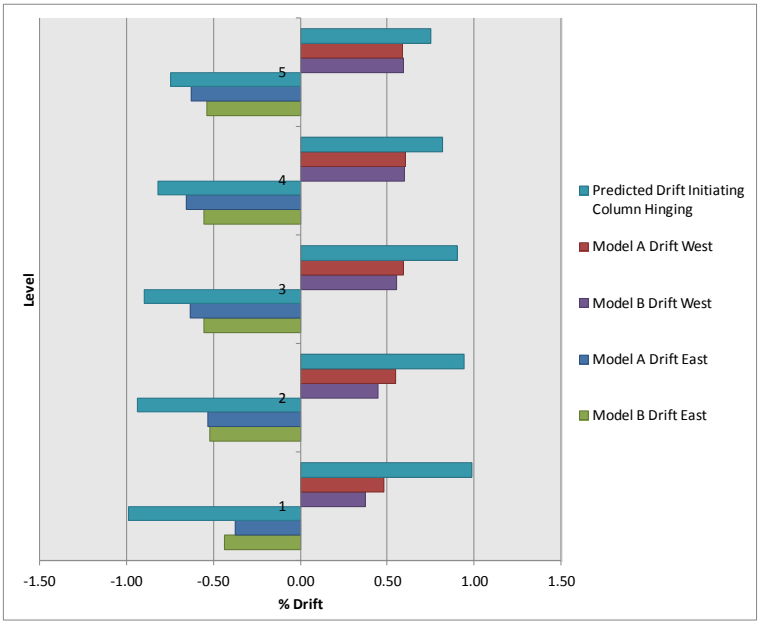

Figure 40: Frame 1 east/west storey drifts - Darfield.

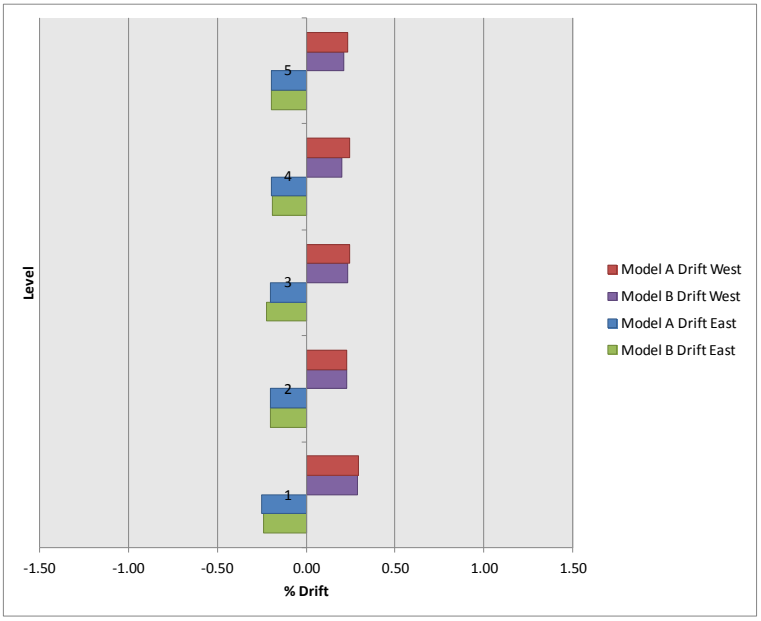

Figure 41: Frame 4 east/west storey drifts - Darfield.

The figures above indicate that based upon the static analyses results hinging is predicted to have occurred in the gridline F columns at levels 3, 4, and 5.

9.1.2. Diaphragm Connection Forces.

Table 17 to Table 21 present the diaphragm connection forces acting at each of the north core individual wall interfaces. Results presented are the enveloped maxima recorded over the duration of the time-history record analysed.

Table 17: Wall C diaphragm connection forces - Darfield.

Level	North/South Actions			
	Model A		Model B	
	Maximum Northward (kN)	Maximum Southward (kN)	Maximum Northward (kN)	Maximum Southward (kN)
Level 6	828	-919	1561	-1094
Level 5	619	-482	516	-342
Level 4	531	-329	701	-321
Level 3	504	-441	450	-538
Level 2	452	-746	467	-844

Table 18: Wall C/D diaphragm connection forces - Darfield.

Level	North/South Actions			
	Model A		Model B	
	Maximum Northward (kN)	Maximum Southward (kN)	Maximum Northward (kN)	Maximum Southward (kN)
Level 6	948	-471	885	-1345
Level 5	392	-511	504	-611
Level 4	370	-527	560	-573
Level 3	326	-486	358	-522
Level 2	538	-580	498	-574

Table 19: Wall D diaphragm connection forces - Darfield.

Level	North/South Actions			
	Model A		Model B	
	Maximum Northward (kN)	Maximum Southward (kN)	Maximum Northward (kN)	Maximum Southward (kN)
Level 6	352	-261	399	-603[1]
Level 5	356	-274	348	-353
Level 4	338	-300	353	-302
Level 3	335	0	279	0
Level 2	359	0	292	0

Notes: 1. Tensile limit of connection was exceeded.

Table 20: Wall D/E diaphragm connection forces - Darfield.

Level	North/South Actions			
	Model A		Model B	
	Maximum Northward (kN)	Maximum Southward (kN)	Maximum Northward (kN)	Maximum Southward (kN)
Level 6	374	-412	519	-540[1]
Level 5	218	-503[1]	250	-503[1]
Level 4	261	-403[1]	180	-403[1]
Level 3	461	0	357	0
Level 2	635	0	592	0

Notes: 1. Tensile limit of connection was exceeded.

Table 21: Wall 5 (C to C/D) diaphragm connection forces - Darfield.

Level	East/West Actions			
	Model A		Model B	
	Maximum Westward (kN)	Maximum Eastward (kN)	Maximum Westward (kN)	Maximum Eastward (kN)
Level 6	900	-999	888	-1117
Level 5	604	-800	679	-864
Level 4	528	-729	847	-1094
Level 3	351	-660	363	-666
Level 2	298	-666	363	-666

It can be seen from Table 19 and Table 20 that the addition of the masonry results in an increased number of diaphragm drag bar disconnections on walls D and D/E. Once the diaphragms have disconnected at these wall lines any torsion on the north core must be resisted by a couple between walls C and C/D. This can be observed in Table 17 and Table 18 where the increase in wall C and C/D actions at level 6 from Model A to Model B is the result of the diaphragm disconnection in Model B at this level that does not occur in Model A.

Table 22 and Table 23 present the diaphragm connection actions summarised for the entire north core at each floor level. Results presented are the enveloped maxima recorded over the duration of the time-history record analysed.

Table 22: North core total diaphragm connection forces - Darfield.

Level	East/West Actions					
	Model A			Model B		
	Maximum Westward (kN)	Maximum Eastward (kN)	Maximum In-Plane Moment (kNm)	Maximum Westward (kN)	Maximum Eastward (kN)	Maximum In-Plane Moment (kNm)
Level 6	1111	-1175	7696	1090	-1296	9410
Level 5	991	-1060	2656	1139	-994	3101
Level 4	886	-936	2345	1390	-1264	3644
Level 3	676	-752	4686	991	-871	5152
Level 2	504	-801	7227	591	-847	7775

Table 23: North core total diaphragm connection forces - Darfield.

Level	North/South Actions					
	Model A			Model B		
	Maximum Northward (kN)	Maximum Southward (kN)	Minimum In-Plane Moment (kNm)	Maximum Northward (kN)	Maximum Southward (kN)	Minimum In-Plane Moment (kNm)
Level 6	1315	-930	-7414	1348	-1124	-8805
Level 5	1333	-1195	-4486	1071	-1158	-4963
Level 4	1196	-1014	-4815	1319	-865	-6352
Level 3	1174	-824	-2425	1264	-911	-2226
Level 2	778	-997	-2180	898	-1027	-2412

Table 24 and Table 25 present the actions acting along the slab interface along gridline 4 between grids C and C/D. Figure 42 indicates (in dark blue) the location of slab elements used to determine the actions presented. Results presented are the enveloped maxima recorded over the duration of the time-history record analysed.

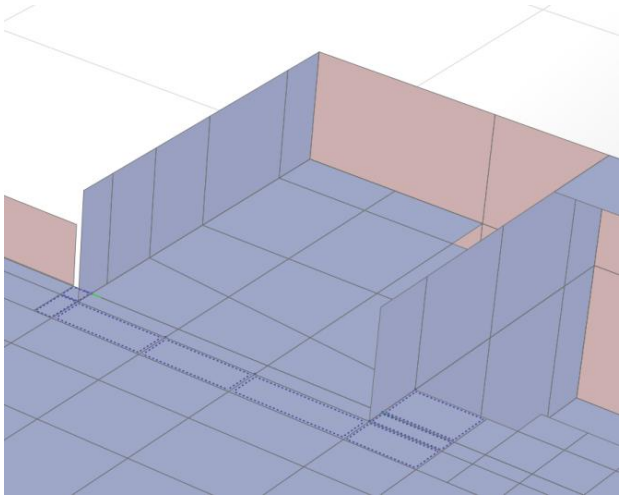

Figure 42: Slab 4 C-C/D section cut line.

It can be seen from these tables that the largest variation in demand between the two models occurs at levels 4 and 6. At level 6 there is a significant increase in in-plane moment which is the result of disconnection of the diaphragm drag bar ties at wall D and D/E at level 6. At level 4, the stiffening effect of the masonry (which terminates at level 4) creates a 'kick-back' effect resulting in higher N/S diaphragm forces at this level.

Table 24: Slab 4 C to C/D diaphragm N/S actions - Darfield

Level	East/West Actions					
	Model A			Model B		
	Maximum Westward (kN)	Maximum Eastward (kN)	Maximum In-Plane Moment (kNm)	Maximum Westward (kN)	Maximum Eastward (kN)	Maximum In-Plane Moment (kNm)
Level 6	1045	-952	5127	1166	-930	7930
Level 5	913	-879	3842	854	-984	4137
Level 4	793	-801	3317	1096	-1246	4540
Level 3	659	-575	3096	775	-869	2910
Level 2	729	-427	2356	755	-503	3186

Table 25: Slab 4 C to C/D diaphragm E/W actions - Darfield

Level	North/South Actions					
	Model A			Model B		
	Maximum Northward (kN)	Maximum Southward (kN)	Minimum In-Plane Moment (kNm)	Maximum Northward (kN)	Maximum Southward (kN)	Minimum In-Plane Moment (kNm)
Level 6	1126	-1272	-3802	1550	-1363	-4683
Level 5	906	-963	-2719	757	-860	-3336
Level 4	690	-705	-2518	900	-991	-4033
Level 3	803	-792	-1890	871	-694	-2988
Level 2	1113	-532	-2451	1121	-482	-2369

Table 26 presents the diaphragm connection actions at each floor level of the South wall located on grid 1. Results presented are the enveloped maxima recorded over the duration of the time-history record analysed.

Table 26: South wall diaphragm connection forces - Darfield

Level	East/West Actions			
	Model A		Model B	
	Maximum Westward (kN)	Maximum Eastward (kN)	Maximum Westward (kN)	Maximum Eastward (kN)
Level 6	522	-499	584	-653
Level 5	599	-707	628	-681
Level 4	596	-705	741	-678
Level 3	646	-628	641	-594
Level 2	615	-544	713	-583

9.1.3. Inelastic Wall Demands.

Results have shown that inelastic demand for the cantilever bending of the north core and the south wall only occurs in the lower part of level 1. Table 27 below presents the peak strains that occur during the Darfield CBGS event. Strains listed have been taken from the bottom shell elements at the extremities of each wall, and have been averaged over the height of the shell (998mm for the north core walls, and 1150 mm for the south wall piers). Note that ε_y = 0.00219 for the wall longitudinal reinforcement.

Table 27: Wall strains - Darfield

Location	Wall Element	Model A		Model B	
		Maximum	Minimum	Maximum	Minimum
North Core	Wall C gl 4	0.00960	-0.00191	0.00248	-0.00149
	Wall C gl 5	0.00682	-0.00062	0.00420	-0.00031
	Wall C/D gl 4	0.00942	-0.00192	0.00266	-0.00153
	Wall C/D gl 5	0.00485	-0.00021	0.00300	-0.00011
	Wall D gl 4	0.00974	-0.00181	0.00249	-0.00150
	Wall D gl 5	0.00381	-0.00019	0.00239	-0.00011
	Wall D/E gl 4	0.00938	-0.00102	0.00287	-0.00099
	Wall D/E gl 5	0.00214	-0.00047	0.00133	-0.00033
South Wall	Pier D gl D	0.00571	-0.00162	0.00628	-0.00138
	Pier D gl E	0.00251	-0.00012	0.00177	-0.00018
	Pier E gl D	0.00189	-0.00016	0.00223	-0.00025
	Pier E gl E	0.00672	-0.00143	0.00465	-0.00142

The analysis results indicate that only one of the diagonally reinforced coupling beams is subject to inelastic demand for Model A and Model B. A single set of diagonal bars, located in the level 1 coupling beam are predicted to yield, with a maximum strain of 0.00352 (which corresponds to $2.25\varepsilon_y$) reported for Model A, and 0.00255 ($1.63\varepsilon_y$) reported for Model B.

9.1.4. Inelastic Column Actions.

Analysis results indicate that minor column hinging occurs for both Model A and Model B with the number of hinges, and plastic rotation demand smaller for Model B. Hinges are predominantly located in the eastern perimeter frame (Frame F), with hinge formation initiated in the level 5 columns. Hinge formation progresses to lower levels as the displacement demand on the frame increases.

Figure 43 presents the progression of hinges forming in the Levels 5 to 1 columns for Model A, whilst Figure 44 presents the progression of column hinging occurring in Model B.

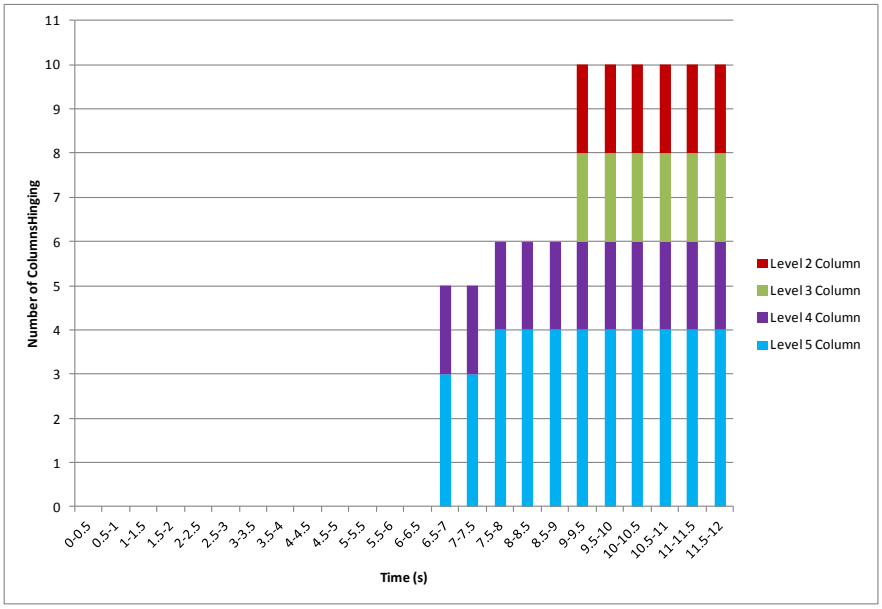

Figure 43: Column hinge progression - Darfield, Model A.

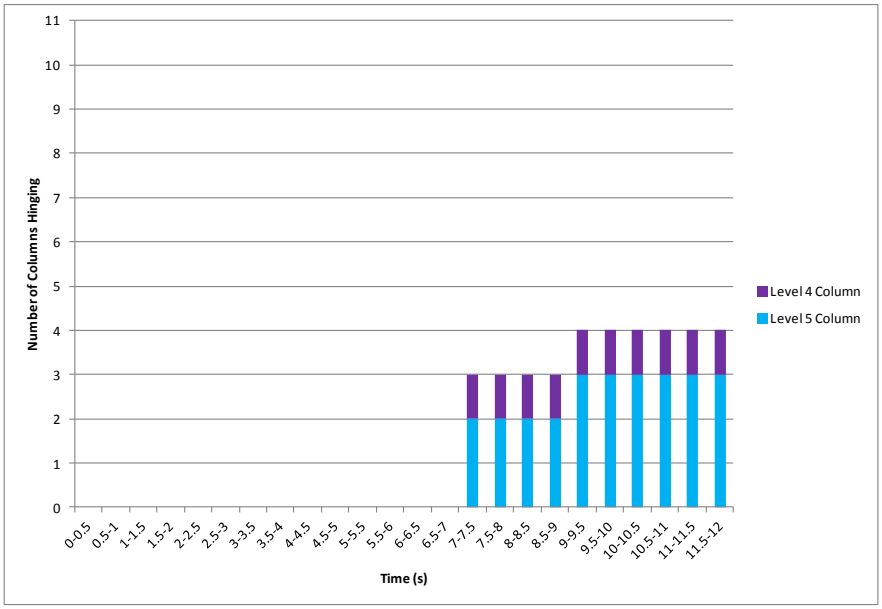

Figure 44: Column hinge progression - Darfield, Model B.

Hinge plastic rotation demand predicted by the analysis model are presented in Table 28 below.

Table 28: Column hinge plastic rotations - Darfield

Column	Level	Model A Maximum (rad)	Model B maximum (rad)
F1	5	0.00109	-
F2	5	0.00231	0.00047
	4	0.00131	-
	3	0.00057	-
	2	0.00024	-
F3	5	0.00502	0.00139
	4	0.00269	0.00036
	3	0.00149	-
	2	0.00033	-
F4	5	0.00010	-

9.1.5. Base shears.

Peak seismic base shear recorded during the time history analysis are shown in Table 29 below for Model A and Model B. Results presented have been recorded at the top of the foundation beams.

With the exception of the southward direction, maximum base shears are larger for Model B although displacement demands are typically smaller for this model (as seen in the storey drift plots of Section 9.1.1). This can be attributed to a combination of higher mode effects and the period shift caused by the masonry stiffening the structure, resulting in the structure being subject to higher spectral accelerations. Table 9 and Table 10 indicate that the addition of masonry to the structure reduces the first mode of vibration by approximately 0.15 seconds, which results in an increase in acceleration demand for the CBGS record (refer Figure 21 and Figure 22 of Section 7.3.1).

Table 29: Darfield base shears

Direction	Model A Base Shear (kN)	Model B Base Shear (kN)
Maximum Northward	4229	4790
Maximum Southward	-5392	-4987
Maximum Westward	6934	7195
Maximum Eastward	-7298	-7409

10. Non Linear Time History: Lyttelton Results

Results presented in this section are primarily for the earthquake acceleration time history recorded at the Christchurch Botanical Gardens (CBGS), and are a summary of the analyses only. Results from the Christchurch Hospital (CHHC) and Christchurch Cathedral College (CCCC) time history records are included in sections 10.1.1, 10.1.2, and 10.1.5 for comparison purposes. Additional CBGS results can be found in Appendix F. In all cases analyses results include all three components of the appropriate time history record.

10.1.1. Drifts and Displacements

Figure 45, and Figure 46, below present the maximum north/south percent storey drifts recorded for the perimeter frames located on grids A, and F respectively. Drifts are presented for the CCCC, CBGS, and the CHHC records.

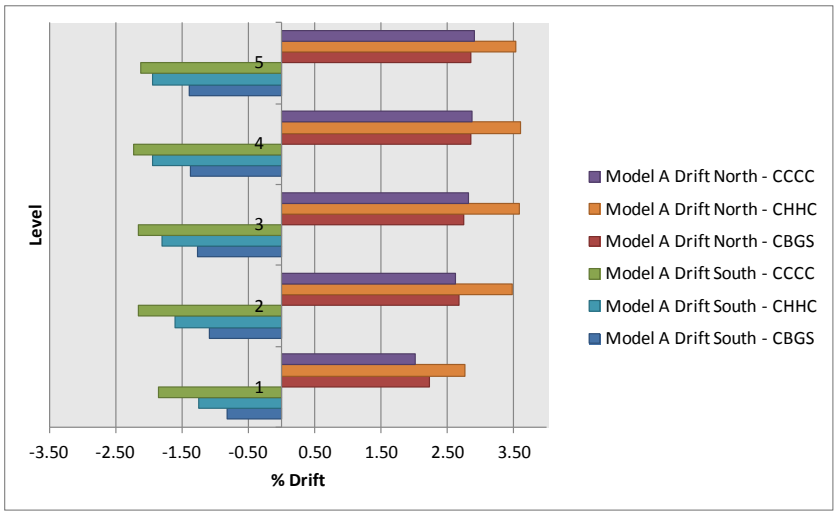

Figure 45: Frame A north/south storey drifts - Lyttelton.

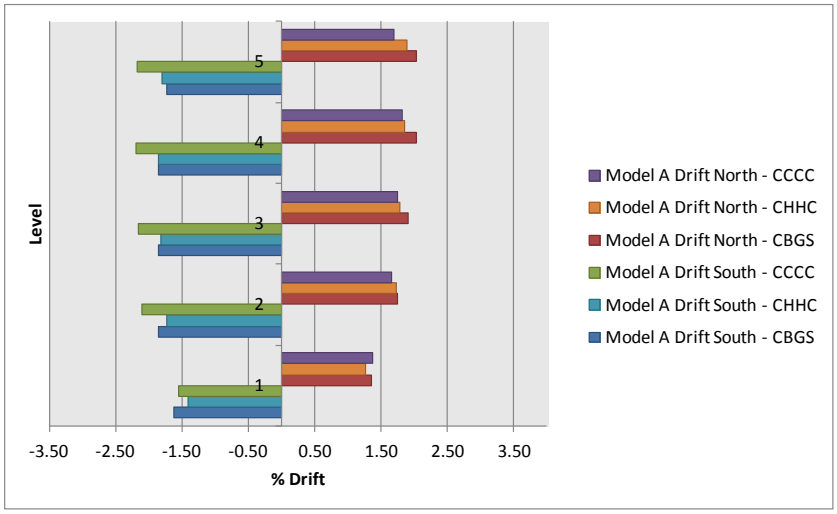

Figure 46: Frame F north/south storey drifts - Lyttelton.

Figure 47, and Figure 48, below present the maximum east/west percentage storey drifts recorded for the perimeter frames located on grids 1, and 4 respectively. Drifts are presented for the CCCC, CBGS, and the CHHC records.

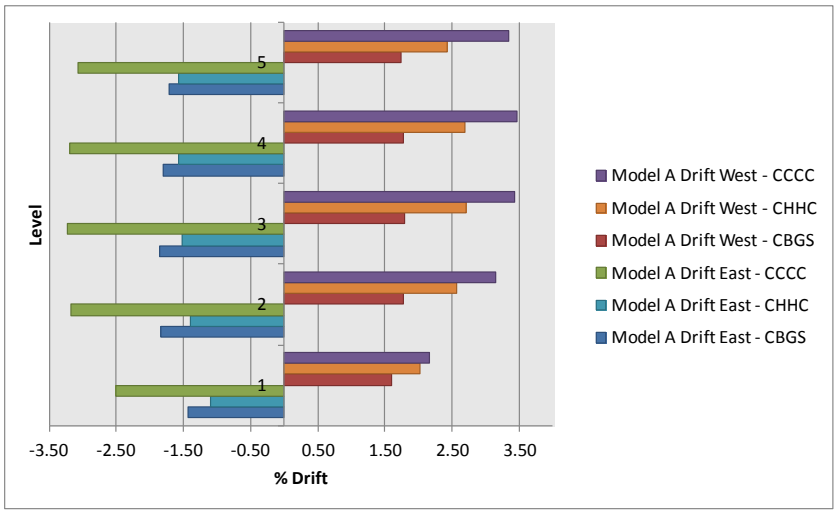

Figure 47: Frame 1 east/west storey drifts - Lyttelton.

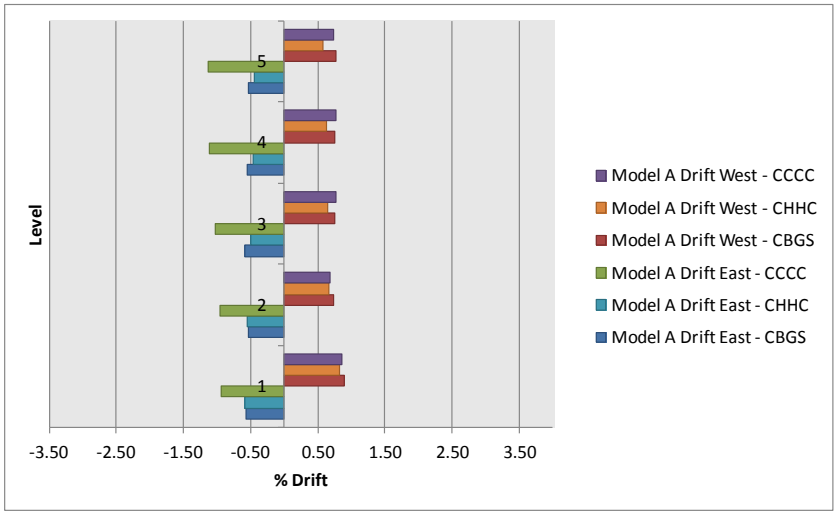

Figure 48: Frame 4 east/west storey drifts - Lyttelton.

It can be seen from the storey drift plots above that the CCCC record has larger displacement demands in the E/W direction than the other records. Drift variations of up to 1.7% are predicted in the easterly direction with the CHHC record producing the smallest drifts. In the westerly direction drifts are similar for Frame 4, although variations of 0.8% are observed between the CCCC (highest drift) the CBGS (lowest drift) records.

North/south drifts are relatively similar between the records, with Frame F drifts within 0.4% over the three records for northerly and southerly directions of drift. Frame A drifts exhibit more variation between records in the southward direction (up to 1% difference), with the CBGS record producing the smallest southward drifts. In the northerly direction the drifts are more closely matched with the CBGS and the CCCC records producing similar drifts, with the CHHC record producing drifts up to 0.8% higher.

10.1.2. Diaphragm Connection Forces.

Table 30 to Table 34 present the diaphragm connection forces acting at each of the north core individual wall interfaces. Results presented are the enveloped maxima recorded over the duration of the time-history record analysed.

Table 30: Wall C diaphragm connection forces - Lyttelton.

Level	North/South Actions					
	CCCC		CHHC		CBGS	
	Maximum Northward (kN)	Maximum Southward (kN)	Maximum Northward (kN)	Maximum Southward (kN)	Maximum Northward (kN)	Maximum Southward (kN)
Level 6	4186	-2747	2845	-2552	3235	-2642
Level 5	1133	-1004	1326	-930	1009	-906
Level 4	1214	-1548	1301	-1392	1276	-1644
Level 3	1252	-1580	1260	-1456	1305	-1756
Level 2	1452	-1452	1292	-2002	1007	-2070

Table 31: Wall C/D diaphragm connection forces - Lyttelton.

Level	North/South Actions					
	CCCC		CHHC		CBGS	
	Maximum Northward (kN)	Maximum Southward (kN)	Maximum Northward (kN)	Maximum Southward (kN)	Maximum Northward (kN)	Maximum Southward (kN)
Level 6	1477	-3886	1350	-2663	1252	-2497
Level 5	730	-956	884	-955	792	-1026
Level 4	1301	-913	1102	-1346	745	-1399
Level 3	1385	-1316	1221	-1260	1220	-1840
Level 2	1076	-1470	1226	-1233	1536	-1381

Table 32: Wall D diaphragm connection forces - Lyttelton.

Level	North/South Actions					
	CCCC		CHHC		CBGS	
	Maximum Northward (kN)	Maximum Southward (kN)	Maximum Northward (kN)	Maximum Southward (kN)	Maximum Northward (kN)	Maximum Southward (kN)
Level 6	854	-603[1]	907	-603[1]	1075	-603[1]
Level 5	723	-420[1]	552	-420[1]	662	-420[1]
Level 4	680	-320[1]	666	-320[1]	772	-320[1]
Level 3	648	0	722	0	621	0
Level 2	874	0	710	0	685	0

Notes: 1. Tensile limit of connection was exceeded.

Table 33: Wall D/E diaphragm connection forces - Lyttelton.

Level	North/South Actions					
	CCCC		CHHC		CBGS	
	Maximum Northward (kN)	Maximum Southward (kN)	Maximum Northward (kN)	Maximum Southward (kN)	Maximum Northward (kN)	Maximum Southward (kN)
Level 6	1054	-540[1]	1084	-540[1]	1640	-540[1]
Level 5	362	-503[1]	939	-503[1]	660	-503[1]
Level 4	352	-403[1]	718	-403[1]	772	-403[1]
Level 3	606	0	830	0	740	0
Level 2	925	0	880	0	932	0

Notes: 1. Tensile limit of connection was exceeded.

Table 34: Wall 5 (C to C/D) diaphragm connection forces - Lyttelton.

Level	East/West Actions					
	CCCC		CHHC		CBGS	
	Maximum Westward (kN)	Maximum Eastward (kN)	Maximum Westward (kN)	Maximum Eastward (kN)	Maximum Westward (kN)	Maximum Eastward (kN)
Level 6	2023	-2405	1718	-2007	1985	-2203
Level 5	1675	-2315	1357	-1813	1429	-1957
Level 4	1379	-2328	1055	-1413	1430	-2142
Level 3	1233	-1620	1053	-1226	1009	-1630
Level 2	825	-1373	1147	-1036	1134	-1194

Table 35, Table 36 and Table 37 present the diaphragm connection actions summarised for the entire north core at each floor level. Results presented are the enveloped maxima recorded over the duration of the time-history record analysed.

Table 35: North core total diaphragm connection E/W forces - Lyttelton.

Level	East/West Actions					
	CCCC		CHHC		CBGS	
	Maximum Westward (kN)	Maximum Eastward (kN)	Maximum Westward (kN)	Maximum Eastward (kN)	Maximum Westward (kN)	Maximum Eastward (kN)
Level 6	2481	-2895	2111	-2359	2392	-2451
Level 5	2697	-2054	2131	-1813	2154	-2198
Level 4	2262	-2299	1673	-1543	2337	-1861
Level 3	1928	-1958	1755	-1322	1849	-1957
Level 2	1243	-1735	1538	-1325	1573	-1534

Table 36: North core total diaphragm connection N/S forces - Lyttelton.

Level	North/South Actions					
	CCCC		CHHC		CBGS	
	Maximum Northward (kN)	Maximum Southward (kN)	Maximum Northward (kN)	Maximum Southward (kN)	Maximum Northward (kN)	Maximum Southward (kN)
Level 6	2352	-1641	2503	-2108	2220	-2268
Level 5	1875	-1585	2328	-2045	1877	-1718
Level 4	1897	-2039	2678	-2145	2195	-2896
Level 3	2472	-2565	3316	-2455	2665	-3818
Level 2	2779	-3155	2796	-2402	3062	-2924

Table 37: North core total diaphragm connection forces - Lyttelton.

Level	In Plane Moments					
	CCCC		CHHC		CBGS	
	Maximum + Moment (kNm)	Maximum -Moment (kNm)	Maximum + Moment (kNm)	Maximum -Moment (kNm)	Maximum + Moment (kNm)	Maximum -Moment (kNm)
Level 6	20055	-19638	20846	-14015	24478	-14897
Level 5	8167	-9937	8023	-8483	6550	-6326
Level 4	7420	-7986	8318	-6685	7258	-7301
Level 3	8331	-7072	8798	-6851	8443	-5890
Level 2	16099	-7591	13841	-7267	14548	-7217

Table 38, Table 39, and Table 40 present the actions acting along the slab interface along gridline 4 between grids C and C/D. Results presented are the enveloped maxima recorded over the duration of the time-history record analysed.

Table 38: Slab 4 C to C/D diaphragm E/W actions - Lyttelton.

Level	East/West Actions					
	CCCC		CHHC		CBGS	
	Maximum Westward (kN)	Maximum Eastward (kN)	Maximum Westward (kN)	Maximum Eastward (kN)	Maximum Westward (kN)	Maximum Eastward (kN)
Level 6	2550	-2307	2090	-1900	2295	-2076
Level 5	1635	-2544	1547	-1909	1843	-1926
Level 4	2050	-2007	1362	-1493	1612	-2002
Level 3	1554	-1737	1152	-1555	1698	-1626
Level 2	1575	-1026	1267	-1382	1427	-1474

Table 39: Slab 4 C to C/D diaphragm N/S actions - Lyttelton.

Level	North/South Actions					
	CCCC		CHHC		CBGS	
	Maximum Northward (kN)	Maximum Southward (kN)	Maximum Northward (kN)	Maximum Southward (kN)	Maximum Northward (kN)	Maximum Southward (kN)
Level 6	2862	-2259	2834	-1631	2895	-2018
Level 5	1410	-1612	1773	-1833	1517	-1347
Level 4	1781	-1772	2058	-2084	2854	-1993
Level 3	2382	-2144	2311	-2358	3645	-2317
Level 2	2966	-2110	2372	-2276	2781	-2024

Table 40: Slab 4 C to C/D diaphragm connection forces - Lyttelton.

Level	In-Plane Moments					
	CCCC		CHHC		CBGS	
	Maximum + Moment (kNm)	Maximum -Moment (kNm)	Maximum + Moment (kNm)	Maximum -Moment (kNm)	Maximum + Moment (kNm)	Maximum -Moment (kNm)
Level 6	20656	-12495	15717	-8151	14397	-11083
Level 5	9522	-9433	9143	-5553	8251	-6248
Level 4	19450	-7883	5777	-5948	8732	-6194
Level 3	28094	-5834	4523	-5789	7138	-5077
Level 2	26354	-6134	4152	-5611	7343	-5190

Table 40 presents the diaphragm connection actions at each floor level of the south wall located on grid 1. Results presented are the enveloped maxima recorded over the duration of the time-history record analysed.

Table 41: South wall diaphragm connection forces - Lyttelton.

Level	East/West Actions					
	CCCC		CHHC		CBGS	
	Maximum Westward (kN)	Maximum Eastward (kN)	Maximum Westward (kN)	Maximum Eastward (kN)	Maximum Westward (kN)	Maximum Eastward (kN)
Level 6	970	-929	1017	-1401	1076	-1200
Level 5	1168	-1245	1163	-1153	1092	-1097
Level 4	1083	-1228	1098	-1164	1145	-1331
Level 3	1138	-1063	1328	-1462	1080	-1681
Level 2	1313	-1388	1480	-1315	1347	-2042

10.1.3. Inelastic Column Actions.

Results presented in this section are for the CBGS record only.

Analysis results indicate that the onset of column hinging commences at 2.25 seconds of the run time history record with minor column hinging occurring in up to 15 columns after 4.75 seconds has been run. During this time frame hinges are predominantly located in the eastern perimeter frame (Frame F), with hinge formation initiated in the level 5 columns. Hinge formation progresses to lower levels as the displacement demand on the frame increases. Between 4.75 and 5 seconds an additional 61 columns (61% of the total number of structural

columns) undergo plastic rotational demand. This increase in hinge numbers corresponds with a large increase in inter-storey drifts that occur during the same time period (as shown in Figure F.3 in Appendix F).

Figure 49 presents the progression of hinges forming in the levels 1 to 5 columns.

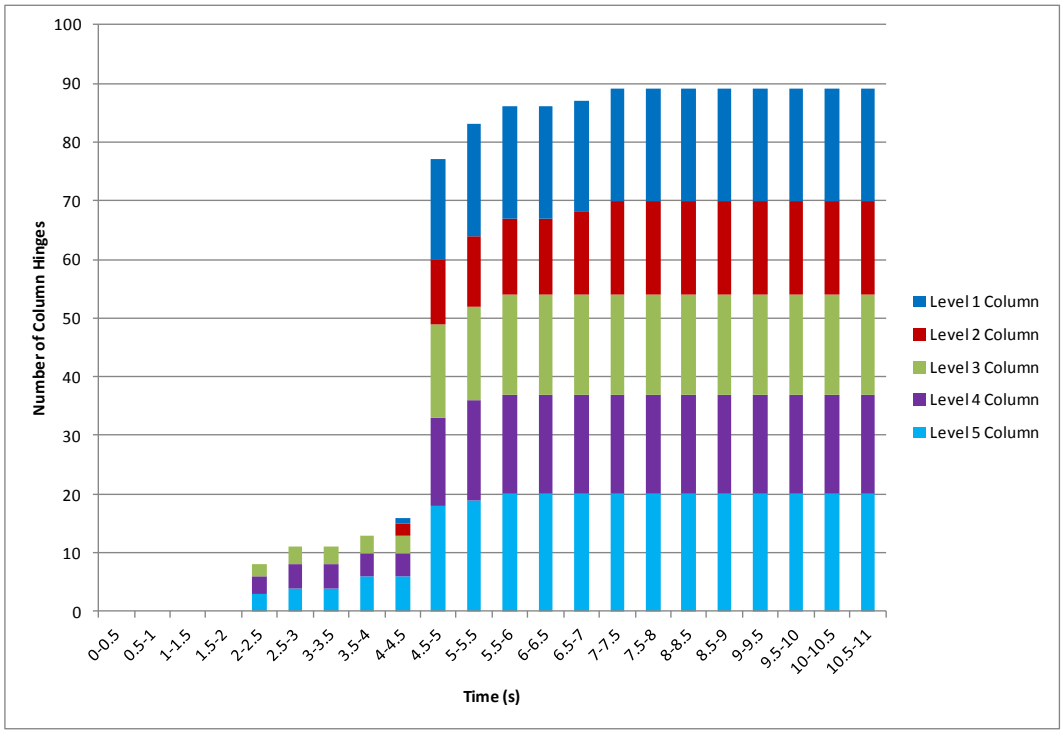

Figure 49: Column hinge progression - CBGS, Lyttelton.

10.1.4. Beam-Column Joints.

Post processing of the beam column joint results has indicated that the limiting capacity for most joints is via joint shear failure rather than bar anchorage pullout. There is the potential for bar pullout to limit the capacity in the joints located at F1 & F4 at level 6, F1 at level 5 and A1 at level 2.

Results show that the joint shear was exceeded in the column lines F2 and F3 first, closely followed by column line F1. Approximately 18 joint capacities are close to, or slightly exceed capacity between 2.3 to 3.6 seconds with a further 26 joints being becoming overstressed between 4.5 to 5.7 seconds. The trends shown for the demand/capacity vs time of the beam column joints is similar to that exhibited by the hinge formation detailed in Section 10.1.3 above. It should be noted that the capacity of the beam-column joints is

sensitive to variances in material strength, and axial load and the ductility demand of adjacent beam hinges.

10.1.5. Base Shears.

Peak seismic base shear recorded during the time history analysis are shown in Table 42 below for the three records investigated. Results presented have been recorded at the top of the foundation beams.

Maximum base shear for the time history analyses exceed those predicted by the pushover analyses (refer Figure 28 of Section 8.1). This can be attributed to higher mode effects, and approximations made in the distribution of load in the pushover analyses.

Table 42: Lyttelton base shear

Direction	CCCC Base Shear (kN)	CHHC Base Shear (kN)	CBGS Base Shear (kN)
Maximum Northward	9479	6570	8796
Maximum Southward	-5827	-6959	-7269
Maximum Westward	12659	10447	11277
Maximum Eastward	-13348	-12873	-13022

10.1.6. L6 Core Slab Out Of Plane Actions.

In addition to the in-plane actions detailed in section 10.1.2 the floor slab around each shear walls would have been subject to out of plane demands due to the vertical movement of the wall when subject to seismic actions. Of particular interest is the bending demands of the section of floor slab located along gridline 4 between the north core walls C and C/D.

Figure 50 presents the vertical displacements at the tips of the core walls located on grids C and C/D at level 6. Out of plane slab moments that occur between these walls are presented in Figure 51 with positive (sagging) moments shown as negative in sign. Moments have been presented for two locations. Firstly (referenced as GL4 C to C/D Slab) is located along a plane joining the tips of wall C and wall C/D i.e. 250 mm from gridline 4. The second is located along a parallel plane located 1.75 m to the south of gridline 4, which roughly corresponds with the termination location of the saddle bars that straddle gridline 4. Note that as an average of the positive and negative slab out of plane stiffness was used in the analysis model,

negative (hogging) moments presented are likely to be underestimated as the negative bending stiffness at gridline 4 would be stiffer than the average used in this location. In addition, as elastic shell elements have been used peak moments presented may exceed bending capacity. As such moments should be viewed as indicative only.

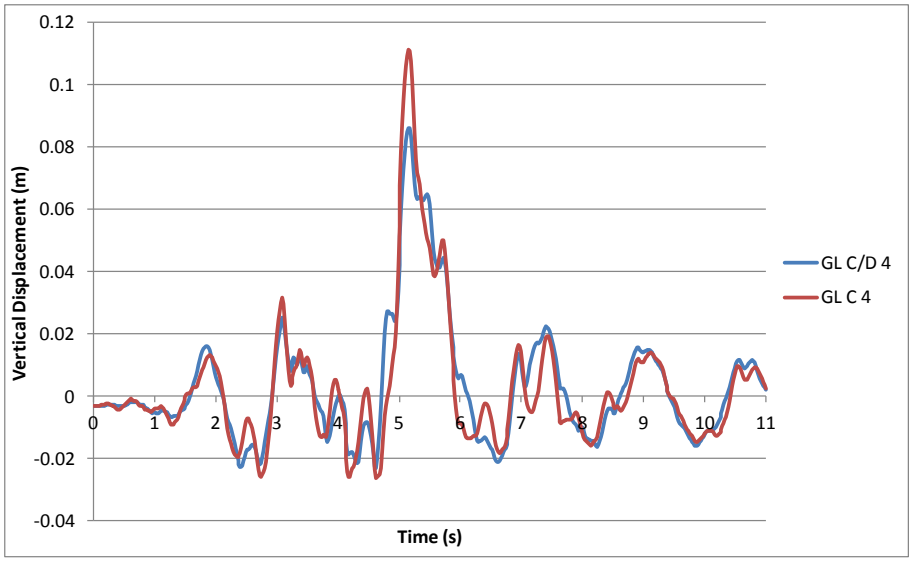

Figure 50: North core wall C & C/D vertical displacements at GL 4.

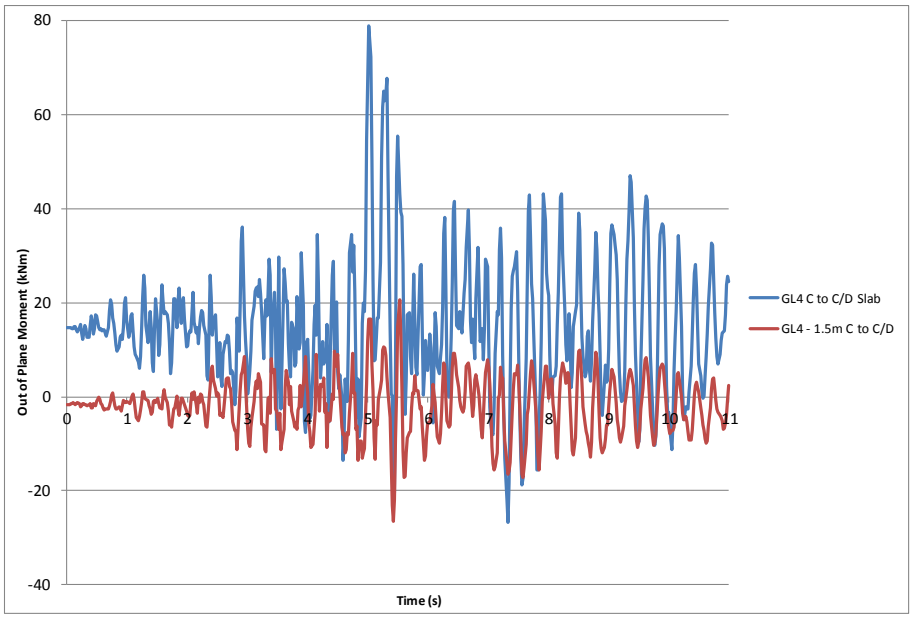

Figure 51: GL 4 slab C to C/D out of plane moments.

11. Vertical Earthquake Effects

To quantify and assess the effect of vertical accelerations on the building response and performance separate inelastic time history analyses were undertaken using only the vertical components of the CBGS and CCCC Lyttelton records, the results of which are contained within the following section. Further to this a sensitivity analysis was undertaken to investigate the effect slab flexibility has on the vertical earthquake response using the CBGS record only.

11.1. Axial Load Effects

Figure 52 through Figure 55 present the maximum variation in axial force obtained during the analysis for a selection of columns under the CBGS and CCCC record demands.

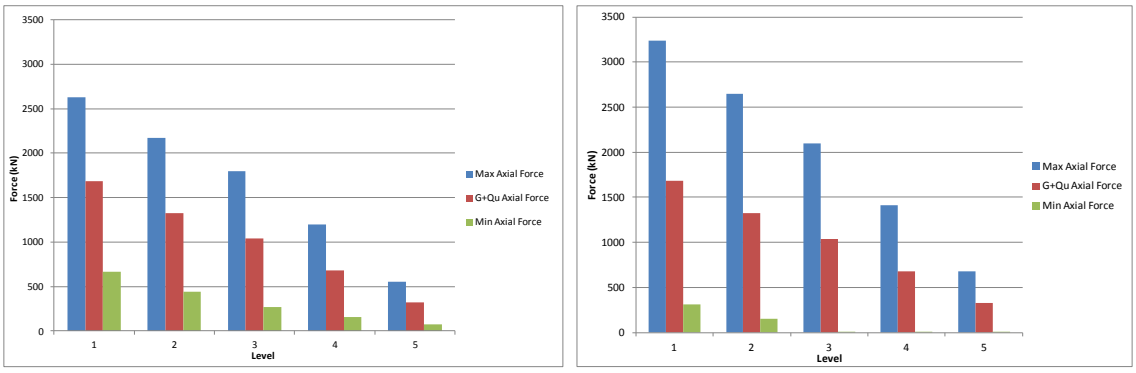

Figure 52: Column D2 axial load variation - CBGS (left) & CCCC (right), Lyttelton

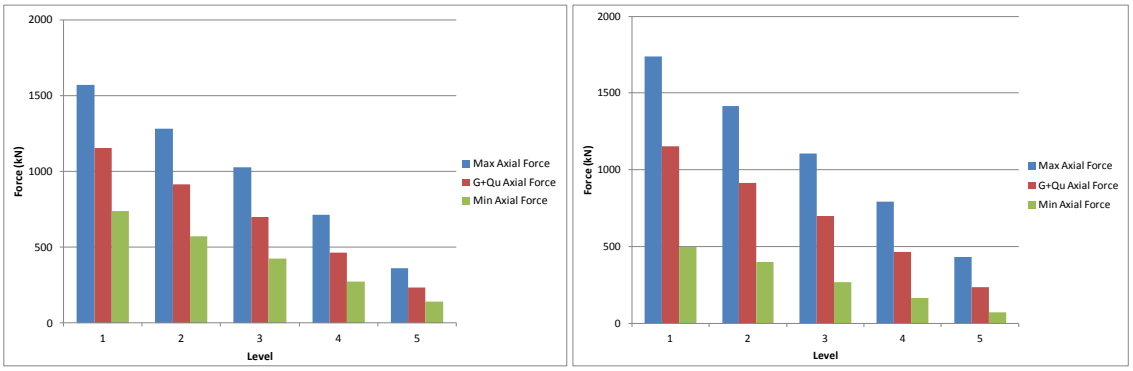

Figure 53: Column F2 axial load variation - CBGS (left) & CCCC (right), Lyttelton

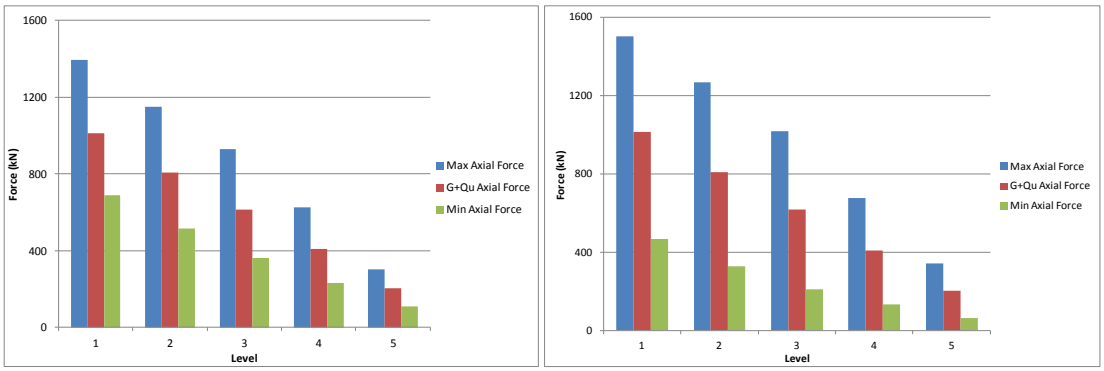

Figure 54: Column F1 axial load variation - CBGS (left) & CCCC (right), Lyttelton

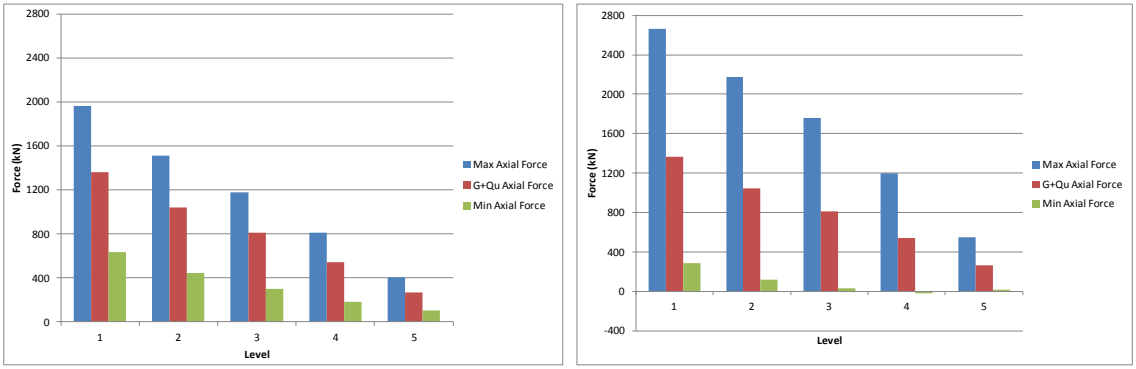

Figure 55: Column 4 D/E axial load variation - CBGS (left) & CCCC (right), Lyttelton

Columns with a larger tributary area of floor slab such as column D2 exhibit a larger variation in axial force than columns with a smaller axial load contribution from the slabs e.g. column F2. In addition to the slab component some of the axial load variation can be attributed to the stiffness of the beams spanning onto the column. Table 43 presents a comparison of the Level 1 axial force maxima and minima for selected elements between each record.

It can be seen that the CCCC record produces a much larger variation in axial load in the elements considered than the CBGS record. This can be attributed to the difference in frequency components between the two records and the magnitude of the vertical accelerations present in each. Figure D.2 and Figure D.3 contain the vertical acceleration time history records for the CBGS and the CCCC stations. From these it can be seen that the vertical accelerations were considerably higher at the CCCC station than for the CBGS station.

Table 43: Level 1 axial force demands - CBGS and CCCC vertical earthquake components.

Element	CGBS Record		CCCC Record	
	Maximum (kN)	Minimum (kN)	Maximum (kN)	Minimum (kN)
Column D2	2629	666	3239	308
Column F2	1572	736	1738	496
North Core	10679	2591	15891	-325
South Wall	3608	1499	4770	741

It should also be noted that the peak axial demands may not be concurrent with the peak bending actions that occur as a result of building drift. Consequently when assessing vertical earthquake demands, consideration should be given to the concurrency of actions. An example of the concurrency effect can be seen in Figure 56 in which it can be seen that the peak axial column demands do not occur at the same time as peak column drift for column D2 at level 1.

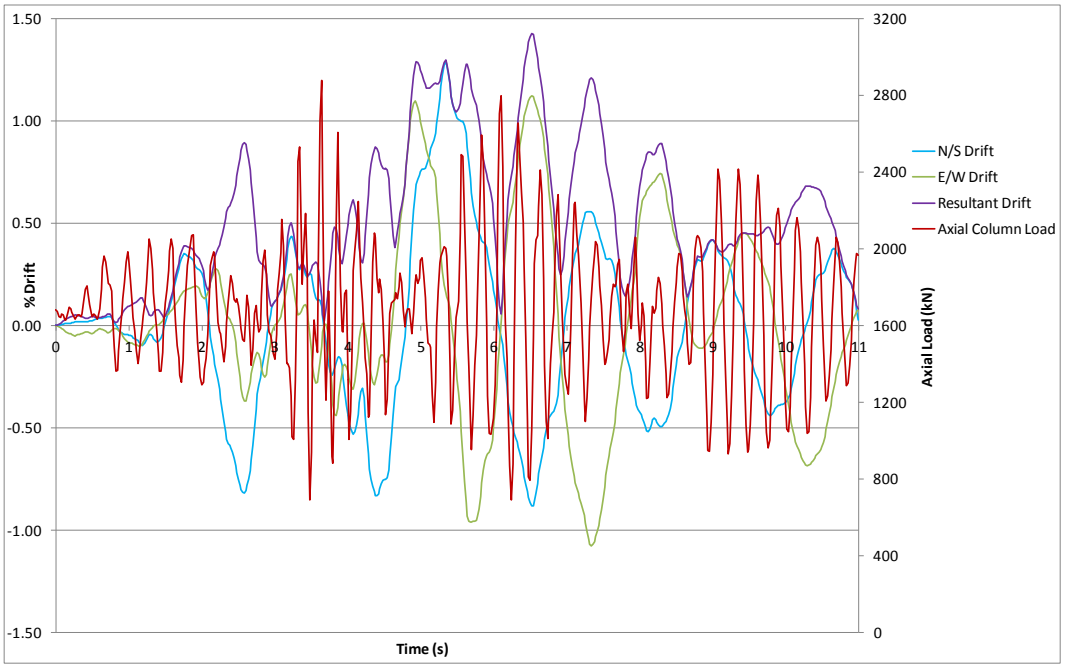

Figure 56: Column D2 Level 1 axial load and drift plot - CBGS, Lyttelton

11.2. Bending Effects

Vertical excitation of the beams induces bending in both the beam elements and the supporting columns. A selection of column bending actions induced by the vertical component of the CBGS and the CCCC records are presented in Table 44 for information. Column moments presented have been recorded at the column head, and column capacities correspond to the moment at which concrete strain of 0.004 is reached and have been based upon the initial G + Qu axial gravity force in the column. It should be noted that the actions presented will be an upper bound as the demands from the horizontal components of the earthquake record may result in beam hinging, if so concurrent actions from the vertical component may not increase column bending actions significantly (but could influence hinge rotations).

Table 44: Induced column moments - CBGS and CCCC vertical earthquake components.

Level	Column D2			Column F2		
	CBGS Moment (kNm)	CCCC Moment (kNm)	Moment Capacity (kNm)	CBGS Moment (kNm)	CCCC Moment (kNm)	Moment Capacity (kNm)
5	24	38	140	15	27	137
4	24	50	162	15	21	150
3	20	45	173	10	18	169
2	25	36	192	10	18	184
1	15	24	211	9	16	204

11.3. Sensitivity Study

A sensitivity study has been undertaken to determine the influence slab stiffness has on the vertical excitation of structural elements and the associated design actions. To investigate this two additional models were investigated to provide a basis of comparison with the analysis model used to determine the structural actions documented in this report. Sensitivity model characteristics were as follows;

1) Stiff Slab: This model used double the slab plate stiffness used in the main analysis model.

2) Flexible Slab: This model used half the plate stiffness of the slabs used in the main analysis model.

It is expected that the stiffness of the slab have been more closely represented in the main analysis model, with the two additional models providing an upper and lower bound on the slab response. Beam hinging from concurrent horizontal actions may also influence the vertical response, however this has not been examined in this study.

Numerical differences in axial load are presented in Table 45 for selected structural elements recorded at level 1. Figure 57 and Figure 58 below indicate the axial load variation with time for Column D2 and the North Core for Level 1 of the structure.

Table 45: Range of Level 1 axial force due to vertical earthquake.

Element	Half Slab Stiffness		Main Model		Double Slab Stiffness	
	Maximum (kN)	Minimum (kN)	Maximum (kN)	Minimum (kN)	Maximum (kN)	Minimum (kN)
Column D2	2156	1274	2629	666	2450	794
Column F2	1546	702	1572	736	1611	633
North Core	9575	3788	10679	2591	10138	2988
South Wall	3483	1886	3608	1499	3754	1023

From Table 45 it can be seen that the axial actions for column F2 and the north core are relatively insensitive to slab stiffness with only a 7% to 18% difference in the range of actions respectively. The south wall and column D2 exhibit more variation in the range axial load (27% to 34% respectively).

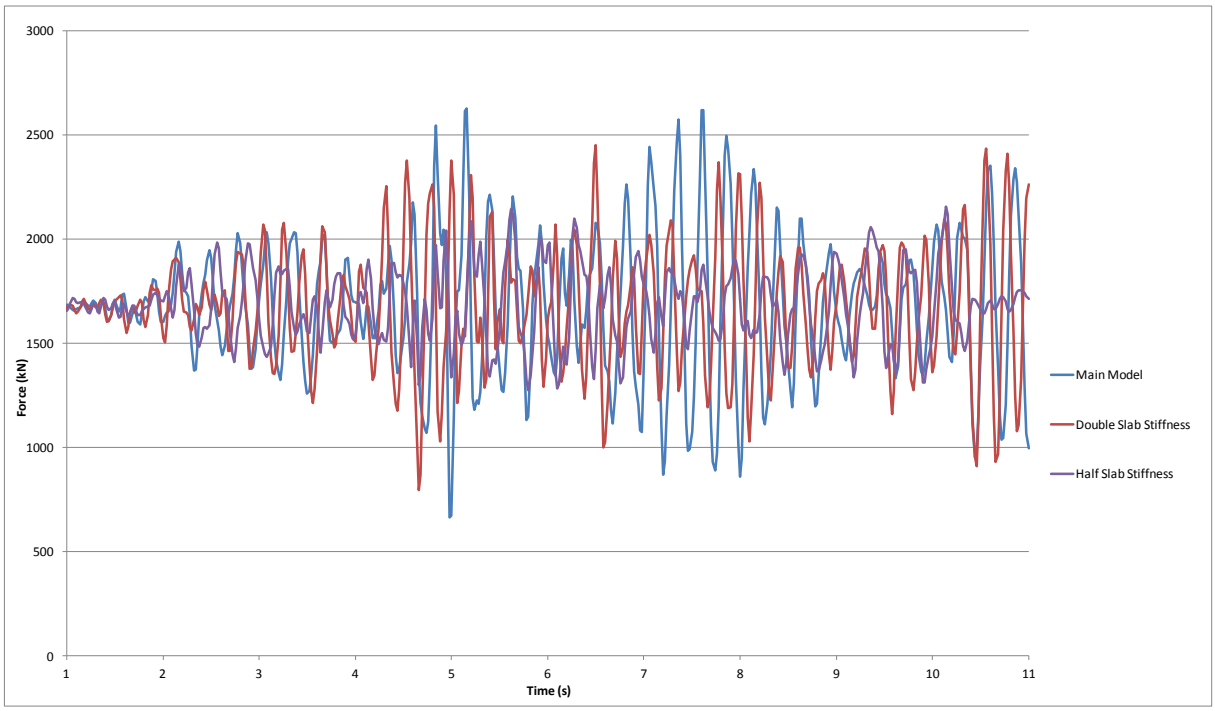

Figure 57: Column D2 axial load variation with time - CBGS, Lyttelton.

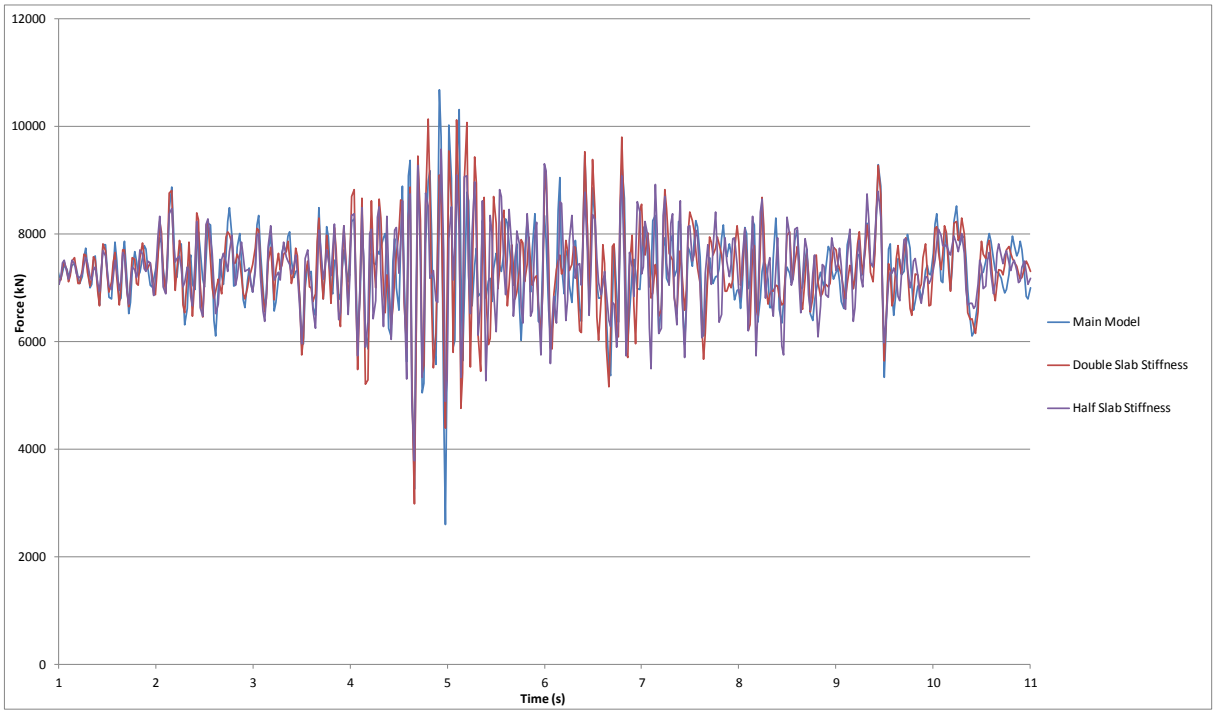

Figure 58: North core axial load variation with time - CBGS, Lyttelton.

12. References

1. Design Engineer (1986) *Structural Drawings: Office Building - 249 Madras Street*. Set No. 7, Issued 30 September. 39p.
2. Hyland, C (2011) *CTV Building Site Examination and Materials Tests*. Hyland Fatigue and Earthquake Engineering, Auckland, New Zealand. 158p.
3. CSI Berkeley (2011) *Computer program SAP2000 v14.2.4*. Computers and Structures Inc., Berkeley, California.
4. Sinclair, T (2011) *Ref. 52118: CTV Geotechnical Advice (11 July)*. Tonkin & Taylor, Auckland, New Zealand. 14p.
5. NZSEE (2006) *Assessment and Improvement of the Structural Performance of Buildings in Earthquakes*. New Zealand Society for Earthquake Engineering, Wellington, New Zealand. ~400p.
6. NZS 3101 (2006) *Concrete Structures Standard*. Standards New Zealand, Wellington, New Zealand. 646p.
7. Priestley, M J N, Calvi, G M, and Kowalsky, M J (2007) *Displacement-Based Seismic Design of Structures*. IUSS Press, Pavia, Italy. 721p.
8. Andriono, T and Park, R (1986) *Seismic Design Considerations of the Properties of New Zealand Manufactured Steel Reinforcing Bars.* Bulletin of the New Zealand National Society for Earthquake Engineering. **19**(3): pp.213-246.
9. Carr, A J (1994) *Dynamic Analysis of Structures.* Bulletin of the New Zealand Society for Earthquake Engineering. **27**(2).
10. Takeda, T, Sozen, M A, and Nielsen, N N (1970) *Reinforced Concrete Response to Simulated Earthquakes.* Journal of Structural Engineering. **96**(12): pp.2257-2273.
11. Mander, J B, Priestley, M J N, and Park, R (1988) *Theoretical Stress-Strain Model for Confined Concrete.* ASCE Journal of Structural Engineering. **114**(8): pp.1804-1826.
12. NZS 1170.0 (2002) *Structural design actions, Part 0: General Principles*. Standards New Zealand, Wellington, New Zealand. 36p.
13. NZS 1170.5 (2004) *Structural design actions, Part 5: Earthquake Actions - New Zealand*. Standards New Zealand, Wellington, New Zealand. 154p.
14. DBH (2011) *Changes for Christchurch Seismicity: Changes to Verification Method B1/VM1 - Hazard Factor for Christchurch*. accessed 22 August 2011; Available from: http://www.dbh.govt.nz/UserFiles/File/Publications/Building/Guidance-information /pdf/information-sheet-on-seismicity-changes.pdf.
15. Geonet (2010) *M 7.1, Darfield (Canterbury), September 4 2010*. Webpage; accessed 05 August 2011; Available from: www.geonet.org.nz/earthquake/historic-earthquakes/top-nz/quake-13.html.
16. Geonet (2011) *M 6.3, Christchurch, February 22 2011*. Webpage; accessed 05 August 2011; Available from: www.geonet.org.nz/earthquake/historic-earthquakes/top-nz/quake-14.html.
17. Geonet (2010) *Darfield Mainshock Records*. FTP Site; accessed 05 August 2011; Available from: ftp.geonet.org.nz/strong/processed/Proc/2010/09_Darfield_ mainshock_extended_pass_band/Vol2/data/.
18. Geonet (2011) *Christchurch Mainshock Records*. FTP Site; accessed 05 August 2011; Available from: ftp.geonet.org.nz/strong/processed/Proc/2011/02_Christchurch_ mainshock_extended_pass_band/Vol2/data/.
19. Hindi, R A and Hassan, M A (2004) *Shear Capacity of Diagonally Reinforced Coupling Beams.* Engineering Structures. **26**(10): pp.1437-1446.

20. Priestley, M J N (1997) *Displacement-Based Seismic Assessment of Reinforced Concrete Buildings.* Journal of Earthquake Engineering. **1**(1): pp.157-192.
21. Joh, O and Shibata, T (1996) *Anchorage Behaviour of 90-Degree Hooked Beams in Reinforced Concrete Beam-Column Joints*. in *Proc. Eleventh World Conference on Earthquake Engineering*. Acapulco, Mexico.
22. Joh, O, Goto, Y, and Shibata, T (1993) *Anchorage of Beam Bars with 90-Degree Bend in Reinforced Concrete Beam-Column Joints*. in *Proc. Tom Paulay Symposium "Recent Developments in Lateral Force Transfer in Buildings"*. La Jolla, California: University of California, San Diego.

List of appendices

Appendix A :Nonlinear analysis of diagonally reinforced coupling beams

A.1 Considered model

A method for considering the nonlinear load-deformation behaviour of diagonally reinforced coupling beams is proposed in [19]. In this method a simple truss mechanism is considered to provide all strength and stiffness to the system. When the system is subjected to sway actions the resulting shear force and bending moment is carried via two diagonal members with one in compression and one in tension. The compression member includes the confined concrete core and the diagonal reinforcing bars whereas the tension member includes only the diagonal reinforcing bars. It is considered that the concrete core provides sufficient stiffness to ensure that the member cannot buckle in compression. The proposed truss model is as presented in Figure A.1 below.

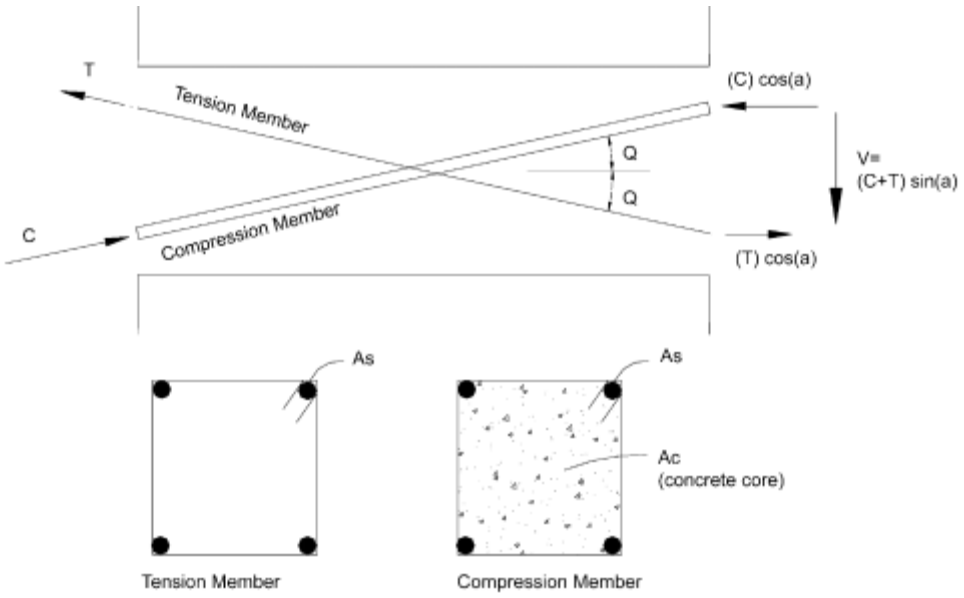

Figure A.1: Proposed model (from [19])

A.2 Example structure

The proposed model has been implemented for an example structure as presented in Figure A.2 below. In this structure two 2050 m long reinforced concrete walls are joined by a coupling beam measuring 900 m long by 1650 m high. The wall thickness is 400 mm throughout.

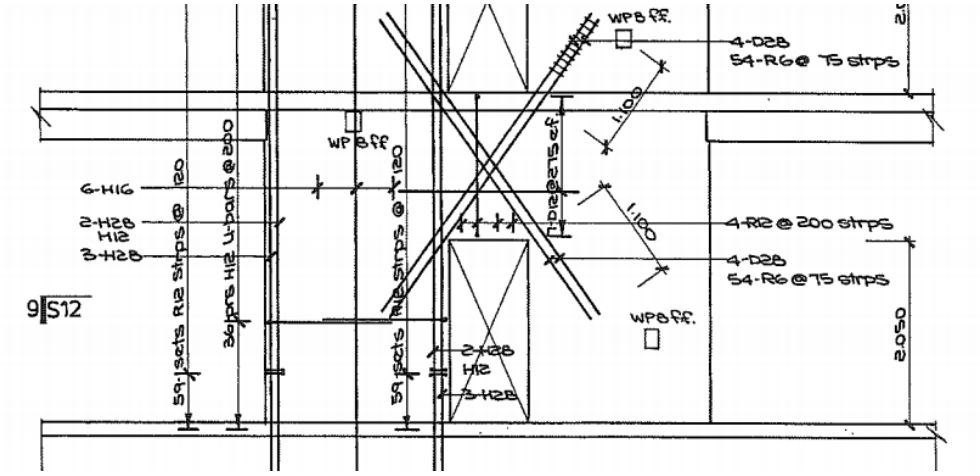

Figure A.2: Example wall reinforcement

A.3 Analysis model definition

The example structure has been analysed considering the proposed model using SAP2000 (v14). In this model axially "stiff" diagonal struts (oriented at 54° to the horizontal from Figure A.2) are included to consider the behaviour of the coupling beam following the model presented in Section A.1. The strut dimensions are taken as 150 mm square. Axial deformation in the struts is provided via fibre type hinge element which incorporates both concrete and reinforcement fibres. The walls are modelled using membrane elements that have sufficient stiffness to ensure that deformation is restricted to the coupling beam. As the conventional beam reinforcement also present in the coupling beam is not included, this modelling analogy will underestimate the stiffness of the coupling beam for elastic response, but will provide a reasonable representation of the wall response in the inelastic range. The analysis model is presented in Figure A.3 below.

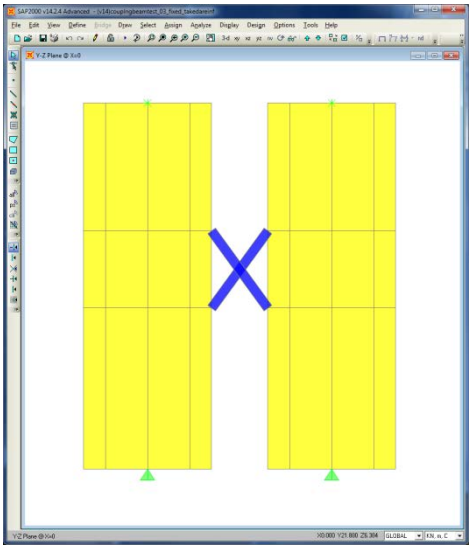

Figure A.3: SAP2000 analysis model

The reinforcement in the diagonal struts is included as a fibre type element with stress-strain behaviour as defined by Park and is presented in Figure A.4 below. The hysteretic form of the reinforcing is taken as kinematic type. The area of the reinforcing steel is taken as the sum of all longitudinal reinforcement present in the strut (i.e. A_s=4-D28=2463 mm^2). Strain penetration of the diagonal reinforcement into the walls have been excluded in this model.

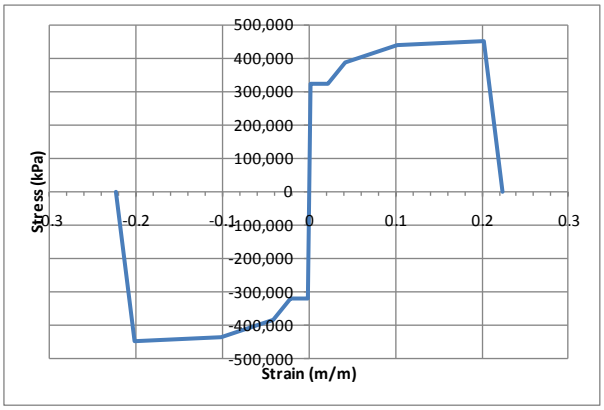

Figure A.4: Reinforcing nonlinear steel stress-strain plot

The concrete core of the diagonal strut elements is included fibre type element with material behaviour based on a Mander confined concrete model [11] with an unconfined compressive strength, f_c'=33.5 MPa, ε_{c0}=0.002, ultimate unconfined strain capacity given as 0.004, and confining reinforcing as presented in Figure A.4 above (i.e. R6@75crs confining hoops). The hysteretic form of the concrete fibre is considered exhibit Takeda type behaviour. The area of the concrete is taken as the total concrete core area (i.e. A_c=A_g-A_s=150^2-2,464=20,036 mm^2).

The nonlinear stress-strain behaviour for the concrete is as presented in Figure A.5 below (note that the tensile capacity has been taken as zero).

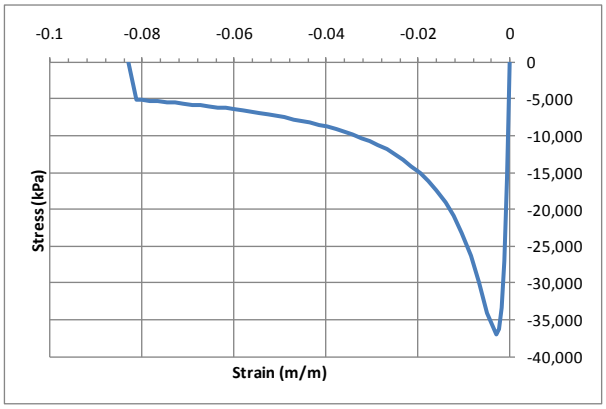

Figure A.5: Concrete nonlinear stress-strain plot

A.4 Analysis results

A nonlinear analysis has been undertaken to derive the force-deformation behaviour of the system. The backbone curve for the coupling beam system plotted as wall rotation (=drift) vs coupling beam shear force is presented in Figure A.6 below.

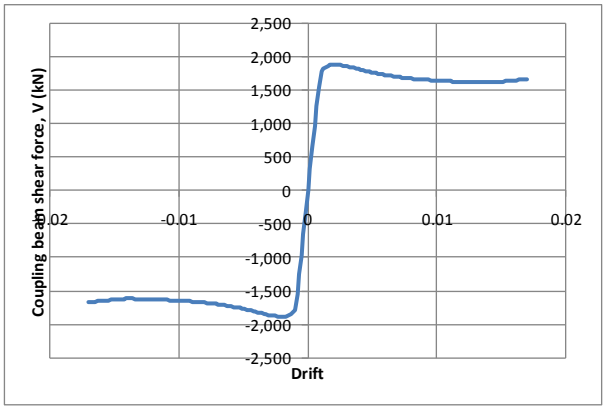

Figure A.6: Nonlinear backbone curve

A qualitative comparison of the resulting backbone curve and those presented in [19] indicates that the model adequately predicts the force-displacement behaviour for monotonic loading.

In order to assess the hysteretic form, a nonlinear displacement time history analysis has been undertaken. Figure A.7 below plots the wall rotation (=drift) vs coupling beam shear force for the cyclic analysis.

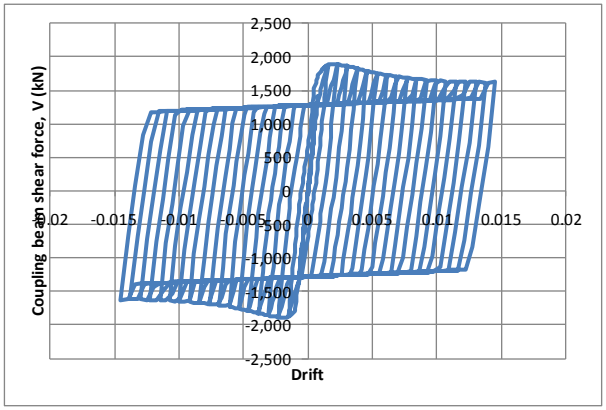

Figure A.7: Coupling beam hysteretic response

It can be seen that for the level of drift considered the analysis model behaves essentially in an elastic-perfectly plastic manner due to the reinforcing with additional strength enhancement as a result of the concrete. A limitation of the analysis undertaken is that the hysteretic behaviour does not reflect the softening that would normally be expected under cyclic loading due to the Bauschinger effect, and other mechanisms such as concrete spalling etc.

In an attempt to approximate these effects an additional analysis model has been developed whereby the hysteresis type for the reinforcement has been changed from the default kinematic type to instead be a Takeda type. The resulting hysteretic response is presented in Figure A.8 below which plots the wall rotation (=drift) vs coupling beam shear force.

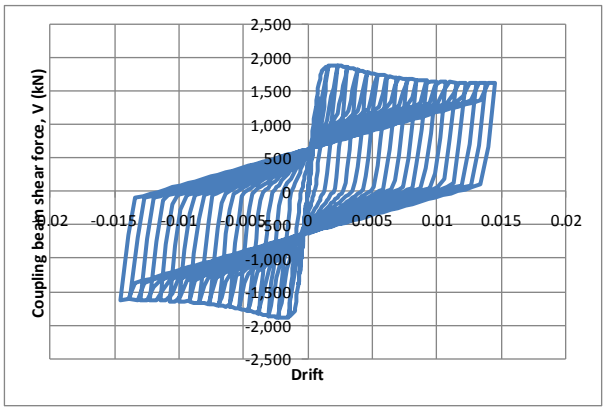

Figure A.8: Coupling beam hysteretic response (Takeda reinforcement)

It can be seen that whilst the hysteretic behaviour is not perfect, the total amount of energy dissipated for the considered loading history is reduced by approximately 50%.

A.5 Strain penetrations

The effects of strain penetration of the diagonal reinforcement into the wall has not been incorporated into the analysis models. In order to incorporate these the nonlinear stress-strain curve for the reinforcing steel element as presented in Figure A.4 has been scaled in the strain domain based on the following:

$$\varepsilon_s' = \varepsilon_s \left(\frac{L + L_{SP}}{L} \right)$$

Where $\varepsilon_s^{"}$ is the scaled strain, ε_s is the material strain obtained from Figure A.4, L is the length of the element as considered in the model, and L_{SP} is given as the strain penetration length which has been adapted from [20] as below:

$$L_{SP} = 0.022 f_s d_b$$

Where f_s and d_b are the stress and diameter of the longitudinal reinforcement respectively.

For the example structure the modelled length of the strut is given as 1531 mm and the diagonal bar is given as 28 mm diameter which then gives a modified nonlinear stress-strain curve for the reinforcing fibre as presented in Figure A.9 below.

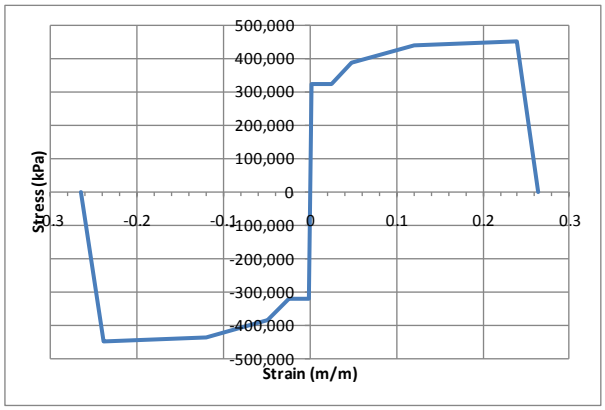

Figure A.9: Reinforcing nonlinear stress-strain plot (modified for strain penetrations)

Appendix B :Assessment of beam-column joint capacity

This appendix describes the methods used to assess the capacity of the beam-column joints in the CTV Building. Two aspects of the joints were considered possible causes of premature failure, these being the joint shear capacity and the potential pullout of inadequate hook anchorages.

B.1 Beam-column joint shear capacity

The beam-column joints of the CTV building do not meet the requirements of NZS 3101:2006 [6] due to their small size and lack of joint core reinforcement. Joint shear capacities have therefore been assessed using published procedures for deficient beam-column joints [5, 20]. The approach taken has been based on determining appropriate limits for joint core principal tension and principal compression stresses. The limit value for the principal tension stress was calculated as $f_{tp,max} = k\sqrt{f_c'}$ [5], with the value of k dependent on whether the joint was an interior or exterior joint and on the curvature ductility developed in the adjacent beam plastic hinge (see Figure B.1). The limiting value for the principal compression stress in the joint core was taken as $f_{cp,max} = 0.5f_c'$ based on a recommendation made by Priestley [20].

The principal tension and compression stresses existing in the joint core were calculated as $0.5f_a \pm \sqrt{(0.5f_a)^2 + (v_{jh})^2}$, where f_a is the column axial stress and v_{jh} is the horizontal joint shear stress. For circular columns, the joint shear stress was calculated assuming a square cross section with width and depth equal to the column diameter, while the column axial stress f_a was calculated based on the gross cross sectional area of the column. Consideration of the principal stresses shows that the joint shear stress required to cause tensile failure increases as the column axial compressive stress increases, while the joint shear stress required to cause compression failure in the joint decreases as the column axial compressive stress increases.

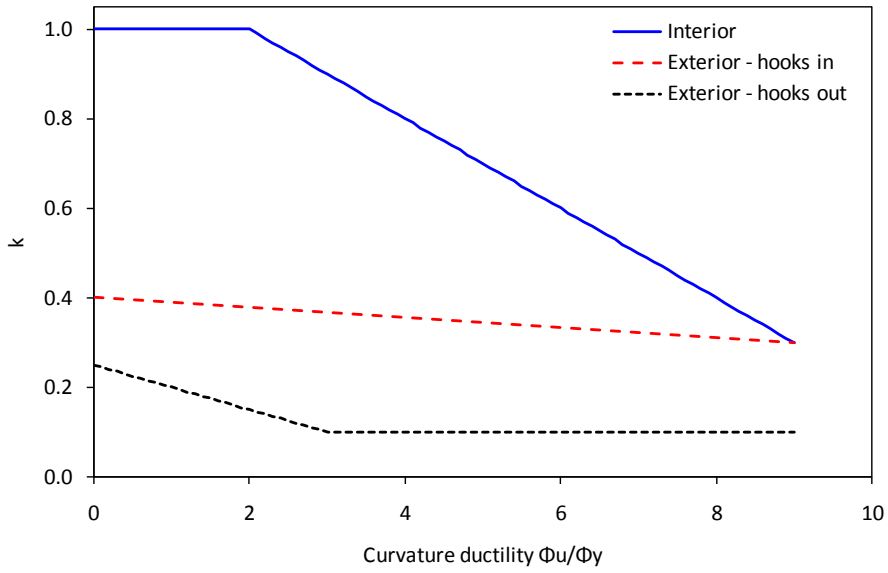

Figure B.1: Relationship of factor K to curvature ductility for different joint types (after [5])

B.2 Hook anchor capacity

The method of construction used for the CTV building required that the bottom reinforcement of the beams typically be terminated at each column, with reinforcement being hooked into the joint at these locations. Based on engineering drawings (see Figure B.2) the hook length for either H28 or H24 bars from the column face was approximately 275 mm (although 175 mm was also detailed as anchorage lengths into columns F2 and F3). Similar conditions applied for anchorage of top steel into corner columns. The hook length provided is not adequate to develop the full strength of the reinforcement according to the provisions of NZS 3101:2006 [6]. Assuming the joint core concrete strength was 25 MPa (i.e. that the beam-column joint was poured at the same time as the floor slab and the upper parts of the beams) and the yield strength of the HD28 reinforcing bars was 448 MPa, the hooked development length required by NZS 3101:2006 would be L_{dh} = 602 mm (cl. 8.6.10.3.1) if the beam was to be designed with a ductile hinge adjacent to the columns face. This hook length would be required to be placed the lesser of $8d_b$ or $0.5h_c$ from the column face (cl. 9.4.3.2), which in this case is 200 mm from the face. Thus the total anchor length inside the joint would need to be at least 800 mm to sustain ductile yielding of the beam steel.

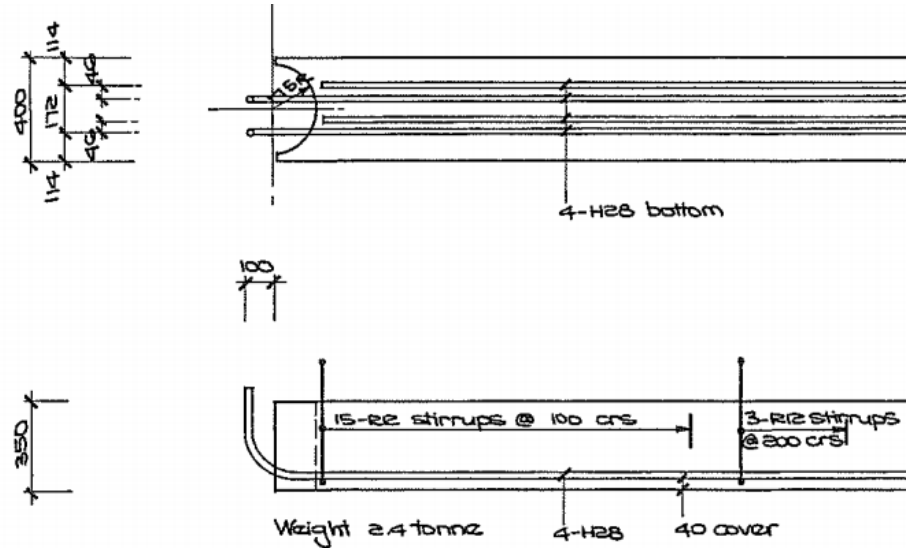

Figure B.2: CTV building hook detail for interior beam

Joh and Shibata [21, 22] identified three failure modes for hooked anchorages, namely side splitting, local compression failure at the bar bend, and "raking-out" failure or pullout of the entire bar group (see Figure B.3). Based on experimental tests they suggest a method for determining the capacity of hooks based on raking-out failure. According to their method the anchor strength is dependent on the column axial force, the embedment length, and the amount of joint core reinforcement. The design method suggests significant bar anchorage can be expected even when hook lengths are severely deficient according to NZS 3101:2006. For example, calculation for a 275 mm anchorage indicates that the CTV beam bar anchorages could develop the yield strength of the beam reinforcement providing the column axial load on a circular column exceeded 265 kN compression.

Consideration has not been given to the potential for "side split" failure in the CTV Building joints. Preliminary calculations have been undertaken to determine whether local compression failure at the inside of the hooked anchor would be expected. The procedures of NZS 3101:2006 cl.8.4.2.1 indicate that prevention of local crushing at the inside of the hook would require a bend radius of approximately 250 mm, which is smaller than the bend radius provided. It therefore seems reasonable to assume localised crushing at the inside of the hooks was not likely.

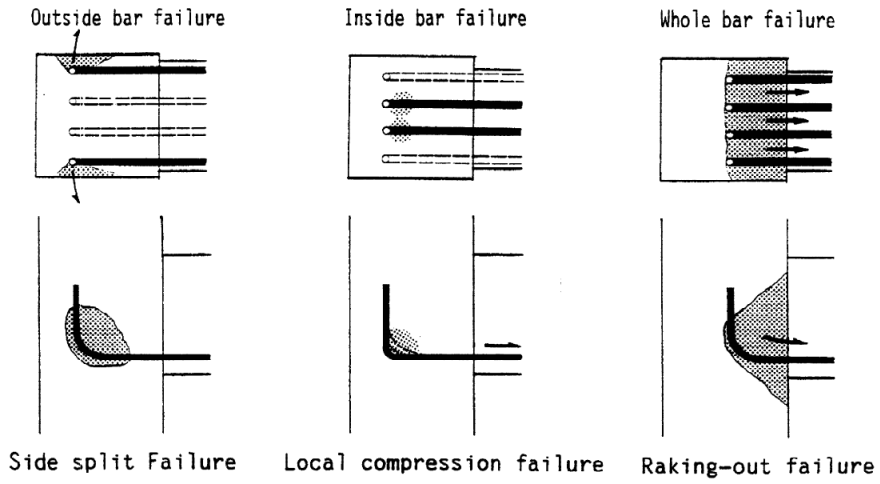

Figure B.3: Hooked anchorage failure modes (from [21])

B.3 Joint region capacity hierarchy

A useful method of assessing beam-column joint performance is to plot a graph showing the joint capacities based on failure loads of the various mechanisms. This allows a failure hierarchy to be established and thus identifies the probable failure mechanism at the joint. This type of plot is shown in Figure B.4 for an interior joint of the CTV building.

Figure B.4 was developed by calculating the beam moment that would coincide with development of the capacity of joint tension failure, joint compression failure, and beam reinforcement anchor failure. For each failure type a range of column axial loads were considered. Comparison of the resulting curves with the approximate beam yield and ultimate moment capacities indicates that joint tension or anchorage failure are likely to occur before beam yielding when the column axial load is small. However, for moderate column axial loads the plot indicates that plastic hinges would be able to form in the beams without joint failure occurring.

The data shown in Figure B.4 should be considered indicative only. The data was developed treating the beam-column joint as if it were an isolated subassembly subjected to a simple moment pattern with inflection points at the beam and column midpoints (see Figure B.5). This simplification allows joint shear forces to be directly related to beam moments, and thus makes presentation of the relative strengths more simple. However, the assumed moment distribution was not used during assessment of the performance of the CTV building. Instead, beam and column moments, shears, and axial forces were tabulated directly from the analysis

and used to assess the joint core demands at each time step for a selection of critical beam column joints.

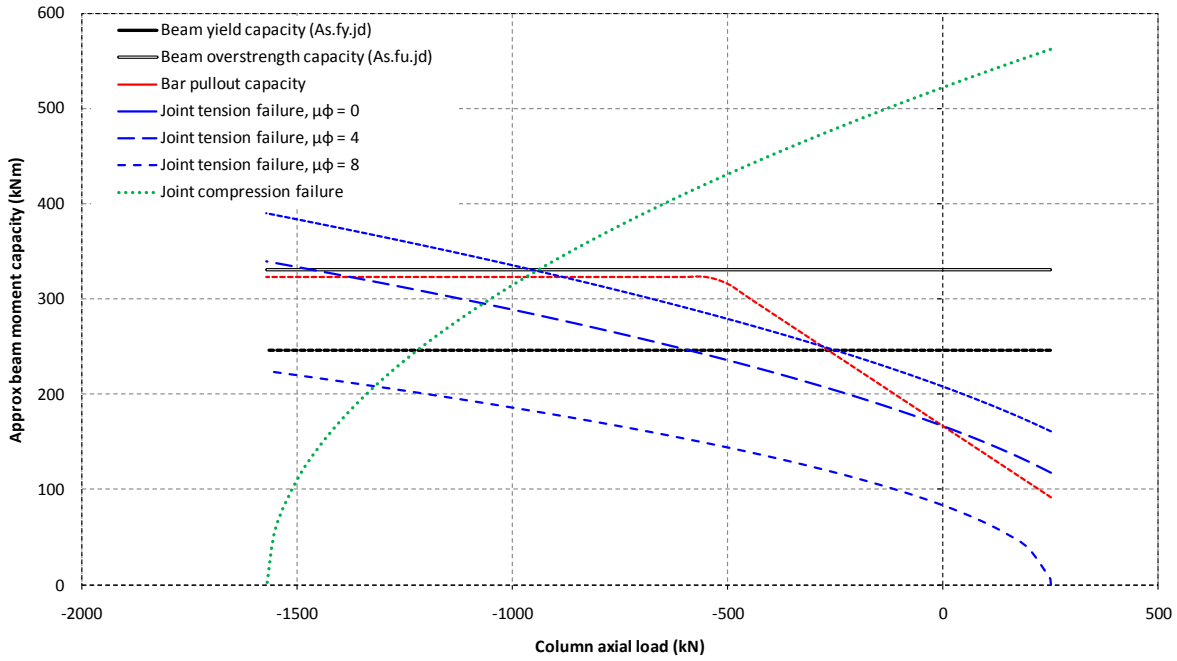

Figure B.4: Failure hierarchy plot for interior joint, 2-HD28 beam reinforcing bars, 25 MPa concrete strength, circular column, 275 mm anchorage.

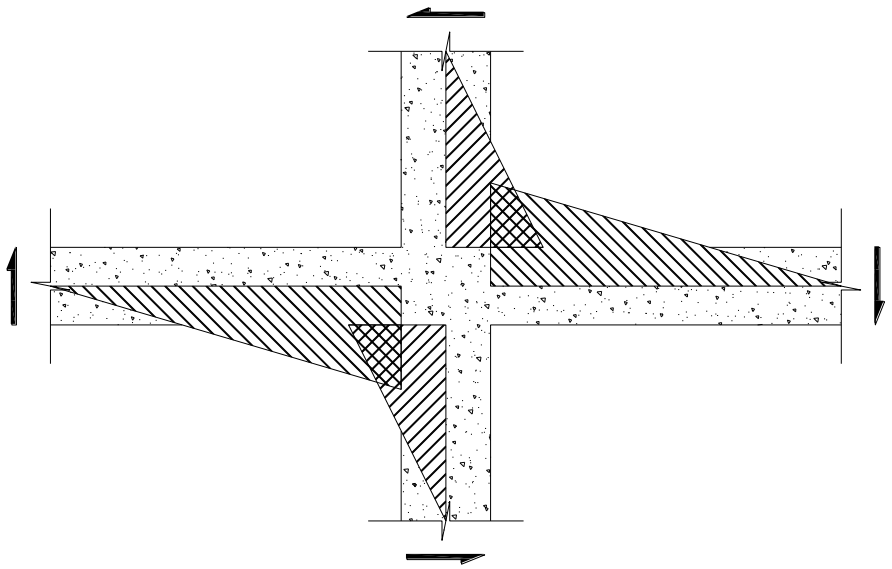

Figure B.5: Moment diagram assumed for development of Figure B.4

Appendix C :Foundation Modelling Properties

CTV BUILDING FOUNDATION SPRING STIFFNESS

31/05/2011 16:02

Most likely values

Shear wave velocity:

Stiff area	300 m/s
Soft area	200 m/s

Shear modulus:

Stiff area	162.00 MPa
Soft area	70.00 MPa

Density:

Stiff area	1800 kg/m^3
Soft area	1750 kg/m^4

Poissons Ratio:

Stiff area	0.3
Soft area	0.4

Footing type	B (m)	L (m)	D (m)	L/B	D/B	Depth factor	Barcan: β_z	Spring (MN/m^3)	Comment
1	4	4	1	1.00	0.25	1	2.12	122.71	
1a	4.5	4.5	1	1.00	0.22	1.2	2.12	130.89	
1b	4.5	4.5	1	1.00	0.22	1.2	2.12	65.98	Soft area
2	7.3	7.7	1.8	1.05	0.25	1.3	2.13	85.40	
2a	5.4	7.7	1.8	1.43	0.33	1.35	2.18	53.14	Soft area
3	3.3	5.8	1	1.76	0.30	1.33	2.22	117.22	
3a	3.3	5.8	1	1.76	0.30	1.33	2.22	78.59	Soft area
4	2.5	9.8	1	3.92	0.40	1.4	2.44	159.69	
4a	2.5	12.5	1	5.00	0.40	1.4	2.53	73.94	Soft area
5	3	21.6	1	7.20	0.33	1.35	2.69	104.35	
6	1.7	20	1	10.00	0.59	1.5	2.87	185.42	

Figure C.1: Expected Soil Stiffness [4]

Appendix D :Acceleration Time History Records.

D.1 Darfield CBGS

Christchurch Botanical Gardens (CBGS) time history records [17] used to determine the structural response for the Darfield event are presented in Figure D.1 below.

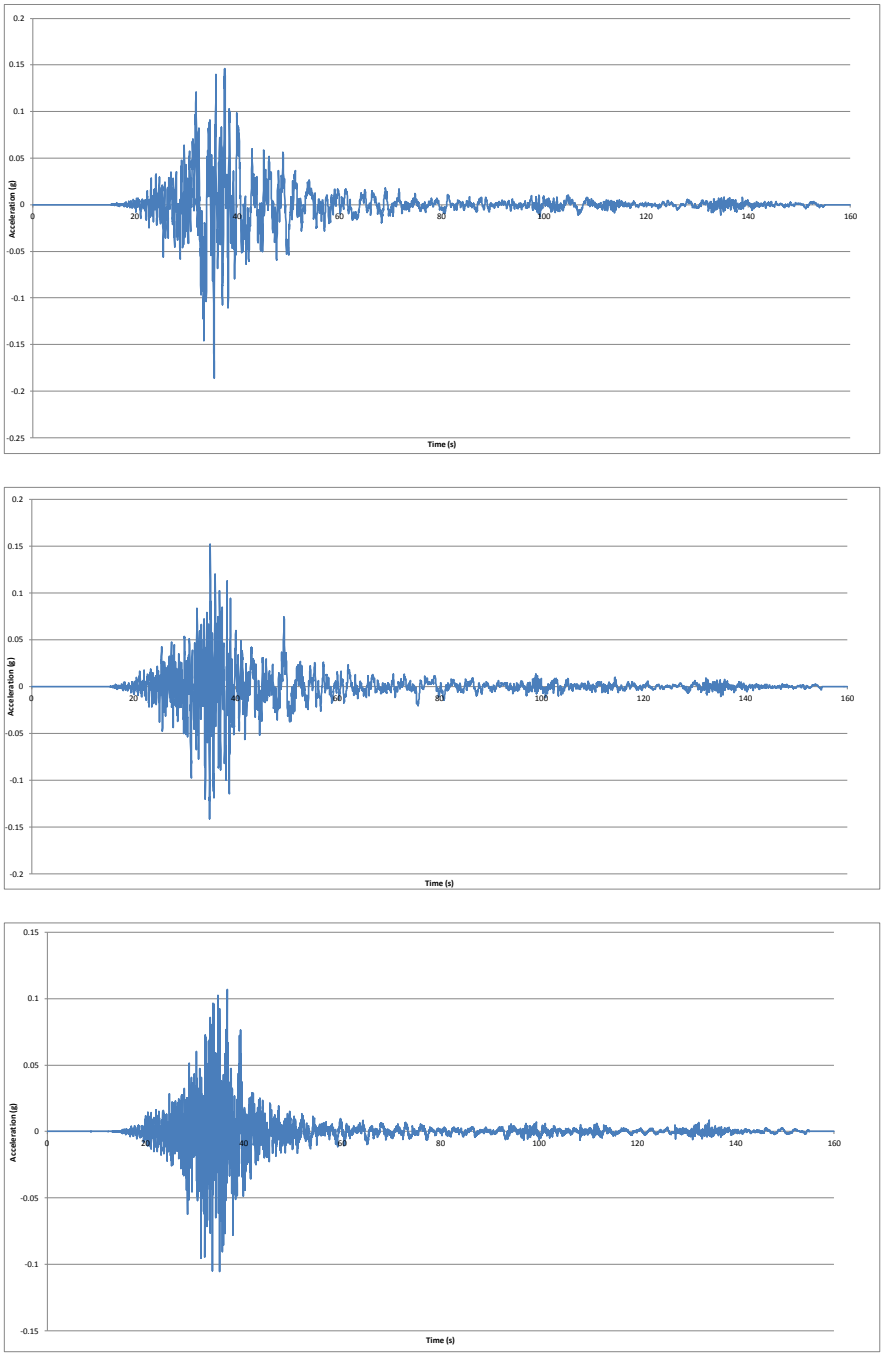

Figure D.1: Darfield 20100903_163541_CBGS N00E (top), N90E (middle), and Vertical (bottom) acceleration time history record plots.

D.2 Lyttelton CBGS

Christchurch Botanical Gardens (CBGS) time history records [18] used to determine the structural response for the Lyttelton aftershock are presented in Figure D.2 below.

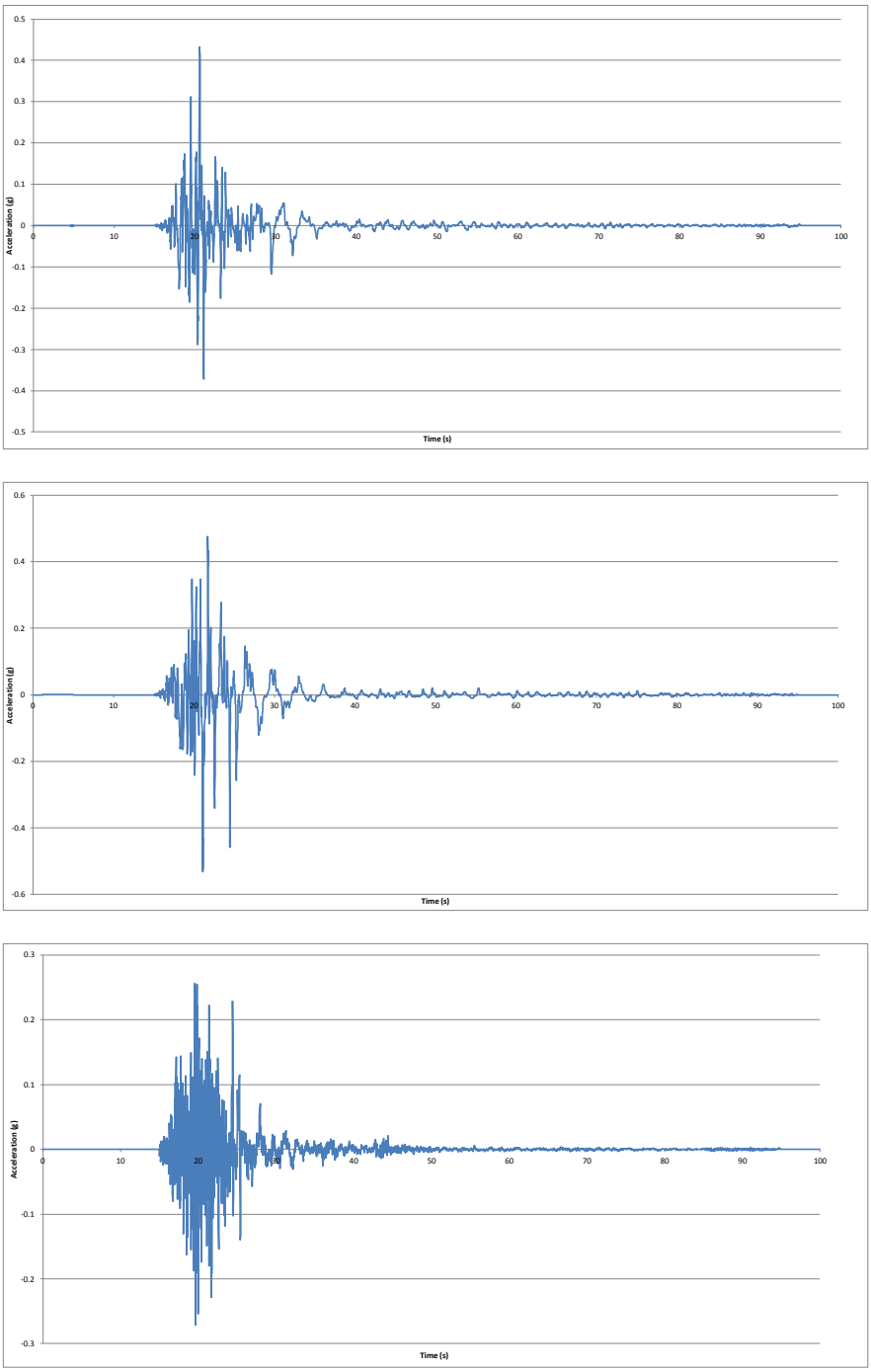

Figure D.2: Lyttelton 20110221_235142_CBGS N00E (top), N90E (middle), and Vertical (bottom) acceleration time history record plots.

D.3 Lyttelton CCCC

Christchurch Cathedral College (CCCC) time history records [18] used to determine the structural response for the Lyttelton aftershock are presented in Figure D.3 below.

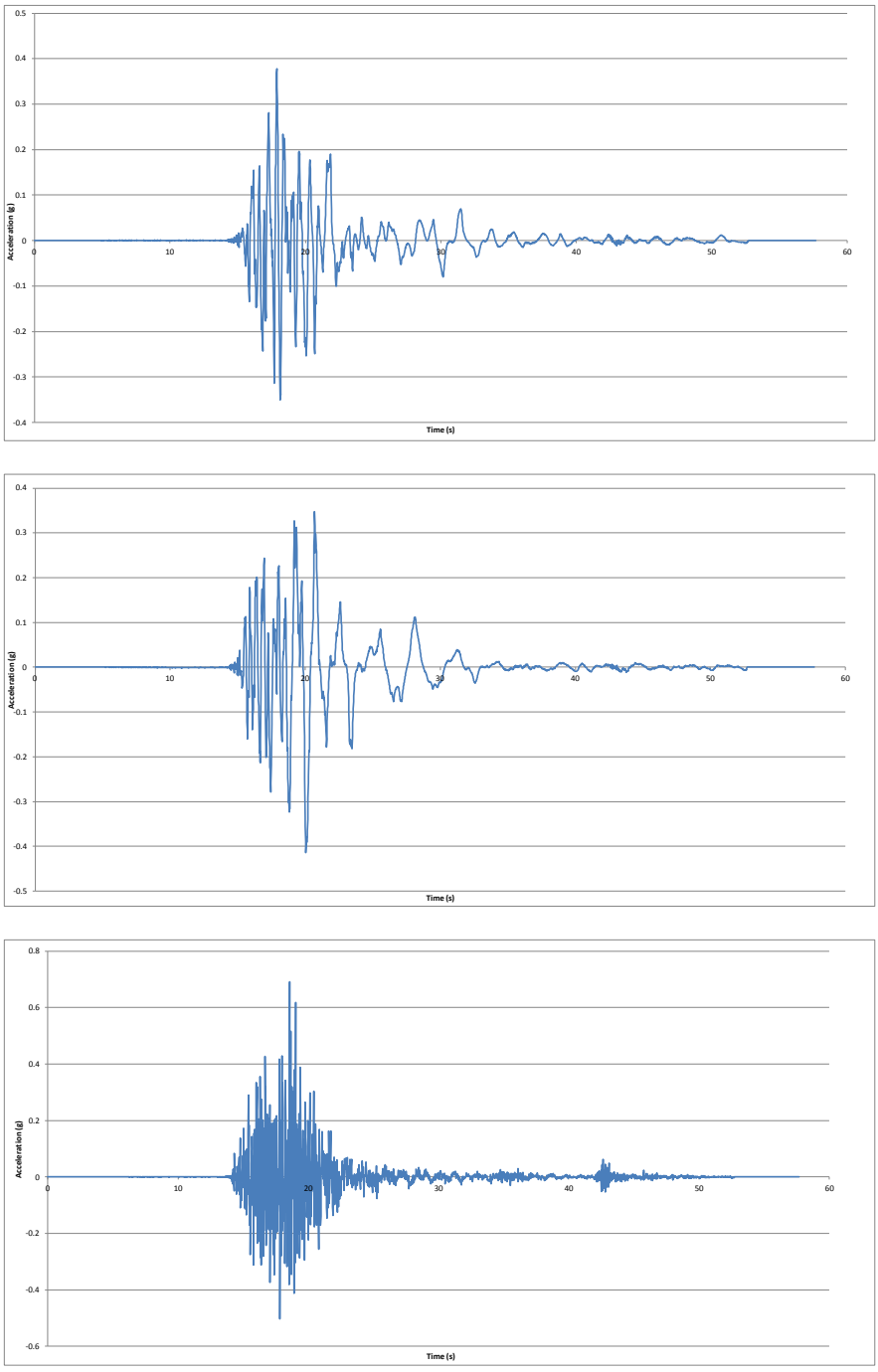

Figure D.3: Lyttelton 20110221_235142_CCCC N00E (top), N90E (middle), and Vertical (bottom) acceleration time history record plots.

D.4 Lyttelton CHHC

Christchurch Hospital (CHHC) time history records [18] used to determine the structural response for the Lyttelton aftershock are presented in Figure D.4 below.

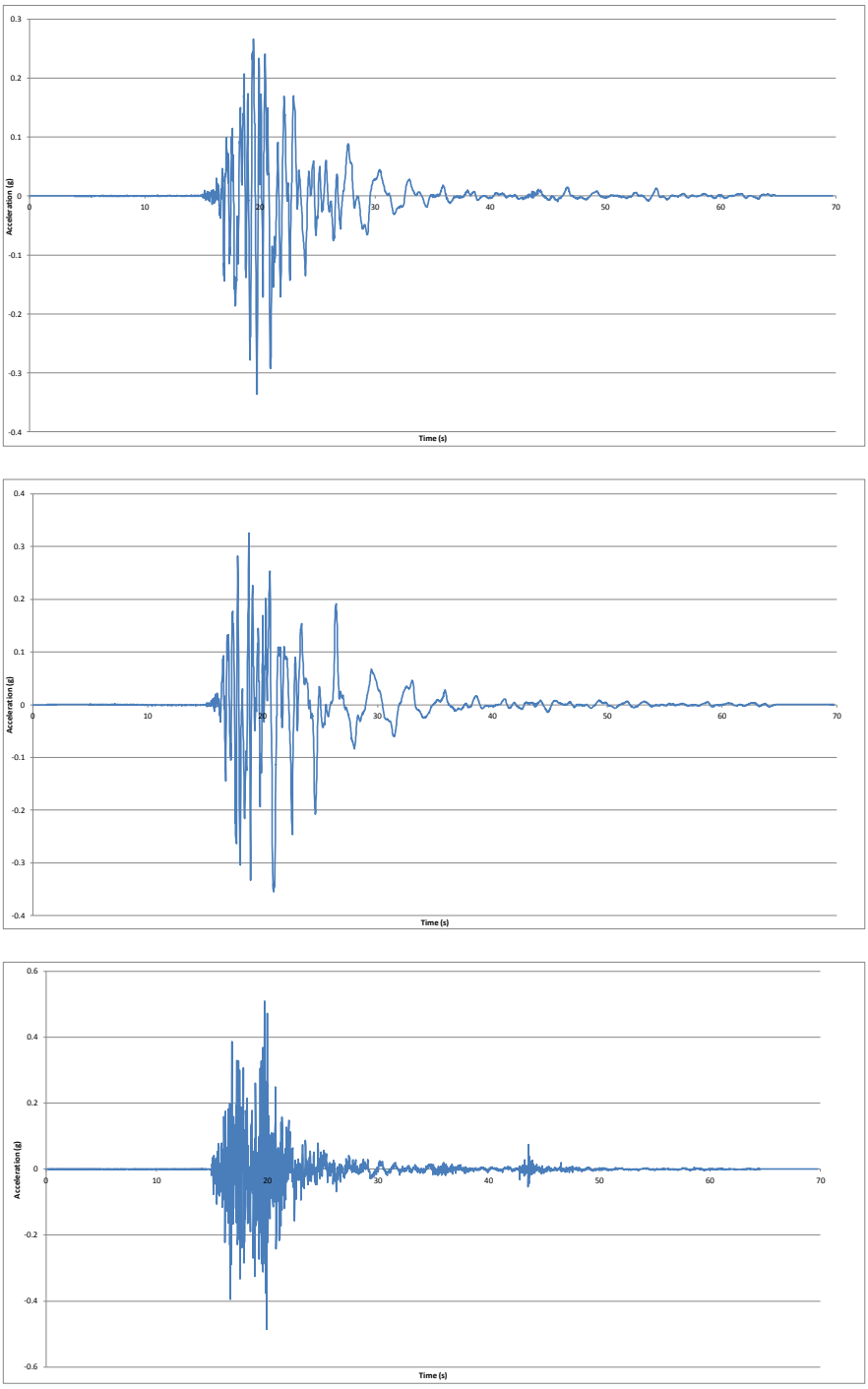

Figure D.4: Lyttelton 20110221_235142_CHHC N00E (top), N90E (middle), and Vertical (bottom) acceleration time history record plots.

Appendix E :Analysis Results - Darfield Event: CBGS Record

The following details the structural actions reported by the analysis as a function of time, for the Darfield event using the acceleration time history recorded at the CBGS station using all components of the record.

E.1 Building Displacements and Drifts.

Building Level 6 displacements are presented in Figure E.1 and Figure E.2 below for the Southeast and Northwest corners of the building respectively.

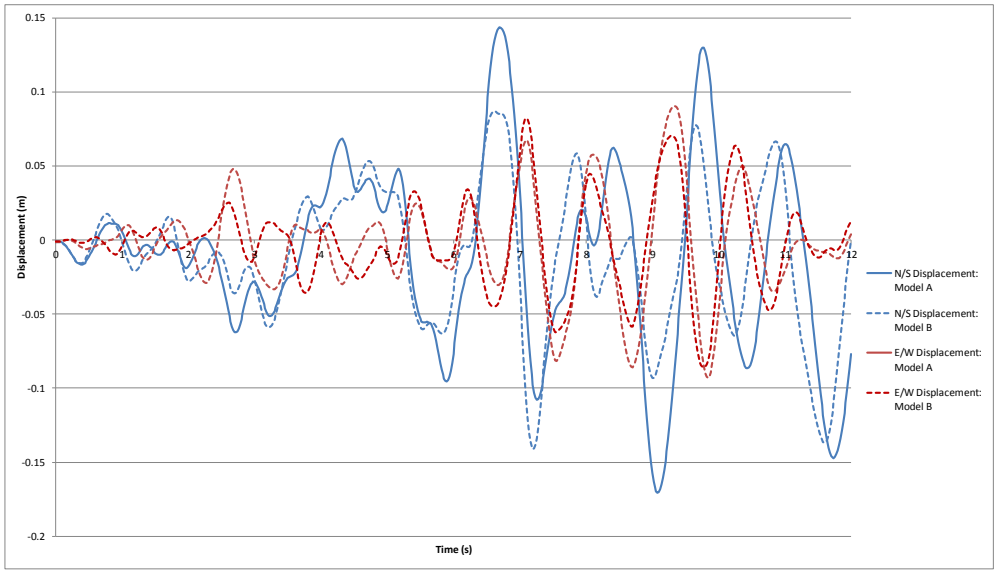

Figure E.1: Level 6 Southeast corner displacements.

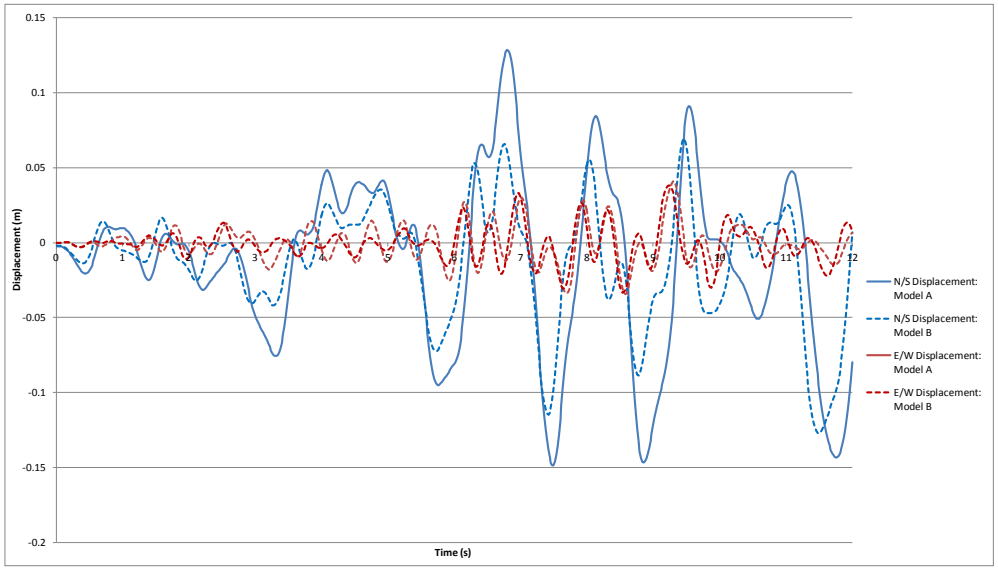

Figure E.2: Level 6 Northwest corner displacements.

Inter-storey displacements for the perimeter frame lines A and F in the north/south direction are presented in Figure E.3, and Figure E.4 below. For the purposes of comparison, plots contain both Model A and Model B inter-storey displacements.

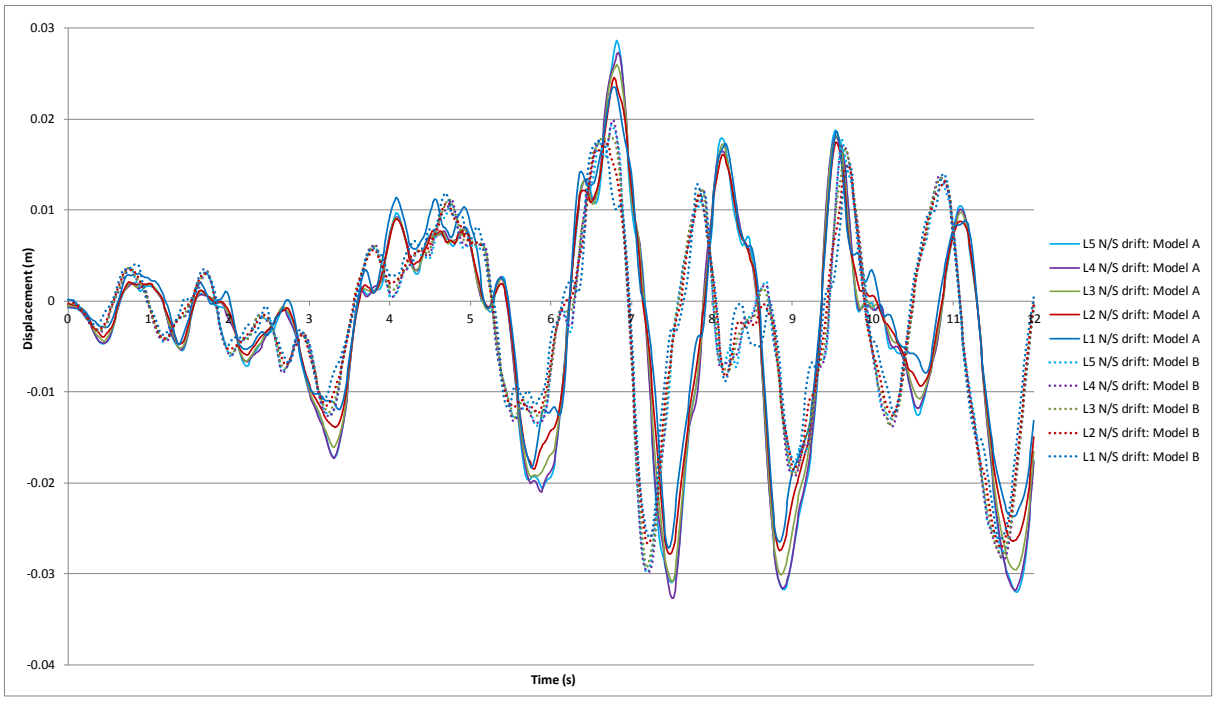

Figure E.3: Frame A north/south inter-storey displacements.

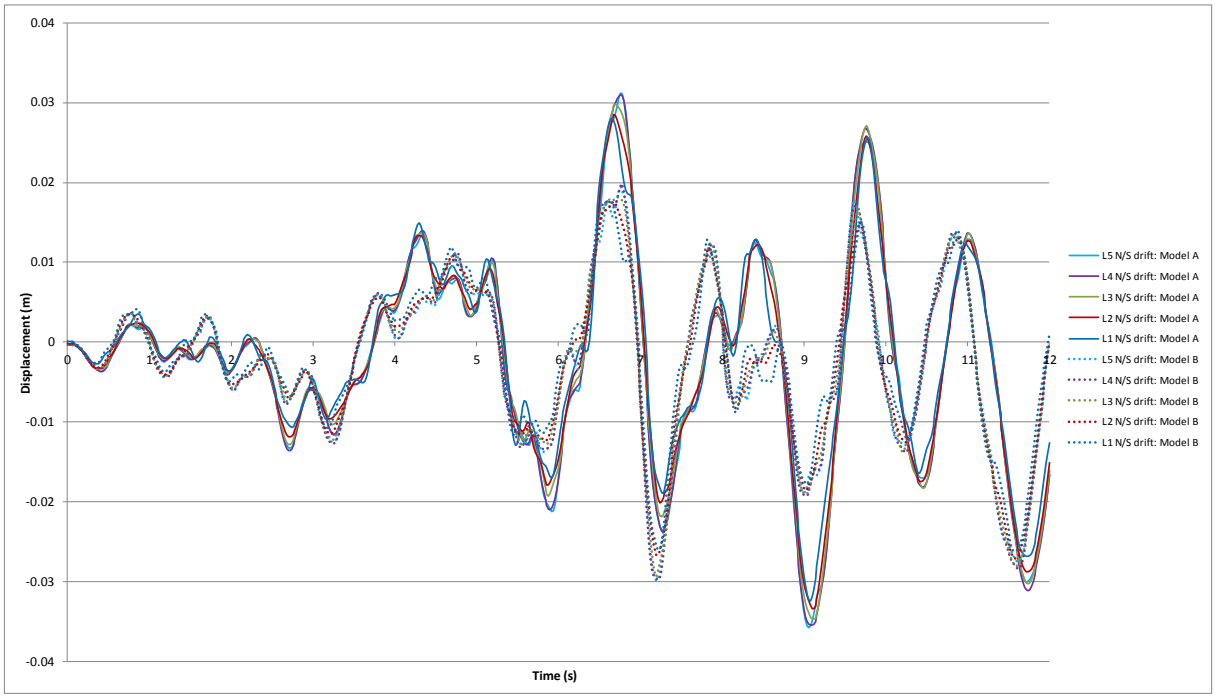

Figure E.4: Frame F north/south inter-storey displacements.

Inter-storey displacements for the perimeter frame lines 1 and 4 in the east/west direction are presented in Figure E.5, and Figure E.6 below. For the purposes of comparison, plots contain both Model A and Model B inter-storey displacements.

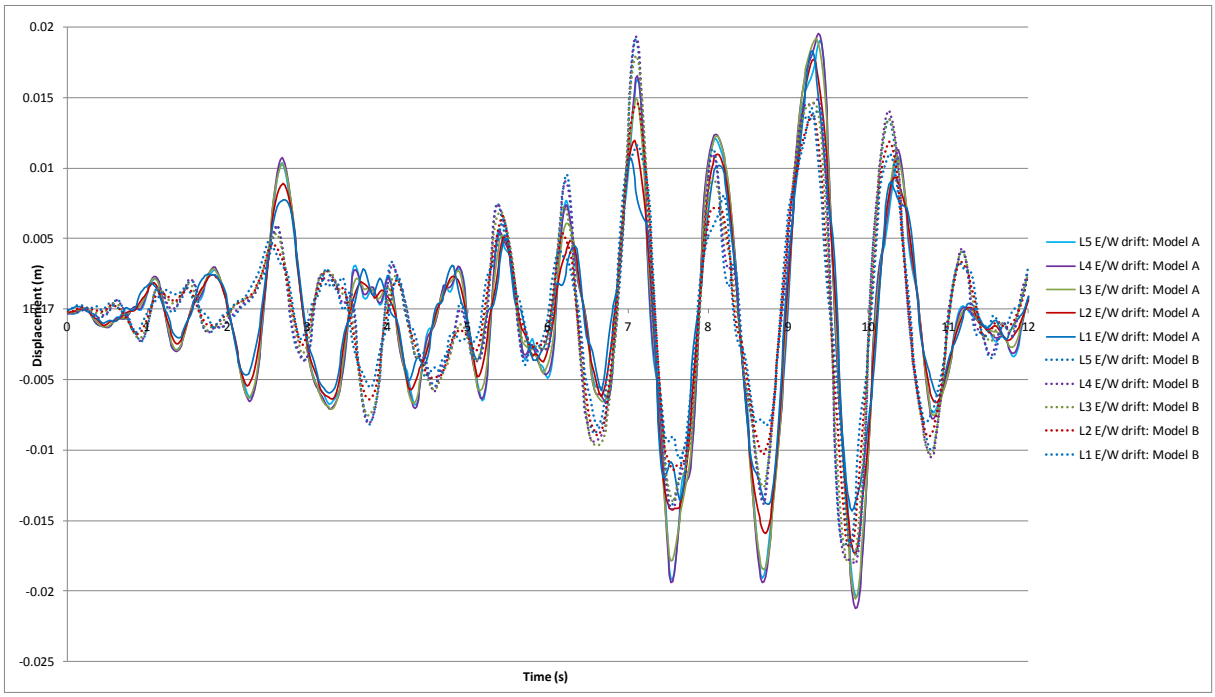

Figure E.5: Frame 1 east/west inter-storey displacements.

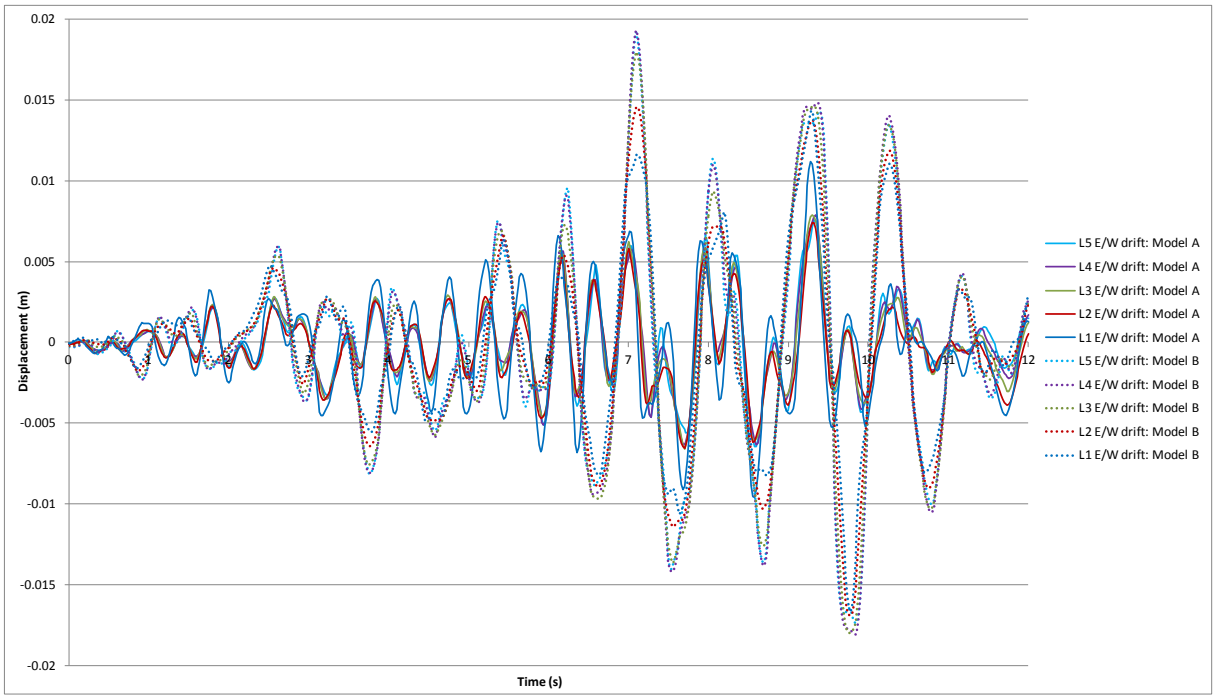

Figure E.6: Frame 4 east/west inter-storey displacements.

E.2 Diaphragm Connection Forces

Diaphragm connection forces are presented in Figure E.7 to Figure E.18 below. Note that moments are reported about the geometric centroid of the element being considered.

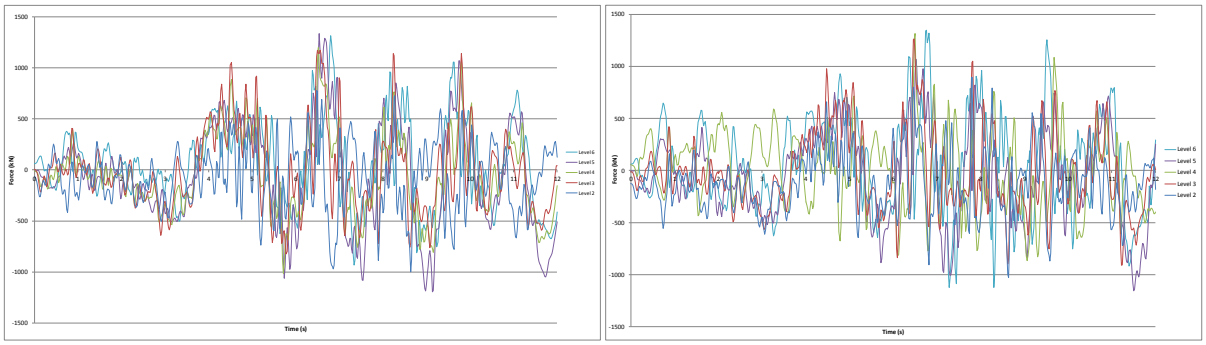

Figure E.7: North core total diaphragm north/south actions (no masonry left, with masonry right)

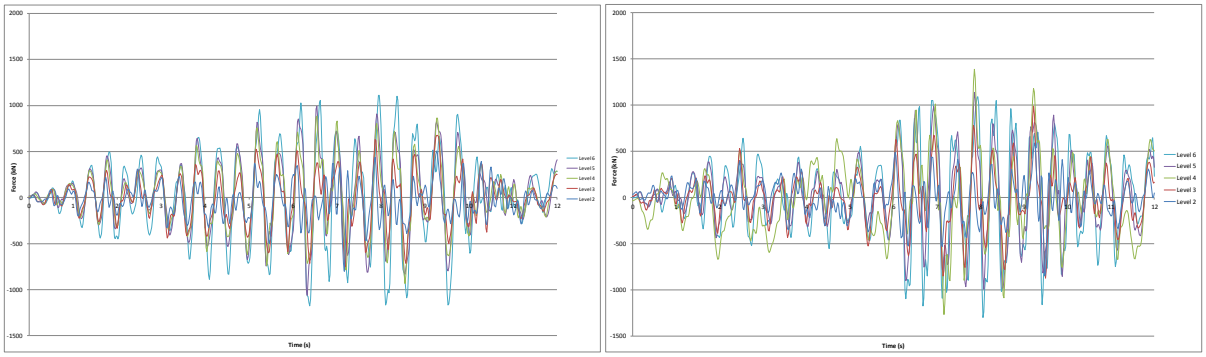

Figure E.8: North core total diaphragm east/west actions (no masonry left, with masonry right)

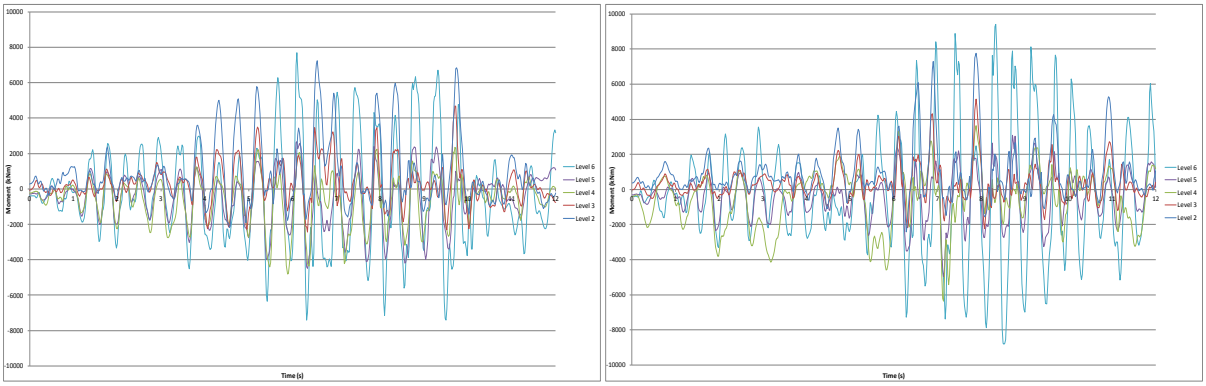

Figure E.9: North core total diaphragm in-plane moments (no masonry left, with masonry right)

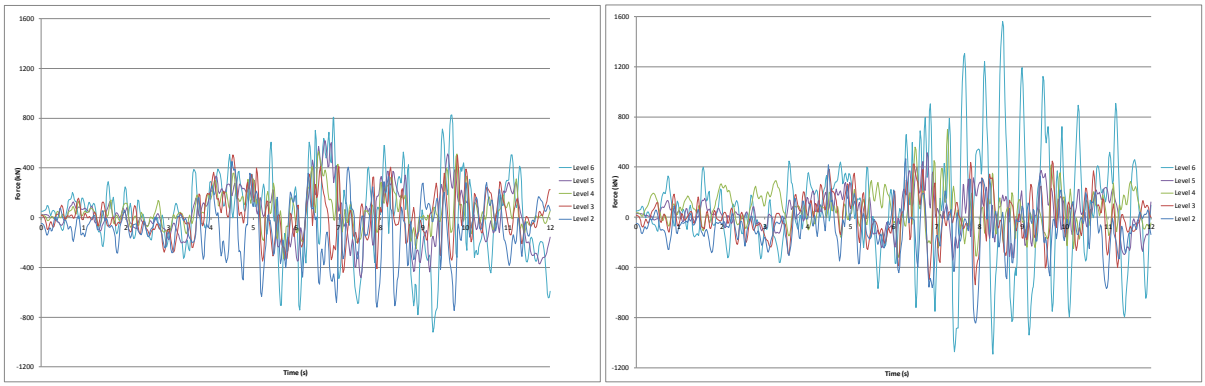

Figure E.10: North core Wall C diaphragm north/south actions (no masonry left, with masonry right)

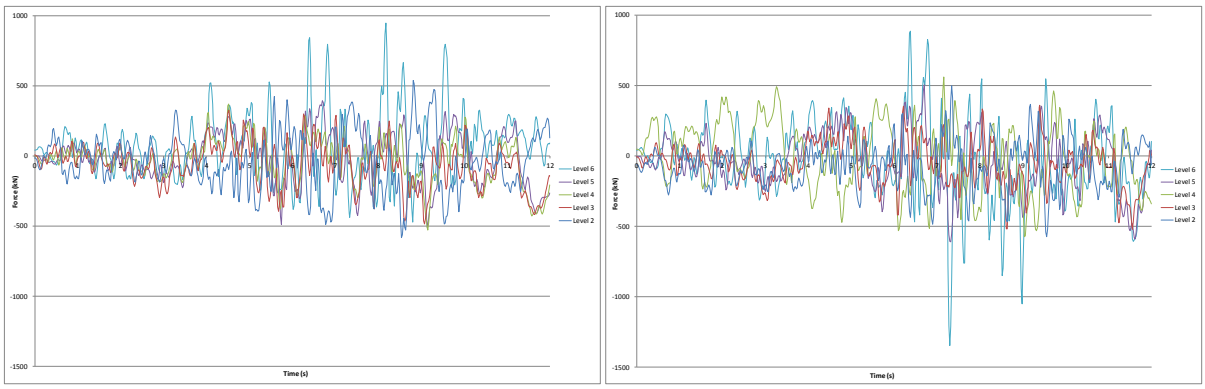

Figure E.11: North core Wall C/D diaphragm north/south actions (no masonry left, with masonry right).

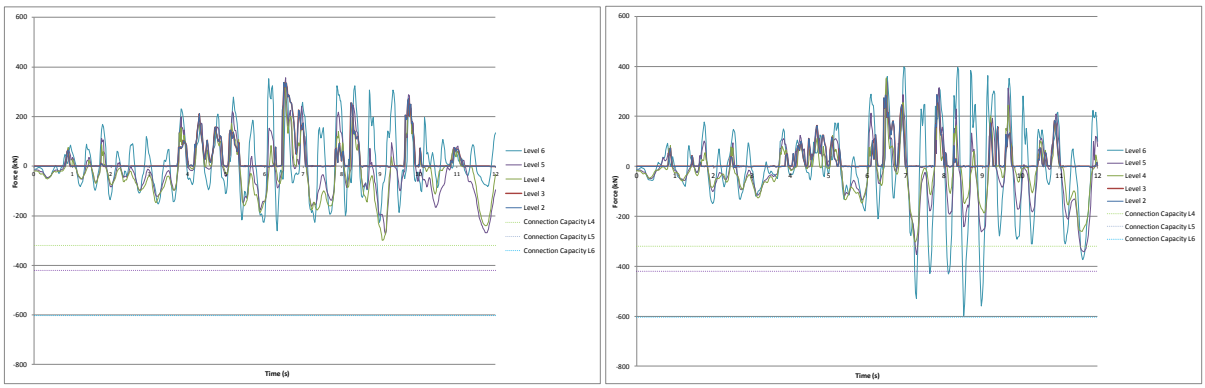

Figure E.12: North core Wall D diaphragm north/south actions (no masonry left, with masonry right).

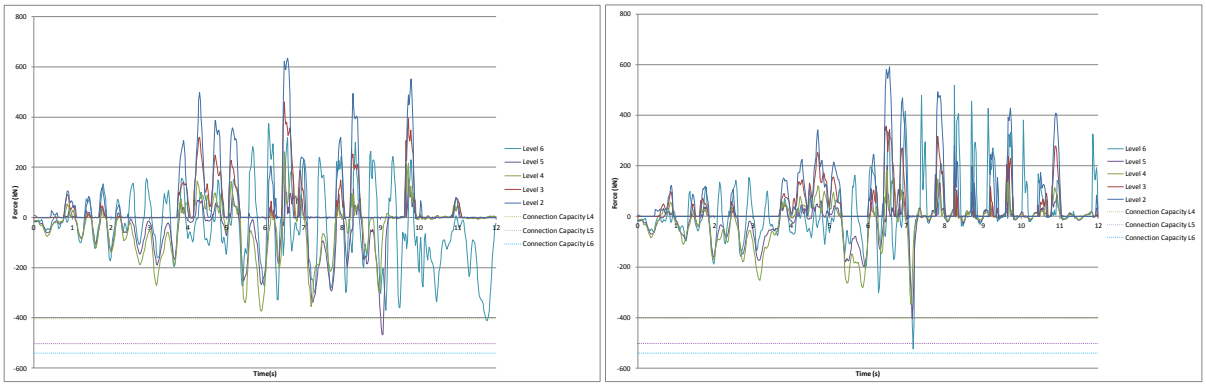

Figure E.13: North core Wall D/E diaphragm north/south actions (no masonry left, with masonry right).

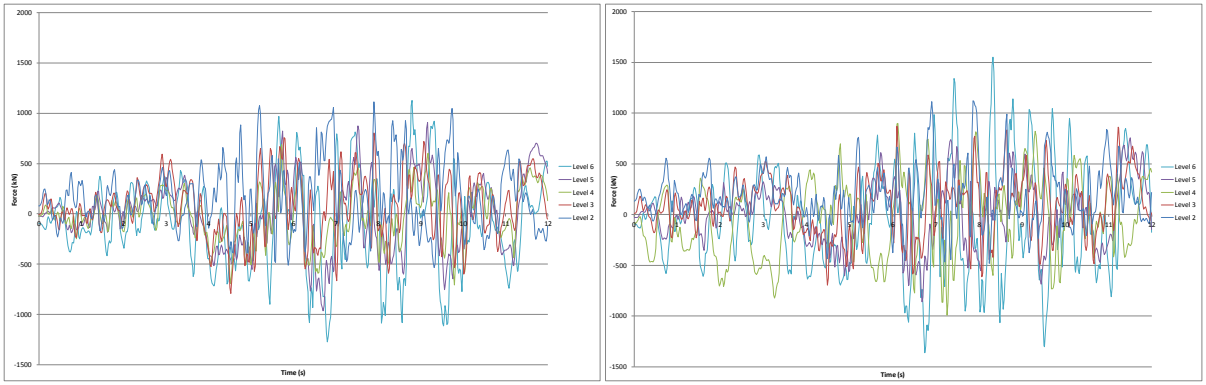

Figure E.14: North core Slab 4/C to C/D diaphragm north/south actions (no masonry left, with masonry right).

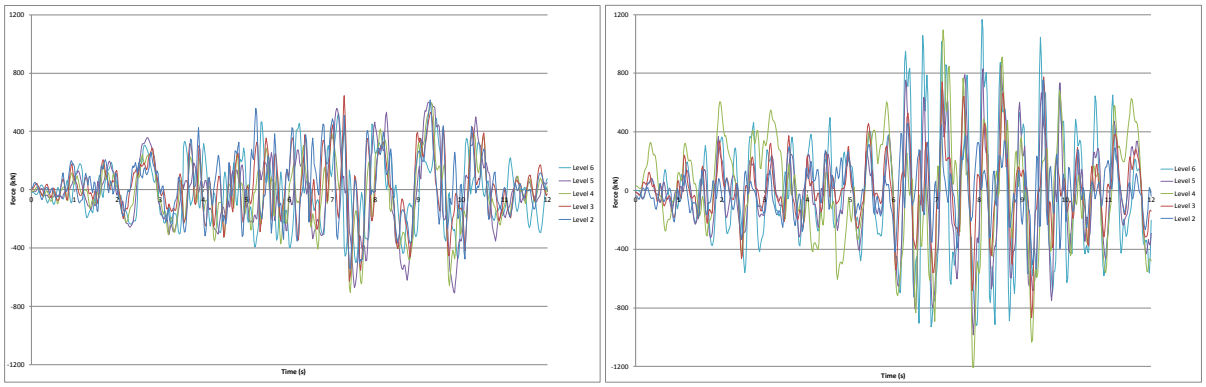

Figure E.15: North core Slab 4/C to C/D diaphragm east/west actions (no masonry left, with masonry right).

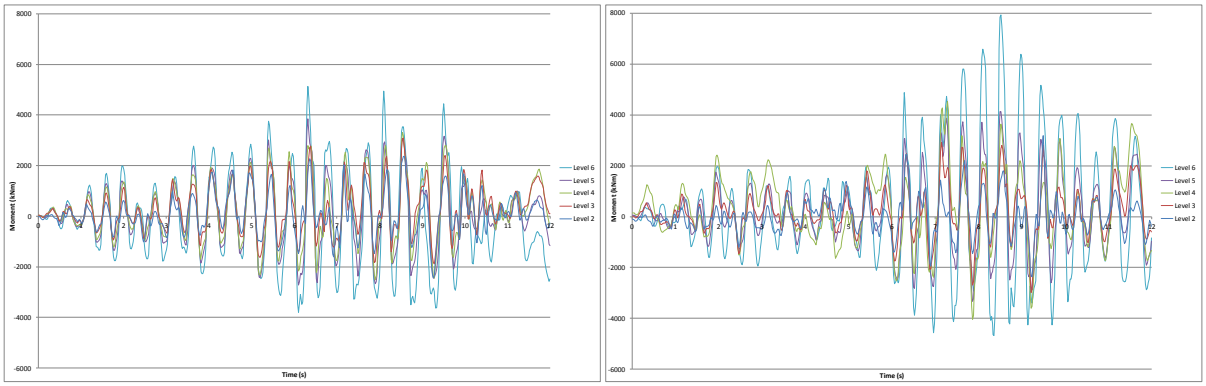

Figure E.16: North core Slab 4/C to C/D diaphragm in-plane moments (no masonry left, with masonry right).

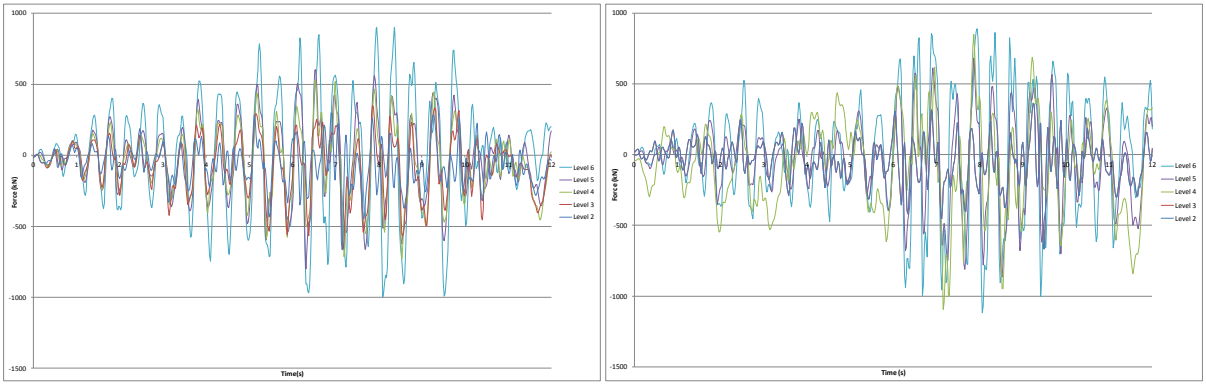

Figure E.17: North core Wall 5 diaphragm east/west actions (no masonry left, with masonry right).

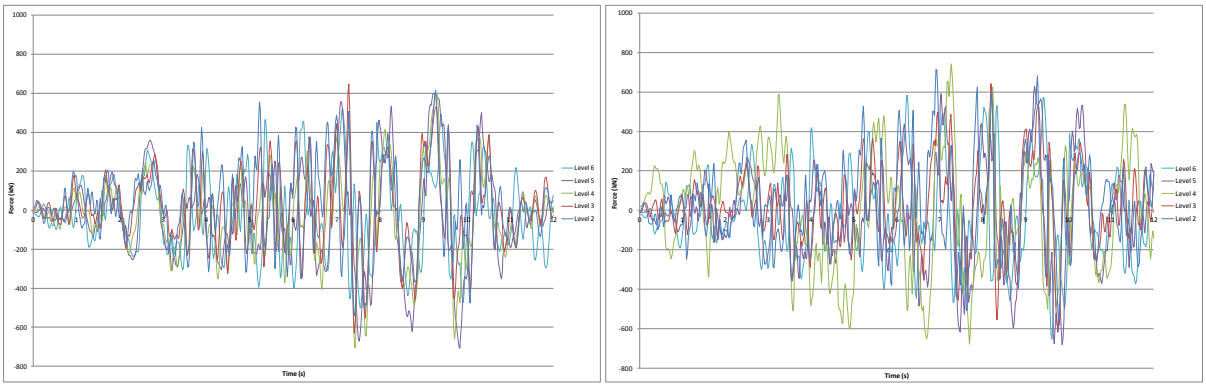

Figure E.18: South wall diaphragm east/west actions (no masonry left, with masonry right).

Appendix F :Analysis Results - Lyttelton Aftershock: Model A: CBGS record

The following details the structural actions reported by the analysis as a function of time, for the Lyttelton aftershock using the acceleration time history recorded at the CBGS station using all components of the record.

F.1 Building Displacements and Drifts.

Building Level 6 displacements are presented in Figure F.1 and Figure F.2 below for the southeast and northwest corners of the building respectively.

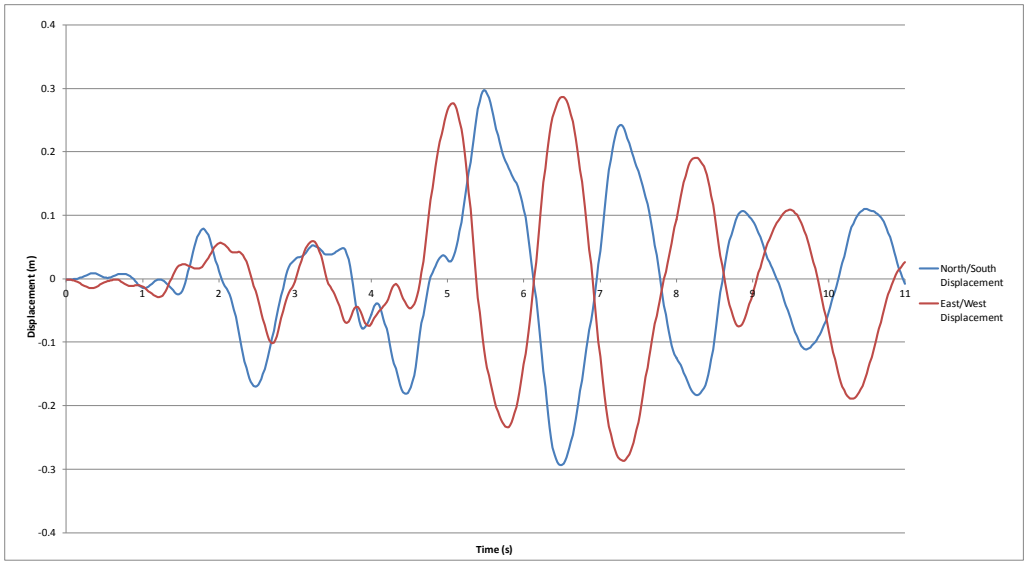

Figure F.1: Level 6 Southeast corner displacements.

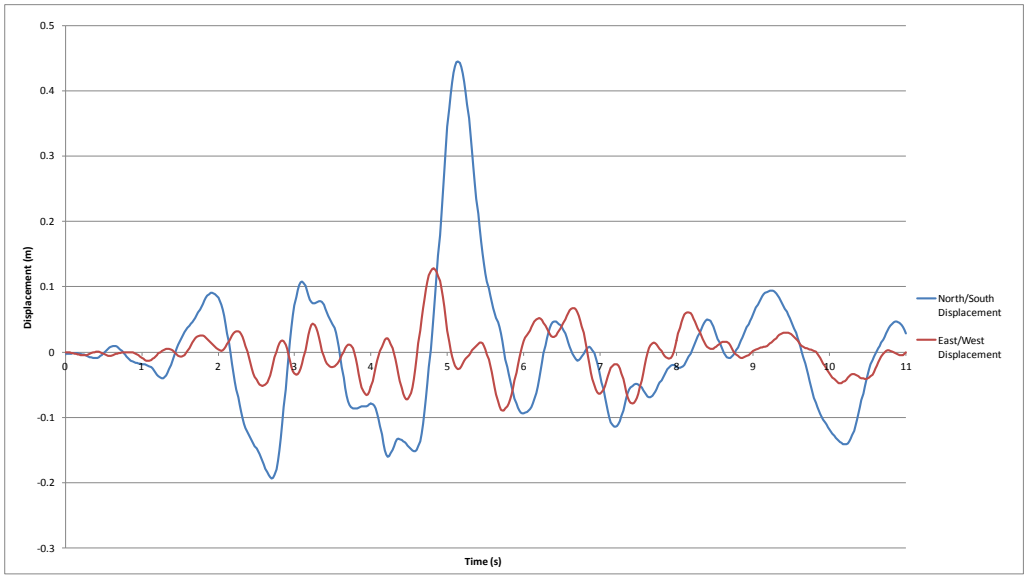

Figure F.2: Level 6 Northwest corner displacements.

As can be seen in Figure F.2 above a significant increase in the northward building displacement is observed in the northwest corner of the building between 5 and 5.5 seconds of the record. This occurs after the tension ties capacities on levels 4 to 6 of the core are exceeded allowing increased building rotation clockwise from west to north. The peak displacement corresponds to a clockwise rotation in conjunction with a net northward building translation. Table F.1 presents the sequence of failure of the north core wall ties throughout the record.

Table F.1: Wall D and D/E diaphragm disconnection times.

Level	Wall D Failure (sec)	Wall D/E Failure (sec)
6	2.56	2.48
5	2.54	2.46
4	2.50	2.38

Inter-storey displacements for the perimeter frame lines A and F in the north/south direction are presented in Figure E.3, and Figure F.4 below. North core tie tensile failure is identified on the plots for reference.

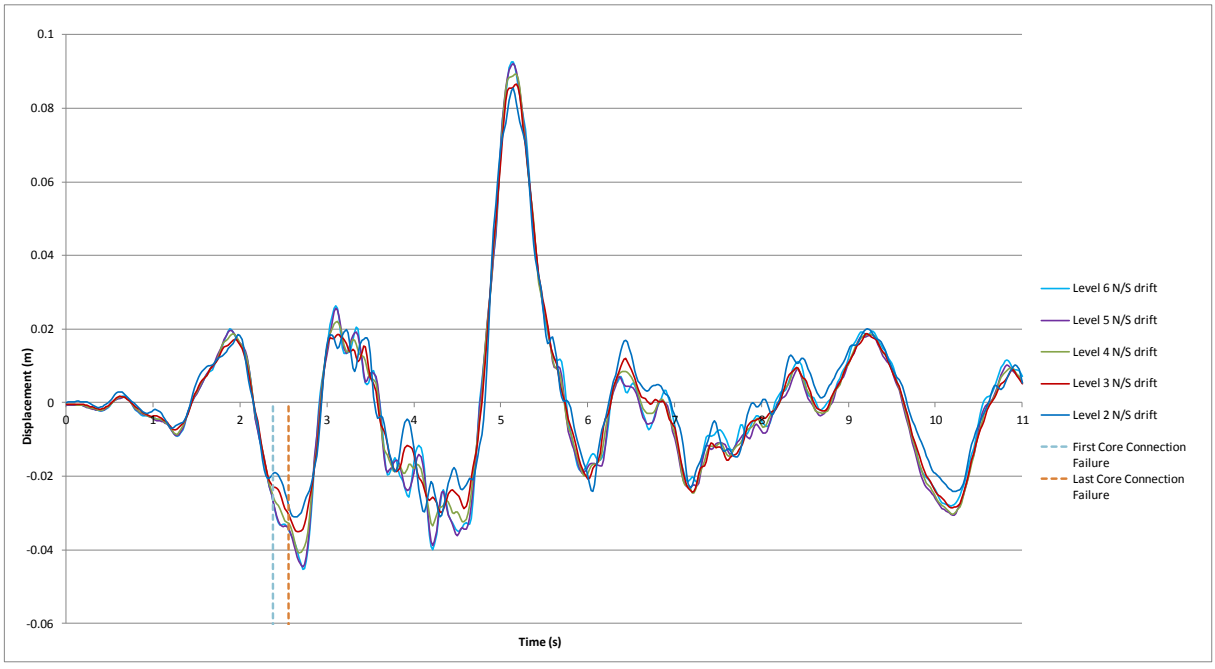

Figure F.3: Frame A north/south inter-storey displacements.

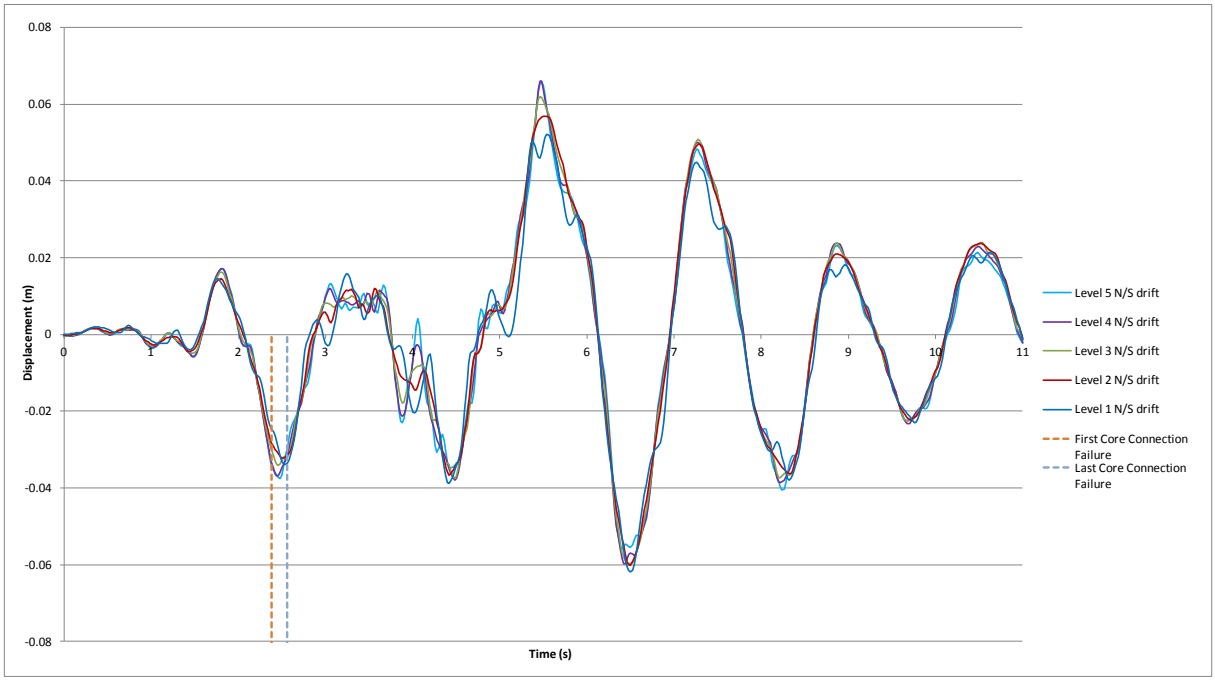

Figure F.4: Frame F north/south inter-storey displacements.

Inter-storey displacements for the perimeter frame lines 1 and 4 in the East/West direction are presented in Figure F.5, and Figure F.6 below.

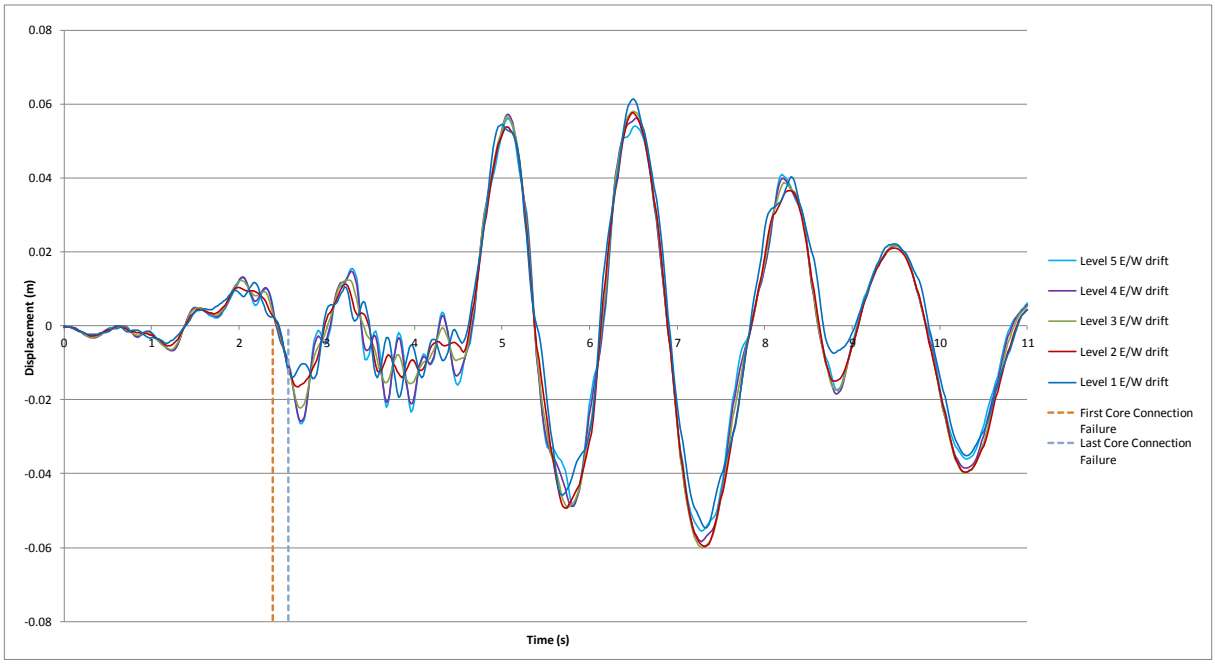

Figure F.5: Frame 1 east/west inter-storey displacements.

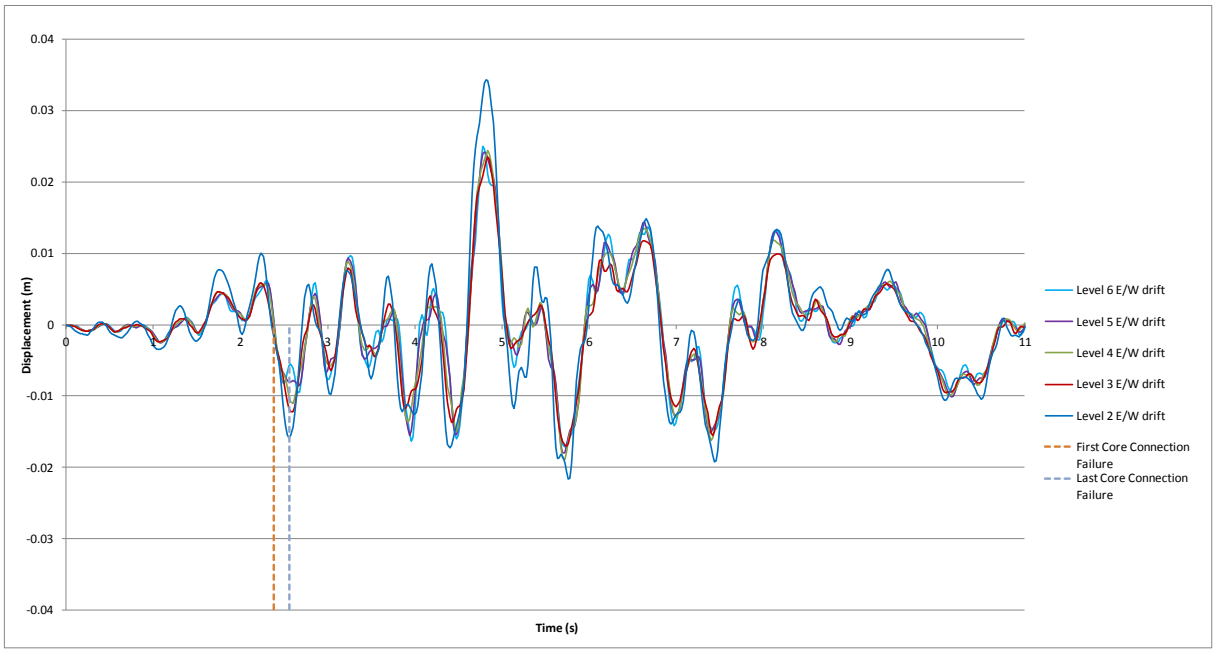

Figure F.6: Frame 4 east/west inter-storey displacements.

F.2 Diaphragm Connection Forces

Diaphragm connection forces are presented in Figure F.7 to Figure F.18 below. Note that moments are reported about the geometric centroid of the element being considered.

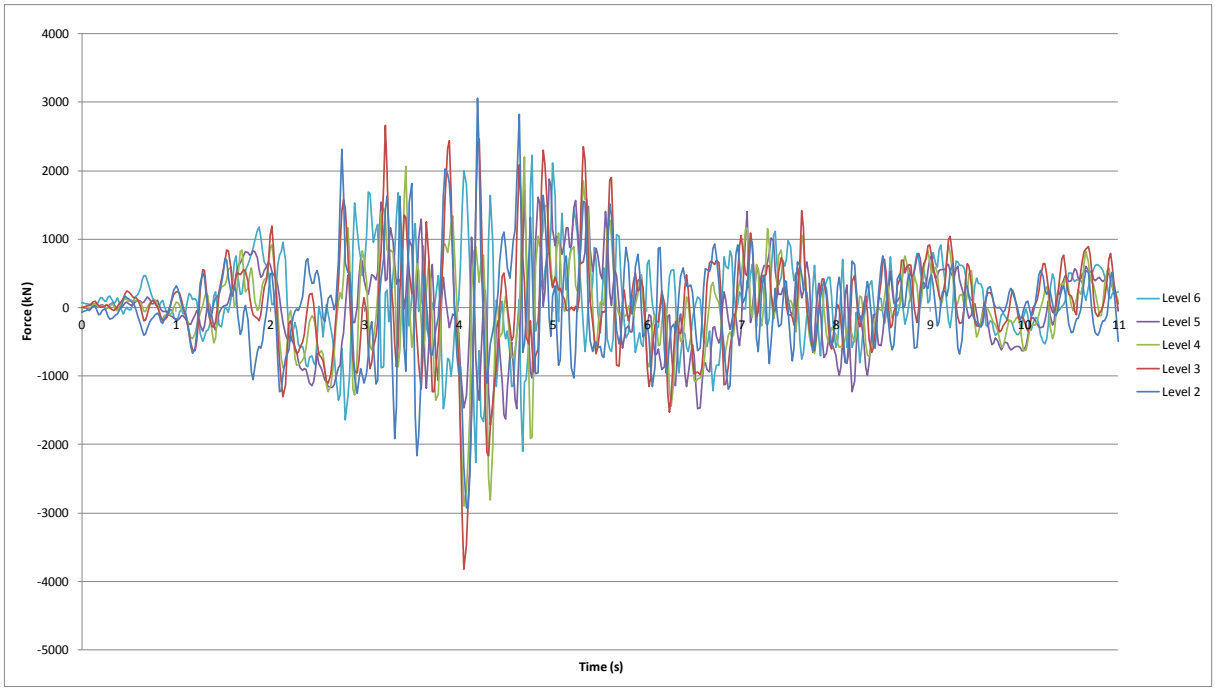

Figure F.7: North core total diaphragm north/south actions

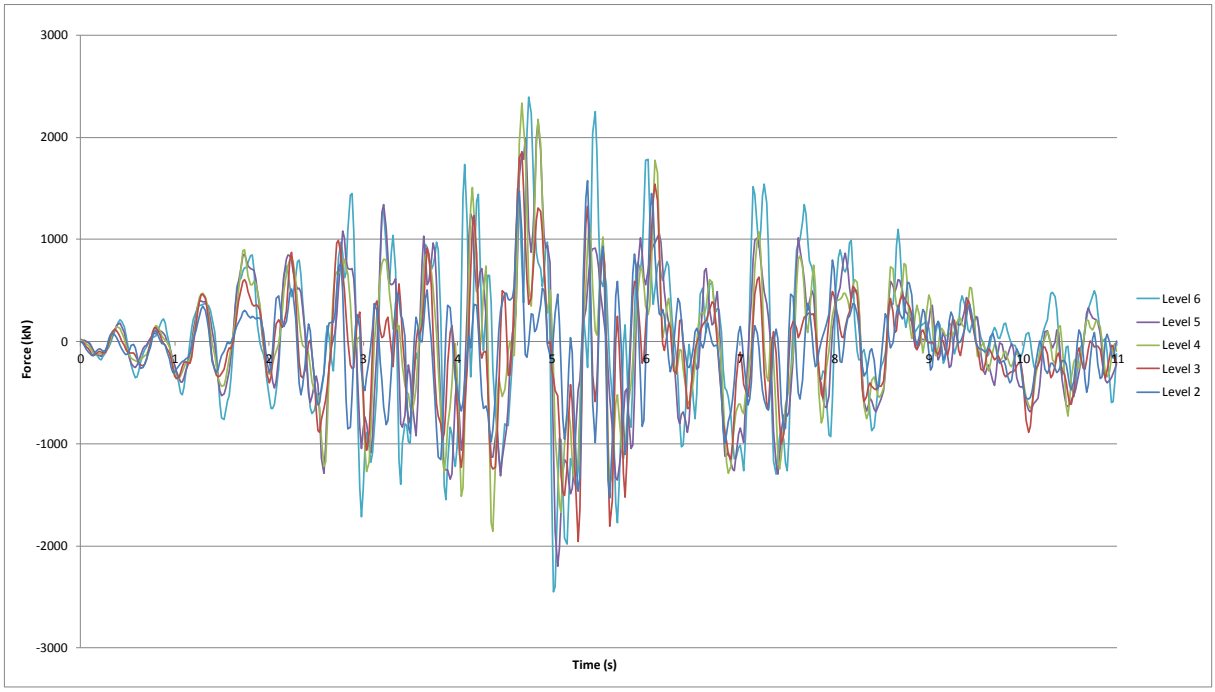

Figure F.8: North core total diaphragm east/west actions

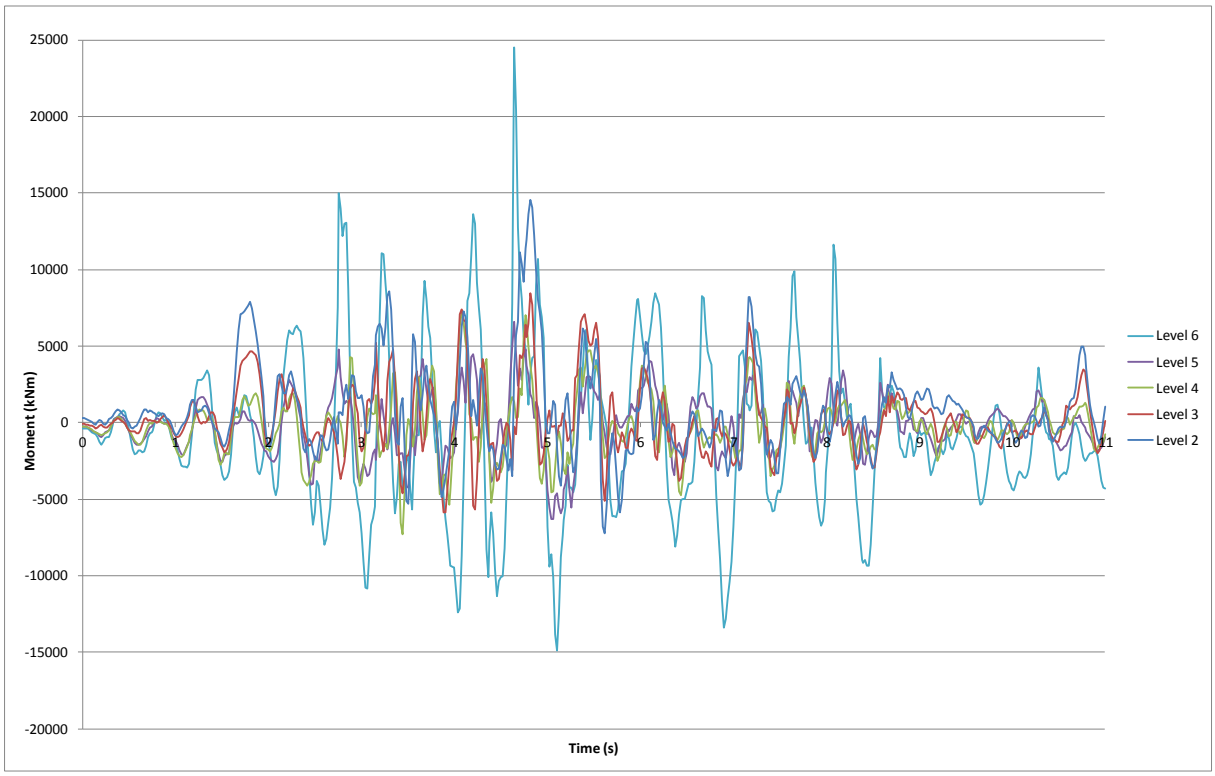

Figure F.9: North core total diaphragm in-plane moments

Figure F.10: North core Wall C diaphragm north/south actions

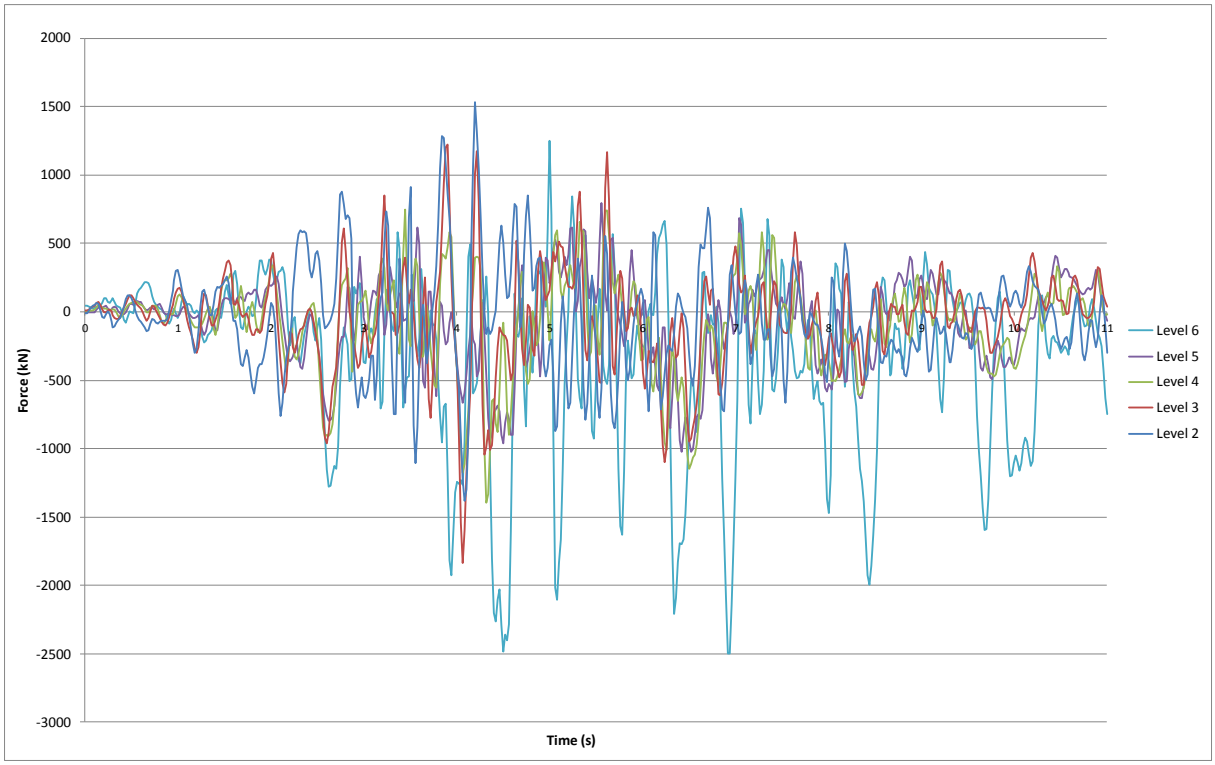

Figure F.11: North core Wall C/D diaphragm north/south actions.

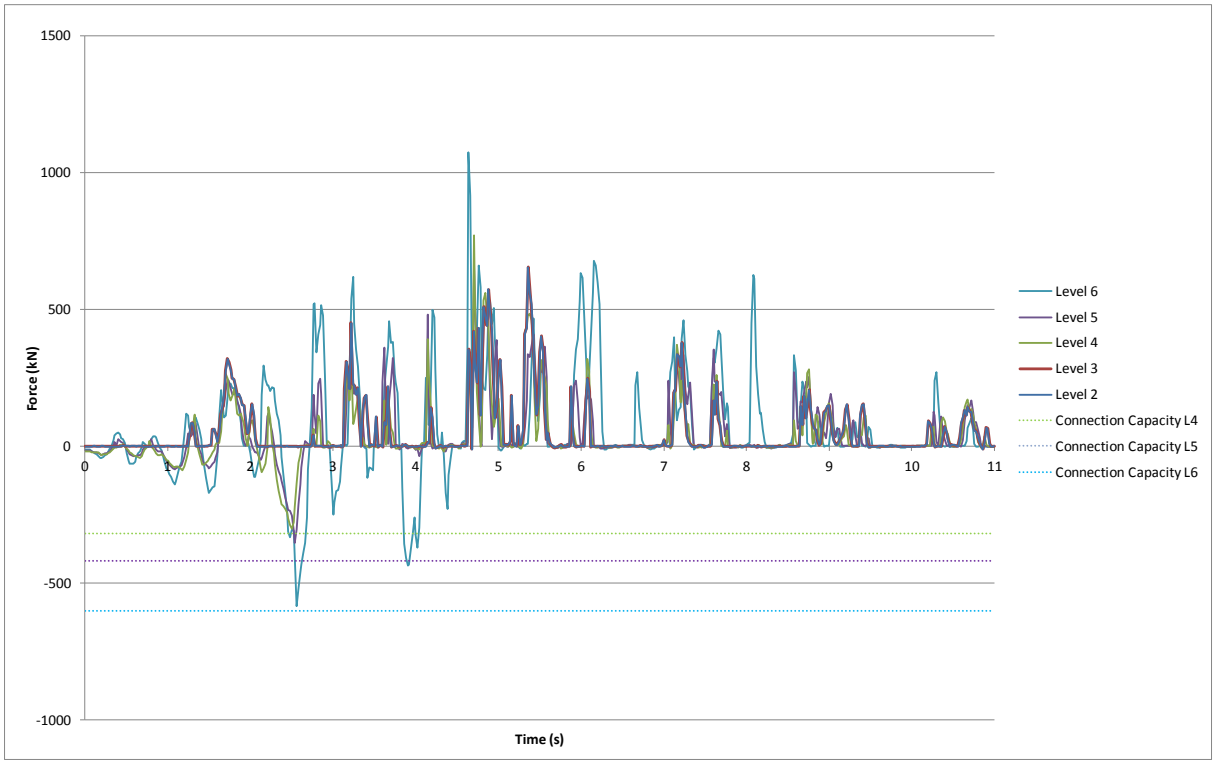

Figure F.12: North core Wall D diaphragm north/south actions.

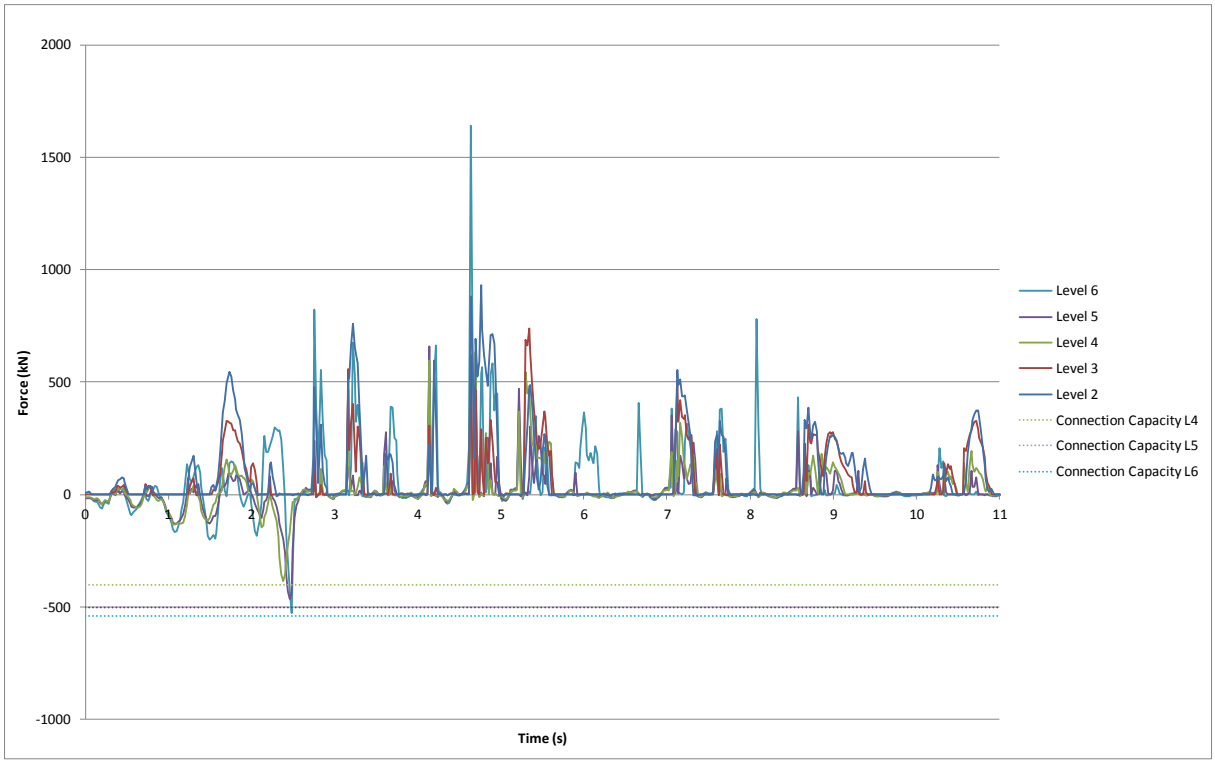

Figure F.13: North core Wall D/E diaphragm north/south actions.

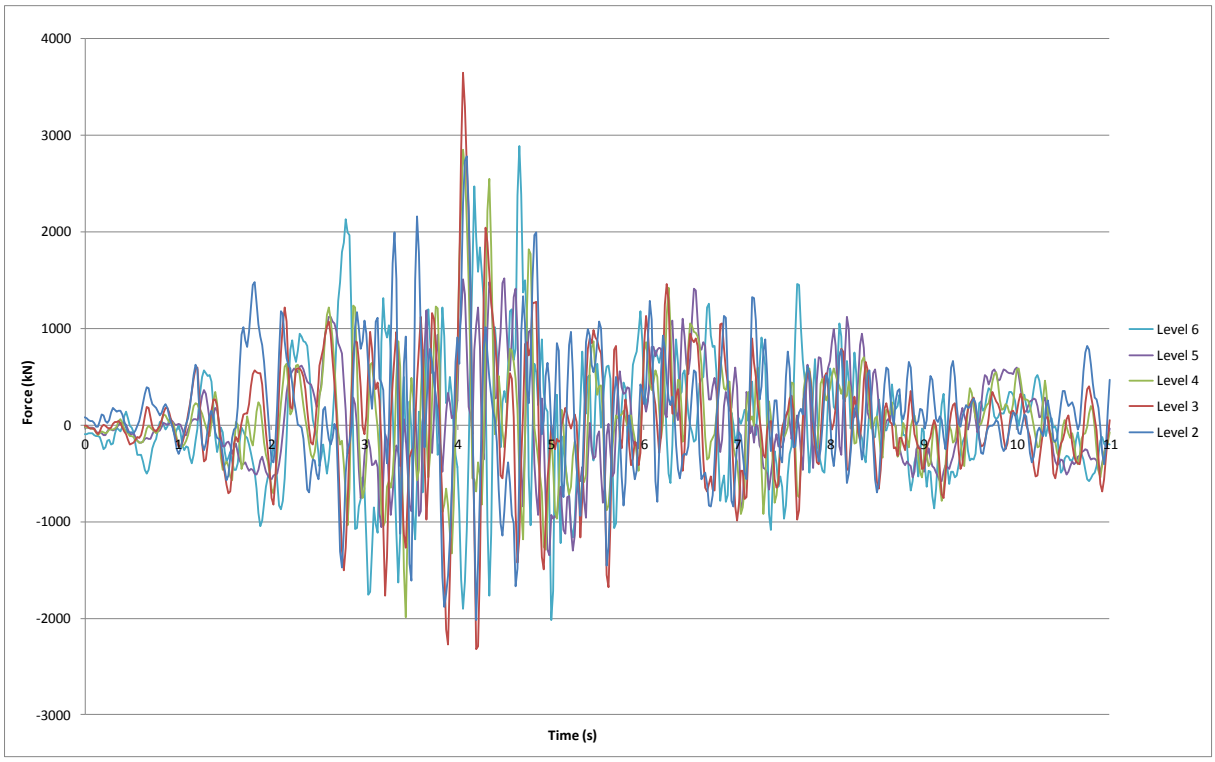

Figure F.14: North core Slab 4/C to C/D diaphragm north/south actions.

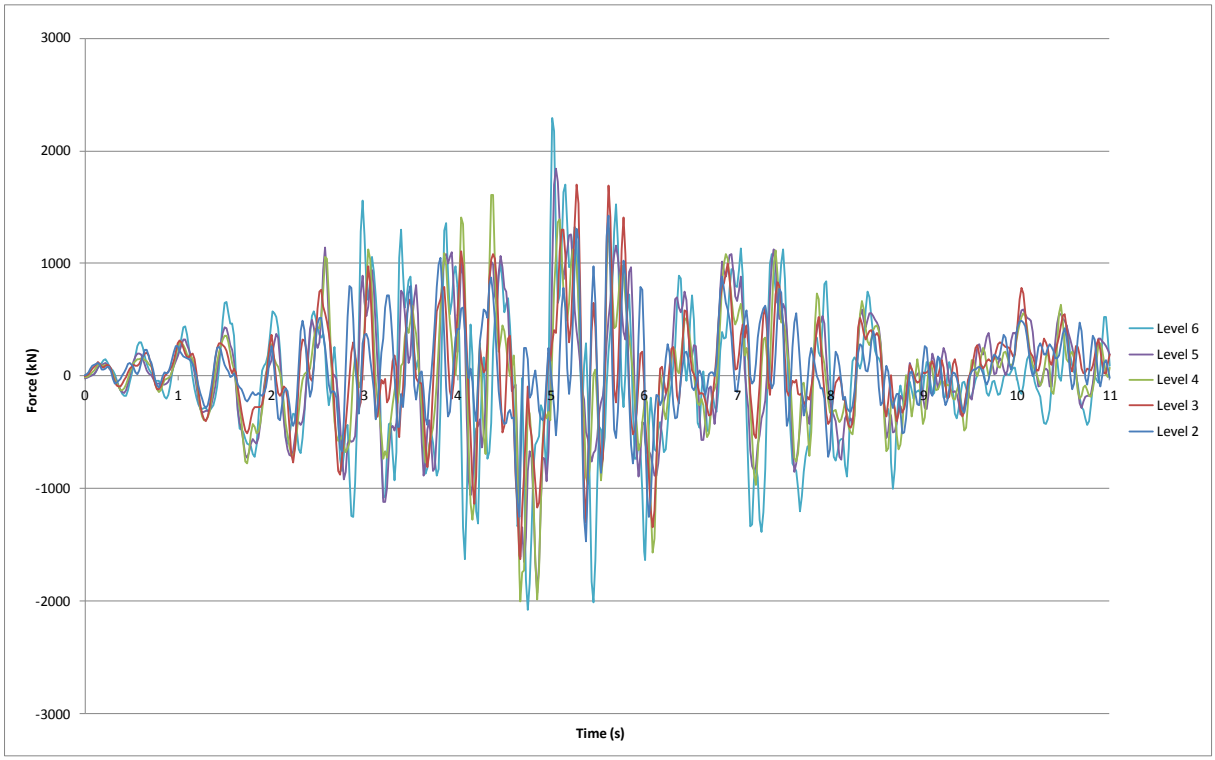

Figure F.15: North core Slab 4/C to C/D diaphragm east/west actions.

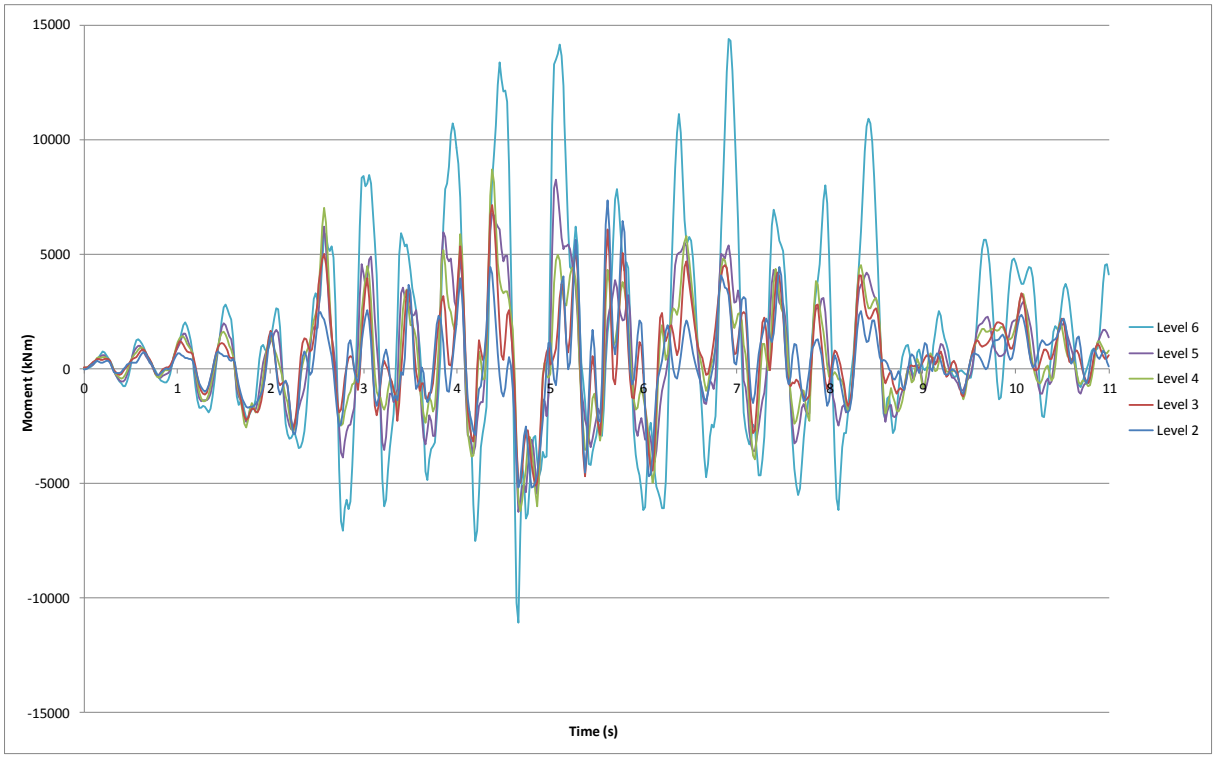

Figure F.16: North core Slab 4/C to C/D diaphragm in-plane moments.

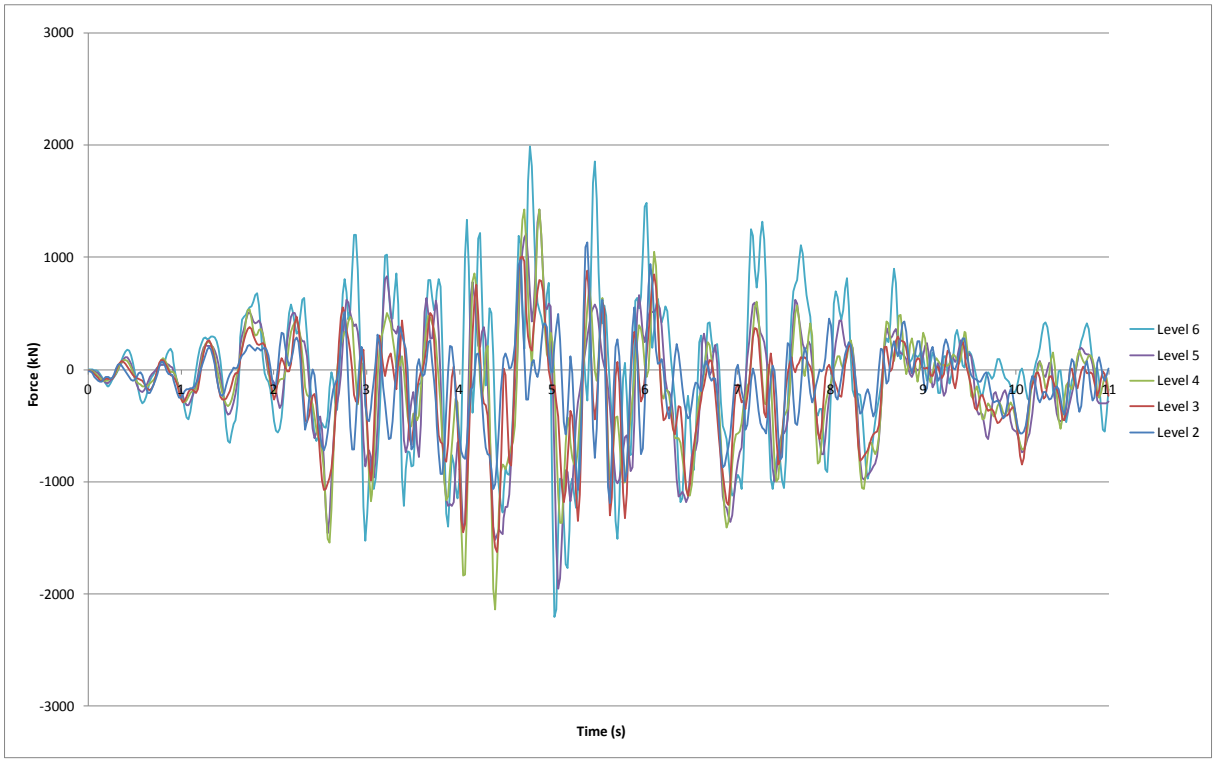

Figure F.17: North core Wall 5 diaphragm east/west actions.

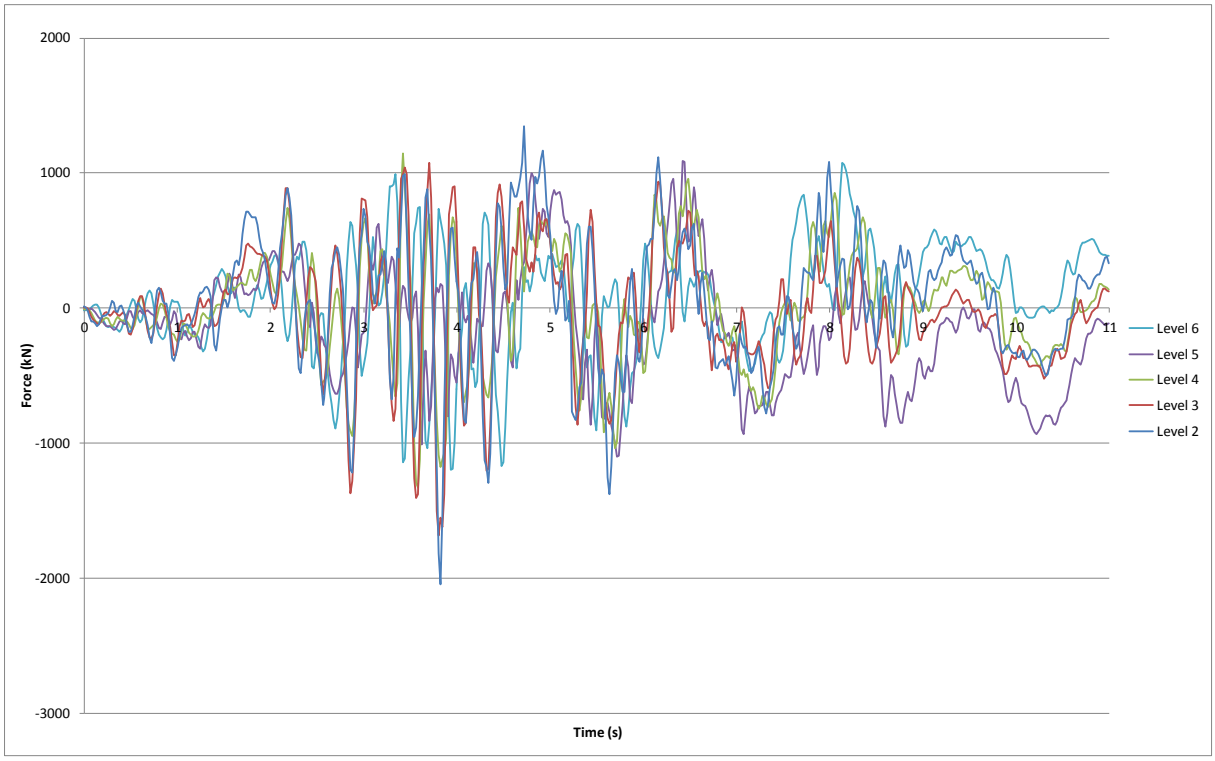

Figure F.18: South wall diaphragm east/west actions.

Appendix G :Analysis Results - Lyttelton Aftershock: Model A: CCCC record

The following details the structural actions reported by the analysis as a function of time, for the Lyttelton aftershock using the acceleration time history recorded at the CCCC station using all components of the record.

G.1 Building Displacements and Drifts.

Building Level 6 displacements are presented in Figure G.1 and Figure G.2 below for the southeast and northwest corners of the building respectively.

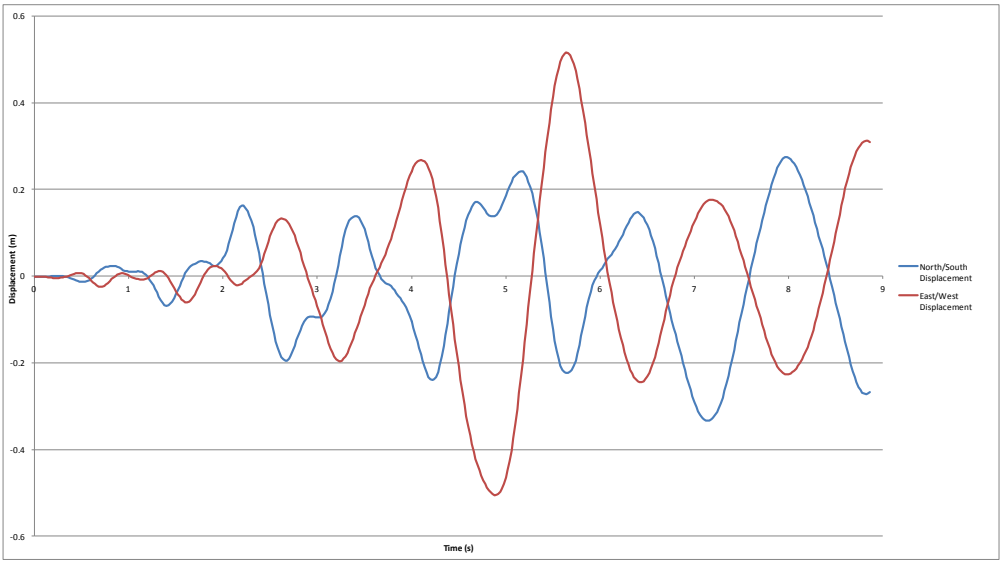

Figure G.1: Level 6 Southeast corner displacements.

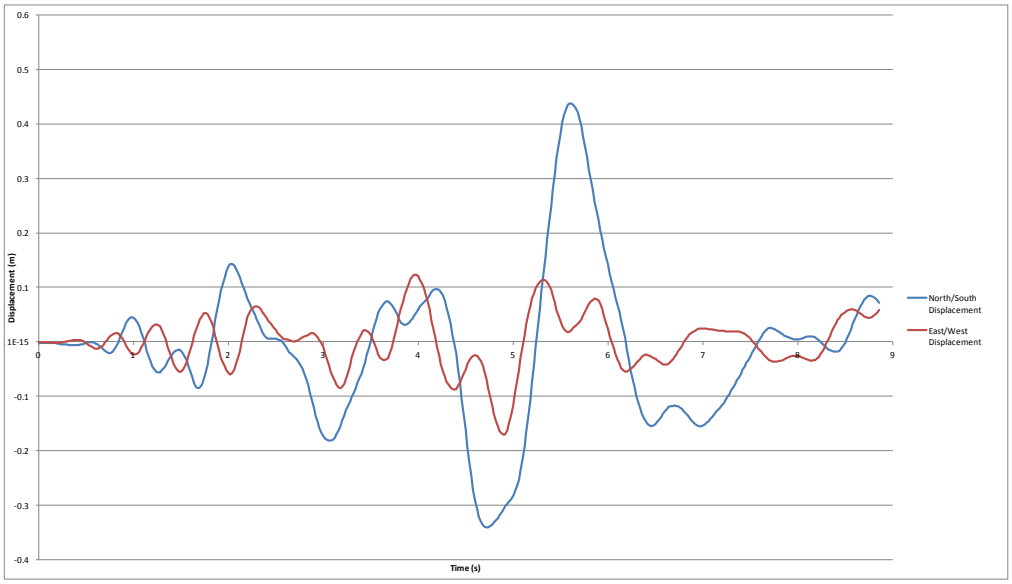

Figure G.2: Level 6 Northwest corner displacements.

As can be seen in Figure G.2 above a significant increase in the northward building displacement is observed in the northwest corner of the building between 5.5 and 6 seconds of the record. This occurs after the tension ties capacities on levels 4 to 6 of the core are exceeded allowing increased building rotation clockwise from west to north. The peak displacement corresponds to a clockwise rotation in conjunction with a net northward building translation. Table G.1 presents the sequence of failure of the north core wall ties throughout the record.

Table G.1: Wall D and D/E diaphragm disconnection times.

Level	Wall D Failure (sec)	Wall D/E Failure (sec)
6	3.10	1.44
5	3.10	1.54
4	1.58	1.46

Inter-storey displacements for the perimeter frame lines A and F in the north/south direction are presented in Figure G.3, and Figure G.4 below. North core tie tensile failure is identified on the plots for reference.

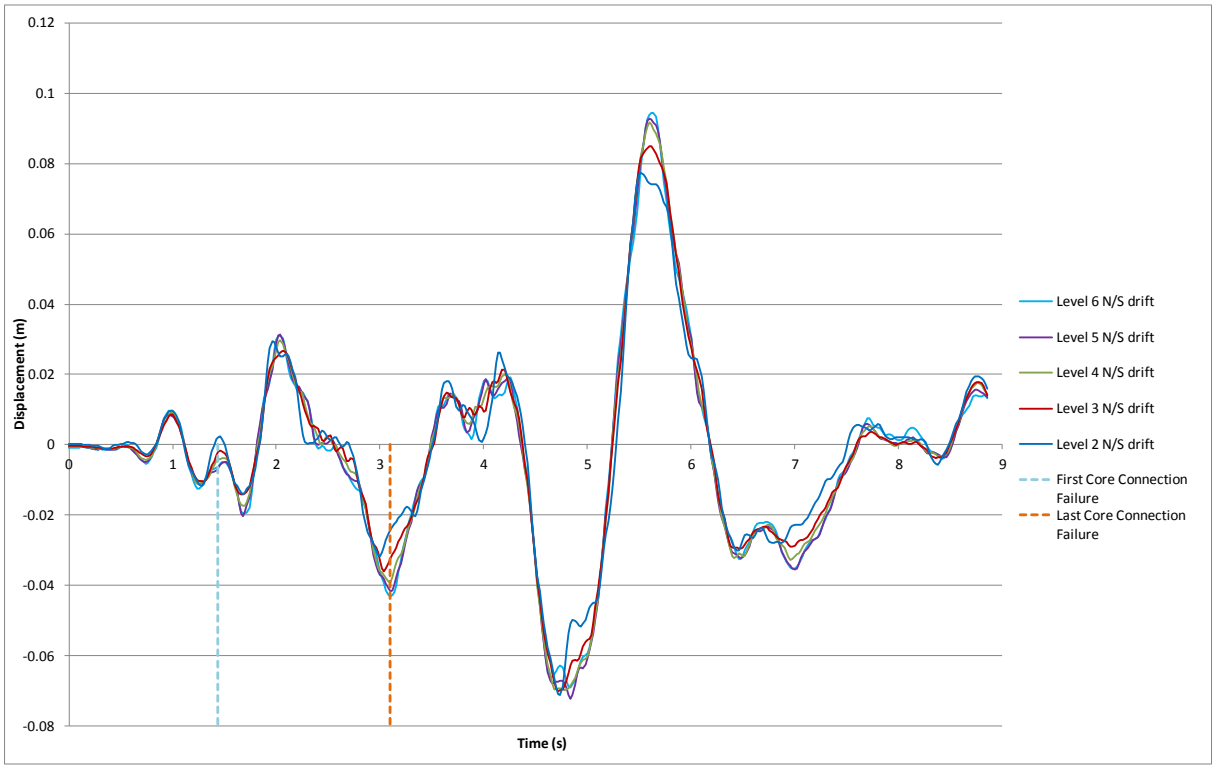

Figure G.3: Frame A north/south inter-storey displacements.

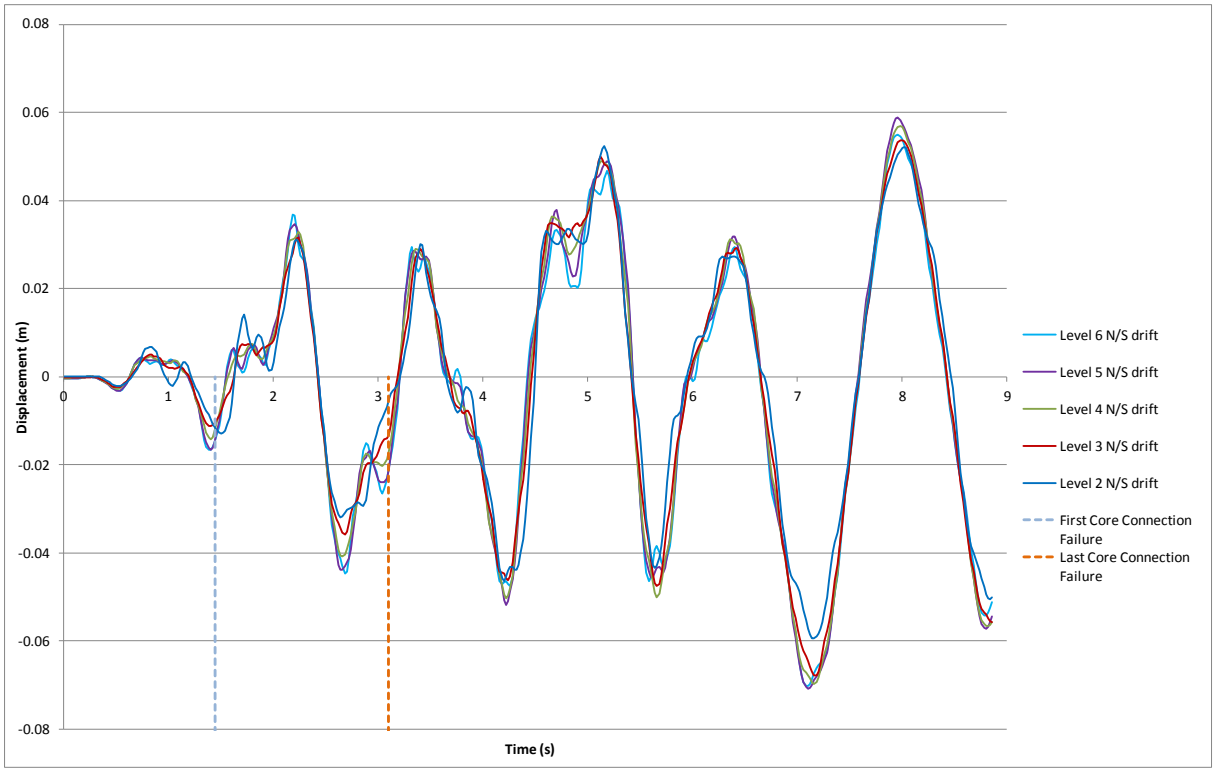

Figure G.4: Frame F north/south inter-storey displacements.

Inter-storey displacements for the perimeter frame lines 1 and 4 in the East/West direction are presented in Figure G.5, and Figure G.6 below.

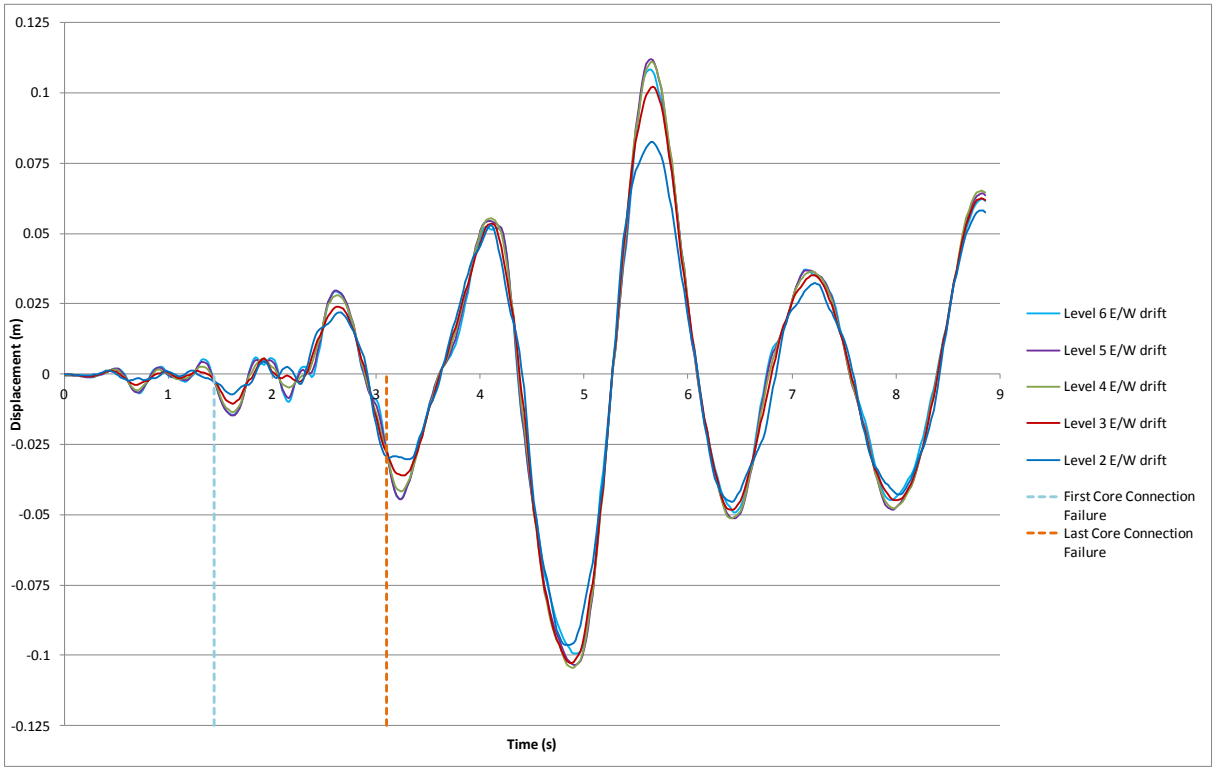

Figure G.5: Frame 1 east/west inter-storey displacements.

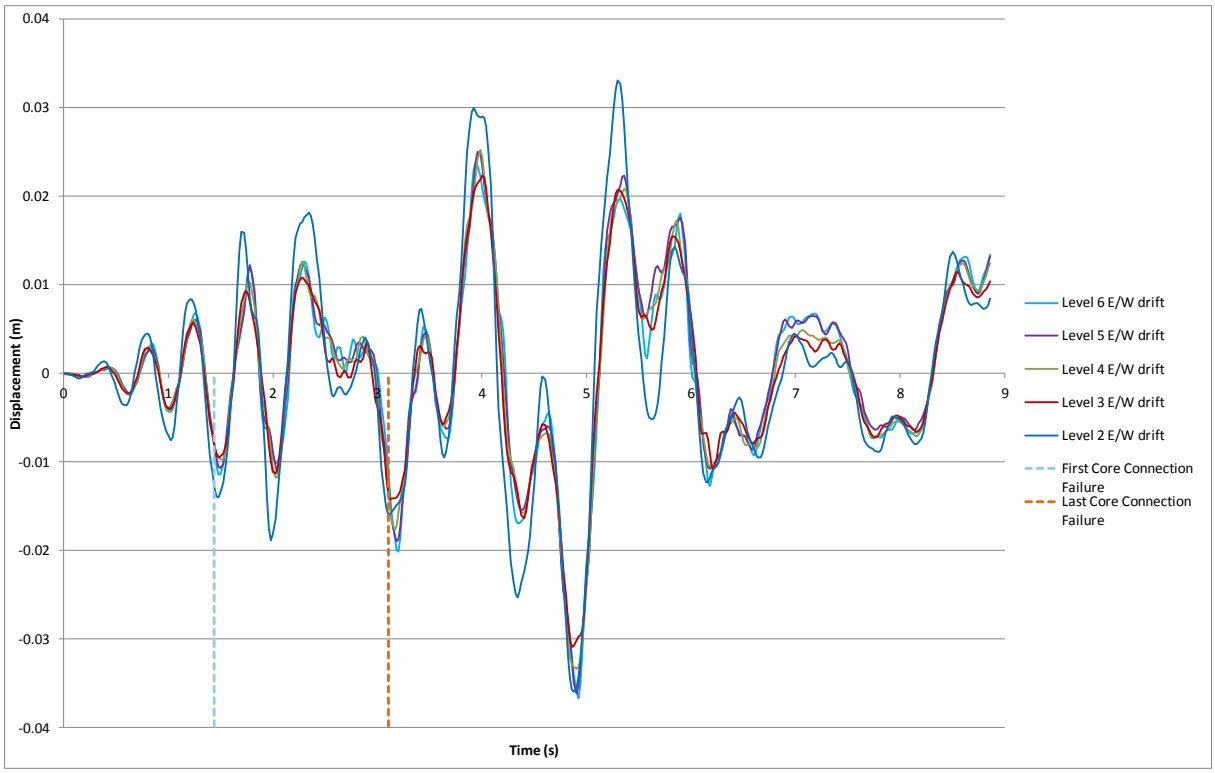

Figure G.6: Frame 4 east/west inter-storey displacements.

G.2 Diaphragm Connection Forces

Diaphragm connection forces are presented in Figure G.7 to Figure G.18 below. Note that moments are reported about the geometric centroid of the element being considered.

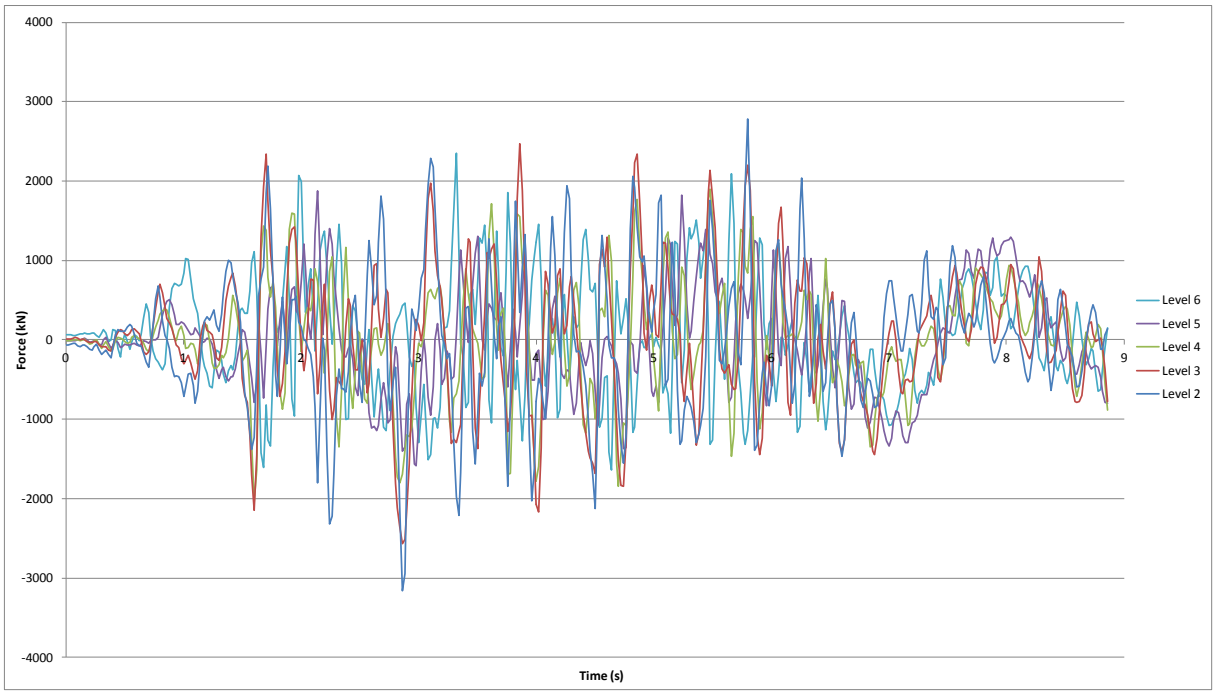

Figure G.7: North core total diaphragm north/south actions

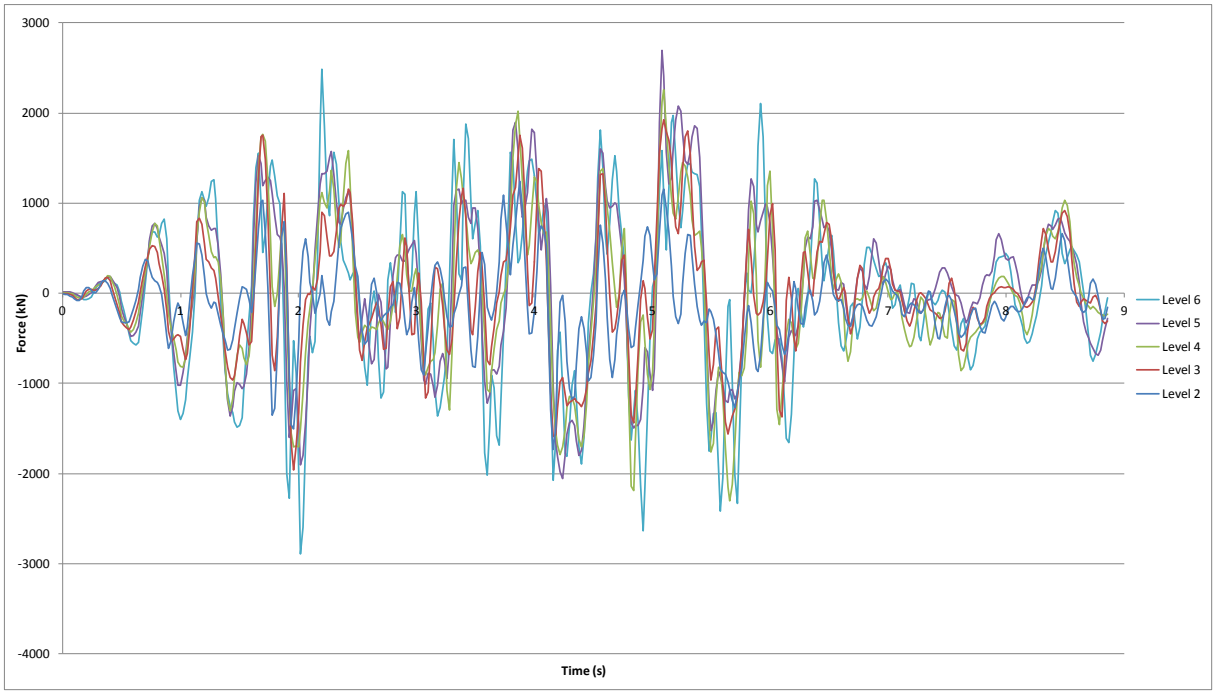

Figure G.8: North core total diaphragm east/west actions

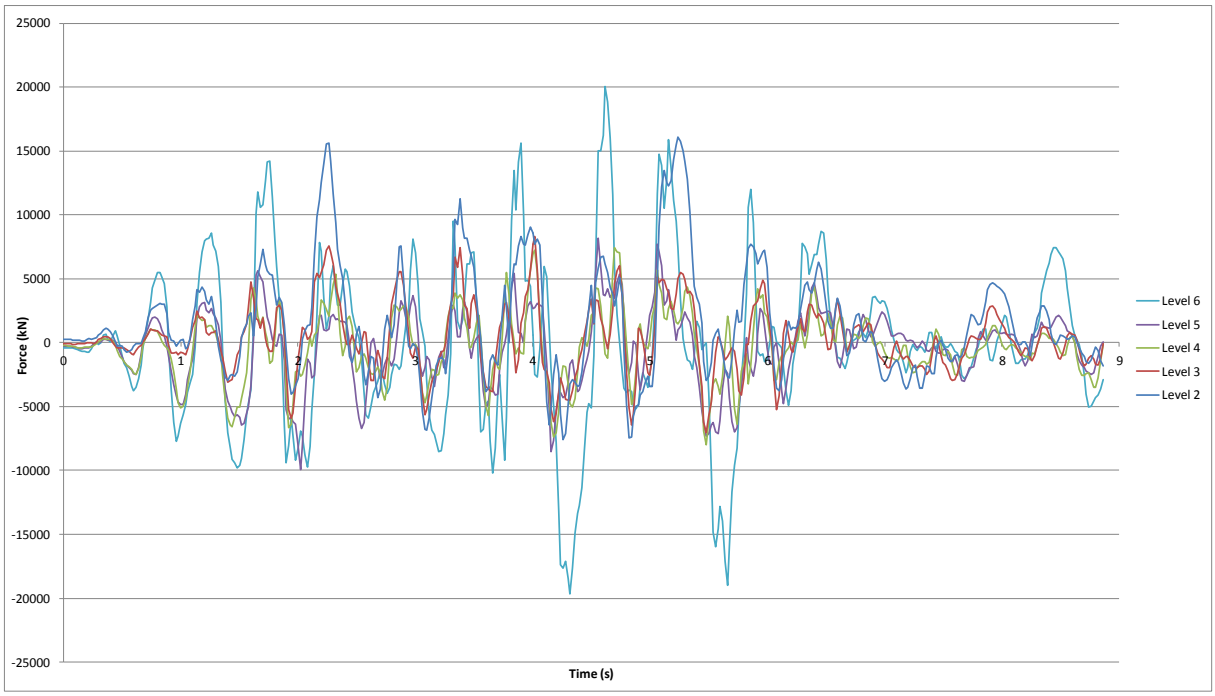

Figure G.9: North core total diaphragm in-plane moments

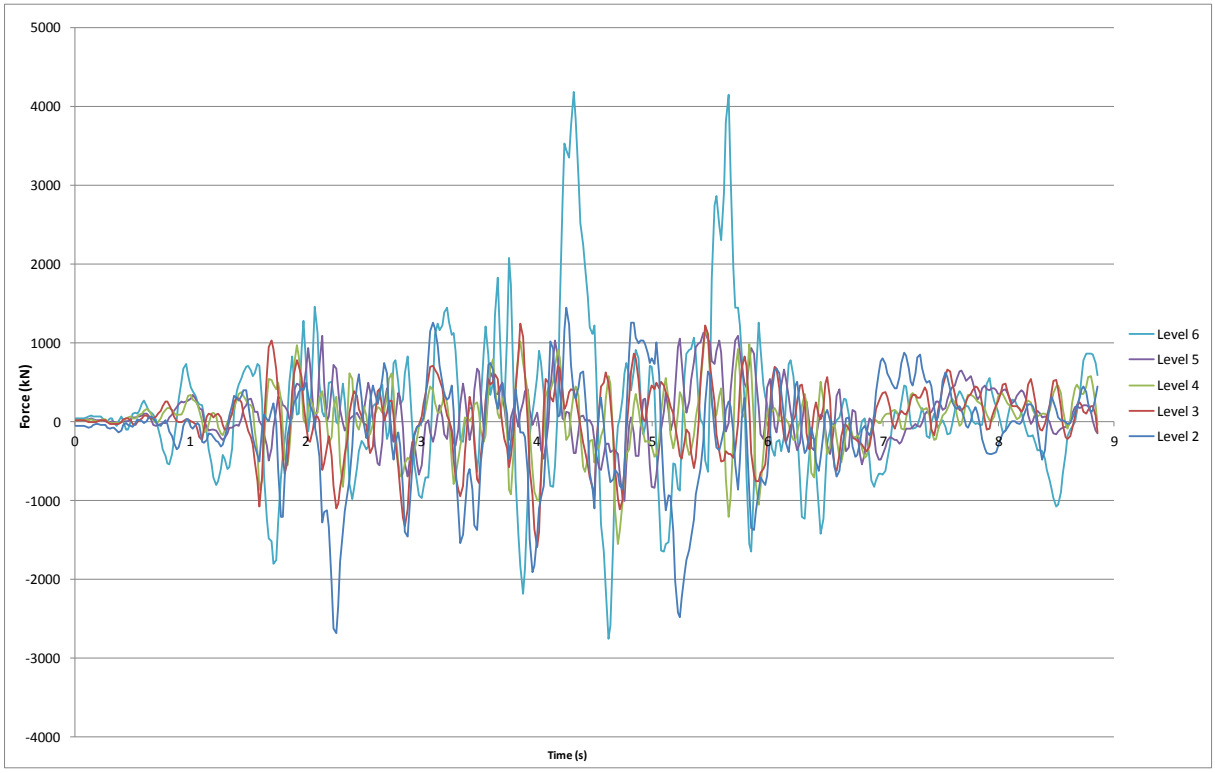

Figure G.10: North core Wall C diaphragm north/south actions

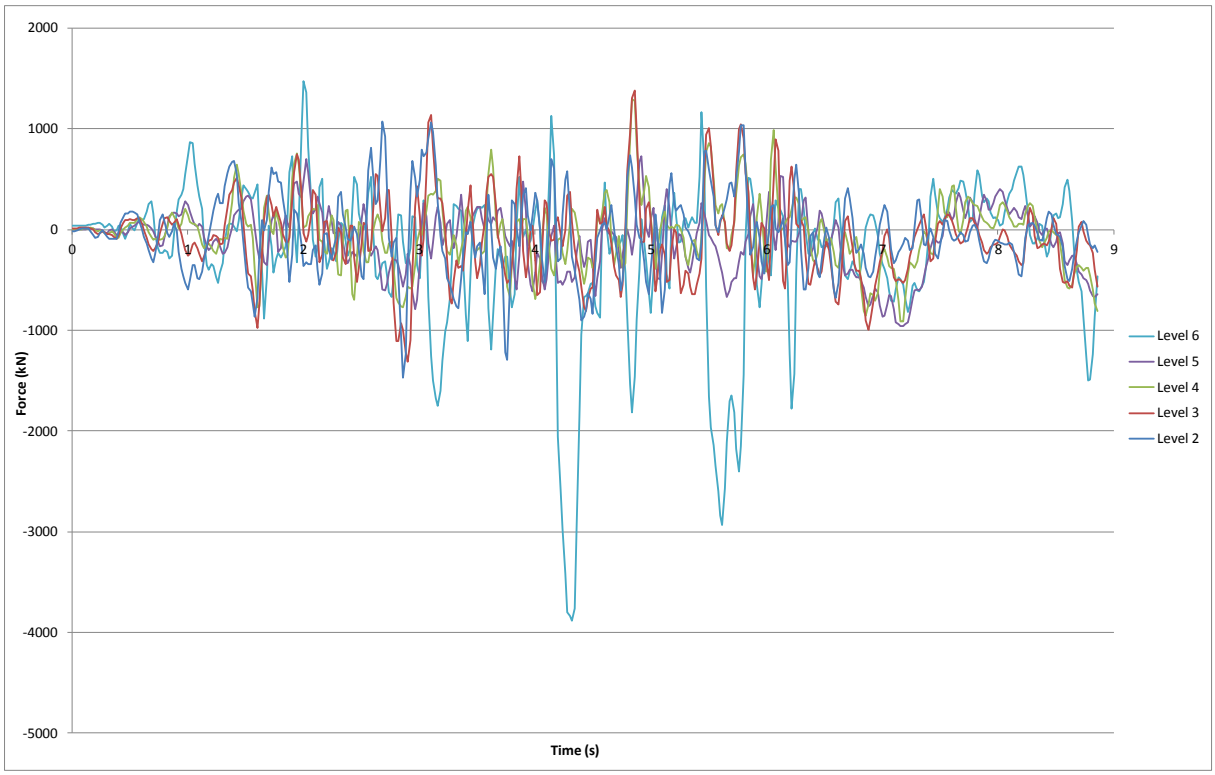

Figure G.11: North core Wall C/D diaphragm north/south actions.

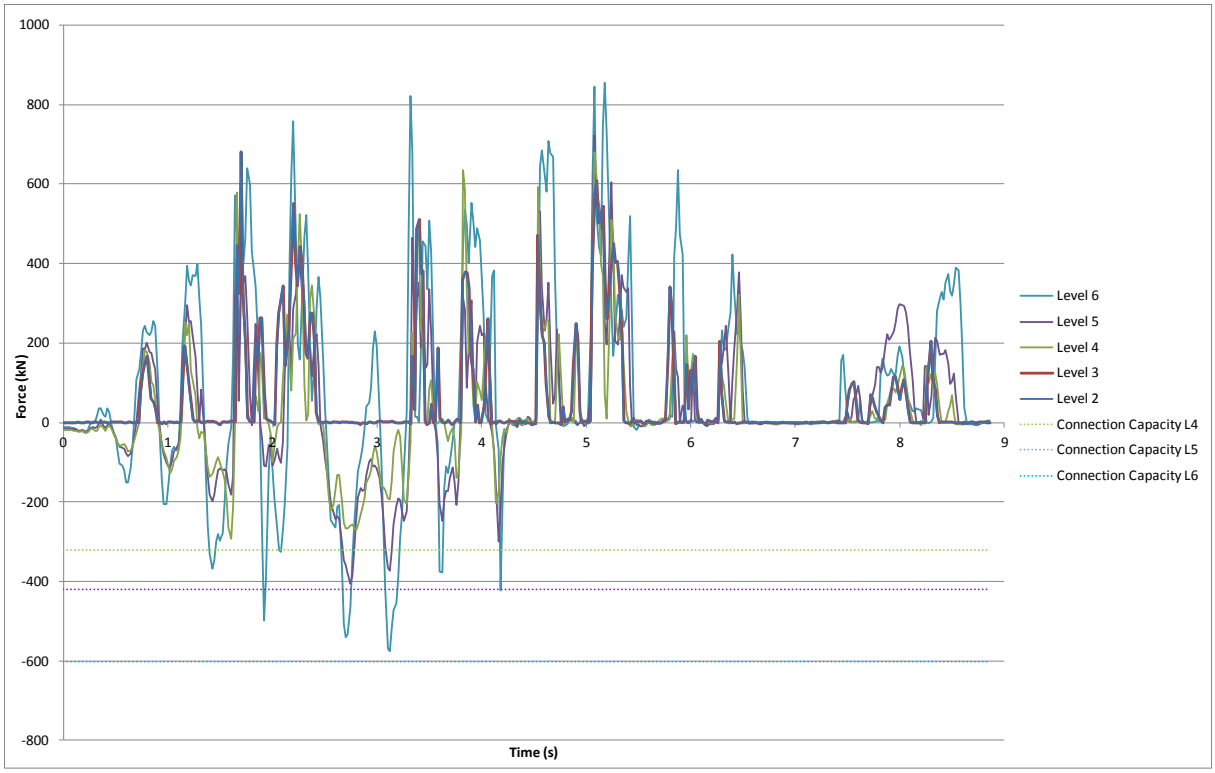

Figure G.12: North core Wall D diaphragm north/south actions.

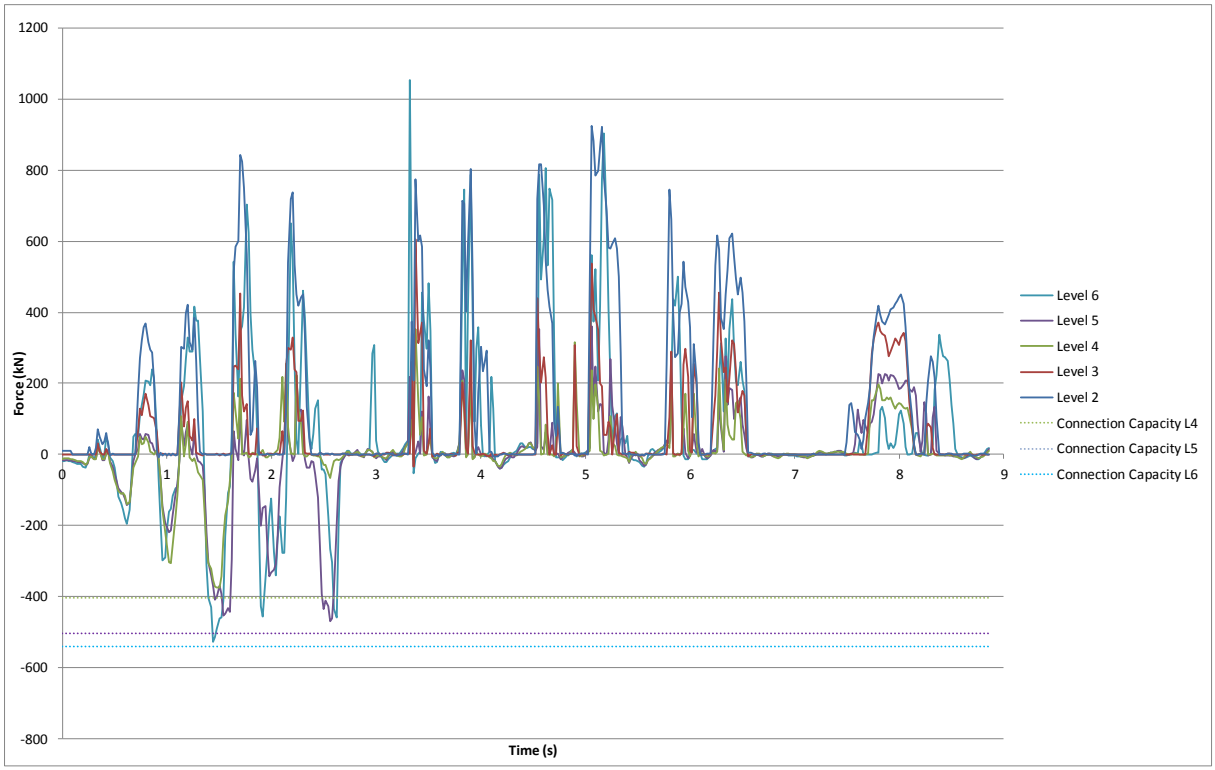

Figure G.13: North core Wall D/E diaphragm north/south actions.

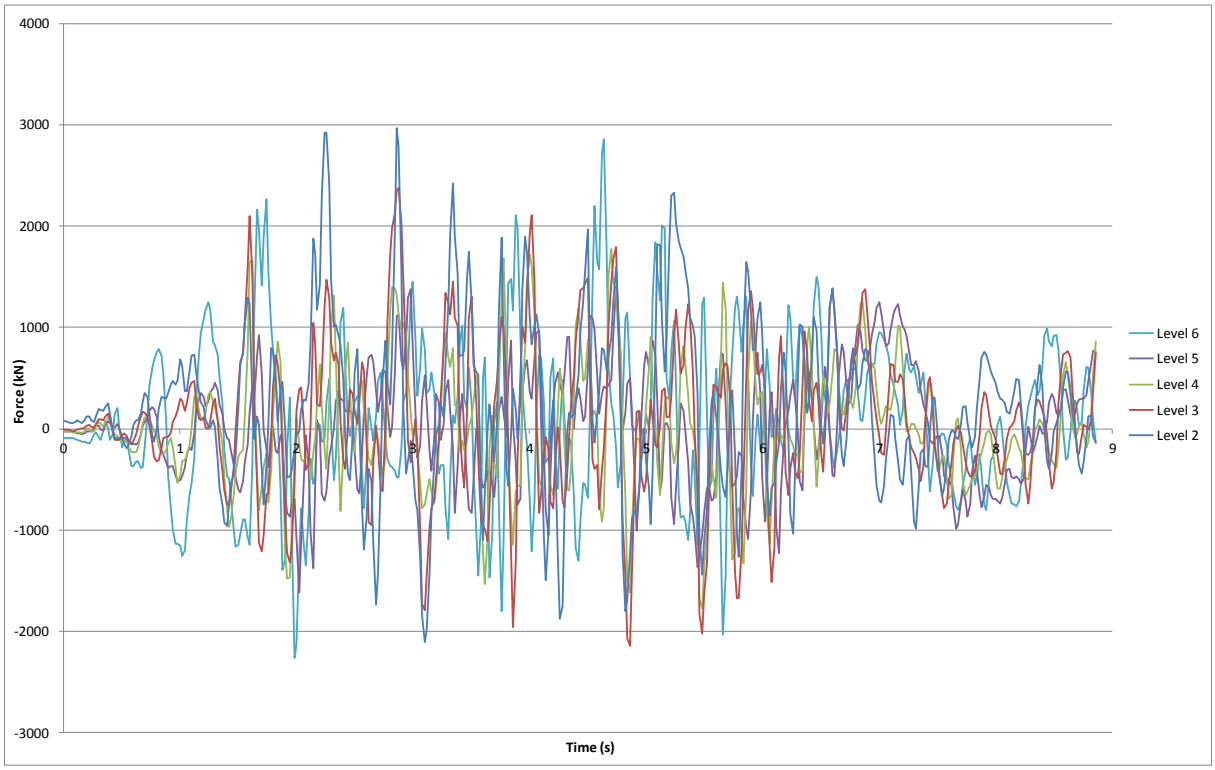

Figure G.14: North core Slab 4/C to C/D diaphragm north/south actions.

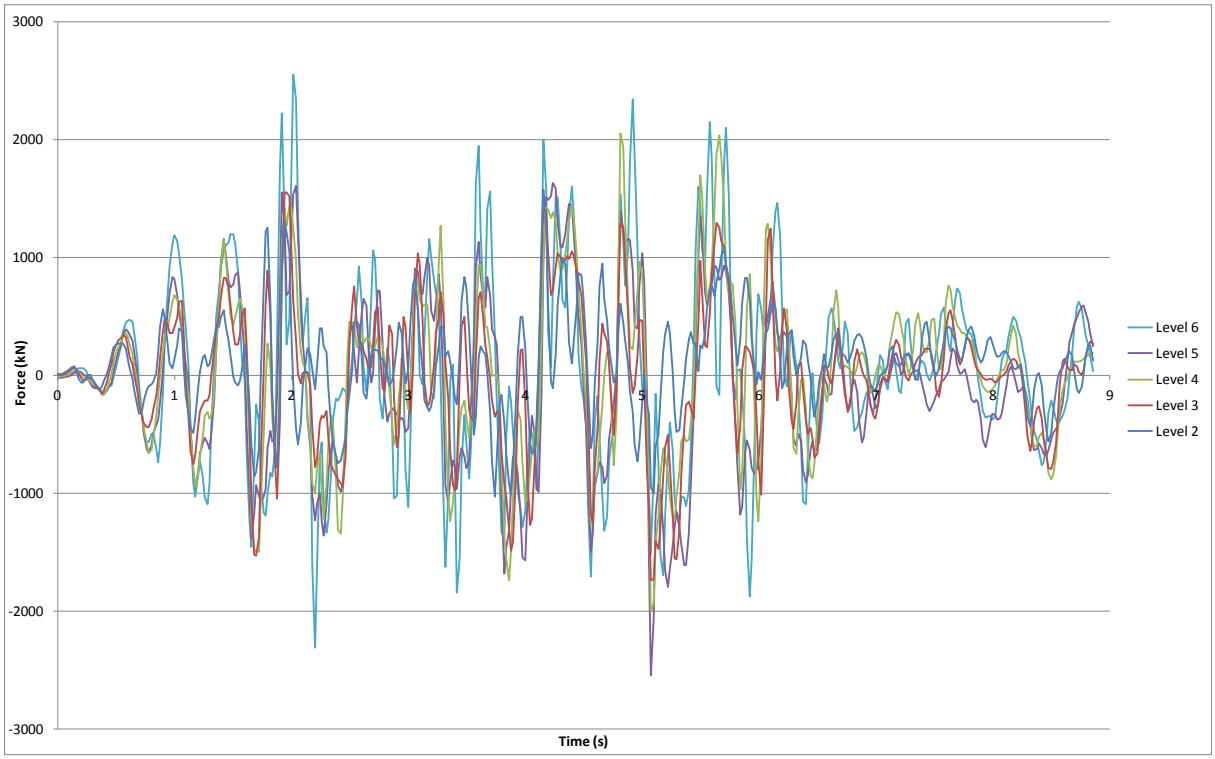

Figure G.15: North core Slab 4/C to C/D diaphragm east/west actions.

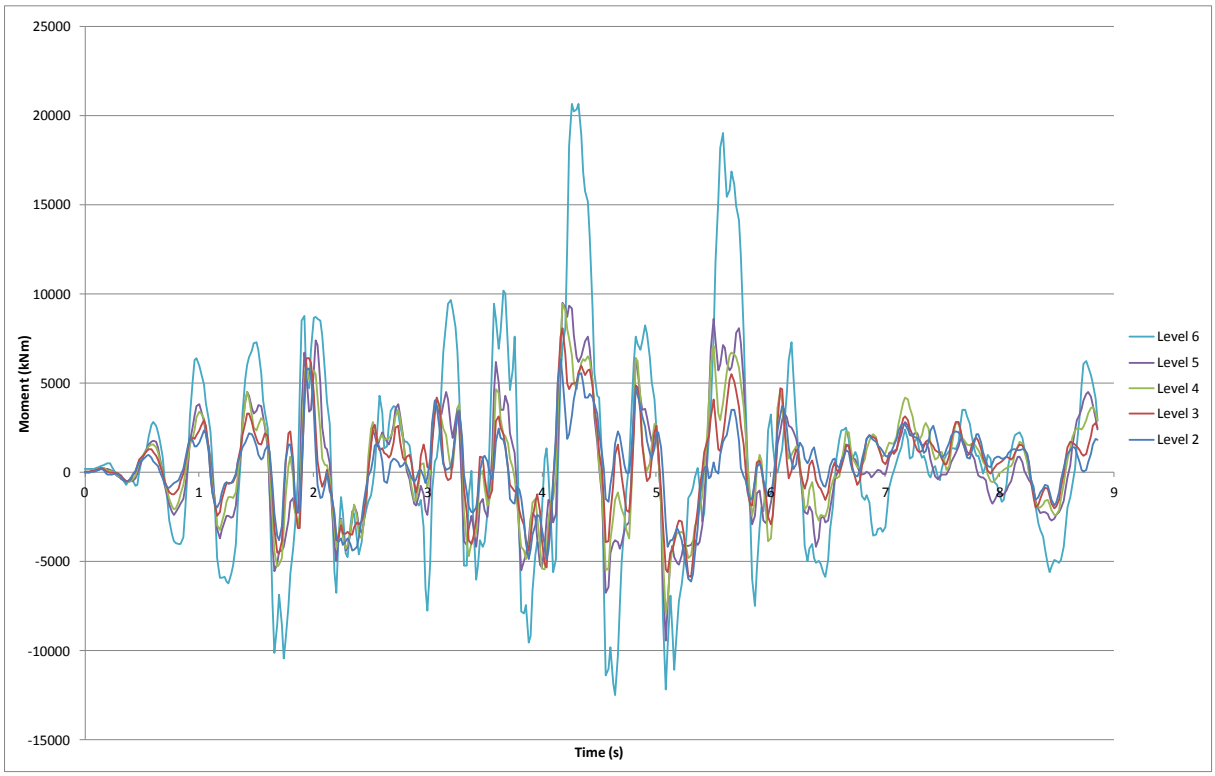

Figure G.16: North core Slab 4/C to C/D diaphragm in-plane moments.

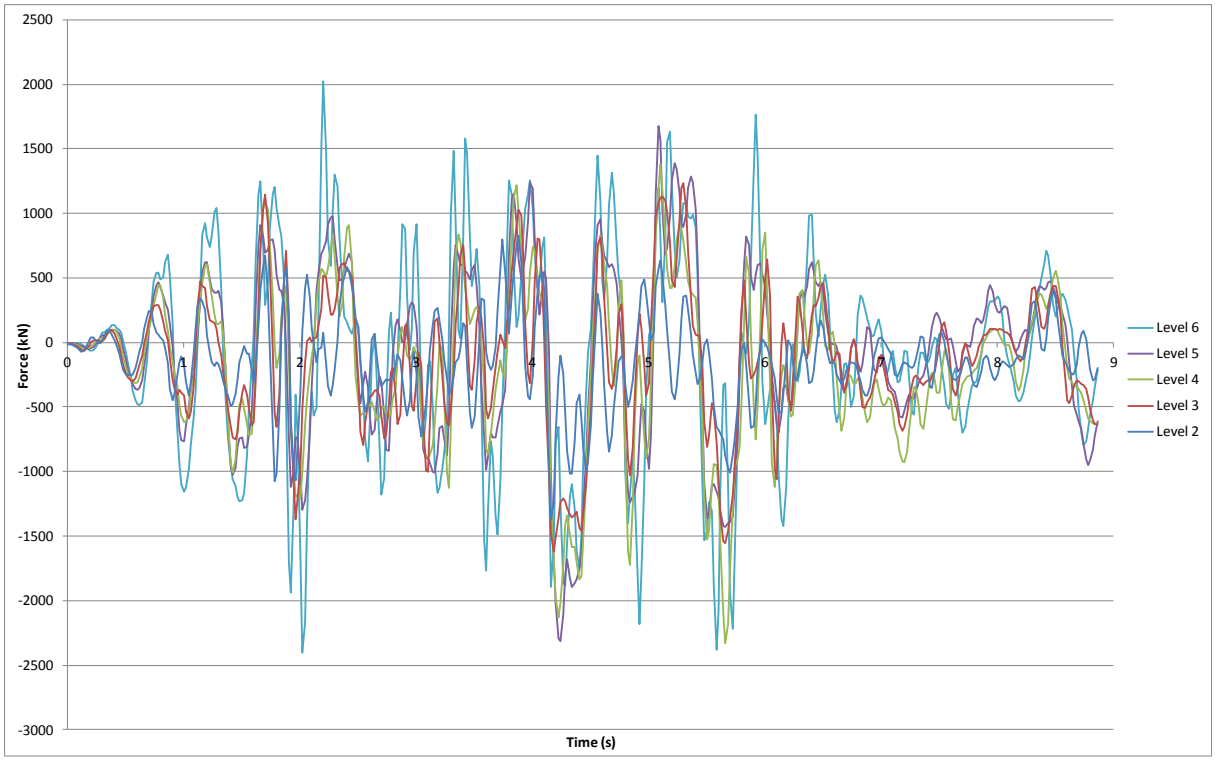

Figure G.17: North core Wall 5 diaphragm east/west actions.

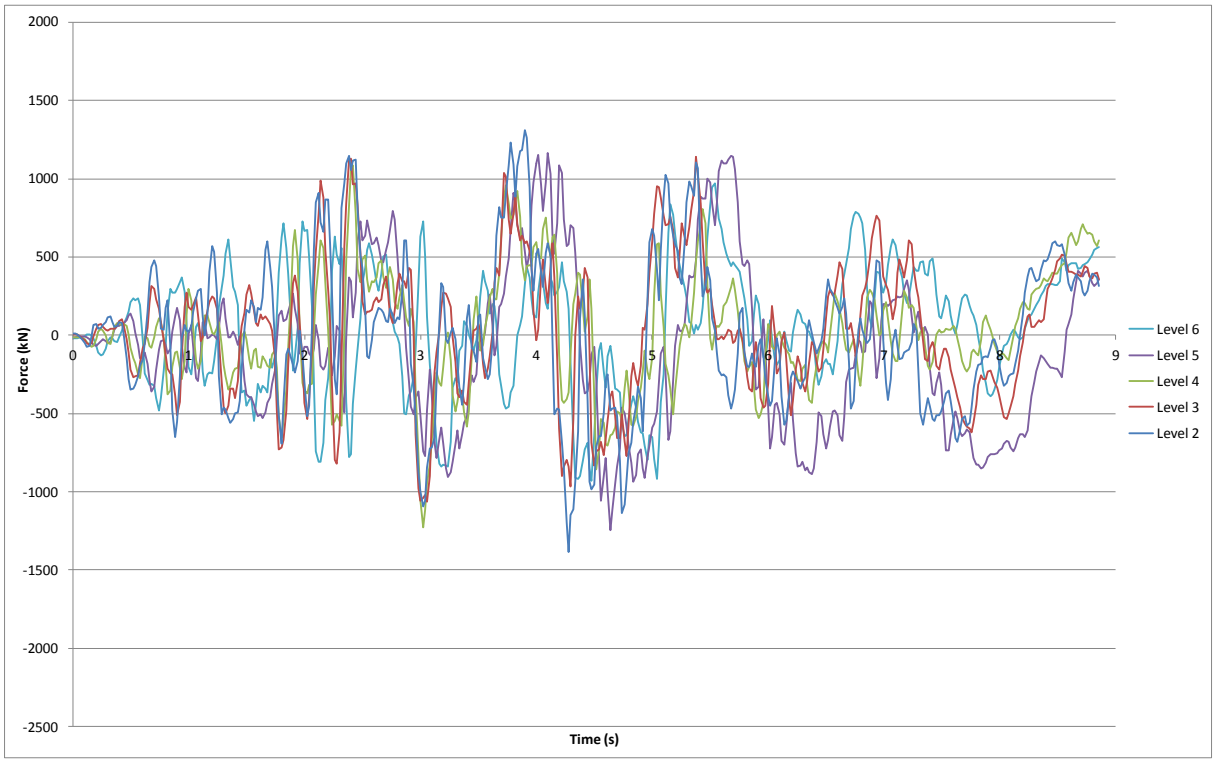

Figure G.18: South wall diaphragm east/west actions.

Appendix H :Analysis Results - Lyttelton Aftershock: Model A: CHHC record

The following details the structural actions reported by the analysis as a function of time, for the Lyttelton aftershock using the acceleration time history recorded at the CHHC station using all components of the record.

H.1 Building Displacements and Drifts.

Building Level 6 displacements are presented in Figure H.1 and Figure H.2 below for the southeast and northwest corners of the building respectively.

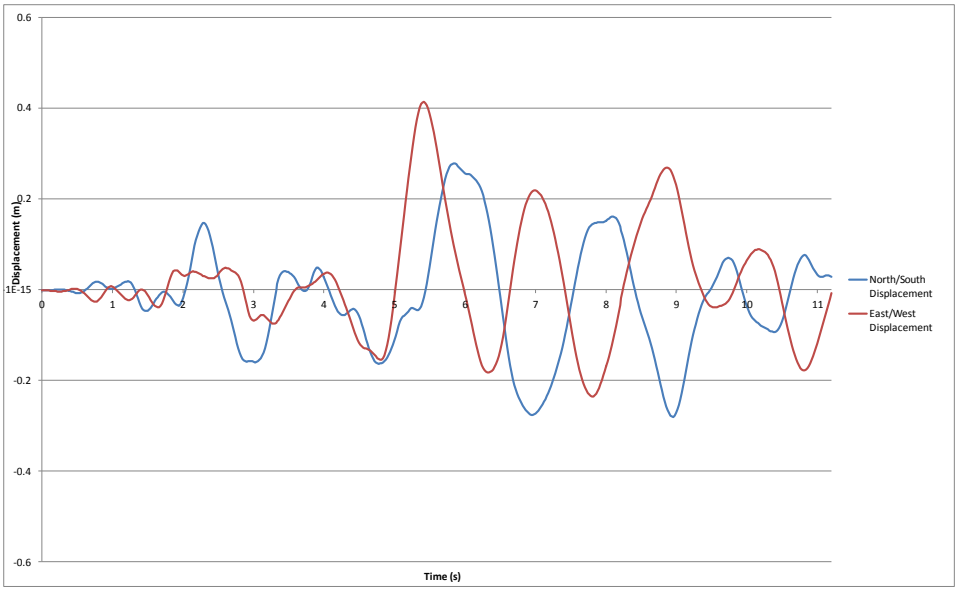

Figure H.1: Level 6 Southeast corner displacements.

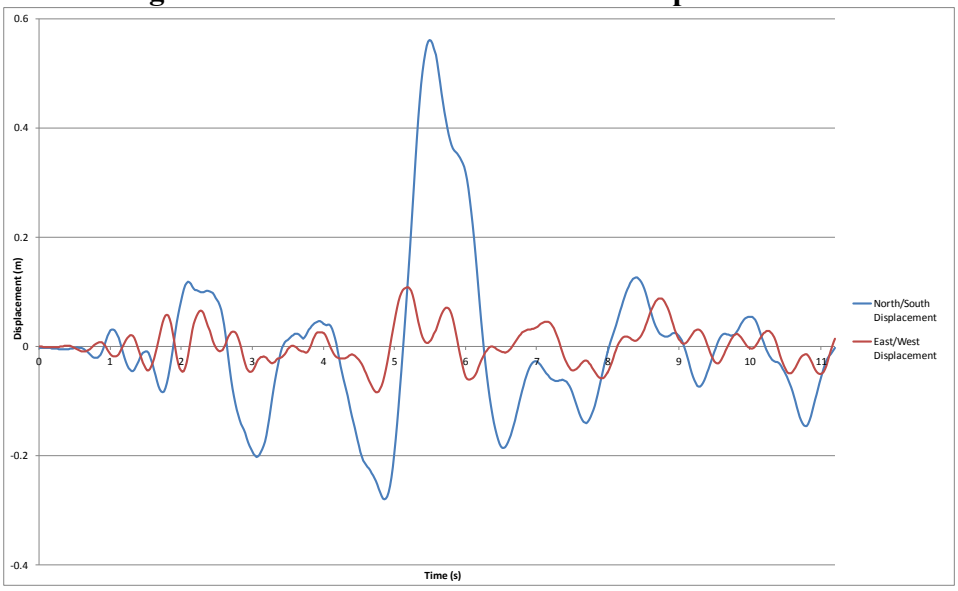

Figure H.2: Level 6 Northwest corner displacements.

As can be seen in Figure H.2 above a significant increase in the northward building displacement is observed in the northwest corner of the building between 5.2 and 6.1 seconds of the record. This occurs after the tension ties capacities on levels 4 to 6 of the core are exceeded allowing increased building rotation clockwise from west to north. The peak displacement corresponds to a clockwise rotation in conjunction with a net northward building translation Table H.1 presents the sequence of failure of the north core wall ties throughout the record.

Table H.1: Wall D and D/E diaphragm disconnection times.

Level	Wall D Failure (sec)	Wall D/E Failure (sec)
6	1.96	1.52
5	2.90	1.54
4	1.60	1.52

Inter-storey displacements for the perimeter frame lines A and F in the north/south direction are presented in Figure H.3 and Figure H.4 below. North core tie tensile failure is identified on the plots for reference.

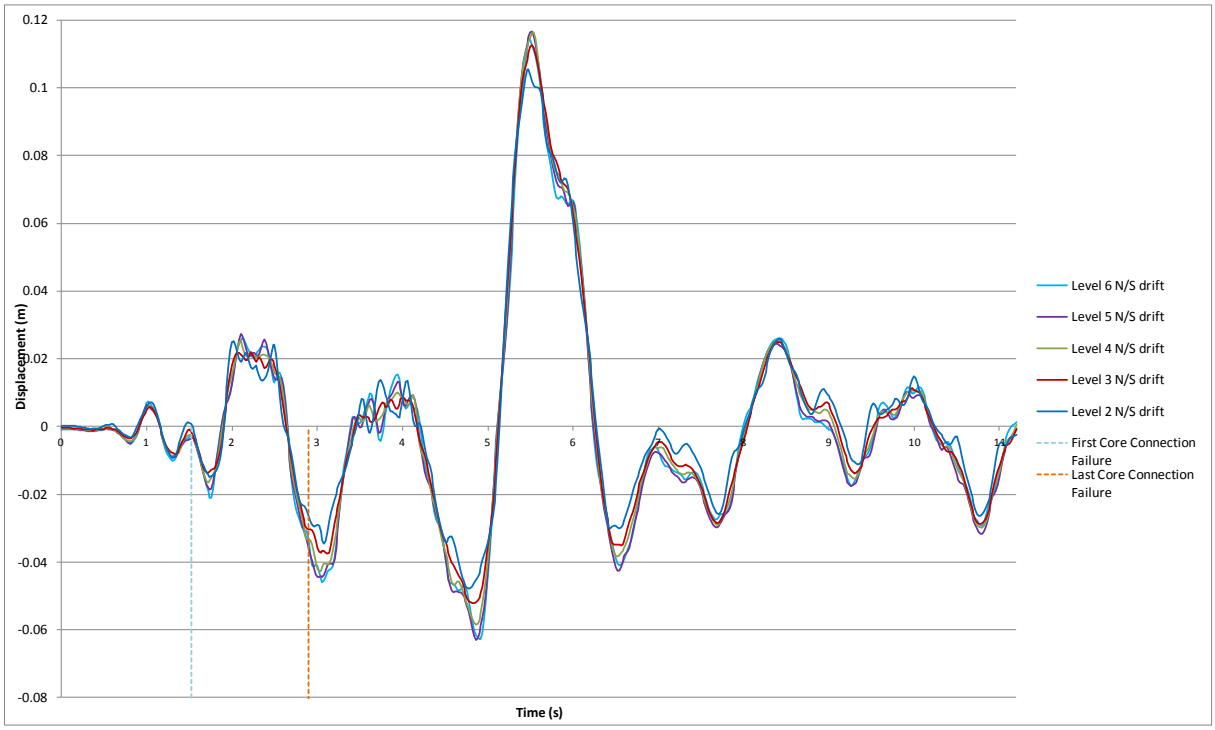

Figure H.3: Frame A north/south inter-storey displacements.

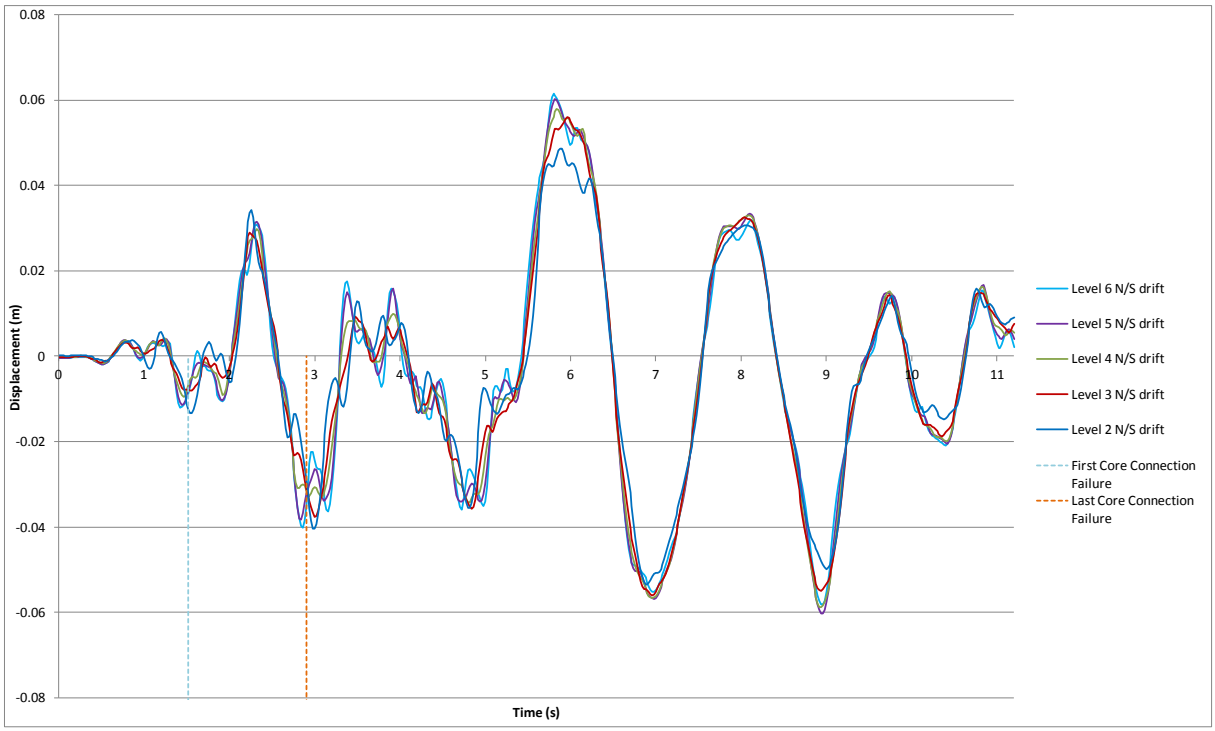

Figure H.4: Frame F north/south inter-storey displacements.

Inter-storey displacements for the perimeter frame lines 1 and 4 in the East/West direction are presented in Figure H.5, and Figure H.6 below.

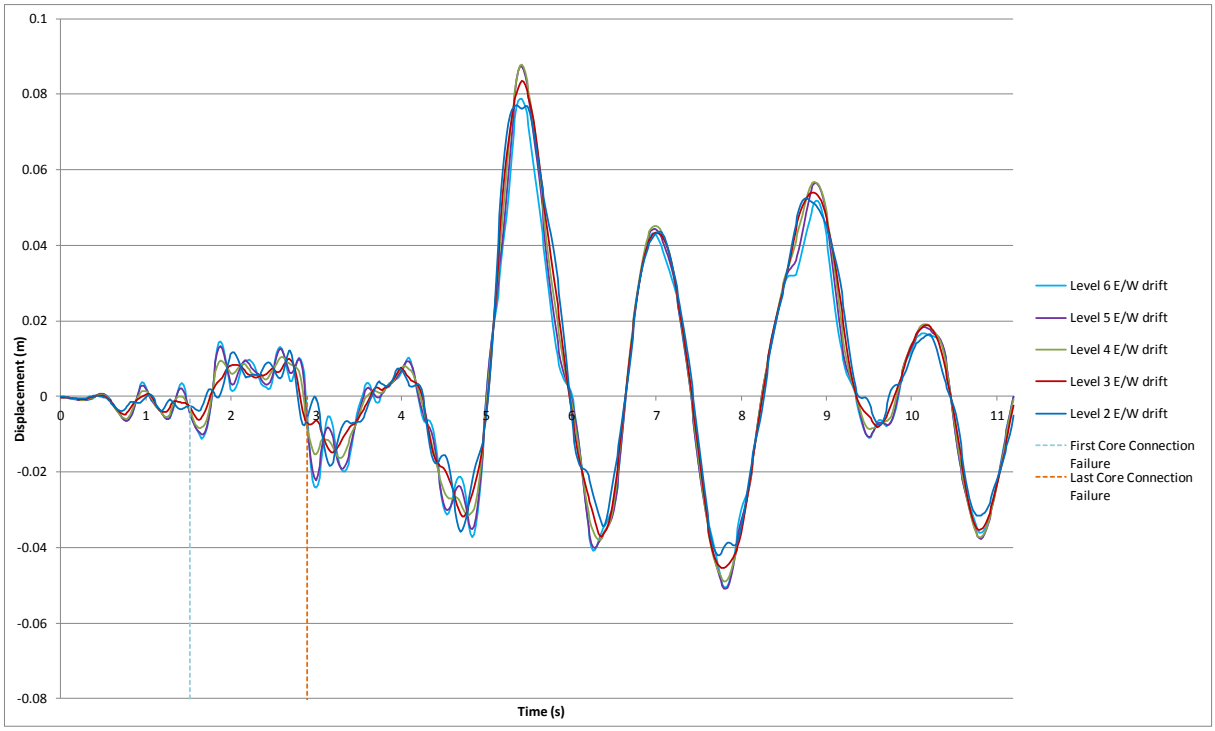

Figure H.5: Frame 1 east/west inter-storey displacements.

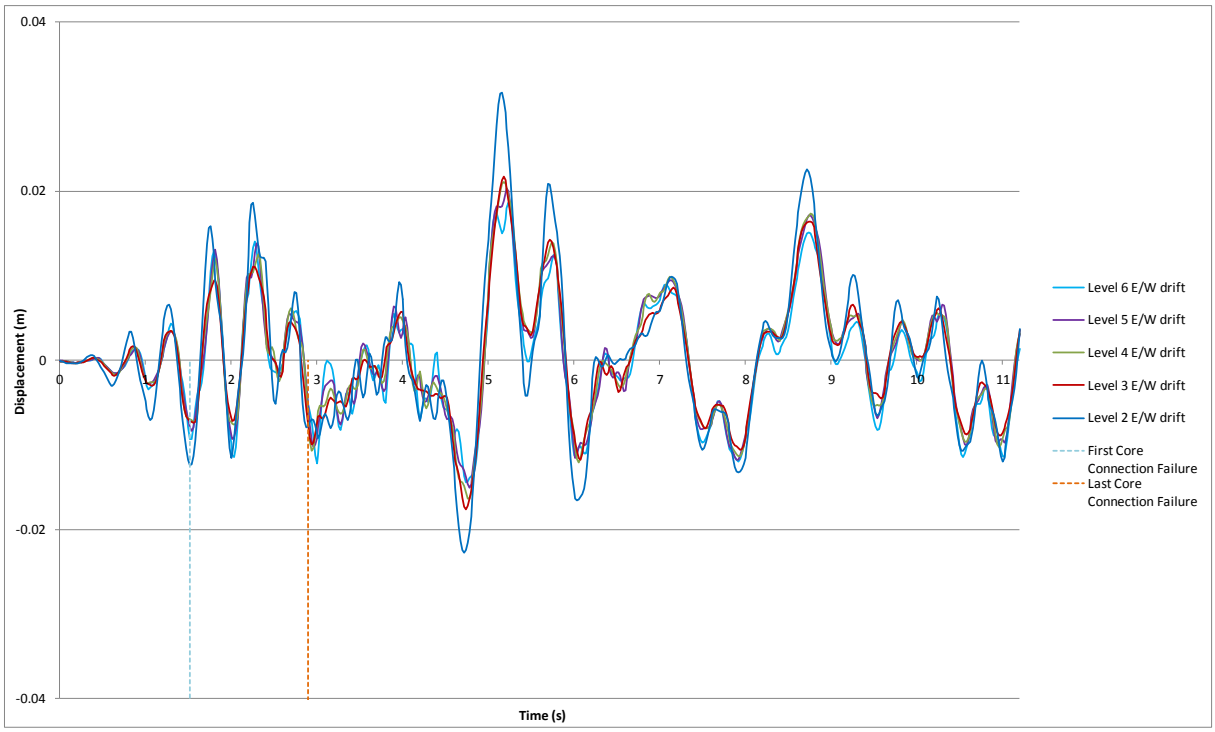

Figure H.6: Frame 4 east/west inter-storey displacements.

H.2 Diaphragm Connection Forces

Diaphragm connection forces are presented in Figure H.7 to Figure H.18 below. Note that moments are reported about the geometric centroid of the element being considered.

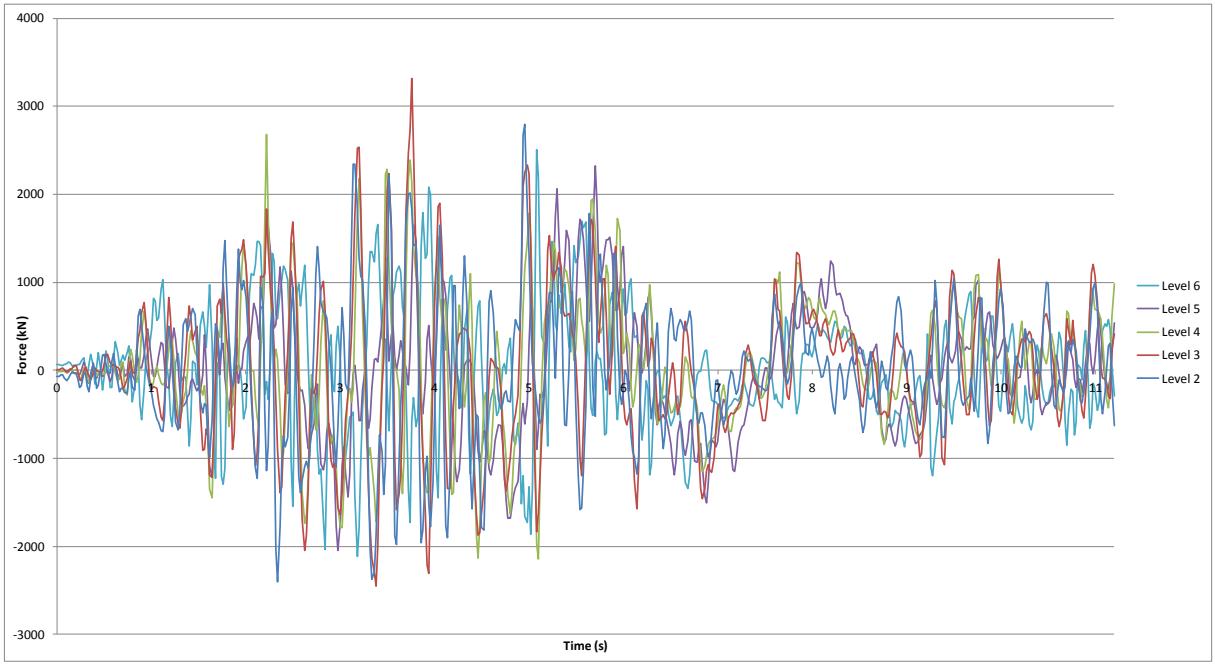

Figure H.7: North core total diaphragm north/south actions

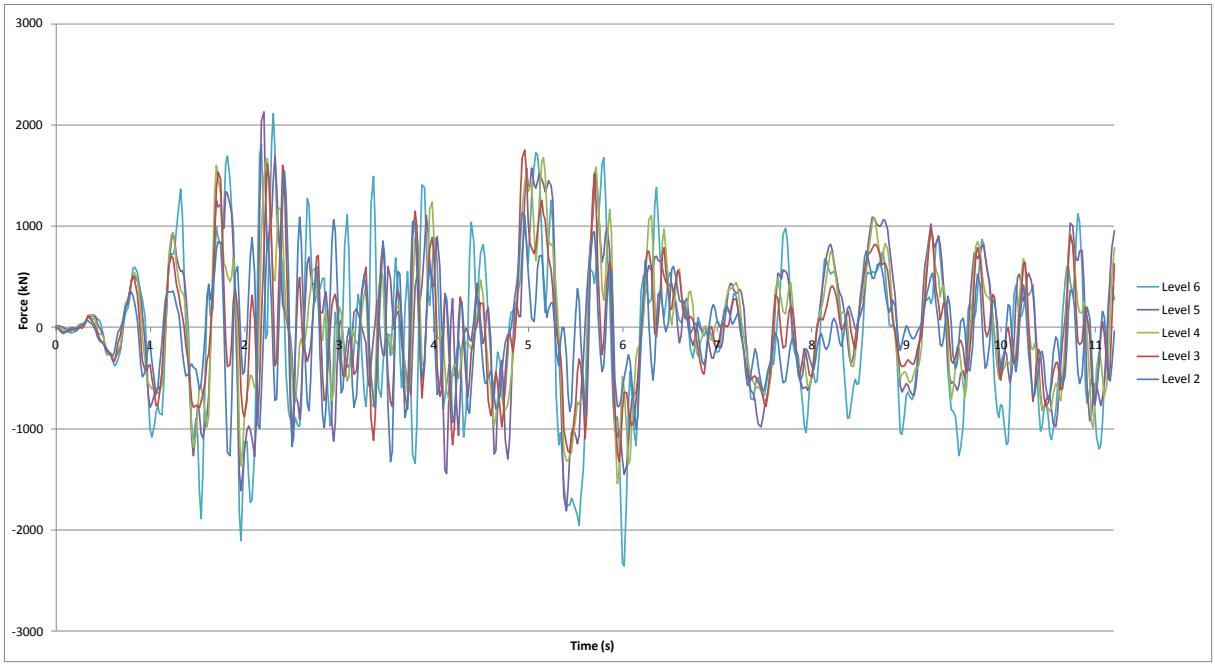

Figure H.8: North core total diaphragm east/west actions

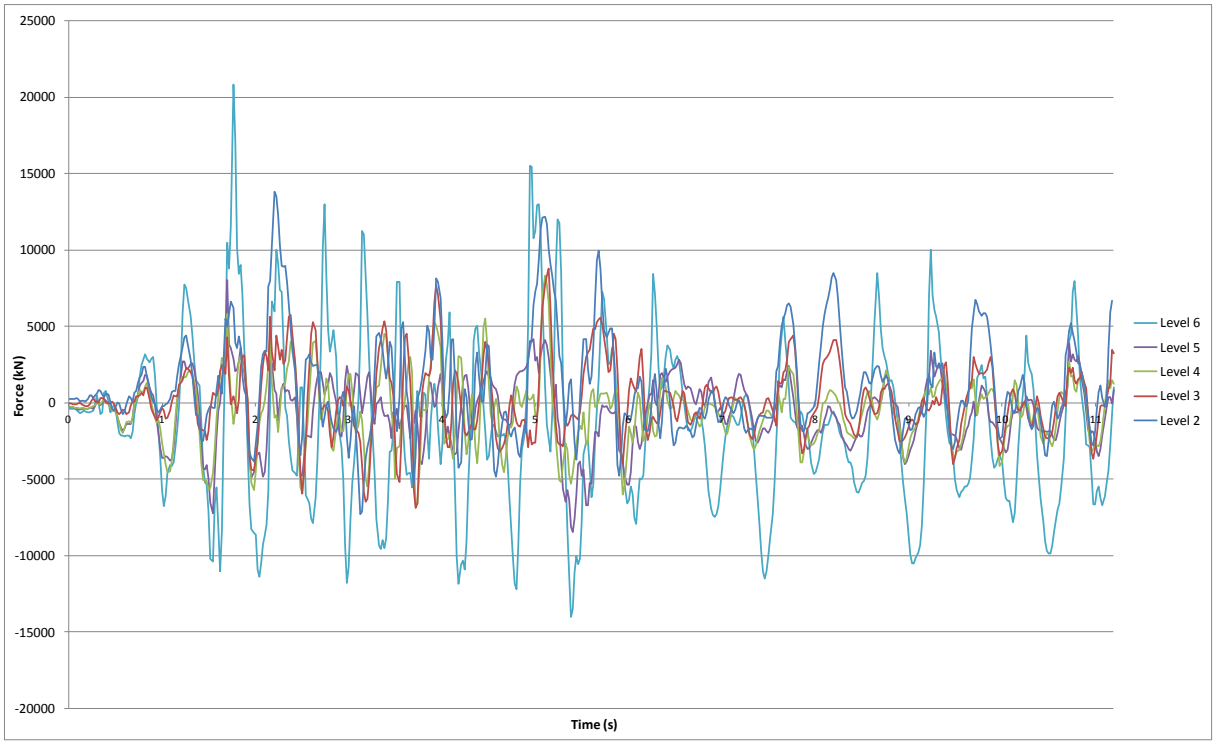

Figure H.9: North core total diaphragm in-plane moments

Figure H.10: North core Wall C diaphragm north/south actions

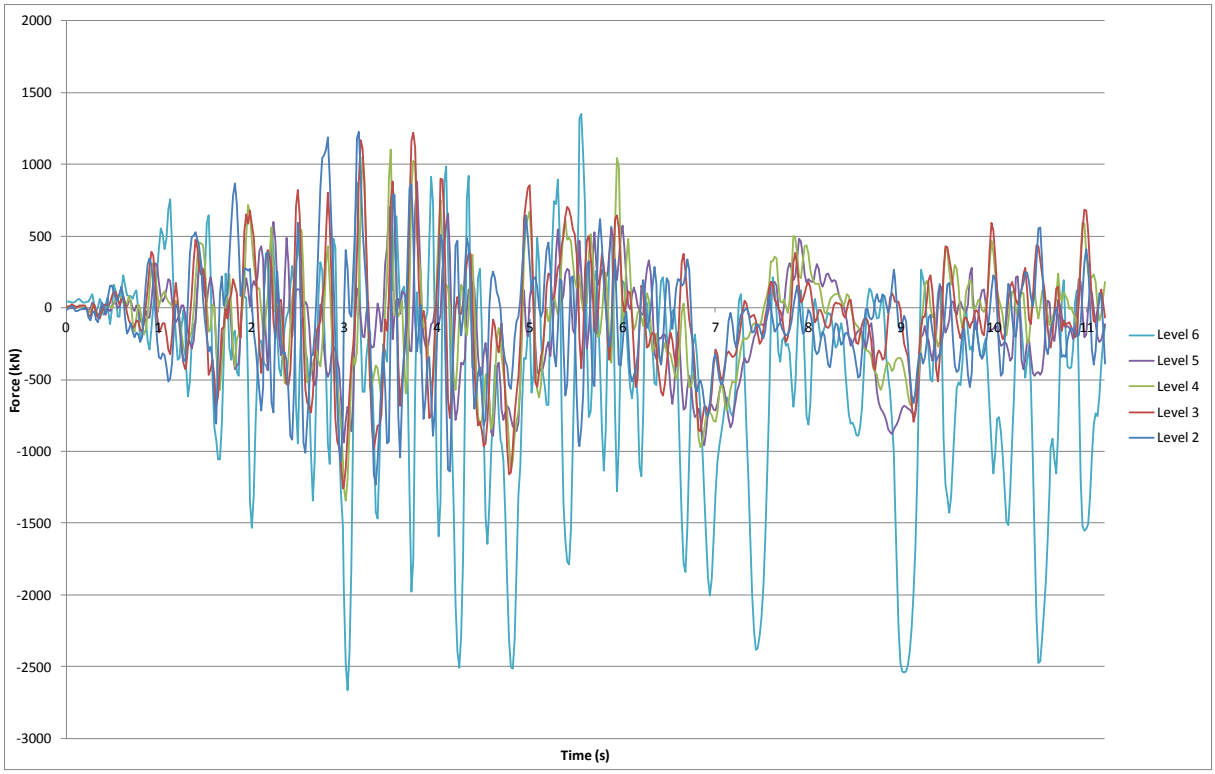

Figure H.11: North core Wall C/D diaphragm north/south actions.

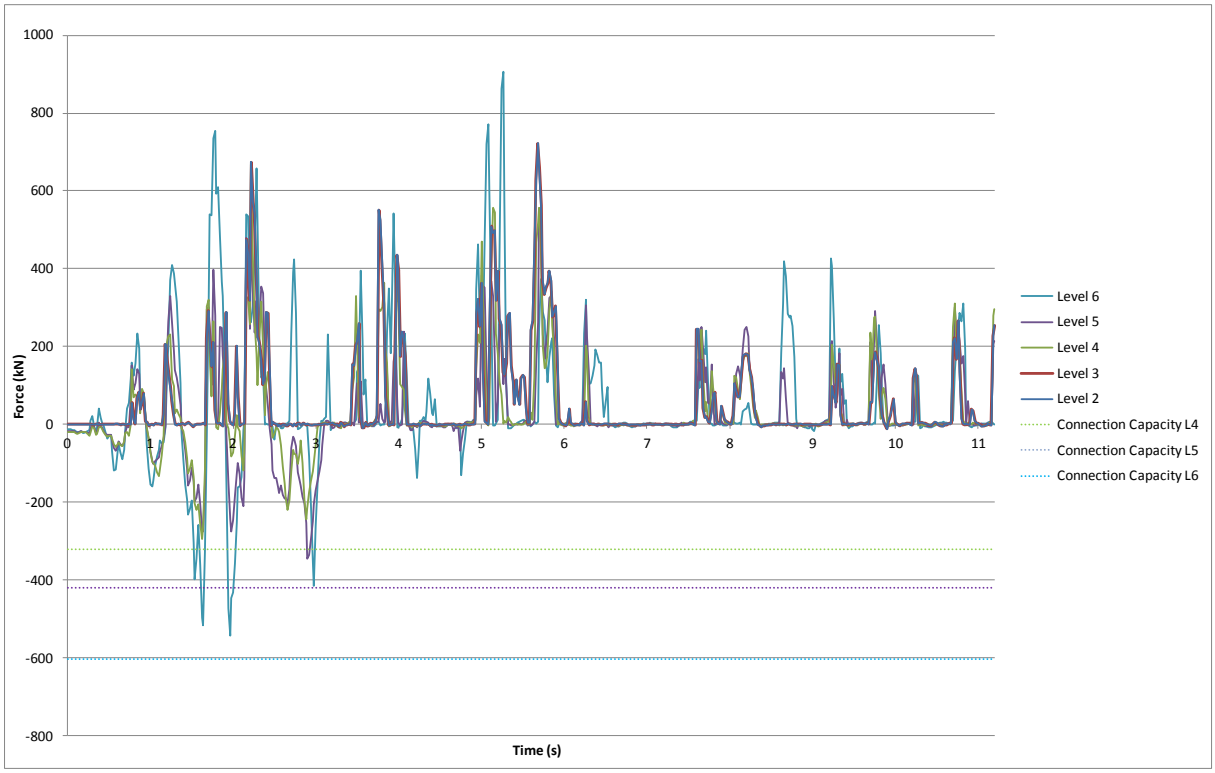

Figure H.12: North core Wall D diaphragm north/south actions.

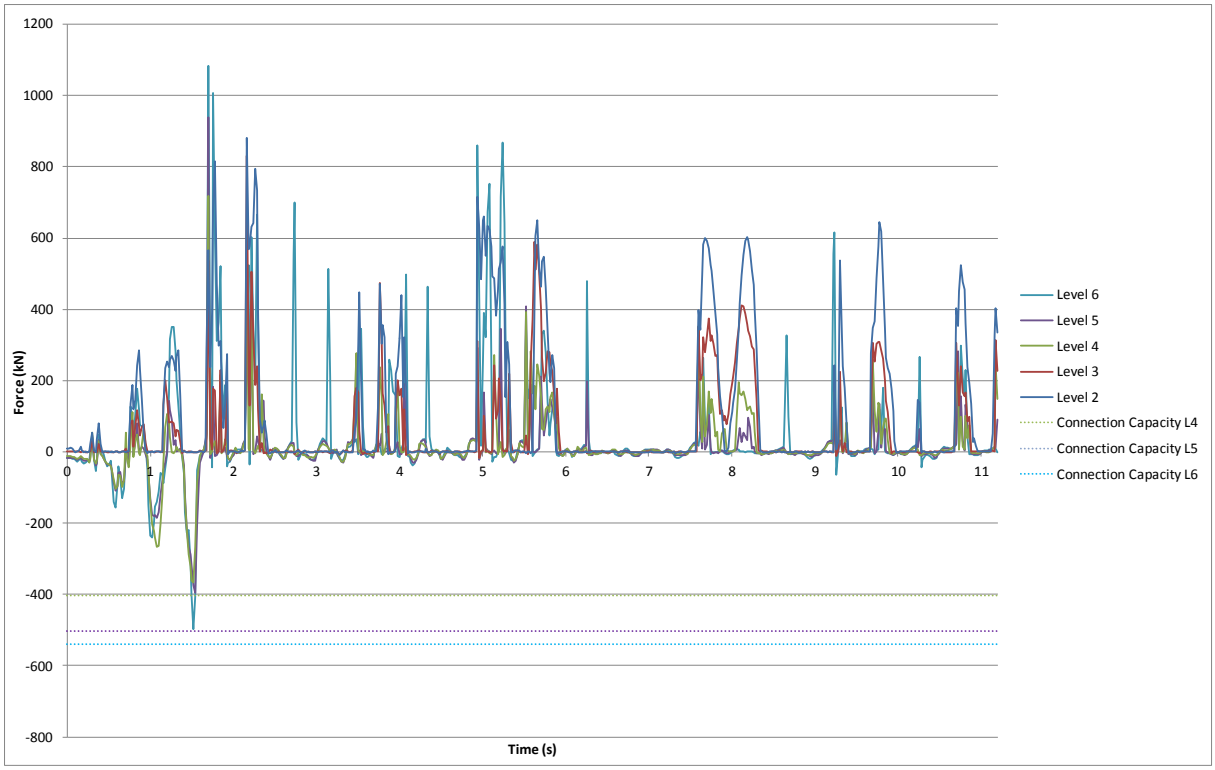

Figure H.13: North core Wall D/E diaphragm north/south actions.

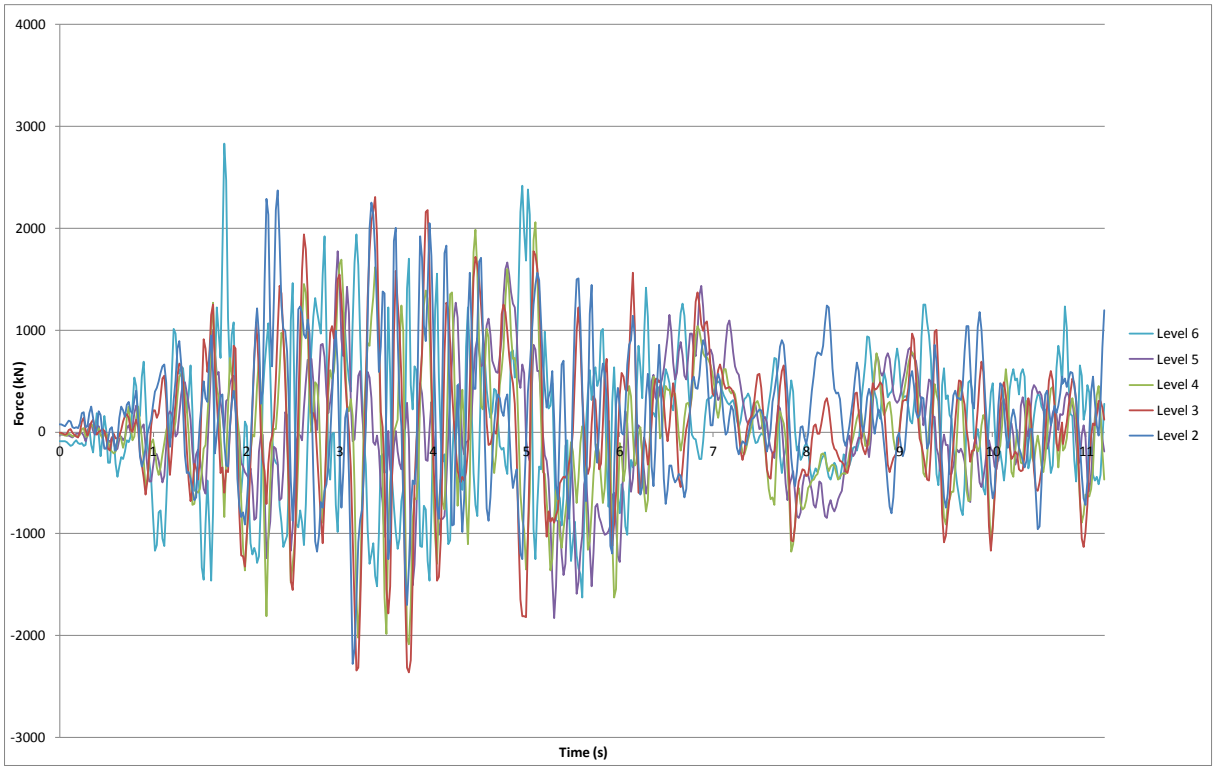

Figure H.14: North core Slab 4/C to C/D diaphragm north/south actions.

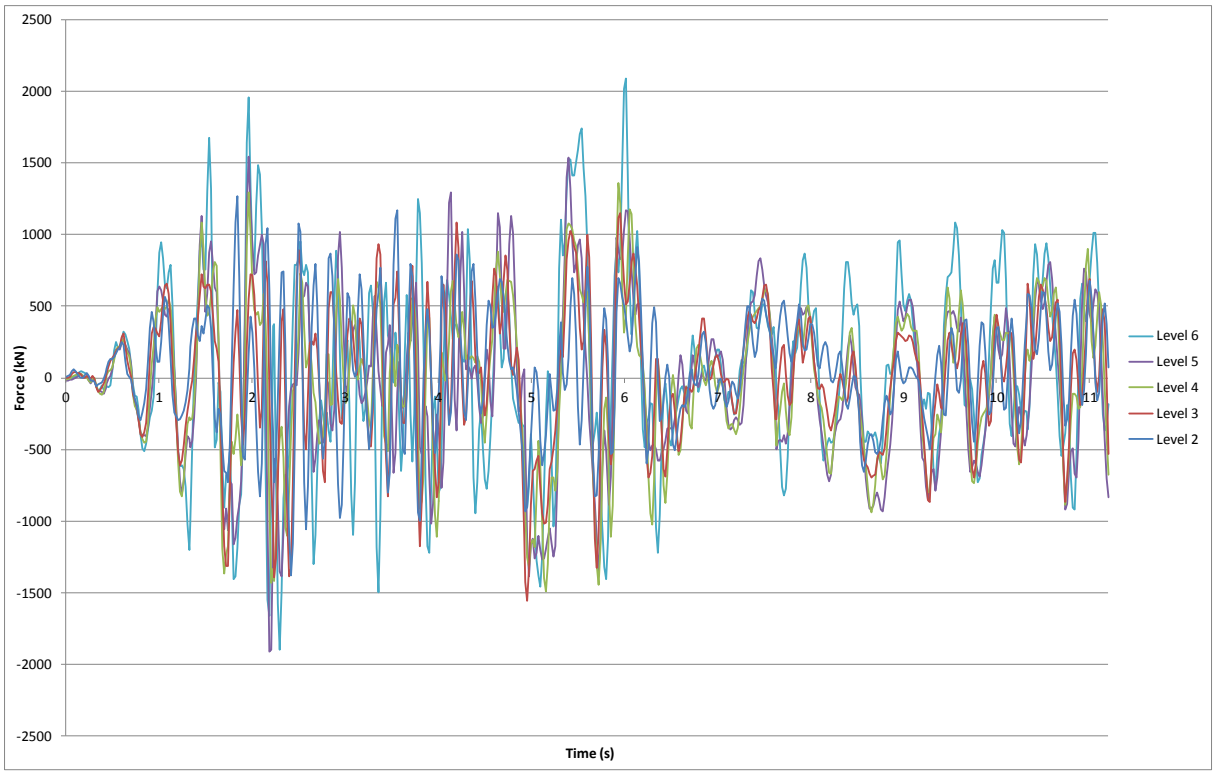

Figure H.15: North core Slab 4/C to C/D diaphragm east/west actions.

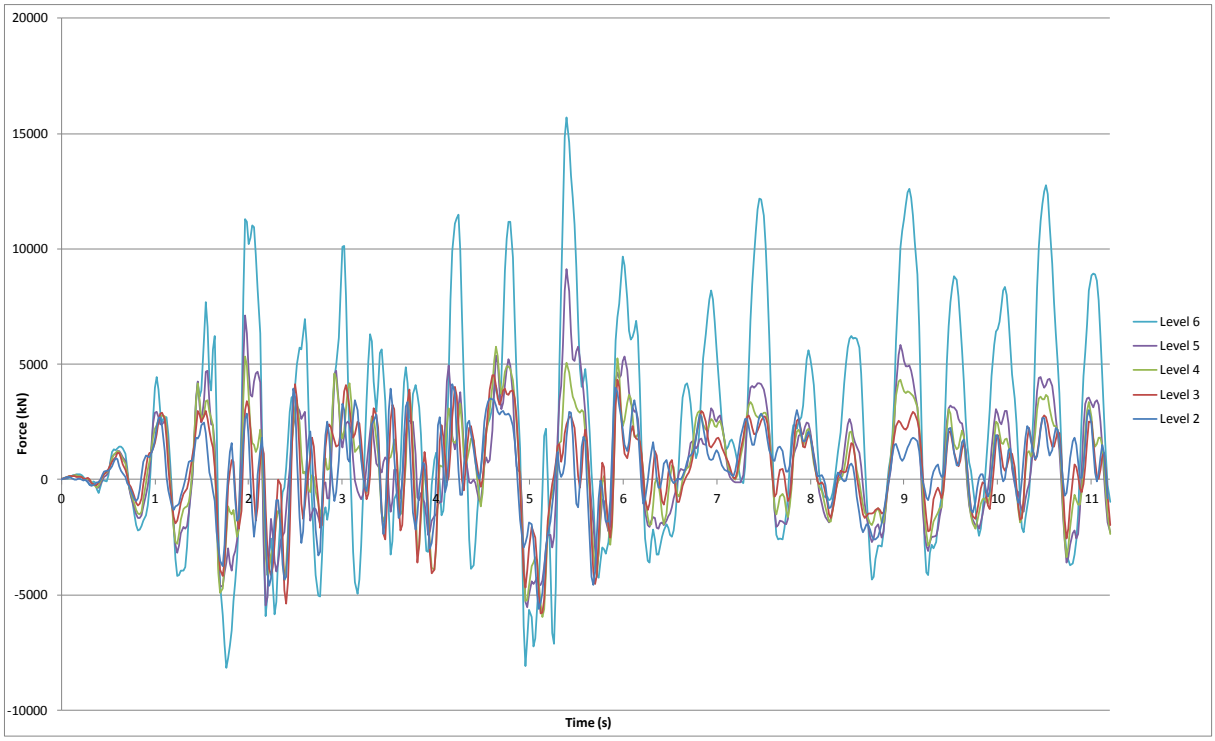

Figure H.16: North core Slab 4/C to C/D diaphragm in-plane moments.

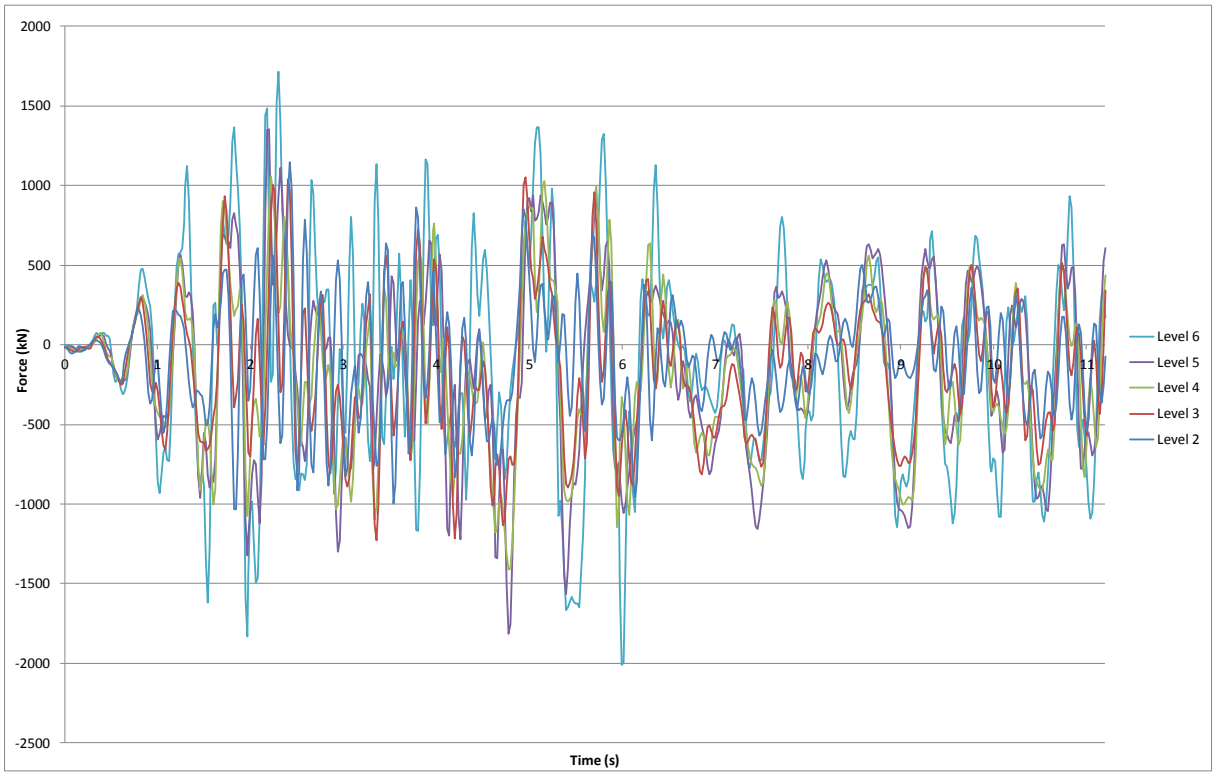

Figure H.17: North core Wall 5 diaphragm east/west actions.

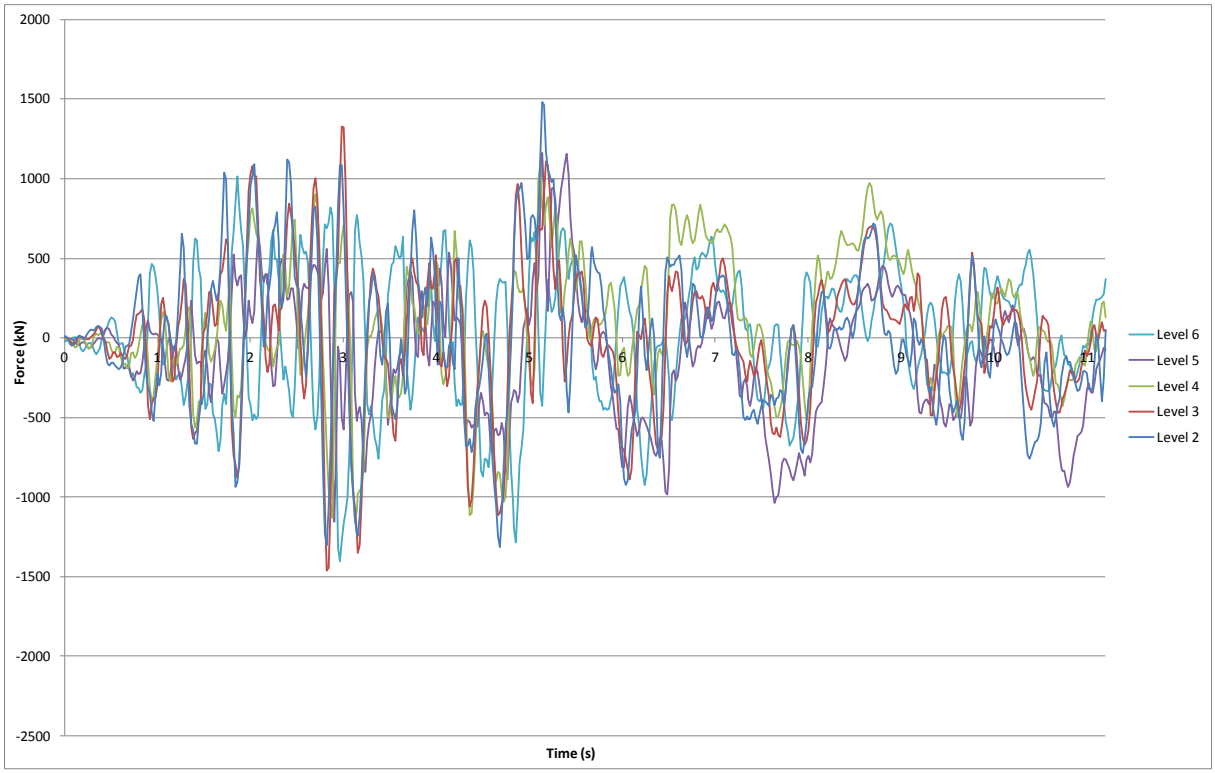

Figure H.18: South wall diaphragm east/west actions.

Appendix I :Analysis Results - Lyttelton Event: CBGS Record Model A & Model B

The following shows a comparison in the structural actions between Model A and Model B reported by the analysis as a function of time, for the Lyttelton event using the acceleration time history recorded at the CBGS station (using all components of the record). Note that to reduce analysis time only 4.84 seconds of Model B has been run, however the results are suitable for the purposes of comparison. At the end of the recorded time steps the masonry has degraded in strength and stiffness significantly (to approximately 40% of its initial strength at level 3, 60% at level 2, and 67% at level 1). It is expected that the performance of the building would converge to that predicted for Model A (no masonry) upon further degradation of the masonry strength and stiffness.

I.1 Building Displacements and Drifts.

Building Level 6 displacements are presented in Figure I.1 and Figure I.2 below for the Southeast and Northwest corners of the building respectively.

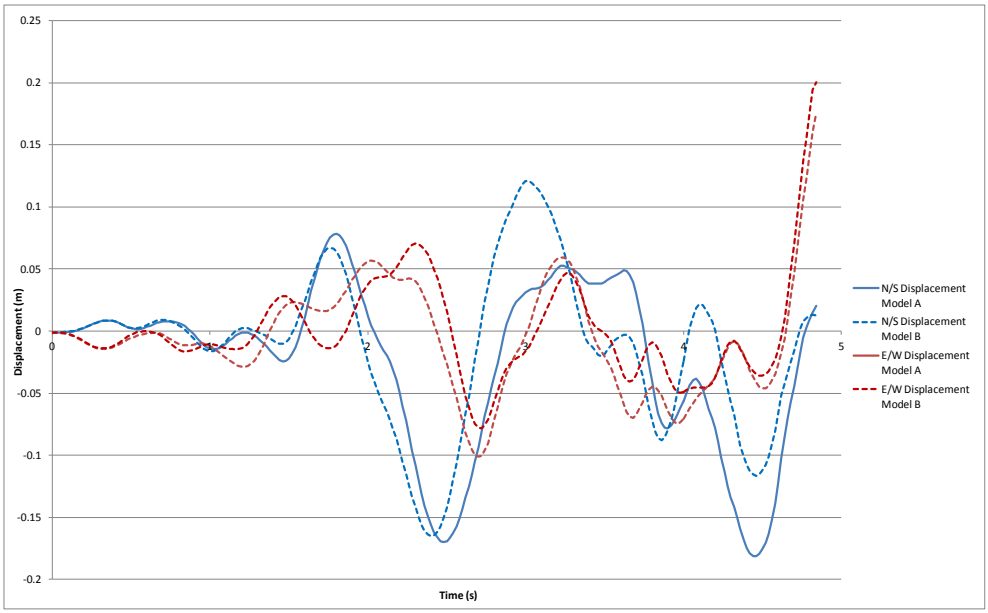

Figure I.1: Level 6 Southeast corner displacements.

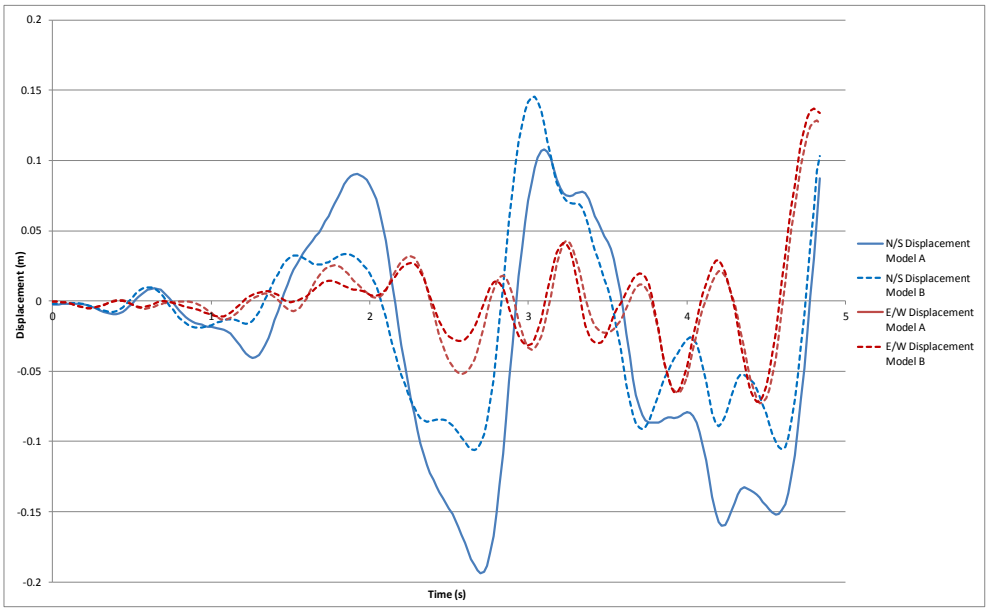

Figure I.2: Level 6 Northwest corner displacements.

Inter-storey displacements for the perimeter frame lines A and F in the north/south direction are presented in Figure I.3, and Figure I.4 below. For the purposes of comparison, plots contain both Model A and Model B inter-storey displacements.

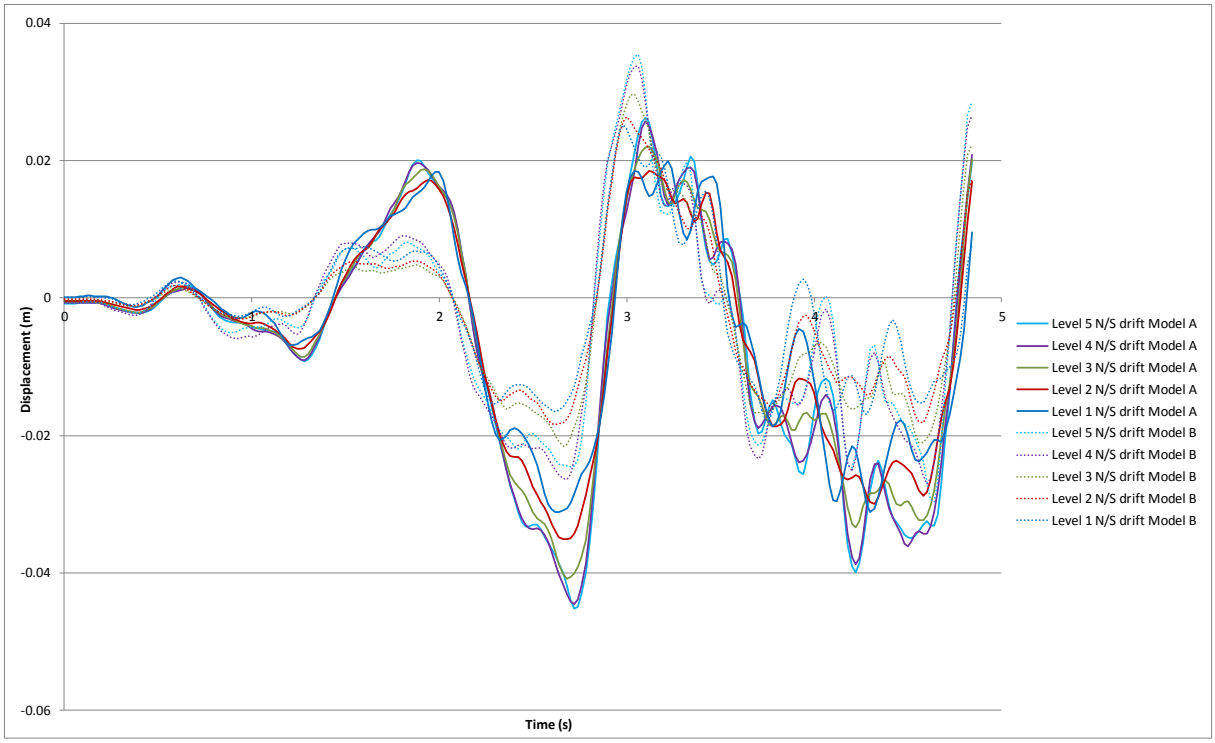

Figure I.3: Frame A north/south inter-storey displacements.

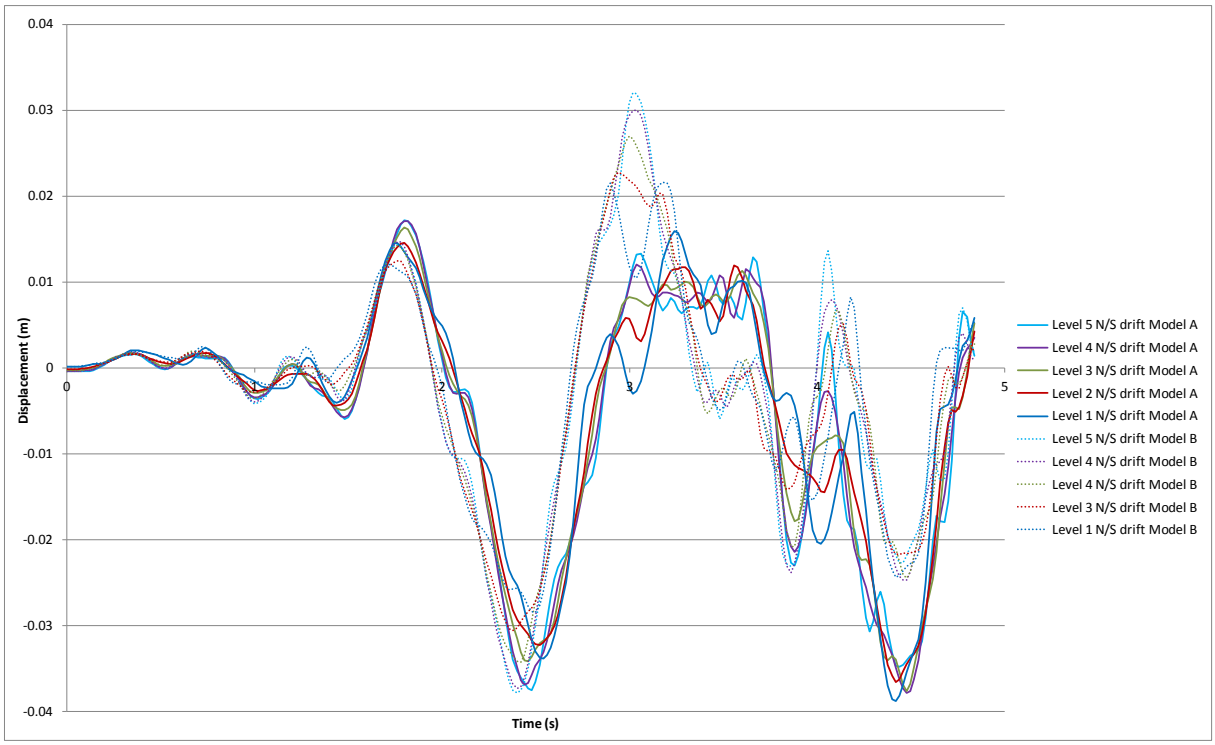

Figure I.4: Frame F north/south inter-storey displacements.

Inter-storey displacements for the perimeter frame lines 1 and 4 in the east/west direction are presented in Figure I.5, and Figure I.6 below. For the purposes of comparison, plots contain both Model A and Model B inter-storey displacements.

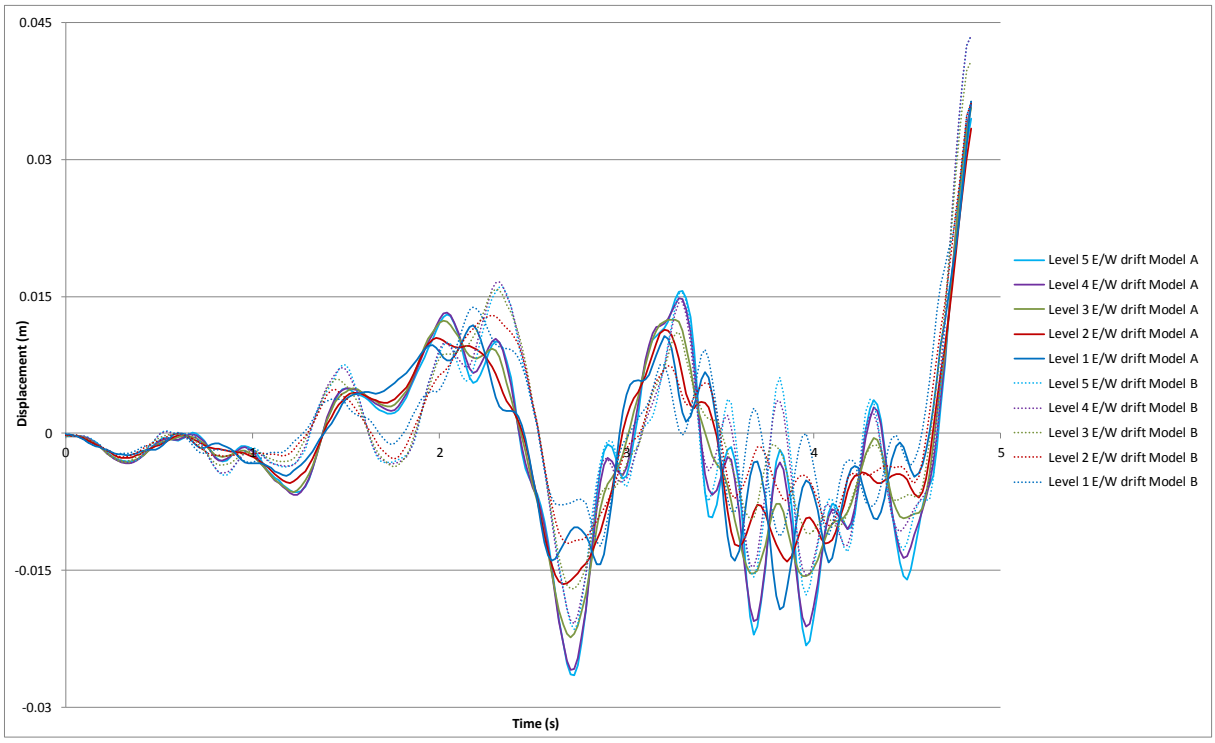

Figure I.5: Frame 1 east/west inter-storey displacements.

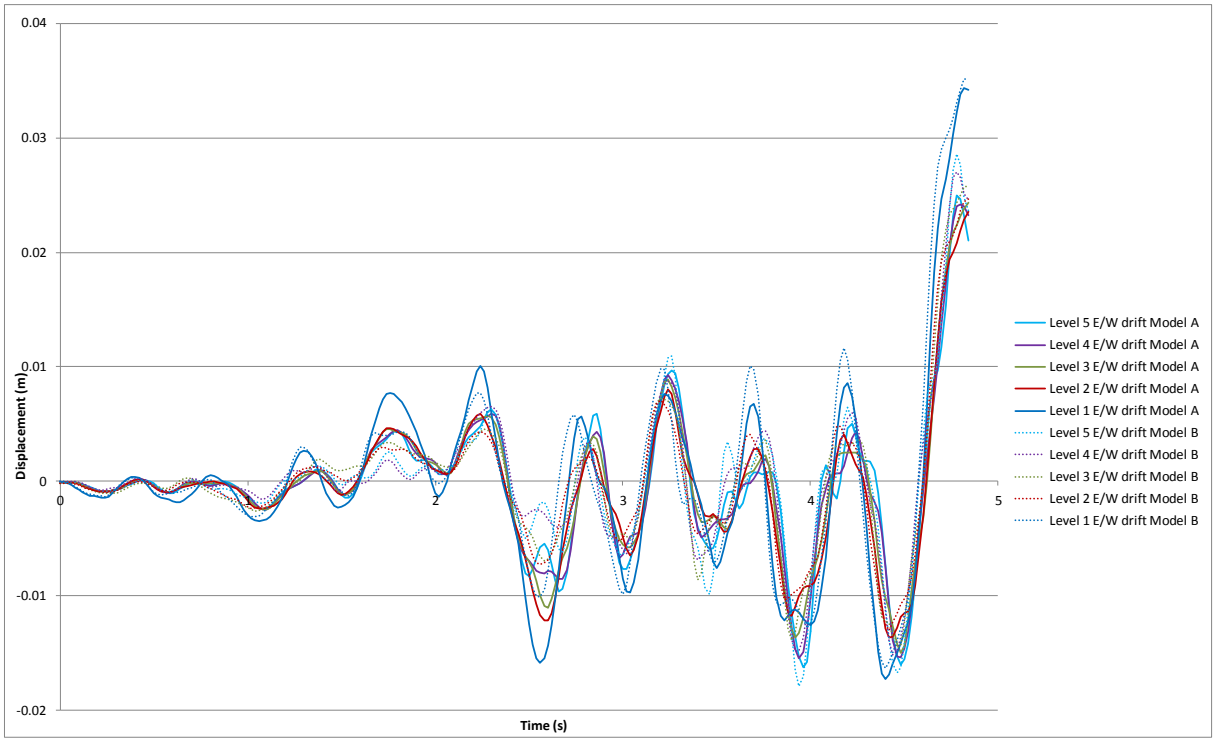

Figure I.6: Frame 4 east/west inter-storey displacements.

I.2 Column Hinge Progression.

Figure I.7 highlights the hinge progression in the columns for the two models considered. As can be seen the two models predict similar numbers of columns hinging, with Model A predicting slightly more hinges prior to 4.5 seconds and Model B predicting slightly more after 4.5 seconds.

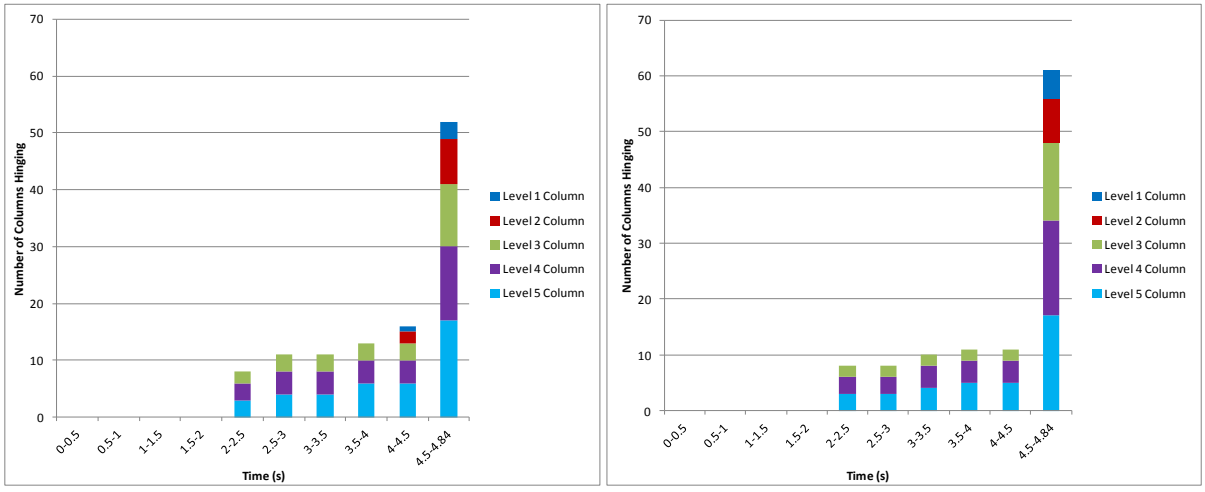

Figure I.7: Column hinge progression - Model A left, Model B right.

I.3 Diaphragm Connection Forces

Diaphragm connection forces are presented in Figure I.8 to Figure I.19 below. Note that moments are reported about the geometric centroid of the element being considered.

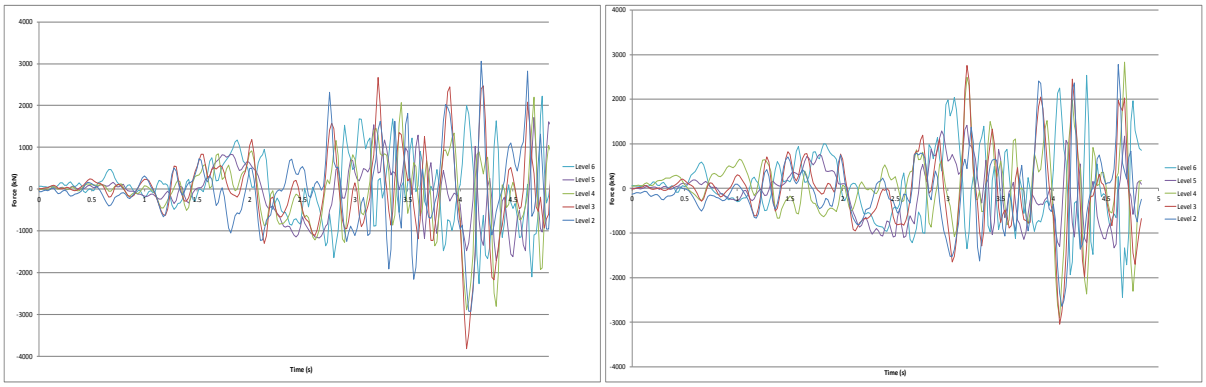

Figure I.8: North core total diaphragm north/south actions (no masonry left, with masonry right)

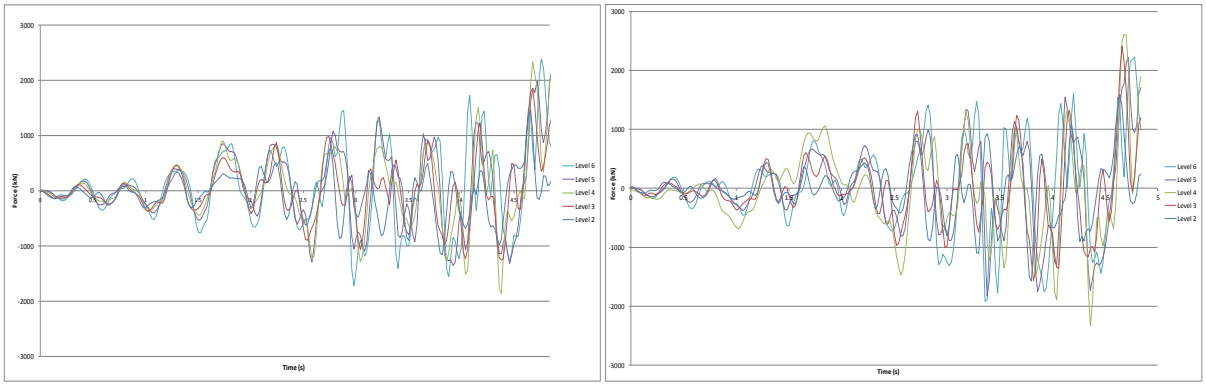

Figure I.9: North core total diaphragm east/west actions (no masonry left, with masonry right)

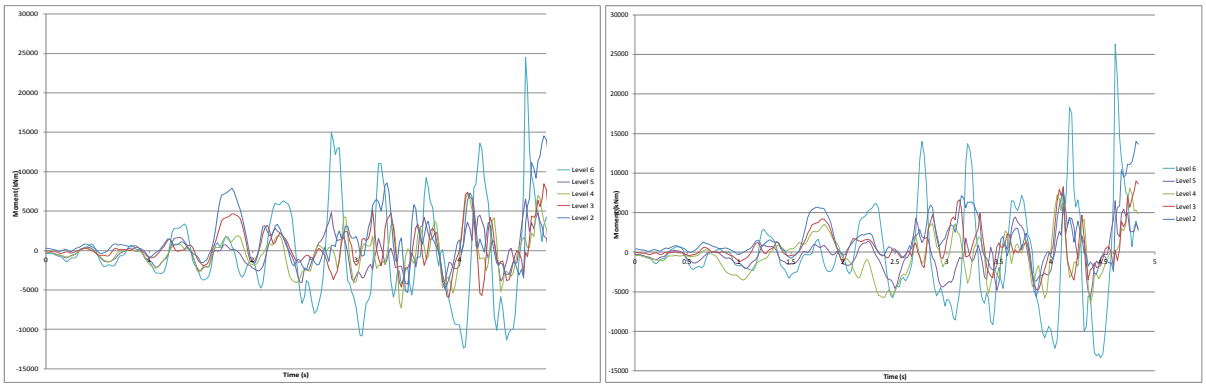

Figure I.10: North core total diaphragm in-plane moments (no masonry left, with masonry right)

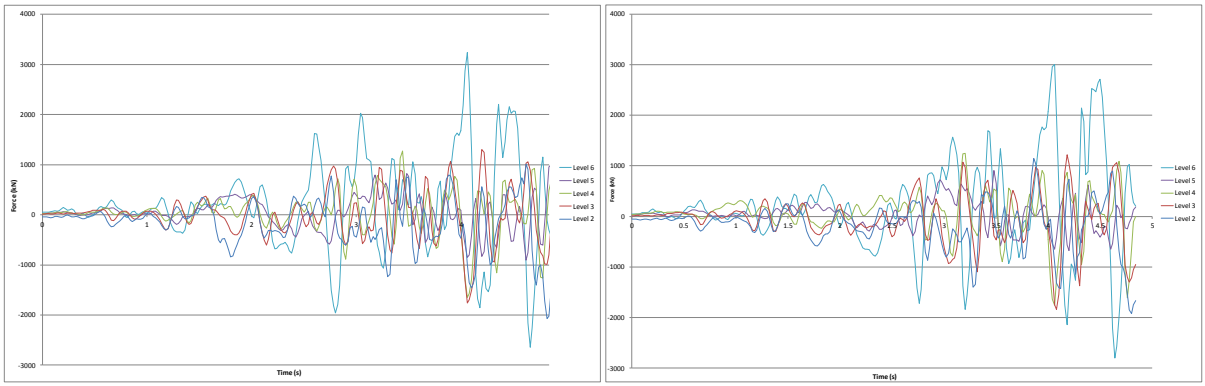

Figure I.11: North core Wall C diaphragm north/south actions (no masonry left, with masonry right)

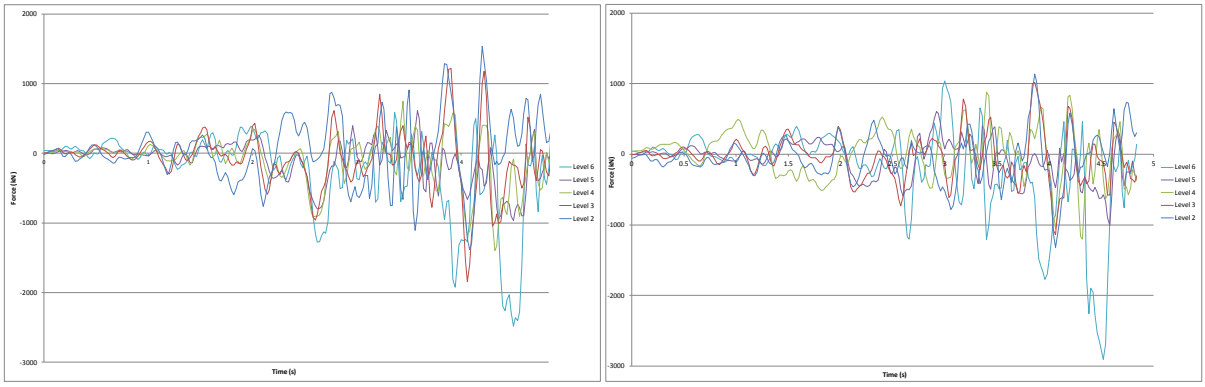

Figure I.12: North core Wall C/D diaphragm north/south actions (no masonry left, with masonry right).

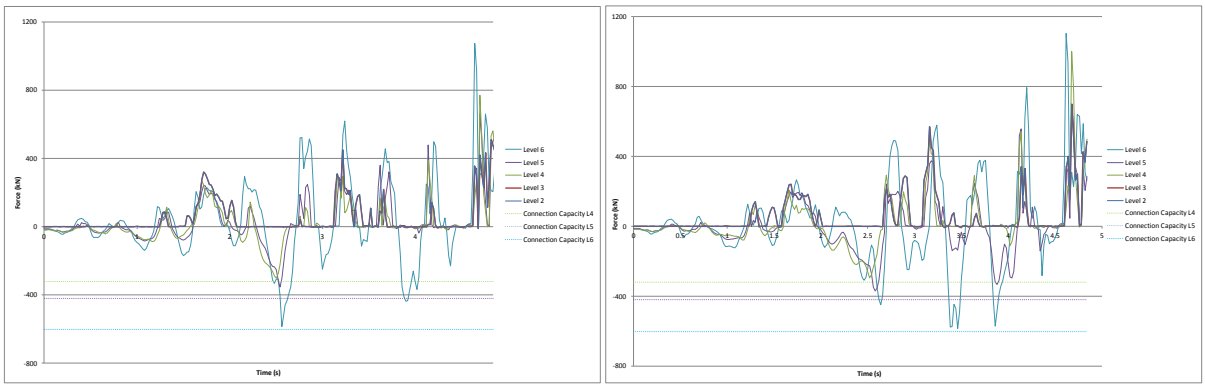

Figure I.13: North core Wall D diaphragm north/south actions (no masonry left, with masonry right).

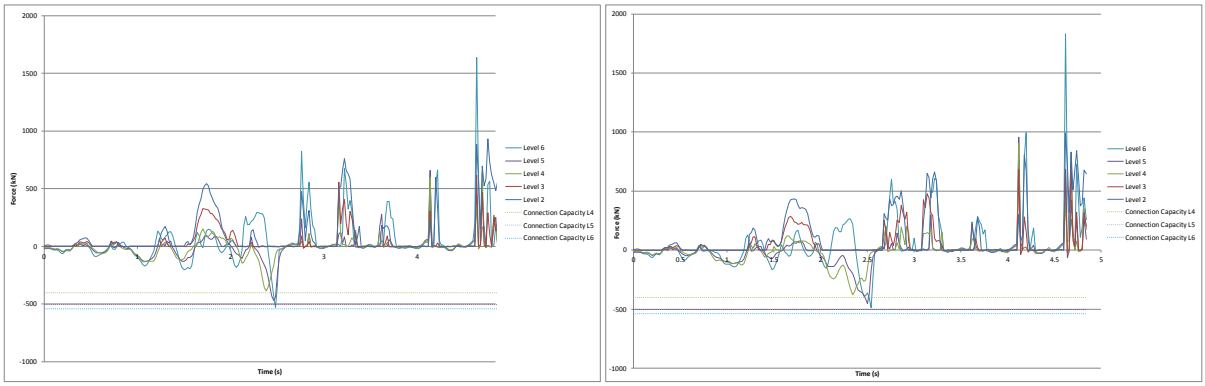

Figure I.14: North core Wall D/E diaphragm north/south actions (no masonry left, with masonry right).

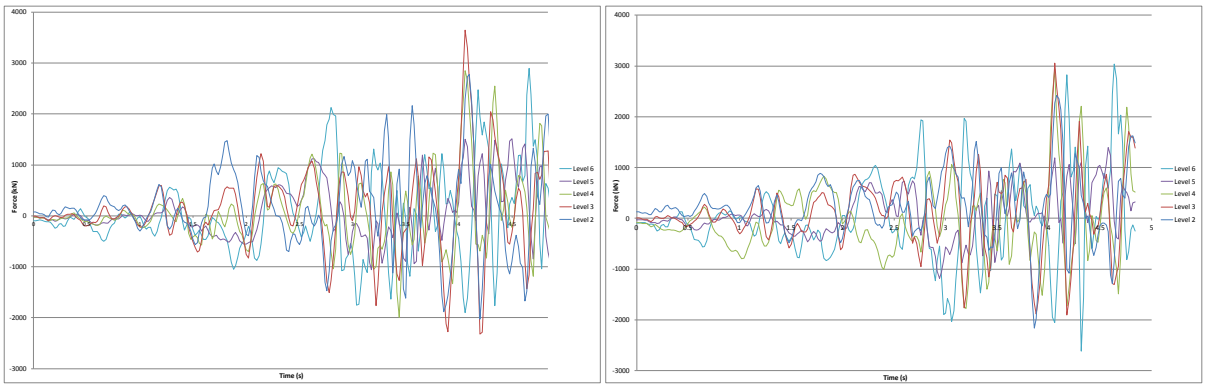

Figure I.15: North core Slab 4/C to C/D diaphragm north/south actions (no masonry left, with masonry right).

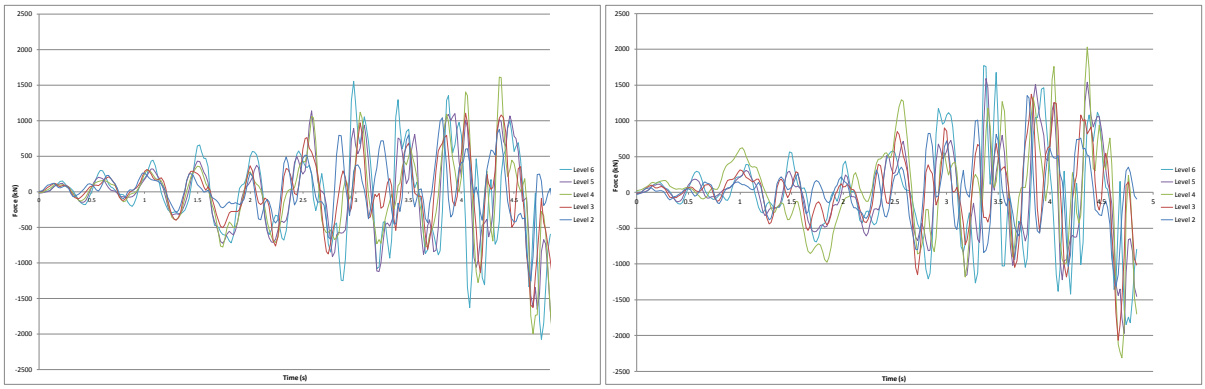

Figure I.16: North core Slab 4/C to C/D diaphragm east/west actions (no masonry left, with masonry right).

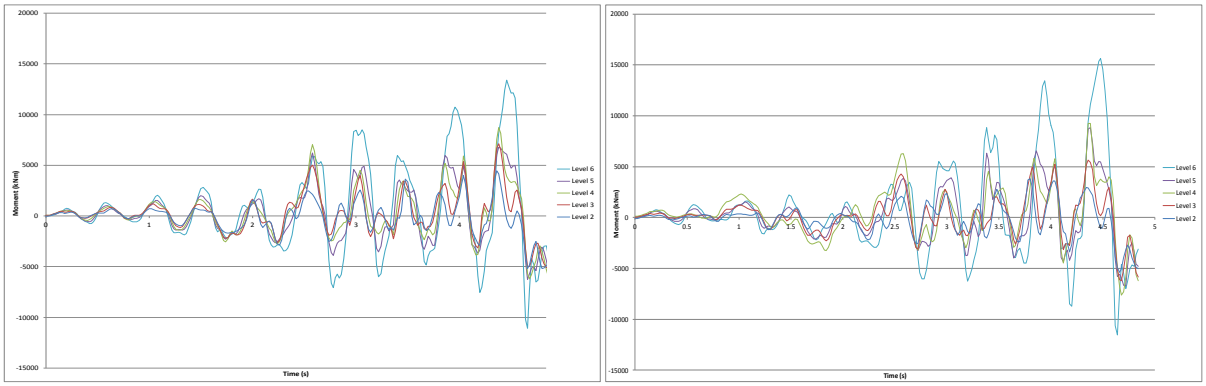

Figure I.17: North core Slab 4/C to C/D diaphragm in-plane moments (no masonry left, with masonry right).

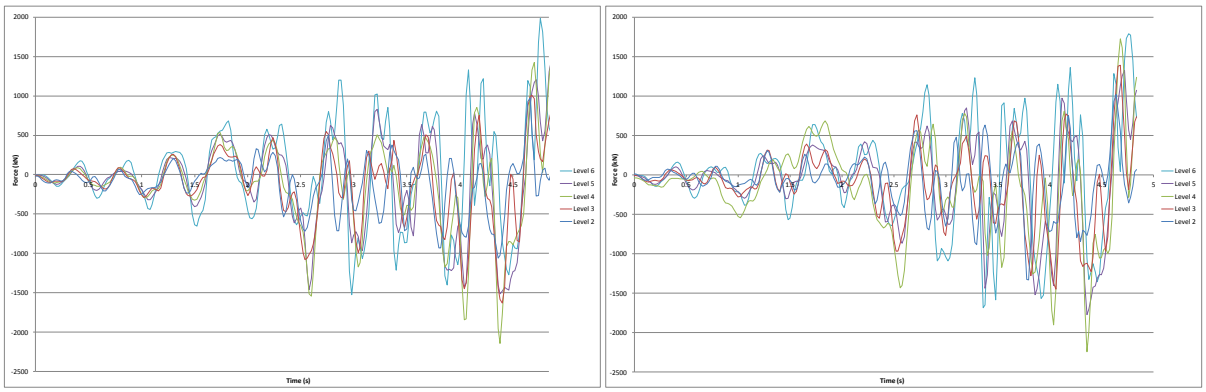

Figure I.18: North core Wall 5 diaphragm east/west actions (no masonry left, with masonry right).

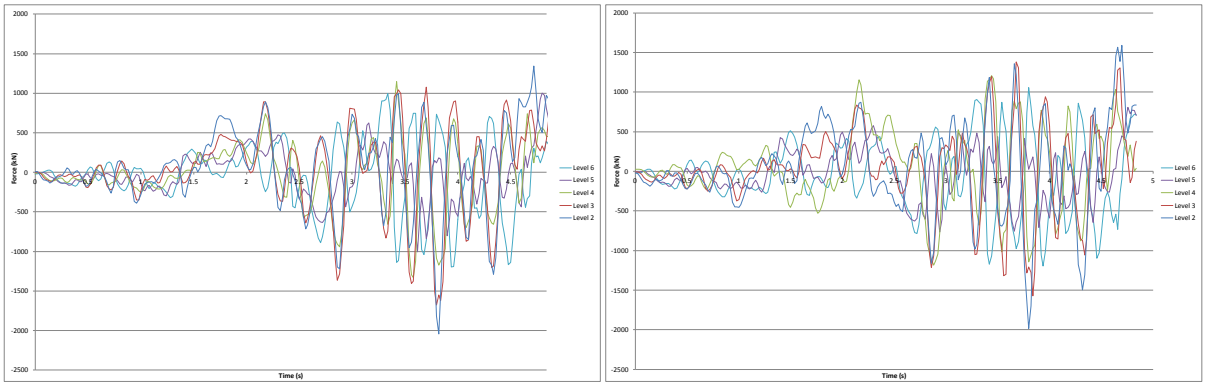

Figure I.19: South wall diaphragm east/west actions (no masonry left, with masonry right).

Appendix J :Analysis Results - Lyttelton: CBGS, Model A - No Diaphragm Disconnection

The following details the structural actions reported by the analysis as a function of time, for the Lyttelton event using the acceleration time history recorded at the CBGS station, assuming the diaphragm connections to the north core walls D and D/E cannot fail. Results for the case where disconnection can occur (as presented in Appendix F) have been included for the purposes of comparison.

J.1 Building Displacements and Drifts.

Building Level 6 displacements are presented in Figure J.1and Figure J.2 below for the Southeast and Northwest corners of the building respectively.

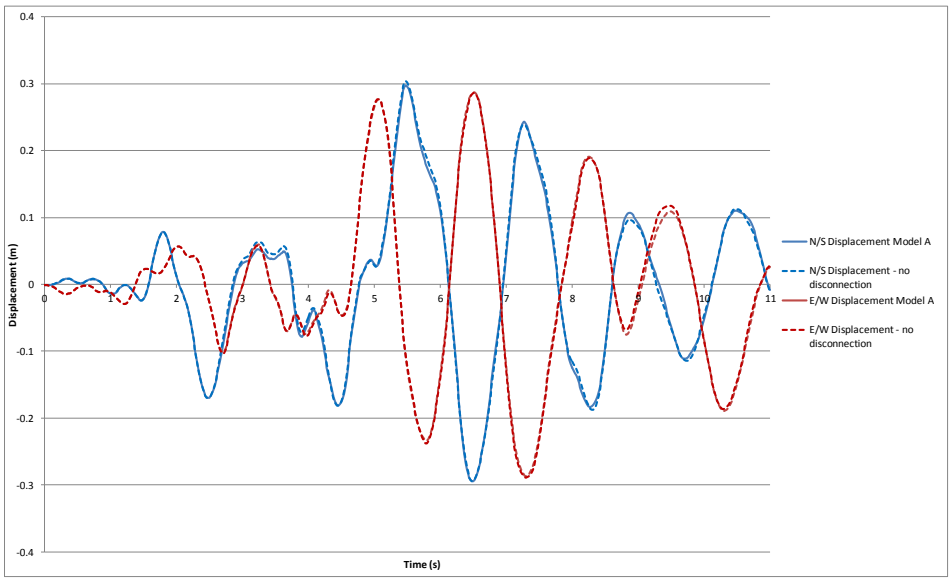

Figure J.1: Level 6 Southeast corner displacements.

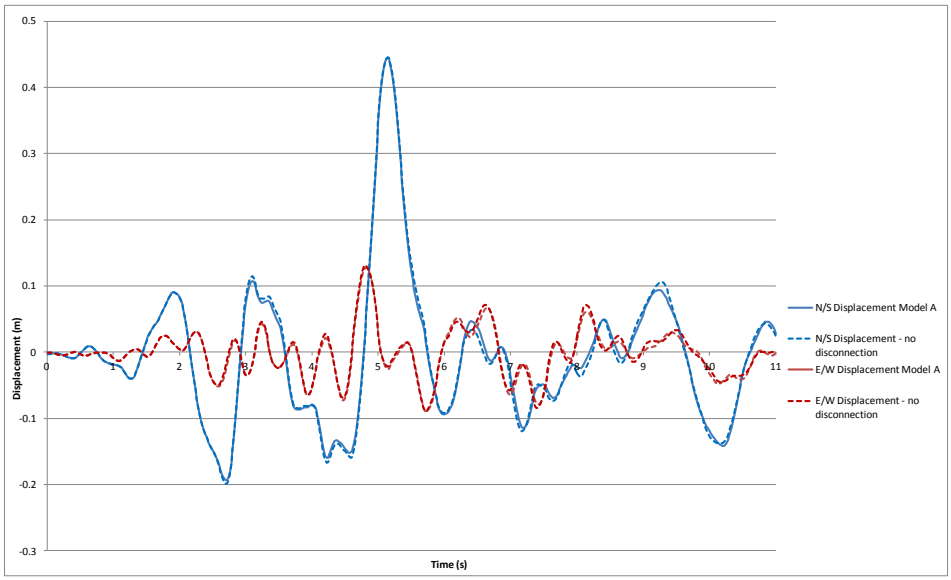

Figure J.2: Level 6 Northwest corner displacements.

Inter-storey displacements for the perimeter frame lines A and F in the north/south direction are presented in Figure J.3, and Figure I.4 below. For the purposes of comparison, plots contain both Model A inter-storey displacements and those obtained when the diaphragm connections are not permitted to disconnect.

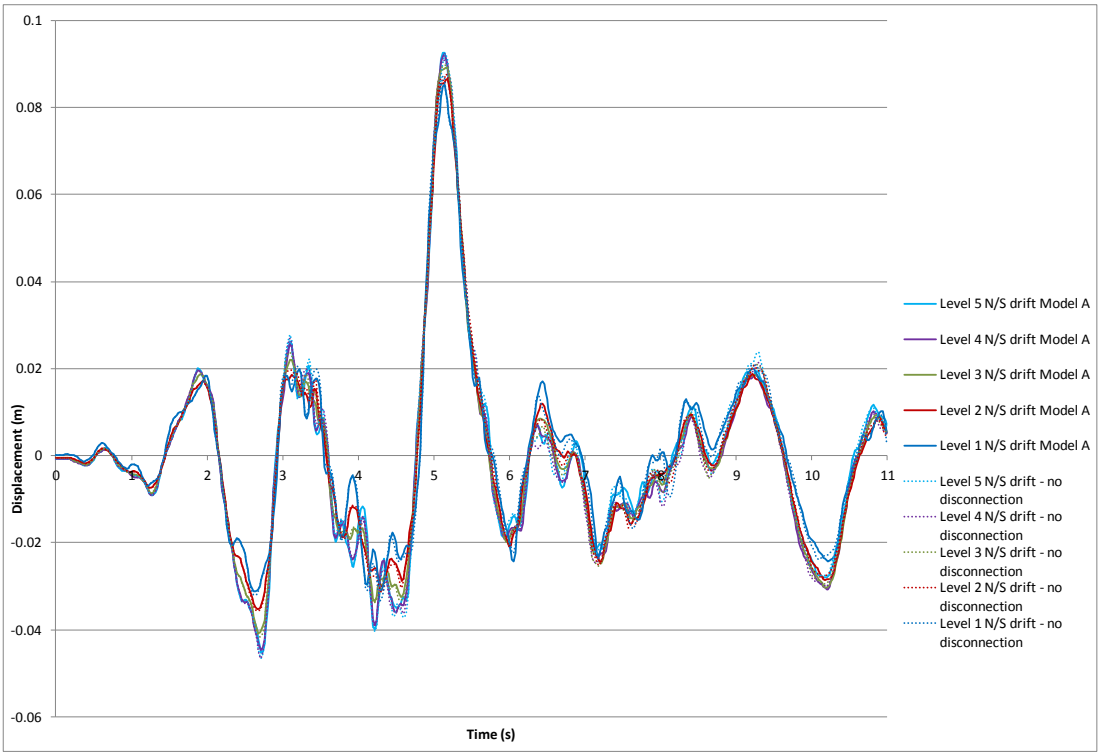

Figure J.3: Frame A north/south inter-storey displacements.

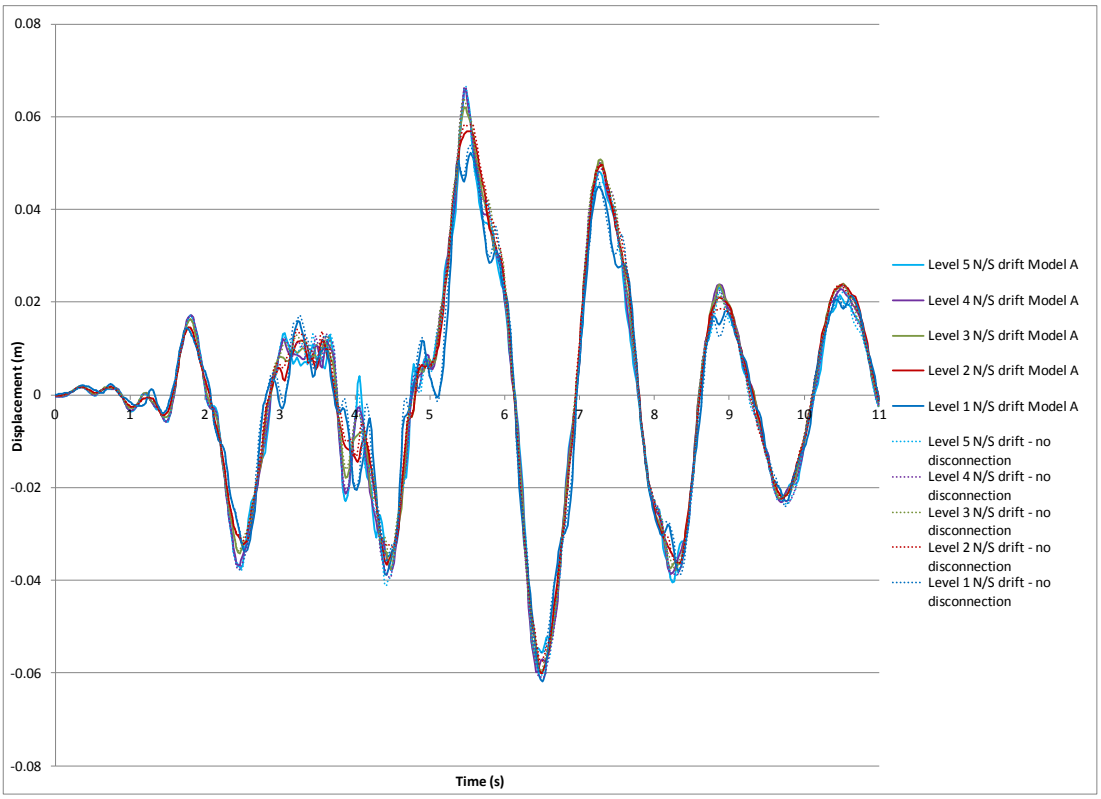

Figure J.4: Frame F north/south inter-storey displacements.

Inter-storey displacements for the perimeter frame lines 1 and 4 in the east/west direction are presented in Figure J.5, and Figure J.6 below. For the purposes of comparison, plots contain both Model A inter-storey displacements and those obtained when the diaphragm connections are not permitted to disconnect.

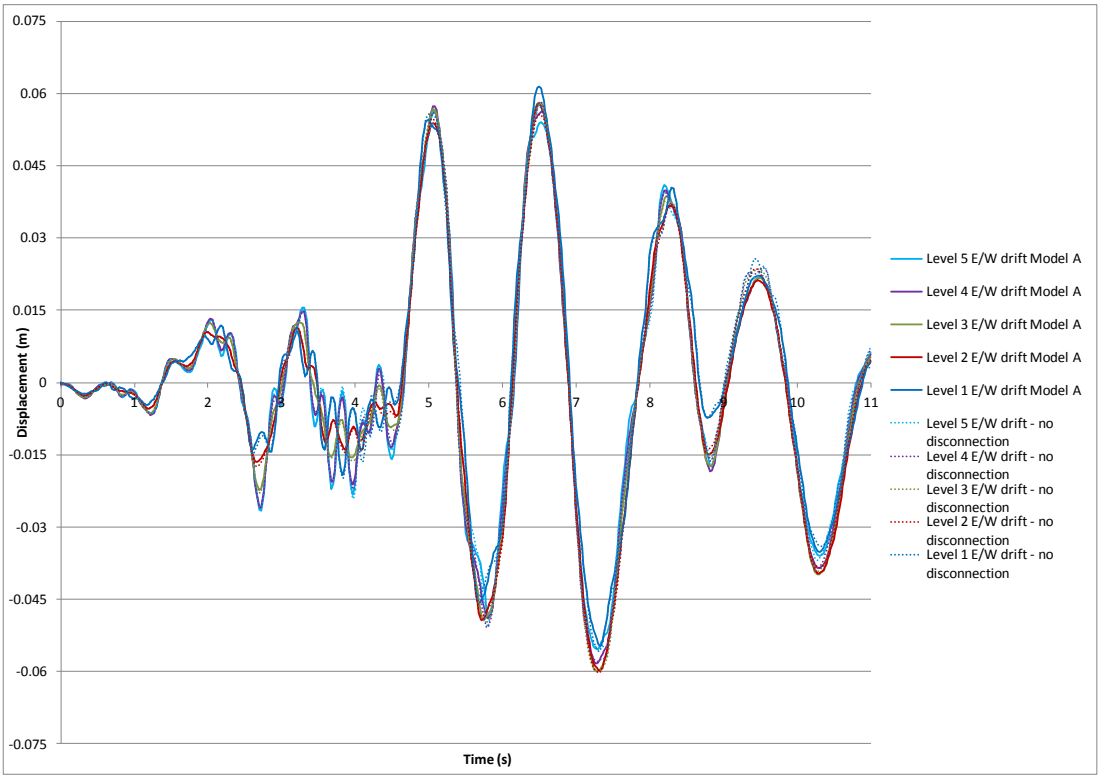

Figure J.5: Frame 1 east/west inter-storey displacements.

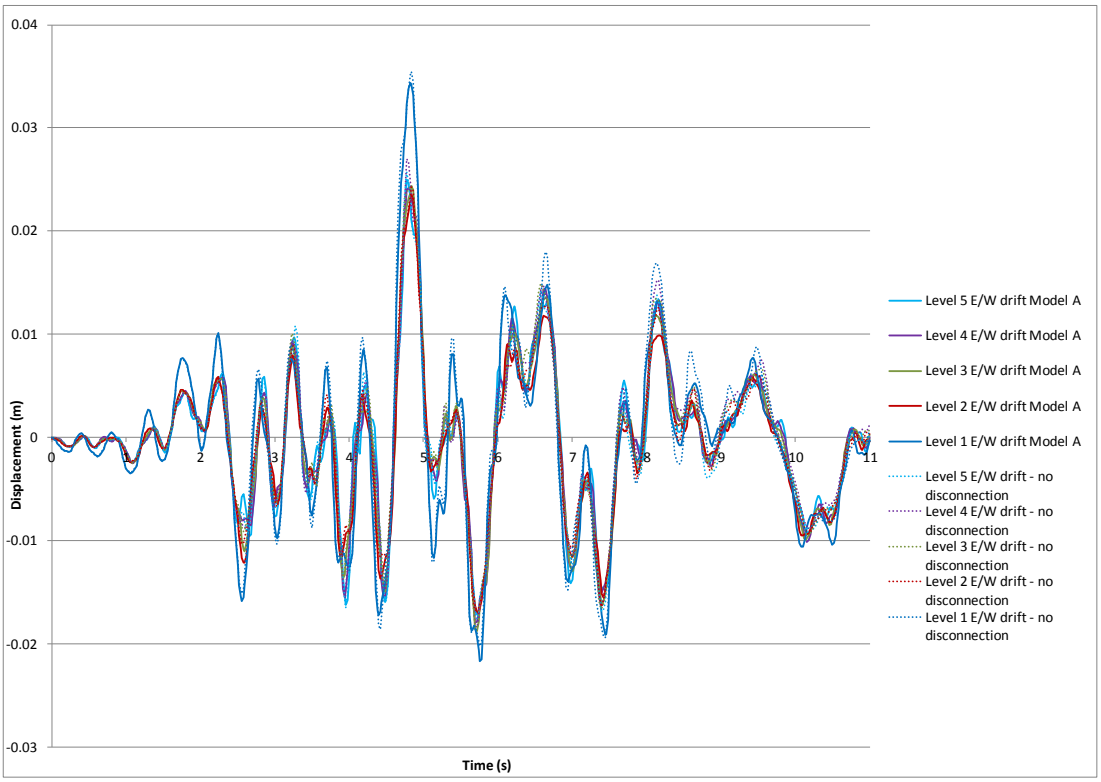

Figure J.6: Frame 4 east/west inter-storey displacements.

J.2 Diaphragm Connection Forces

Diaphragm connection forces are presented in Figure J.7 to Figure J.18 below. Note that moments are reported about the geometric centroid of the element being considered.

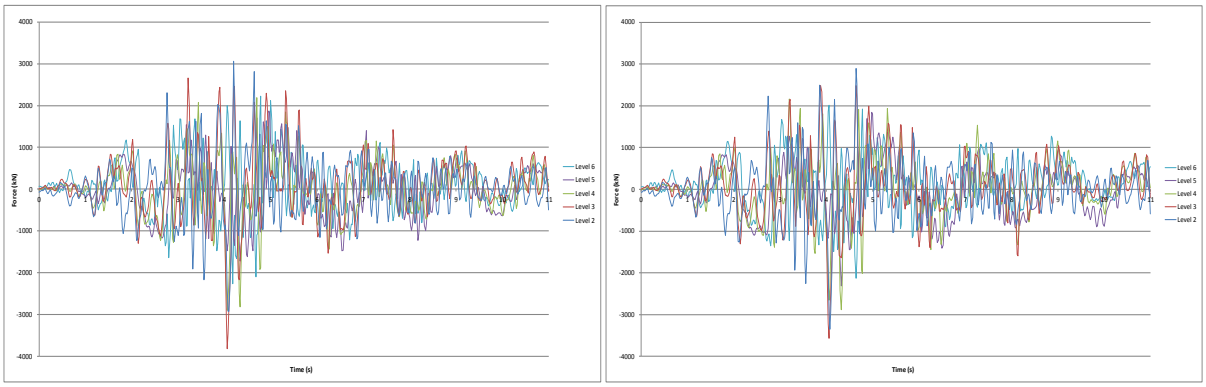

Figure J.7: North core total diaphragm north/south actions (disconnection on left, no disconnection on right).

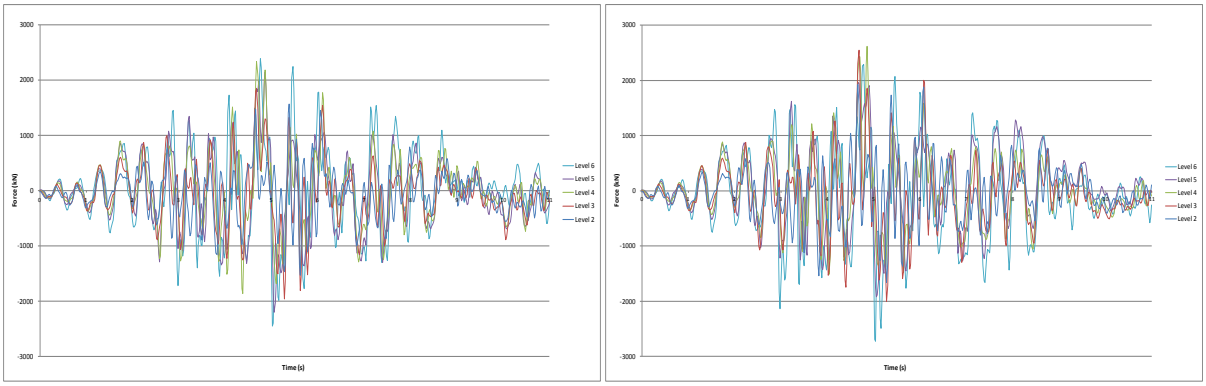

Figure J.8: North core total diaphragm east/west actions (disconnection on left, no disconnection on right).

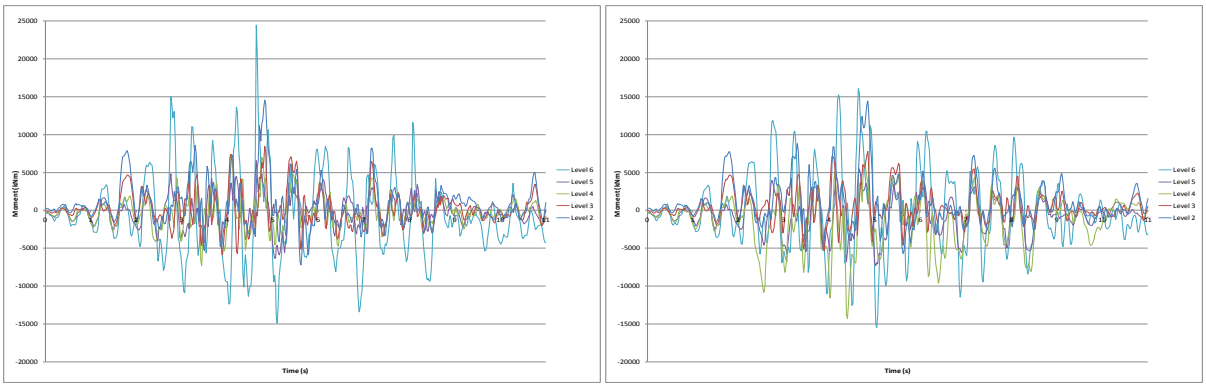

Figure J.9: North core total diaphragm in-plane moments (disconnection left, no disconnection right).

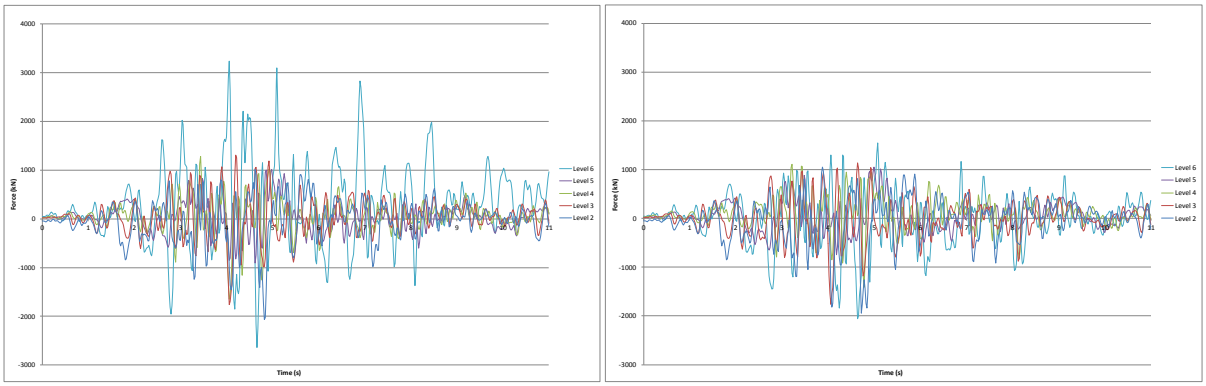

Figure J.10: North core Wall C diaphragm north/south actions (disconnection on left, no disconnection on right).

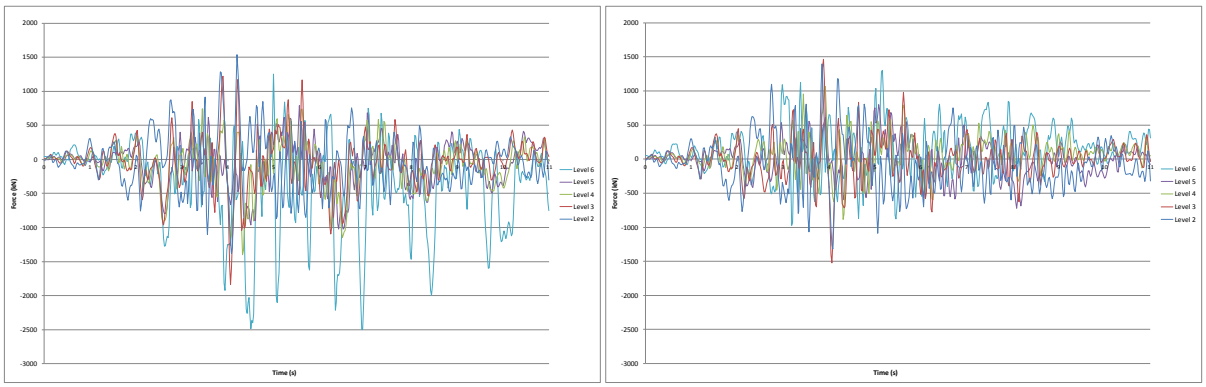

Figure J.11: North core Wall C/D diaphragm north/south actions (disconnection on left, no disconnection on right).

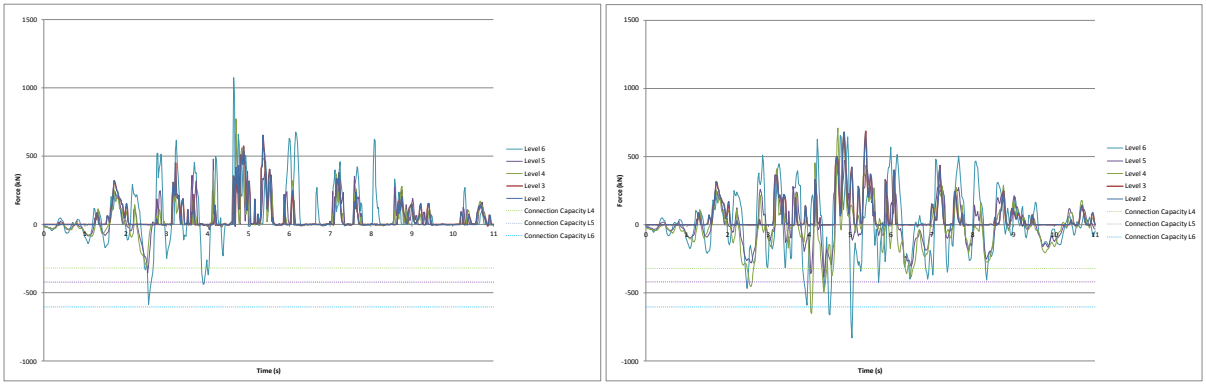

Figure J.12: North core Wall D diaphragm north/south actions (disconnection on left, no disconnection on right).

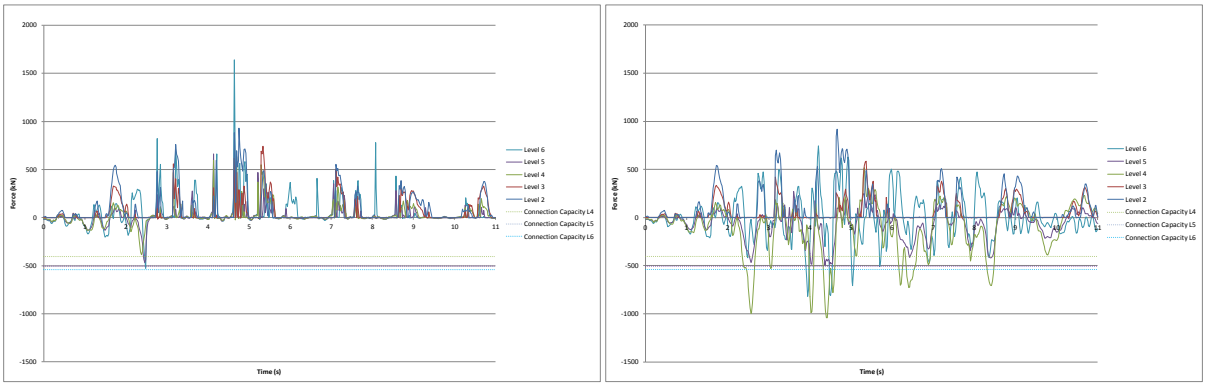

Figure J.13: North core Wall D/E diaphragm north/south actions (disconnection left, no disconnection right).

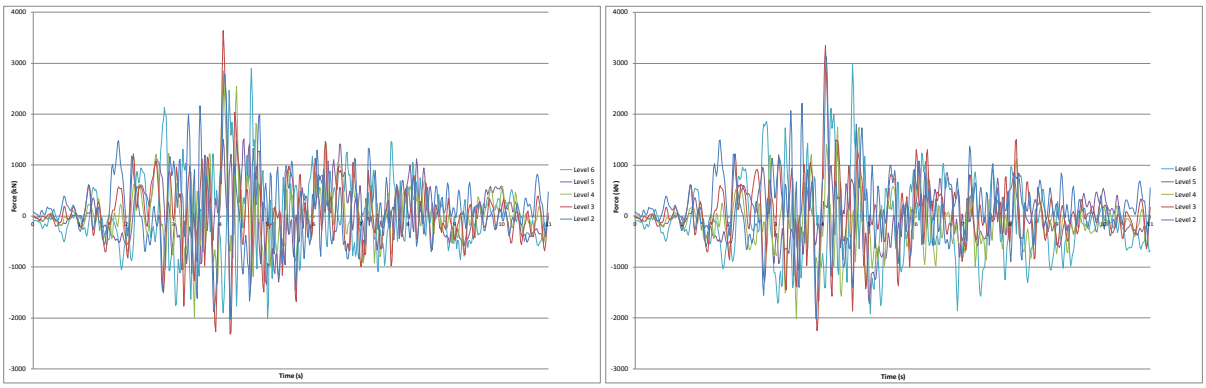

Figure J.14: North core Slab 4/C to C/D diaphragm north/south actions (disconnection on left, no disconnection on right).

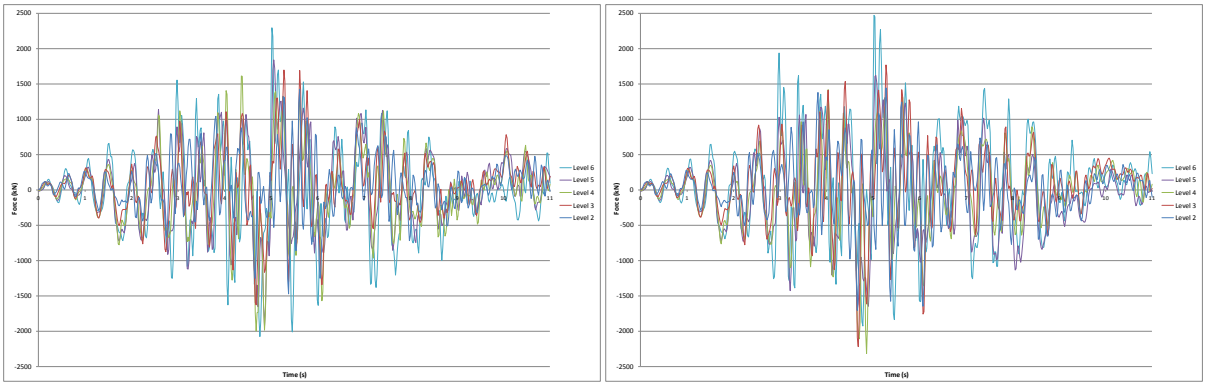

Figure J.15: North core Slab 4/C to C/D diaphragm east/west actions (disconnection on left, no disconnection on right).

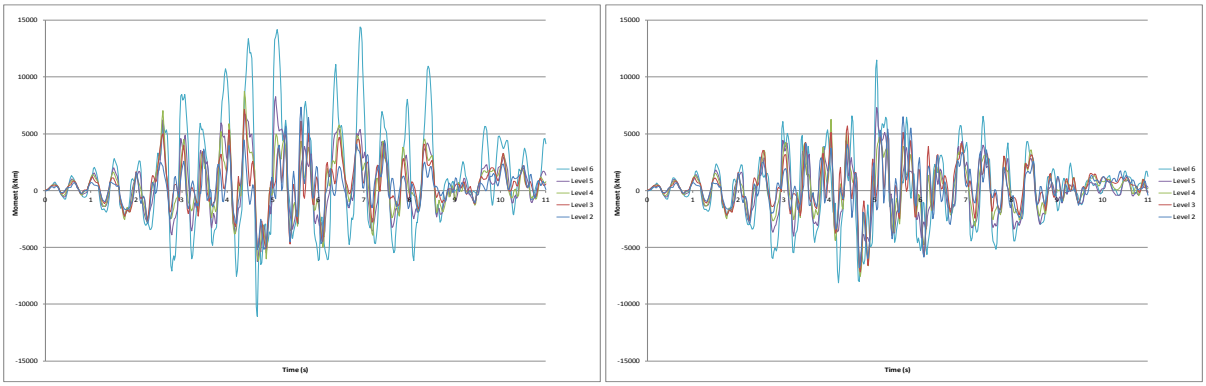

Figure J.16: North core Slab 4/C to C/D diaphragm in-plane moments (disconnection on left, no disconnection on right).

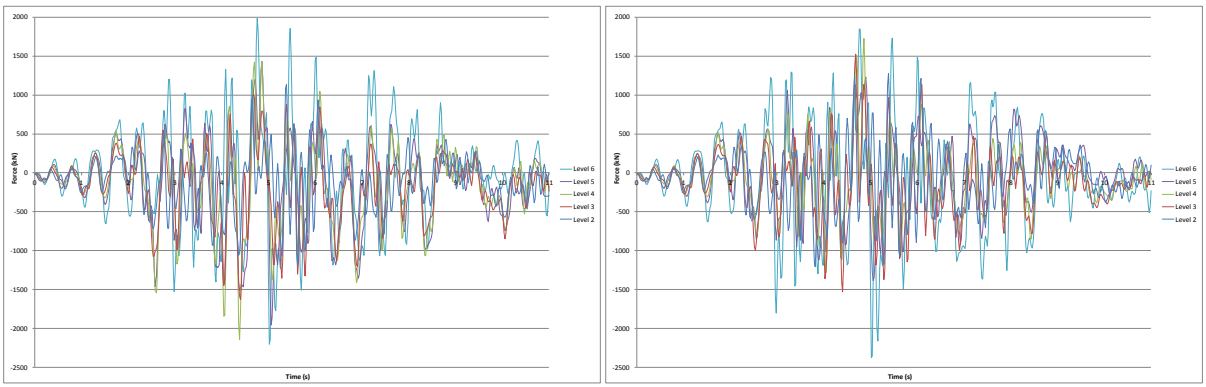

Figure J.17: North core Wall 5 diaphragm east/west actions (disconnection on left, no disconnection on right).

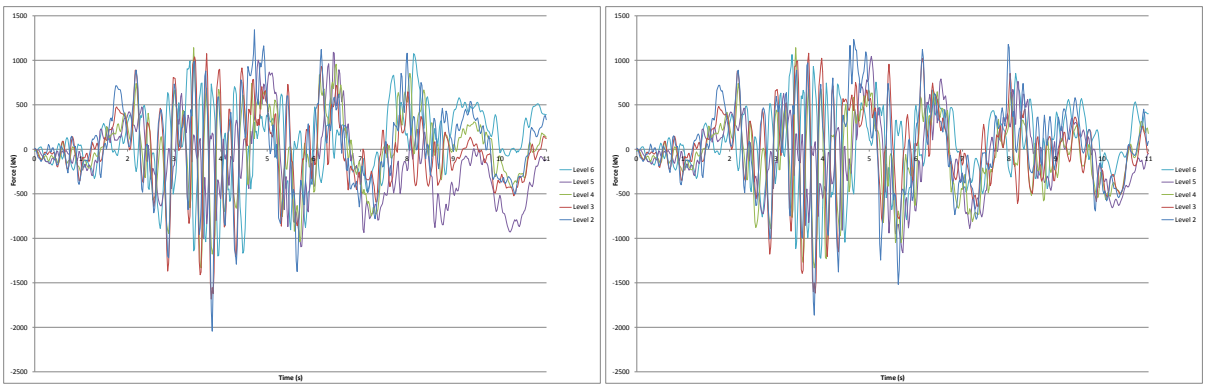

Figure J.18: South wall diaphragm east/west actions (disconnection on left, no disconnection on right).